uni.lu
UNIVERSITÉ DU
LUXEMBOURG

UNIVERSITÀ
DEGLI STUDI
DI GENOVA

PhD-FSTC-2018-79
The Faculty of Sciences, Technology
and Communication

Dipartimento di Fisica

DISSERTATION

Defence held on 17/12/2018 in Genova (Italy)

to obtain the degree of

DOCTEUR DE L'UNIVERSITÉ DU LUXEMBOURG

EN PHYSIQUE

AND

DOTTORE DI RICERCA

by

Alessio CALZONA
born on 07/03/1991 in Genova (Italy)

TOPOLOGY AND INTERACTION EFFECTS IN ONE-DIMENSIONAL SYSTEMS

Dissertation defence committee

Dr Maura Sassetti, Dissertation supervisor
Professor, Università degli Studi di Genova

Dr Thomas Schmidt, Dissertation supervisor
Associate professor, Université du Luxembourg

Dr Thierry Martin, Chairman
Professor, Aix-Marseille Université

Dr Ludger Wirtz, Vice Chairman
Professor, Université du Luxembourg

Dr Laurent Raymond
Associate professor, Aix-Marseille Université

Dr Fabio Cavaliere
Università degli Studi di Genova

Abstract

With the discovery of the integer quantum Hall effect by von Klitzing and collaborators in 1980, the mathematical field of topology entered the world of condensed matter physics. Almost three decades later, this eventually led to the theoretical prediction and the experimental realization of many intriguing topological materials and topology-based devices. In this Ph.D. thesis, we will study the interplay between topology and another key topic in condensed matter physics, namely the study of inter-particle interactions in many-body systems. This interplay is analyzed from two different perspectives.

Firstly, we studied how the presence of electron-electron interactions affects single-electron injection into a couple of counter-propagating one-dimensional edge channels. The latter appear at the edges of topologically non-trivial systems in the quantum spin Hall regime and they can also be engineered by exploiting the integer quantum Hall effect. Because of inter-channel interactions, the injected electron splits up into a couple of counter-propagating fractional excitations. Here, we carefully study and discuss their properties by means of an analytical approach based on the Luttinger liquid theory and the bosonization method. Our results are quite relevant in the context of the so-called *electron quantum optics*, a fast developing field which deeply exploits the topological protection of one-dimensional edge states to study the coherent propagation of electrons in solid-state devices. As an aside, we also showed that similar analytical techniques can also be used to study the time-resolved dynamics of a Luttinger liquid subject to a sudden change of the interaction strength, a protocol known as *quantum quench* which is gaining more and more attention, especially within the cold-atoms community.

Secondly, we study how inter-particle interactions can enhance the topological properties of strictly one-dimensional fermionic systems. More precisely, the starting point is the seminal Kitaev chain, a free-fermionic lattice model which hosts exotic Majorana zero-energy modes at its ends. The latter are extremely relevant in the context of *topological quantum computation* because of their non-Abelian anyonic exchange statistics. Here we show that, by properly adding electron-electron interactions to the Kitaev chain, it is possible to obtain lattice models which feature zero-energy parafermionic modes, an even more intriguing generalization of Majoranas. To this end, we develop at first an exact mapping between $\mathbb{Z}_4$ parafermions and ordinary fermions on a lattice. We subsequently exploit this mapping to analytically obtain an exactly solvable fermionic model hosting zero-energy parafermions. We study their properties and numerically investigate their signatures and robustness even when parameters are tuned away from the exactly solvable point.

To my parents.

Acknowledgements

First of all, I would like to thank my two supervisors Prof. Maura Sassetti and Prof. Thomas Schmidt for their guidance and for the many extremely useful discussions we had. I really appreciate them, both on the human and professional level, and I'm truly grateful for giving me the opportunity to work on intriguing topics with freedom and trust. Likewise, I would like to thank Dr. Matteo Carrega and Dr. Tobias Meng with whom I had the pleasure to collaborate on some projects: their insights and suggestions were priceless.

Secondly, I would like to thank Prof. Ludger Wirtz and Dr. Fabio Cavaliere for joining my thesis advisory committee (and all the entailed commitments) as well as Prof. Thierry Martin and Dr. Tobias Meng for agreeing to serve as referees for the present thesis. I'm also grateful to the Fonds National de la Recherche, Luxembourg.

Since my Ph.D. was done in two different places and teams, there are a lot of people who crossed my scientific path and who I warmly want to acknowledge. In particular, I would like to thank my colleagues in Genova (aka the *stanzino*'s members): Filippo Gambetta, Flavio Ronetti, Luca Vannucci, Matteo Acciai, and Sergio Porta! My lunches wouldn't have been so great without the guys of the self-managed L304 "canteen": Alba Domi, Alessio Bartocci, Anna de Marco, Daniele Rapetti, Enrico Lavagna, Federica Simonelli, Luca Marsicano, and Sebastian Salassi! An important mention goes also to the honorary members of the "canteen" Alex Amato, Chiara Righi, and Vanessa D'Amario since we did have some amazing adventures altogether (as well as some serious beach volleyball training sessions)!

From the Luxembourgish side, I'm extremely grateful to my office mates Hugo Tschirhart and Johan Ekström, as well as to the other members of Thomas' and Ludger's groups: Alejandro Molina-Sánchez, Ayush Kumar, Alexia Rod, Chris Pedder, Edvin Idrisov, Efterpi Kalesaki, Engin Torun, Francesco Naccarato, Fulvio Paleari, Giacomo Dolcetto, Henrique Miranda, Kristof Moors, Matteo Barborini, Patrick Haughian, Solofo Groenendijk, Sven Reichardt, and Thomas Galvani. We had interesting scientific discussions and, even more importantly, I'm sure we all made the first floor of BRB great (again?) by enjoying together so many coffee/tea brakes, lunches, dinners, movie nights, drone flights, Friday's pain au chocolat and so on ...

During my Ph.D. I had a truly great time, both in Genova and in Luxembourg. This has been possible thanks to the aforementioned people but also thanks to some other great friends outside the university... and since things are getting less official here I'll drop the surnames and go for nicknames instead! In Luxembourg, I happened to meet some amazing people: Acerina, Andrea, Andres, Erika, Ilaria, Jennifer, Maria, Momo and Kobi. We are now scattered around the world, but I really hope to keep in touch with you guys! A special mention goes to Johannes, with whom I enjoyed (and I'll hopefully enjoy again) great adventures in the mountains all over Europe!

I also want to thank my former bachelor's classmates Geo and Gianni who came to Luxembourg visiting (and bringing trofie and pesto with them... amazing!) as well as my flatmate in Genova, Nico!

Thinking about the time I spent in Genova, I'm very grateful to a wide group of amazing people which goes under different names (at least according to my WhatsApp conversations list): the ones of “Bisboccia”, of “Favi”, of “Ragashish”, of the various “Magialonghe”, of “Balla coi Cinghiali”... just to name a few. I really had a great time with you guys! So thanks a lot to my (almost) namesakes Ale Cal and Ale Cas, to Bianca, Caro, Cate, Chiara, Chiaretta, Coppe, Den, Dep, Dodo, Fra, Laura, Lollo, Luca, Pisto, Ruben, Rugge, Volpe, and Sivo!

A special thanks goes to FedeFerra, SimoLimo, and SimoMarco: they are not only my best ski buddies but also great Friends with capital F, as SimoLimo always says, even on powder days (and you know what that means!). I'm also extremely grateful to my oldest and dearest friends Elena, Lele, and Toto: we may not see each other so often but you really mean a lot to me!

Last but not least, a very special thanks goes to my parents Loretta and Vittorio for their neverending support!

Table of contents

List of figures

Introduction

With the discovery of the integer quantum Hall (IQH) effect in 1980 [1], the mathematical field of topology entered the world of condensed matter physics. It took a while to fully understand the potential of this interplay but, eventually, in the last decade a vast number of new topological materials have been theoretically predicted and experimentally realized. Beneficial effects on fundamental and applied research are countless and the importance of the topic is well testified by the 2016 Nobel prize in physics earned by David J. Thouless, F. Duncan M. Haldane, and J. Michael Kosterlitz “for their theoretical discoveries of topological phase transitions and topological phases of matter”.

One of the most intriguing features of topological materials is the existence of edge states. Indeed, because of the so-called bulk-boundary correspondence, the non-trivial topology of the bulk emerges also on the boundary of the system, where states with amazing properties can be found. Remarkably enough, because of their topological origin, these properties are robust with respect to perturbations and therefore accessible and exploitable in experiments.

The most known example of edge states is definitely provided by the IQH effect [2, 3], where one-dimensional (1D) gapless channels are present along the edges of a two-dimensional (2D) Hall bar pierced by a strong orthogonal magnetic field. While the bulk is insulating, the edge states act as perfect conductors, allowing for ballistic and coherent transport: electron are indeed topologically protected from backscattering. Their conduction properties are so good that these channels can represent the electronic analogous of the waveguides used in quantum optics for coherent photons transport.

This observation lies at the heart of a new and fast developing field known as electron-quantum optics (EQO) [4], whose aim is to transpose photonic quantum optics setups in electronic solid-state devices (see Fig. 1a). One of the key differences with respect to photons is that electrons do interact with each other, thus allowing for a much richer phenomenology. This is particularly true since effects of interactions in 1D are known to be dramatic and associated with exotic phenomena such as the fractionalization of the charge [5]. The study of interaction effects following a single-electron injection into ballistic 1D systems is precisely one of the

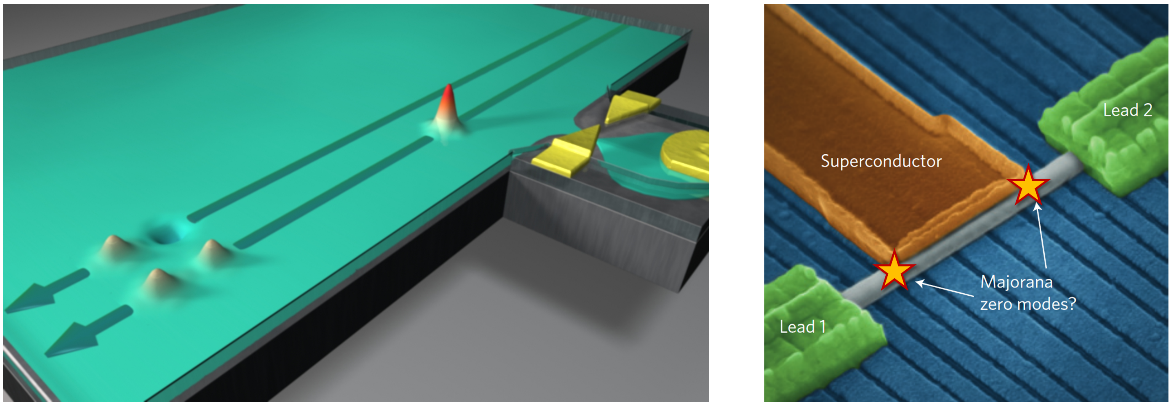

(a)

(b)

Fig. 1 (a) Edge of a 2D Hall bar with two co-propagating 1D ballistic channels. Because of their topological origin, they can be used as electronic waveguides in the context of EQO. In this sketch, an electron injected on the most external channel (red spike to the right) fractionalizes into different excitations (small peaks to the left) because of inter-channel interactions. Note that such a process cannot happen in conventional photonic quantum optics. Credits: B. Plaçais's group at LPA-ENS (http://www.phys.ens.fr/~placais/).
(b) Experimental setup used in L. Kouwenhoven group at TU Delft to create and study Majorana zero modes. They appear at the two ends of a quantum wire (in gray) coupled with a superconductor (orange) and are pictorially represented with two yellow stars. Image taken from Ref. [6].

main tasks addressed in the present thesis. In particular I will study the properties of the two fractional excitations which originate in a couple of counterpropagating channels.

Another seminal example of topological edge states is represented by the so-called Majorana zero energy modes, which arise at the two ends of a 1D topological superconductor. Interestingly enough, these excitations are non-Abelian anyons and they are likely to become the first particles of their kind to be experimentally observed. Theoretically proposed in 2001 [7], Majorana zero modes had in fact sparked a huge interest in the community which eventually leads to the observation of several exciting signatures, albeit not fully compelling yet, of their existence [8, 9] (see Fig. 1b). Their non-Abelian nature, together with the protection associated with their topological origin, makes Majorana zero modes very promising candidates for the so-called topological quantum computation (TQC), a way of performing quantum operations which minimizes decoherence at the hardware level [10].

While the research on Majorana zero modes is still ongoing, the community is also looking for even more exotic edge states of topological 1D systems [11]. In particular, the fact that Majoranas primarily emerge in non-interacting systems raises the question to which degree the presence of interaction allows to generate more complicated and intriguing zero modes. This point is precisely the other main task of the present thesis, where we will discuss the emergence of parafermions, a useful generalization of Majoranas, in interacting systems. In particular I will devise an exact and useful mapping between spinful fermions and parafermions on a lattice.

The thesis is organized as follows:

In **Chapter 1** an overview of topology in condensed matter is presented. After a general introduction, I will mainly focus on three topological systems of great interest: the IQH effect, the quantum spin Hall (QSH) effect and the 1D Kitaev chain (which hosts Majorana zero modes).

In **Chapter 2**, I will review the role of interactions in 1D systems. I will present the Luttinger liquid (LL) theory and discuss fractionalization phenomena both from a theoretical and an experimental point of view. A brief introduction to EQO is also provided, mainly focusing on single-electron injection processes and their relation with electron-electron interactions.

Chapter 3 contains our original results concerning the time evolution of out-of-equilibrium 1D interacting systems. In particular, the majority of the chapter is devoted to the study of single-electron injection into a couple of counterpropagating 1D ballistic channels. Within such a setup, which is relevant for EQO in either IQH or QSH bars, a couple of counterpropagating fractional excitations are created and we fully characterize their properties using LL theory [12, 13]. As an aside, I will also briefly present our results concerning the relaxation dynamics of a LL subject to an interaction quench, that is another protocol used to bring a system out-of-equilibrium [14, 15].

Chapter 4 begins with a review of the anyonic properties of Majorana zero modes, highlighting their relevance for TQC. Parafermions, a useful generalization of Majoranas, are then presented together with their richer and intriguing properties. In the second part of the chapter, I will present our original findings (see Ref. [16]) regarding the existence of an exact mapping between chains of parafermions and fermionic interacting 1D systems. This will allow us to built fermionic Hamiltonians which host zero energy modes obeying $\mathbb{Z}_4$ parafermionic algebra.

List of publications

This thesis is based on the following papers co-authored by myself:

- Ref. [12]: A. Calzona, M. Acciai, M. Carrega, F. Cavaliere, and M. Sassetti *"Time-resolved energy dynamics after single electron injection into an interacting helical liquid"* Phys. Rev. B **94**, 035404 (2016)
- Ref. [13]: M. Acciai, A. Calzona, G. Dolcetto, T. L. Schmidt, and M. Sassetti *"Charge and energy fractionalization mechanism in one-dimensional channels"* Phys. Rev. B **96**, 075144 (2017)[1]
- Ref. [14]: A. Calzona, F. M. Gambetta, F. Cavaliere, M. Carrega, and M. Sassetti *"Quench-induced entanglement and relaxation dynamics in Luttinger liquids"* Phys. Rev. B **96**, 085423 (2017)
- Ref. [15]: A. Calzona, F. M. Gambetta, M. Carrega, F. Cavaliere, T. L. Schmidt, and M. Sassetti *"Universal scaling of quench-induced correlations in a one-dimensional channel at finite temperature"* SciPost Phys. **4**, 023 (2018)
- Ref. [16]: A. Calzona, T. Meng, M. Sassetti, and T. L. Schmidt *"Z4 parafermions in one-dimensional fermionic lattices"* (Editors' suggestion) Phys. Rev. B **98**, 201110(R) (2018).

Other publications not included in this thesis are:

- Ref. [17]: A. Calzona, M. Carrega, G. Dolcetto, and M. Sassetti *"Transient dynamics of spin-polarized injection in helical Luttinger liquids"* Physica E **74**, 630 (2015)
- Ref. [18]: A. Calzona, M. Carrega, G. Dolcetto, and Maura Sassetti *"Time-resolved pure spin fractionalization and spin-charge separation in helical Luttinger liquid based devices"* Phys. Rev. B **92**, 195414 (2015)

---

[1] Despite not being the first author of this publication, I collaborated closely with Matteo Acciai in obtaining all the presented results. The writing of the paper was mainly done by Matteo Acciai.

- Ref. [19]: A. Calzona, F. M. Gambetta, M. Carrega, F. Cavaliere, M. Sassetti
  "Non-equilibrium effects on charge and energy partitioning after an interaction quench"
  Phys. Rev. B **95**, 085101 (2017)

- Ref. [20]: A. Calzona, F. M. Gambetta, M. Carrega, F. Cavaliere, and M. Sassetti
  "Asymmetries in the spectral density of an interaction-quenched Luttinger liquid"
  J. Phys.: Conf. Ser. **969** 012140 (2018)

Chapter 1

Topology in condensed matter

This chapter consists of a general overview of the role played by topology in condensed matter physics. To this end, after a general introduction, we will focus on some key ideas of topology such as the distinction between topological phases and the concept of topological invariant. Concrete examples of their application will be provided by reviewing some famous and important topological phenomena which will play a central role in the present thesis. It is the case of the integer quantum Hall effect (the first topological phenomenon which has been observed in condensed matter), of the quantum spin Hall effect and of the one-dimensional Kitaev chain.

1.1 What is topology?

Topology is a mathematical discipline concerned with all the properties of a system that cannot change continuously and are therefore invariant under smooth deformations of the system. One of the first topological results in history is the solution to the famous problem of the *Bridges of Königsberg*, provided by Leonhard Euler back in 1736 [21]. He demonstrated that it was impossible to find a route through the city of Königsberg (now Kaliningrad, in Russia) that would cross each of its seven bridges exactly once. This result is "topological" since it depends only on the connectivity properties of the system, i.e. which bridges connect to which islands or mainlands, and it is completely insensitive to smooth modifications of the bridges' length, of their mutual distance, of the islands' shape and so on.

Topology knew a rigorous development in the early part of the 20th century and it soon began to show up in many different branches, becoming one of the great unifying ideas of mathematics. With the discovery of the integer quantum Hall effect by von Klitzing and collaborators in 1980 [1], topology began to be explicitly applied also in condensed matter physics. The pioneering works of D. J. Thouless, F. D. M. Haldane, and J. M. Kosterlitz [22–24]

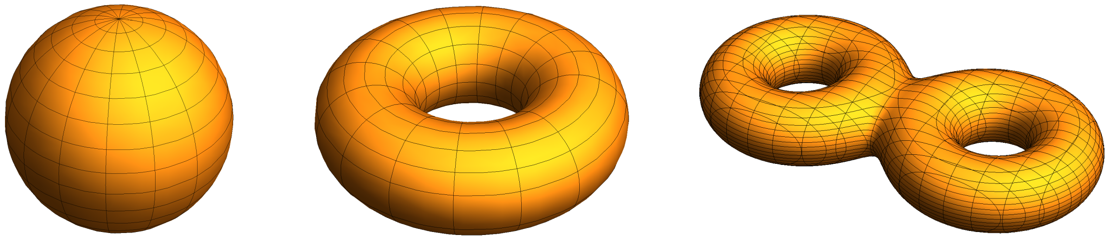

(a) $g = 0$ (b) $g = 1$ (c) $g = 2$

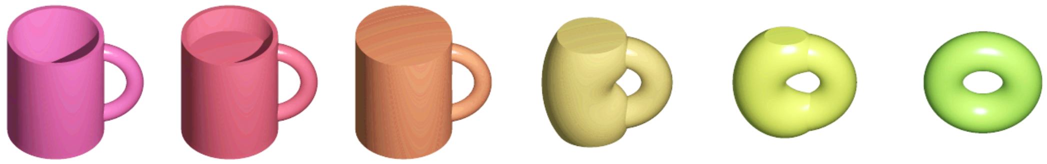

(d) Mugs and donuts are topologcally equivalent with $g = 1$.

Fig. 1.1 Examples of orientable surfaces with different genus g. Fig. 1.1d is taken from https://commons.wikimedia.org/wiki/File:Mug_and_Torus_morph.gif.

eventually led to the exciting and currently extremely active field of "topological quantum matter", earning the three scientists the Nobel Prize in Physics 2016. Nowadays, the interest in the study of topologically non-trivial systems is both at the level of fundamental research and in view of promising applications which exploits the intrinsic robustness of topology-related features. In this respect, a noteworthy research area is the so-called "topological quantum computation" (TQC) which aims at performing quantum computation minimizing decoherence at the hardware level [10, 25, 26]. TQC will be discussed in the fourth chapter (section 4.1.4).

1.1.1 Topological classification of surfaces

Before diving into the study of topologically non-trivial condensed matter systems, it is worth it to step back and consider the topological classifications of orientable surfaces in 3D, such as spheres and tori. This will allow introducing the building concepts of topology in an intuitive way before generalizing them to more abstract objects. In Fig. 1.1 three different orientable surfaces are shown: a sphere, a torus, and a double torus. In order to classify them, we introduce an integer quantity g called *genus* which counts the number of holes featured by each object. It's easy to argue that g is indeed a topological property: being an integer, it cannot change continuously and it is, therefore, invariant with respect to continuous deformation of the objects. The only way to abruptly modify it is to plug or pierce holes. Objects with the same genus belong to the same topological class and share the same topological properties. This can be

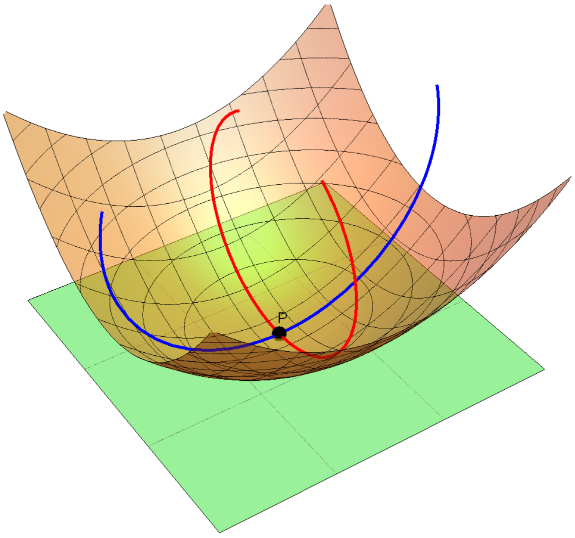

Fig. 1.2 Gaussian curvature at point P (in black). The tangent plane in P is shown in green. The eigenvalues of the Hessian represent the inverse radius of the two circles (red and blue), aligned with the two eigenvectors.

summarized with a traditional joke, stating that a topologist cannot distinguish between a mug and a donut. They indeed both have $g = 1$ and can be continuously deformed into each other as shown in Fig. 1.1d.

A topological invariant, like the genus of orientable surfaces, is clearly a global property of the system and it is not *directly* related to local features, e.g. the particular shape and curvature of the mug's handle in Fig. 1.1d. Interestingly enough, however, integrals of certain local quantities over the *whole* object do provide information about the topology. This is a crucial point and we are going to discuss it in details.

At first, let us introduce the geometric local Gaussian curvature of a smooth surface. Given a generic point P on the surface, it is possible to choose the coordinates such that the tangent plane in P is described by the equation $z = 0$. The surface can be therefore locally specified by a function $z(x,y)$. The Gaussian curvature $\mathcal{G}(P)$ is defined as the determinant of the Hessian of $z(x,y)$ in P

$$\mathcal{G}(P) = \det \begin{pmatrix} \partial_x^2 z\big|_P & \partial_x \partial_y z\big|_P \\ \partial_y \partial_x z\big|_P & \partial_y^2 z\big|_P \end{pmatrix}. \tag{1.1}$$

Its geometric interpretation is easy: the determinant of the Hessian (which is symmetric) is the product of its eigenvalues which, in turn, correspond to the inverse radius of curvature of the surface along the two orthogonal eigenvectors. See the sketch in Fig. 1.2.

According to the Gauss-Bonnet theorem, the integral of the local Gaussian curvature over the whole surface turns out to be a topological invariant. In particular, it is directly related to the genus g of the surface[1]

$$\int_S \mathcal{G}(P)\, ds = 2\pi(2-2g)\,. \tag{1.2}$$

A simple example is provided by considering a sphere with radius r. Its Gaussian curvature is position-independent and simply reads r^{-2}: the integral over the whole surface gives 4π and therefore a genus $g = 0$, as expected.

1.1.2 Topology in condensed matter systems

The very same concepts used to study the topology of orientable surfaces in 3D can be applied in order to classify gapped[2] condensed matter systems. It indeed turned out that there are different gapped systems whose Hamiltonian cannot be continuously modified one into the other *without* closing the energy gap. A gap closure plays therefore exactly the same role of the act of plugging or piercing a hole in a 3D surface: it can separate two phases with different topology, i.e. characterized by different topological invariants. These discrete quantities are unaffected by continuous deformation of the system's Hamiltonian and can only change abruptly when the system goes through a gap closure.

Note that these topological invariants can be usually identified with physical properties of the system such as, for instance, a quantized electrical conductance or a particular ground-state degeneracy. Their topological origin automatically ensures them an extraordinary robustness with respect to perturbations. In this regard, a prototypical example is represented by the conductance plateaux of the quantum Hall effect: here, the measured conductance is quantized to an extraordinary accuracy (one part in 10^9) regardless the particular characteristics of the sample considered. The robustness of topological phenomena and the fact that they don't require fine-tuning of parameters represent key advantages when it comes to experiments and practical applications.

In the following, we are going to describe the topological properties of the integer quantum Hall (IQH) effect, the first discovered and most known topological phase of matter. We then briefly present the whole topological classification of non-interacting systems based on non-spatial symmetries, focusing in particular on the quantum spin Hall (QSH) effect and its helical edge states. Finally, a prototypical example of a topological system in 1D, the so-called Kitaev chain, is presented.

---

[1] This simple expression holds for orientable compact surfaces without boundaries.

[2] A gapped system is a system which features a finite energy gap between the ground state and the first excited states even in the thermodynamic limit.

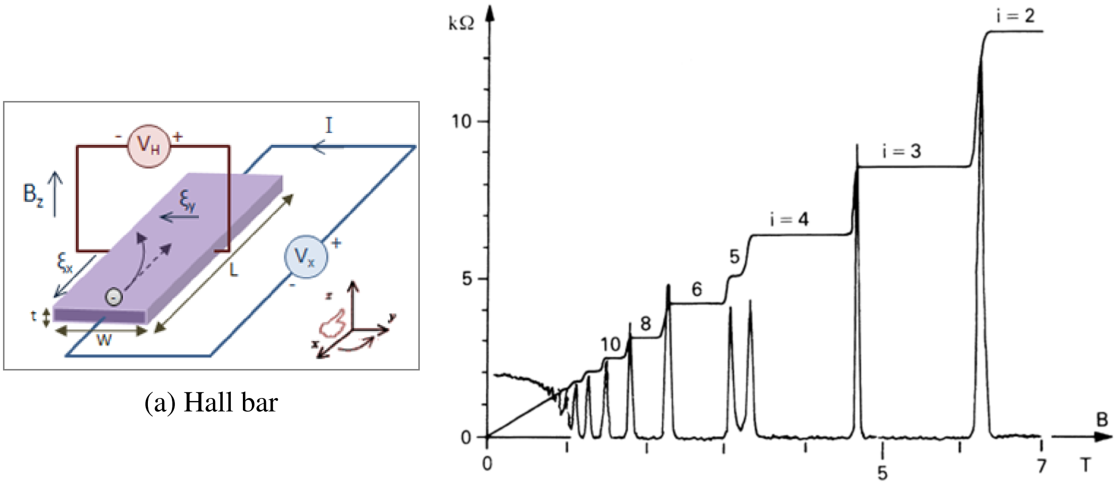

(a) Hall bar

(b) Quantum Hall effect

Fig. 1.3 (a) The typical 4-terminal scheme used to measure the Hall effect. Image taken from: https://upload.wikimedia.org/wikipedia/en/1/19/Hall_Effect_Measurement_Setup_for_Electrons.png. (b) Discovery of the quantum Hall effect: measure of the resistivity tensor ρ as a function of the magnetic field B (ρ_{xy} is the one featuring the plateau while ρ_{xx} is the one featuring the spikes). Image taken from [31].

It is important to note that also gapless systems can feature a non-trivial topology. Noteworthy examples are Weyl and Dirac semimetals [27–30]. These systems, however, won't be discussed in the present thesis.

1.2 Quantum Hall effect

The classical Hall effect was discovered in 1879 by Edwin Hall. He indeed observed that, when a current I is made to flow along the x-direction in a metallic sheet pierced by an orthogonal magnetic field $\vec{B} \parallel \hat{z}$, a Hall voltage V_H develops in the y-direction (see Fig.1.3a). More precisely, the off-diagonal terms of the resistivity tensor

$$\vec{E} = \rho \vec{\mathcal{J}} \tag{1.3}$$

happen to be proportional to the magnetic field

$$\rho_{xy} = \frac{B}{nq}. \tag{1.4}$$

Here n is the charge carrier density, q their charge, $\vec{E}$ the electric field and $\vec{\mathcal{J}}$ the current density.

This effect, experimentally very useful in determining n and the sign of q, is a direct consequence of the classical Lorentz force acting on the charge carries. At low temperature and high magnetic fields, however, quantum effects kick in and lead to a more intriguing phenomenology. The quantum regime was experimentally explored for the first time in 1980 by von Klitzing, using samples prepared by Pepper and Dorda [1]. The observed resistivity deviated strongly from the classical expectation. In particular, as shown in Fig. 1.3b, the Hall resistivity ρ_{xy} is no more linear in the magnetic field and remarkably features quantized plateaux

$$\rho_{xy} = \frac{h}{e^2}\frac{1}{\nu} \qquad \nu \in \mathbb{Z}. \tag{1.5}$$

where the longitudinal resistivity vanishes $\rho_{xx} = 0$. The corresponding conductance tensor $\sigma = \rho^{-1}$ has a vanishing longitudinal conductance $\sigma_{xx} = 0$ and a quantized off-diagonal (or Hall) conductance

$$\sigma_{xy} = \nu\,\frac{e^2}{h} \qquad \nu \in \mathbb{Z}. \tag{1.6}$$

Interestingly enough, the heights of these plateaux depend only on universal quantities and the quantization is extremely accurate (up to one part in 10^9) regardless of the specific properties of the sample. As pointed out in the previous Section, such a robustness strongly suggests that the system is a non-trivial topological phase.

The IQH effect can be analyzed by different means, each one aiming at emphasizing different aspects, as testified by the vast existing literature (see for example [32–34, 31, 35–37]). The traditional microscopic approach, also known as Büttiker theory [33], directly focuses on the transport properties featured by Landau levels in a confined and disordered system. It successfully explains the experimental data and the existence of robust 1D channels at the edges of the Hall sample. This approach, however, does not fulfill the main goal of the present discussion: highlight the topological origin of the Hall effect. To this end, it is convenient to follow another approach which somehow parallels the one used for the topological classification of orientable surfaces in Sec. 1.1.1. Three main steps are in order:

- introduce the key concept of local Berry curvature (analog to the Gaussian curvature);
- relate it to a global topological invariant known as Chern number (thus paralleling the Gauss-Bonnet theorem);
- link the topological invariant to a physical quantity, the Hall conductivity (analogous to the genus, i.e. the “physical” number of holes).

Once the topological nature of the Hall effect is fully established, we will focus on a finite Hall bar in order to discuss the concept of bulk-boundary correspondence and the existence of gapless edge channels.

1.2.1 Berry phase

The Berry phase, introduced in 1984 by Sir M. V. Berry [38], is one the most important concept in topological band theory. The key idea is that adiabatic transport can modify a quantum state by a phase other than just the dynamical phase. To be more precise, let us consider an Hamiltonian $H(\vec{\lambda})$ depending on several parameters $\vec{\lambda} = (\lambda_1, \lambda_2, \ldots, \lambda_j, \ldots)$ which can be slowly varied in time along a path $\mathcal{C}$ in parameter space. The Hamiltonian can be diagonalized at each point in the parameter space

$$H(\vec{\lambda})|n(\vec{\lambda})\rangle = E_n(\vec{\lambda})|n(\vec{\lambda})\rangle \tag{1.7}$$

providing us with a parameter-dependent set of eigenstates $|n(\vec{\lambda})\rangle$. Note that the Schroedinger equation determines these eigenstates up to a phase (or a unitary matrix in presence of degeneracy): there is a gauge freedom, local in the parameter space. It is possible to exploit this freedom in order to pick a gauge such that the phase is locally smooth and single-valued.

Let us now focus on a (non-degenerate) eigenstate $|n_0(\vec{\lambda}(0))\rangle$ of the Hamiltonian and study its time evolution $|\psi(t)\rangle$ as the parameters are varied in time along $\mathcal{C}$. Provided that level crossing are avoided, the adiabatic theorem ensures that at each time one has

$$|\psi(t)\rangle = e^{i\theta(t)}|n_0(\vec{\lambda}(t))\rangle. \tag{1.8}$$

The phase $\theta(t)$ can be easily computed exploiting the time-dependent Schrödinger equation for $|\psi(t)\rangle$ and it consists of two contributes [39]. The first one is the standard dynamical phase while the second one is more subtle and arise from the fact that states at different $\vec{\lambda}$ are not identical[3]. Considering the whole path $\mathcal{C}$, this second contribution (with opposite sign) is called Berry phase and reads

$$\gamma_{n_0,\mathcal{C}} = \int_{\mathcal{C}} \vec{\mathcal{A}}_{n_0}(\vec{\lambda}) \cdot d\vec{\lambda} \tag{1.9}$$

where

$$\vec{\mathcal{A}}_{n_0}(\vec{\lambda}) = i\,\langle n_0(\vec{\lambda})|\vec{\nabla}_{\lambda}|n_0(\vec{\lambda})\rangle \tag{1.10}$$

---

[3] Applying the Schrödinger equation to the eigenstate (1.8), one has indeed

$$E_{n_0}(\vec{\lambda}(t))|n_0(\vec{\lambda}(t))\rangle = \hbar\frac{d\,\theta(t)}{dt}|n_0(\vec{\lambda}(t))\rangle + i\hbar\frac{d}{dt}|n_0(\vec{\lambda}(t))\rangle\,.$$

Taking the scalar product with $\langle n_0(\vec{\lambda}(t))|$, one find the solution for $\theta(t)$

$$\theta(t) = \hbar^{-1}\int_0^t E_{n_0}(\vec{\lambda}(\tau))d\tau - i\int_0^t \langle n_0(\vec{\lambda}(\tau))|\frac{d}{d\tau}|n_0(\vec{\lambda}(\tau))\rangle\,d\tau$$

is known as Berry connection (and it is always real). The latter is obviously a gauge dependent quantity: under a gauge transformation $|n_0(\vec{\lambda})\rangle \to e^{i\zeta(\vec{\lambda})}|n_0(\vec{\lambda})\rangle$ with $\zeta(\vec{\lambda})$ a smooth and single-valued function, the Berry connection transforms in the usual way

$$\vec{\mathcal{A}}_{n_0}(\vec{\lambda}) \to \vec{\mathcal{A}}_{n_0}(\vec{\lambda}) - \vec{\nabla}_\lambda \zeta(\vec{\lambda}). \tag{1.11}$$

As for the Berry phase $\gamma_{n_0,\mathcal{C}}$, it changes by $\zeta(\vec{\lambda}(T)) - \zeta(\vec{\lambda}(0))$ where T is the long time after which the path $\mathcal{C}$ has been completed.

Let us now focus on a closed path $\mathcal{C}$. The question is: can the Berry phase be completely gauged away or not? In a closed loop one obviously has $|n_0(\vec{\lambda}(0))\rangle = |n_0(\vec{\lambda}(T))\rangle$. Such a property is maintained by every gauge transformation, meaning that

$$e^{i\zeta(\vec{\lambda}(0))}|n_0(\vec{\lambda}(0))\rangle = e^{i\zeta(\vec{\lambda}(T))}|n_0(\vec{\lambda}(T))\rangle \quad \Rightarrow \quad \zeta(\vec{\lambda}(T)) - \zeta(\vec{\lambda}(0)) = 2\pi m \quad m \in \mathbb{Z}. \tag{1.12}$$

This result tells us that the Berry phase computed on a closed path $\mathcal{C}$ cannot be completely gauged away (it can only change by multiples of 2π) and therefore it must be physically relevant [39].

Interestingly, in analogy with electromagnetism, it is possible to define also a local gauge-invariant quantity by computing

$$\begin{aligned}\mathcal{F}^{n_0}_{jk}(\vec{\lambda}) &= \partial_{\lambda_j}\left(\vec{\mathcal{A}}_{n_0}(\vec{\lambda})\right)_k - \partial_{\lambda_k}\left(\vec{\mathcal{A}}_{n_0}(\vec{\lambda})\right)_j \\ &= i\langle\partial_{\lambda_j} n_0(\vec{\lambda})|\partial_{\lambda_k} n_0(\vec{\lambda})\rangle - i\langle\partial_{\lambda_k} n_0(\vec{\lambda})|\partial_{\lambda_i} n_0(\vec{\lambda})\rangle\end{aligned} \tag{1.13}$$

which is known as the Berry curvature. If, for the sake of simplicity, we consider a three-dimensional parameter space, the contraction of the Berry curvature with the Levi-Civita symbol

$$\varepsilon_{ijk}\mathcal{F}^{n_0}_{jk} = \left(\vec{\nabla} \times \vec{\mathcal{A}}_{n_0}\right)_i \tag{1.14}$$

can be readily interpreted as a magnetic field in the parameter space. Provided that the Berry connection is smooth, it is possible to use the Stokes theorem in order to express the Berry phase in terms of the Berry curvature

$$\gamma_{n_0,\mathcal{C}} = -\mathrm{Im}\int dS_i \, \varepsilon_{ijk}\mathcal{F}^{n_0}_{jk} \tag{1.15}$$

where the integral runs over a surface whose boundary is $\mathcal{C}$ and whose oriented surface element is $d\vec{S}$.

The Berry curvature plays the same role as the Gaussian curvature in Eq. (1.1). Although defined on different spaces, they are both local and physical quantities. The next task will be to construct a global topological invariant out of the Berry curvature and to clarify its physical meaning, in complete analogy with what we have seen talking about the genus of orientable surfaces and the Gauss-Bonnet theorem.

1.2.2 Chern number and TKNN invariant

In this subsection we will focus on a particular parameter space, namely the first Brillouin zone of a 2D system. Instead of a generic $\vec{\lambda}$, we will therefore consider as parameters the two components of the crystal momentum $\vec{k} = (k_x, k_y)$. Note that, from a geometrical point of view, the first Brillouin zone has no boundaries and can be described as a 2D torus $\mathcal{T}^2$.

The goal is to compute the integral of the Berry curvature over the whole space. If it is possible to find a gauge such that the Berry connection is smooth everywhere on the torus, a straightforward application of the Stokes theorem gives

$$\int_{\mathcal{T}^2} \varepsilon_{ijk}\, \mathcal{F}^{n_0}_{jk}(\vec{k})\, (d\vec{k})_i = \int_{\mathcal{T}^2} \vec{\nabla} \times \vec{\mathcal{A}}_{n_0}(\vec{k}) \cdot d\vec{k} = 0 \tag{1.16}$$

since $\mathcal{T}^2$ has no boundaries. However, it is not always possible to find a such a gauge and the Stokes theorem cannot therefore be applied. As a result, one can show that the integral of the Berry curvature can be non-zero and acquire integer values [39]

$$\int_{\mathcal{T}^2} \varepsilon_{ijk}\, \mathcal{F}^{n_0}_{jk}(\vec{k})\, (d\vec{k})_i = 2\pi\, C_{n_0} \quad C_{n_0} \in \mathbb{Z}\,. \tag{1.17}$$

Here the integer number C_{n_0} is known as the first Chern number of the band n_0. A non-vanishing Chern number can be seen as a global property of the band, resulting from an obstruction to the application of Stokes theorem over the whole torus. In Appendix A.1 we give an intuition why C_{n_0} has to be an integer, referring to literature for more details [40].

Eq. (1.17) can be seen as the analogous of the Gauss-Bonnet theorem and the Chern number represents the topological invariant we were looking for. The next task is to relate it with some physical quantity. Remarkably enough, it turned ou to be directly linked to the Hall conductance of a 2D gapped system. In particular, the sum of the Chern numbers associated with each occupied band α is

$$\sum_\alpha C_\alpha = \sigma_{xy} \frac{h}{e^2}\,. \tag{1.18}$$

This crucial result has been demonstrated a seminal paper by Thouless, Kohmoto, Nightingale and den Nijs [41] in 1982. They basically computed the Hall conductance in terms of current-current correlators, in the framework of linear response theory. Current operators are in turn expressed in terms of group velocity, i.e. derivative of the Hamiltonian with respect to k_x and

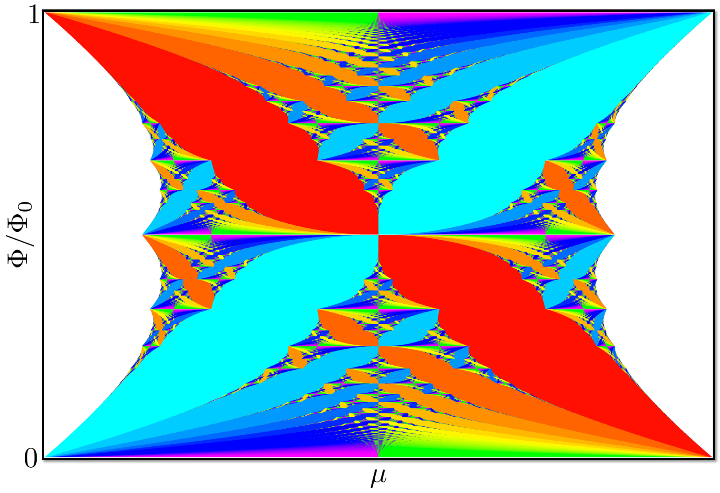

Fig. 1.4 Hofstadter's butterfly. The horizontal axis gives the chemical potential μ (zero electron density at the left side). The vertical axis indicates magnetic flux per unit cell Φ of the crystal lattice (from zero at the bottom to one flux quantum Φ_0 at the top). At higher fluxes, the phase diagram repeats periodically. Warm (cool) colors indicate negative (positive) Chern numbers. White regions indicate a vanishing Chern number. Image taken from https://commons.wikimedia.org/wiki/File:Hofstadter%27s_butterfly.png

k_y, eventually leading to the remarkable identification (1.18). More details can be found in Appendix A.2.

Several comments are in order. Eq. (1.18) relates a physical and measurable quantity, the Hall conductance, to a topological invariant, the Chern number. This nicely explains the robustness of the former with respect to perturbations which continuously modify the band structure of the system[4]. Note, however, that so far we haven't actually computed the Chern number for a given band: this task is not trivial and it won't be addressed in this thesis (the interested reader is referred to the existing literature, e.g. Ref. [41, 39, 31]). That said, it is worth it to mention one famous result which holds for free fermions on 2D square lattice in presence of an external magnetic field. Here, the interplay between the lattice periodicity and the magnetic length leads to a very complicated band structure, with fractal properties [42]. For given chemical potential and magnetic flux per unit cell, it is possible to compute the Hall conductance of the system by summing the Chern numbers of the occupied bands. The result, a structure known as Hofstadter's butterfly, is shown in Fig. 1.4 and it has been recently confirmed experimentally [43].

As a last remark, note that an external magnetic field is not necessary in order to have bands with non-vanishing Chern number: as we will discuss in Subsection 1.3, what really matters is the breaking of time-reversal symmetry. Models with non-zero Hall conductance in absence

---

[4] i.e. perturbations which does not make the system gapless.

of magnetic field are know as *Chern insulators*, see for example Ref. [44] and the seminal Haldane model in Ref. [24].

1.2.3 Edge states

What we have shown so far is that a 2D translational invariant insulators can be characterized in terms of a Chern number, a topological invariant which is remarkably related to an important bulk response function: the Hall conductivity. Moreover, we reported that there are many gapped systems, such as lattice electrons in a magnetic field, which feature bands with non-vanishing Chern numbers. This implies a nonzero Hall conductivity and therefore non-trivial transport properties: how can this be possible in a gapped system? Whenever the system's geometry is finite and conceived in order to allow experimental measurements (e.g. when contacts are present), the answer lies in the presence of edge states [39]: the system is a bulk insulator but features gapless edges channels carrying electrical current. Their existence is an inescapable consequence of many factors and, as it turns out, it represents a peculiar aspect of many other topological insulators.

In order to develop some intuition, it is worth it to present the following simple argument[5]. Let us consider two 2D insulators, with different Hall conductances, placed close together so that they share a 1D boundary. The Hall conductance characterizes the topological phase of each system and it cannot change unless the bulk gap collapses and reopens again. Therefore, the boundary region must have a gap-closing-and-reopening point somewhere, i.e. it must feature 1D edge modes which cross the Fermi level. This kind of arguments applies to boundaries between any two topologically distinct insulators, provided that the boundary respect the symmetry protecting the bulk-insulting phase, and it is a manifestation of the so-called bulk-edge correspondence [39].

The original argument which clarified the role of edge states in IQH effect is due to the seminal work by R. Laughlin [2], later refined by Halperin [3]. The key idea, which allowed to explain even better the meaning of a finite Hall conductance in an insulating material, is that there is a non-standard way of carrying current. In the usual tight-binding picture, current flows as a result of electrons hopping between neighbor orbitals. Interestingly, it is also possible to have a current if the "orbitals" themselves move, without any electron hopping: such a phenomenon is known as spectral-flow and it is quite relevant in the quantum Hall effect as we are going to show.

Let us consider a Hall bar, pierced by an orthogonal magnetic field, wrapped into a cylindrical shape as shown in Fig. 1.5a: periodic boundary conditions are ensured in the y-

---

[5] Note that this argument actually holds only for very smooth edges, so that band structure can be locally well defined. The Laughlin argument discussed below is more general and robust.

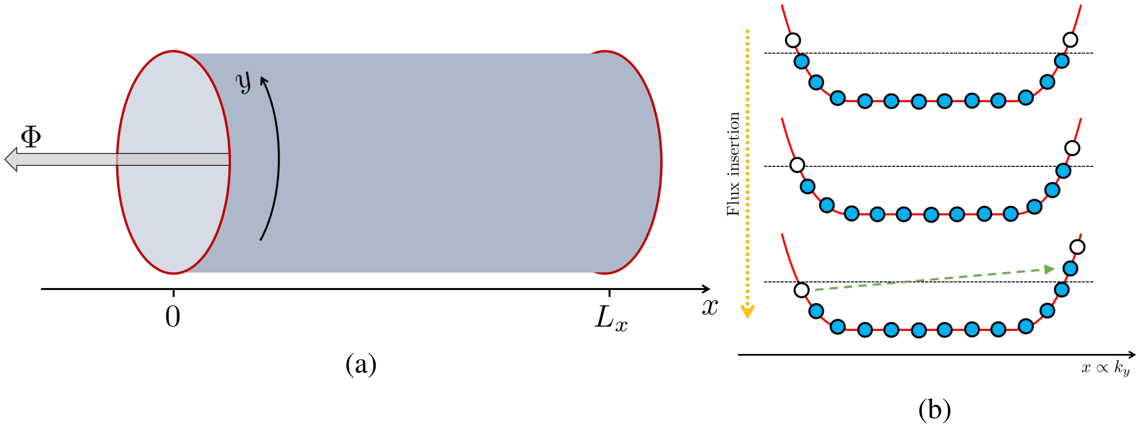

(a)

(b)

Fig. 1.5 (a) Laughlin pumping argument: periodic boundary conditions are imposed along the y direction of an Hall bar. The resulting cylinder is threaded by a magnetic flux Φ. (b) Sketch of the spectral flow in Landau level. Blue (white) spots represent occupied (unoccupied) states. The black dashed lines are the Fermi energy. After the insertion of one flux quantum, an electron has effectively moved from the left to the right edge (green arrow).

direction while edges are placed at $x = 0$ and $x = L_x$. An additional magnetic flux Φ is inserted through the cylinder, parallel to the x-axis. If such a flux changes in time, several things happen.

1. By Faraday's law, an electric field in the y direction is induced on the cylinder $E_y = -L_y^{-1}\partial_t \Phi$. Because of the Hall conductance (1.18), this determines a current density in the x direction $\mathcal{J}_x = \sigma_{xy} E_y$.
2. If the flux changes by a flux quantum $\Phi_0 = h/e$, it can be gauged away meaning that the spectrum of the system's Hamiltonian is unchanged.
3. A change in the flux $\delta\Phi$ shifts the k_y momentum of the electrons, which is a good quantum number in view of the translational invariance, by $k_y \to k_y + 2\pi L_y^{-1}\,\delta\Phi/\Phi_0$.

Considering an adiabatic insertion of a flux quanta, an integer total charge

$$Q = \int dt\, L_y \mathcal{J}_x(t) = -\Phi_0\, \sigma_{xy} = -e\nu \qquad \nu \in \mathbb{Z} \tag{1.19}$$

is transferred between the two edges of the cylinder. Since after the whole process the spectrum is the same, only the electron occupation numbers could have changed. Such a change, however, is not associated with electrons hopping across the insulating bulk but with the aforementioned spectral flow of the Landau levels.

If one consider the Landau gauge to describe the magnetic field orthogonal to the cylinder surface (so that translational symmetry in the y direction is preserved), the wavefunctions of

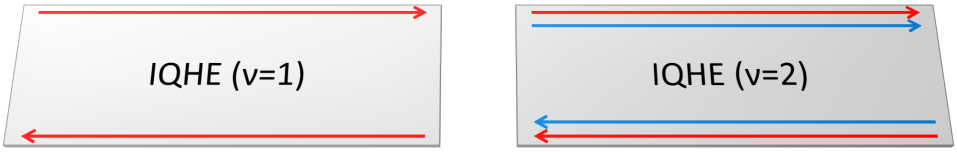

Fig. 1.6 Chiral edge states in IQH effect. At filling factor $\nu = 1$ only one spin polarization is present. At higher filling factors, e.g. $\nu = 2$, channels with both spin projections are present.

the electrons in the n^{th} Landau level read [31]

$$\psi_{n,k_y}(x,y) \sim e^{ik_y y} e^{-\frac{(x+k_y l_\mathrm{B}^2)^2}{2l_\mathrm{B}^2}} \mathfrak{H}_n(x+k_y l_\mathrm{B}^2) \tag{1.20}$$

where $l_\mathrm{B} = \sqrt{\hbar/(eB)}$ is the magnetic length and $\mathfrak{H}_n$ the Hermite polynomials. Since their spatial localization in the x-direction depends on k_y, it is clear that a change in the flux Φ corresponds to a translation of these wave functions along the x-direction! In the end, every adiabatic insertion of a flux quantum effectively moves one electron per occupied Landau level (i.e. ν electron in total) from one edge to the other (see Fig. 1.5b). The edge states involved in this kind of adiabatic transport must be gapless and, as elucidated by Halperin, they carry a chiral current along the edge [3].

Importantly, provided that the system is disordered, the Laughlin and Halperin arguments hold also when a Landau level is not fully occupied, a situation which has not been considered so far. One can indeed show that disorder broadens the Landau levels and localizes the states in the tails of each Landaus level. Localized states are basically unaffected by the spectral flow: the local change of vector potential due to the flux insertion act just as a gauge transformation and does not result in any displacement of the localized wave function. The extended states running along the edges, however, are subject to the spectral flow and behave as described before. This point is crucial for accounting for real quantum Hall experiment, where in general the chemical potential lies within one Landau level.

Before discussing other possible topological phases, it is worth stressing the importance of the chiral edge states in QHE. Because of their chirality, low energy excitations can only propagate in one direction and backscattering is not allowed (see Fig. 1.6). Transport along the edges of a Hall bar is therefore ballistic over very long distances (of the order of tens of μm [45]), a striking property which lies at the heart of many application of quantum Hall physics. Among them, it is worth citing the so-called electron quantum optics (EQO), an interesting and fast developing field which will be discussed in Chapters 2 and 3.

1.3 Other topological phases

The experimental discovery and the theoretical explanation of the quantum Hall effect eventually led to the quest for other systems featuring non-trivial topological property. In the beginning, however, it was long thought that topological phases are rare in nature and occur only under extreme conditions. Things changed drastically with the discovery of spin-orbit-induced topological insulators [40, 46]: it was suddenly clear that topological phases are way more common than expected and many other non-trivial materials have been discovered. In particular, it started to be recognized the great importance of the interplay between symmetries and topology.

The former are long known to play a central role in the classification of different phases of matter within the celebrated Ginzburg-Landau theory of spontaneously symmetry breaking. When intertwined with topology, however, symmetries perform in a rather different way. For instance, it is not possible to distinguish between topological and non-topological insulators by simply looking at their symmetries. Moreover, topological non-trivial phases cannot be detected by a local order parameter [28].

Symmetries kick in when it comes to defining which continuous modifications of Hamiltonians are actually allowed. Let us consider a couple of Hamiltonians obeying some kind of symmetry. It may happen that the two can be continuously deformed into each other only if the symmetry is broken at some point along the deformation. In this case, one can say that the two Hamiltonians belong to two distinct symmetry-protected topological (SPT) classes. Such a distinction clearly vanishes if the symmetry is broken but what is important is that the two classes feature different (and useful) topological properties whose existence relies on the presence of the symmetry.

It is useful to briefly review non-spatial symmetries, time-reversal (TRS), particle-hole (PHS) and chiral symmetry, since they allow developing the celebrated ten-fold topological classification of free-fermion systems [47–49]. Time reversal symmetry $\mathcal{T}$ is an antiunitary operator

$$\mathcal{T} = U_{\mathcal{T}}\mathcal{K} \tag{1.21}$$

where $U_{\mathcal{T}}$ is a unitary operator and $\mathcal{K}$ is the complex-conjugation operator. Applying time-reversal twice one has

$$\mathcal{T}^2 = U_{\mathcal{T}}\mathcal{K}U_{\mathcal{T}}\mathcal{K} = U_{\mathcal{T}}U_{\mathcal{T}}^* = P \tag{1.22}$$

where P has to be a diagonal matrix of phases since $\mathcal{T}^2$ should get us back to the original state up to phases. The transpose of a diagonal matrix is the matrix itself so one has

$$U_{\mathcal{T}}U_{\mathcal{T}}^* = P \quad \Rightarrow \quad U_{\mathcal{T}} = PU_{\mathcal{T}}^T \quad \Rightarrow \quad U_{\mathcal{T}}^T = U_{\mathcal{T}}P \tag{1.23}$$

and hence

$$U_{\mathcal{T}} = P U_{\mathcal{T}} P \tag{1.24}$$

which can happen only if $P = \pm 1$. We have thus proved that the time-reversal operator can square to $(U_{\mathcal{T}})^2 = \pm 1$ [39]. A system is time-reversal symmetric if $\mathcal{T}$ preserves the canonical anticommutator and if the Hamiltonian H obey $\mathcal{T} H \mathcal{T}^{-1} = H$. Particle-hole symmetry $\mathcal{C}$ is represented by an antiunitary operator which mixes fermionic creation and annihilation operators $\mathcal{C} = U_{\mathcal{C}} \mathcal{K}$. A particle-hole invariant Hamiltonian in the Bogoliubov-de Gennes form anticommutes with $\mathcal{C}$:

$$\mathcal{C} H \mathcal{C}^{-1} = -H\,. \tag{1.25}$$

As well as TRS, particle-hole symmetry squares to $(U_{\mathcal{C}})^2 = \pm 1$. The combination of $\mathcal{T}$ and $\mathcal{C}$ leads to a third unitary symmetry called chiral symmetry

$$\mathcal{S} = \mathcal{T}\mathcal{C}\,. \tag{1.26}$$

The Hamiltonian of a system which features chiral symmetry anticommutes with $\mathcal{S} = U_{\mathcal{S}}$

$$\mathcal{S} H \mathcal{S}^{-1} = -H \tag{1.27}$$

and chiral symmetry squares to $(U_{\mathcal{S}})^2 = 1$ [28].

These three symmetries define ten different symmetry classes, depending on whether they square to 1 $(+)$, to -1 $(-)$ or they are not present (0). Such a classification (see Table 1.1) is named after Altland and Zirnbauer who originally discussed it, although in a different context [50]. Within each symmetry class (and for a specified spatial dimension) one can study how many different SPT phases are possible, identifying a topological invariant for each one of them. This is summarized in the last column of Table 1.1 for systems in 2 spatial dimensions. Here, a dot $(\cdot)$ means that the only possible phase is topologically trivial, i.e. a phase containing the atomic insulator limit (a collection of independent atoms). If more (SPT) phases are possible, the allowed values of the corresponding topological invariant are shown.

The first line of Table 1.1, i.e. the symmetry class A, describes systems with neither TRS, PHS or chiral symmetry. Quantum Hall systems and Chern insulators fall in this class: the topological invariant $\mathbb{Z}$ is indeed the Chern number discussed in the previous section. It was long believed that only systems without TRS could exhibit interesting physics: after all, a non-zero Hall conductance clearly requires TRS to be broken[6]! Interestingly enough, Table 1.1

---

[6] This statement can be proved also by brute force formalism, i.e. by looking at the constraints which TRS adds to the wave functions in the Brillouin zone. One can thus show that, because of TRS, the integral of the Berry curvature over the Brillouin zone is always vanishing [39].

Symmetry class	$\mathcal{T}$	$\mathcal{C}$	$\mathcal{S}$	Topological invariant
A	0	0	0	$\mathbb{Z}$
AIII	0	0	+	·
AI	+	0	0	·
BDI	+	+	+	·
D	0	+	0	$\mathbb{Z}$
DIII	−	+	+	$\mathbb{Z}_2$
AII	−	0	0	$\mathbb{Z}_2$
CII	−	−	+	·
C	0	−	0	$2\mathbb{Z}$
CI	+	−	+	·

Table 1.1 Ten-fold classification of topological gapped free-fermion systems in 2 dimensions. The last column shows the absence (·) or the presence of non-trivial topological phases by specifying the kind of topological invariant they are characterized by.

actually shows that adding TRS does not prevent the possibility to have a non-trivial phase in 2D, provided that TRS squares to -1. Although a $\mathbb{Z}$ topological invariant like the Chern number is not possible, the symmetry class AII in 2 dimensions do feature some kind of two-valued $\mathbb{Z}_2$ topological invariant! Systems in this class can indeed exhibit the so-called quantum spin Hall (QSH) effect: this extremely interesting class of materials, as well as their helical edge channels, will be discussed in the next subsection.

Before concluding, I want to stress that the topological classification which I briefly discussed here is far from being completely exhaustive. First of all, it can be extend to free-fermion gapped systems with different dimensionality, as well as to the study of topological defects [51]. Moreover, other symmetries such as the spatial ones can be taken into account, leading to an even richer classification. Finally, one must bear in mind that the presence of interaction can dramatically modify the whole picture [28].

1.3.1 Quantum spin Hall effect

In 2005, C. Kane and G. Mele considered the effect of a strong spin-orbit coupling (SOC) interaction, which does not break TRS, on the electronic structure of graphene. The spin of electrons plays a central role in determining the band structure of such a two-dimensional system and they actually discovered that the constraints imposed by TRS could lead to a new topological phase of matter: the quantum spin Hall effect [52, 53]. It was soon after realized by A. B. Bernevig, T. L. Hughes and SC. Zhang (BHZ) that such a new topological phase could be realized in realistic systems, namely CdTe/HgTe quantum wells [40]. In 2007, the group of L.

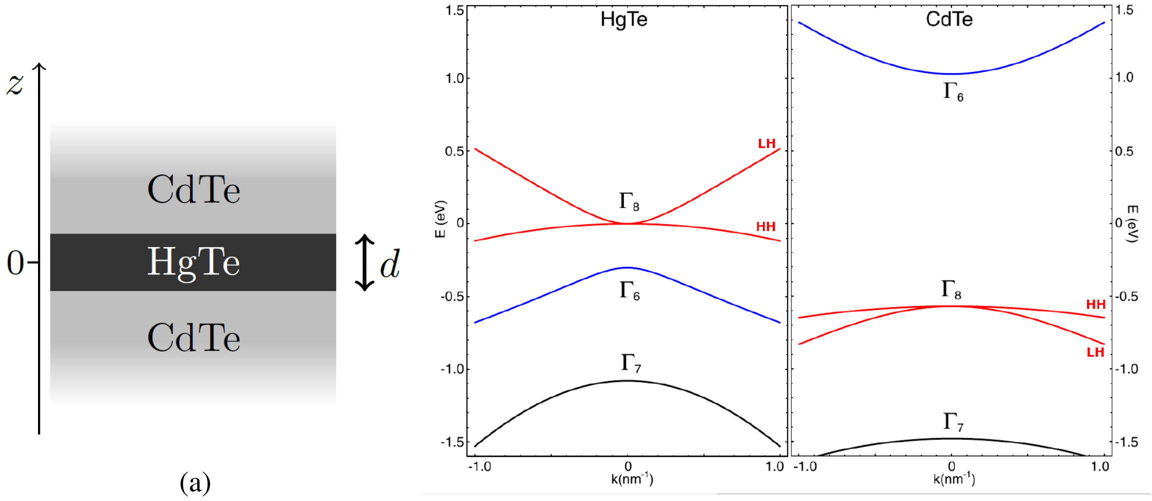

(a)

(b)

Fig. 1.7 (a) CdTe/HgTe quantum well. (b) Band structures of HgTe (inverted) and CdTe (standard).

Molenkamp reported the first experimental evidence of the existence of edge states associated with the $\mathbb{Z}_2$ topological invariant [54]. Before focusing on the properties of these edge states, I will briefly review the BHZ model aiming to highlight its topological aspects.

The BHZ model

Let us focus on a CdTe/HgTe quantum well, as sketched in Fig. 1.7a. CdTe is a semiconductor with a standard band progression: the s-type band Γ_6 lies above the p-type bands Γ_8. By contrast, HgTe features an inverted band structure due to a strong SOC, with Γ_6 lying below Γ_8. In both semiconductors, the gap is smaller near the Γ point, see Fig. 1.7. Symmetry arguments, as well as direct calculations, allow to devise a simple four-band tight-binding model on a square lattice

$$H_{\text{BHZ}} = \begin{pmatrix} h(\vec{k}) & 0 \\ 0 & h^*(-\vec{k}) \end{pmatrix} \tag{1.28}$$

which effectively describes the two-dimensional states in the quantum well [40]. In particular, here we used the basis $\{|E_1,+\rangle, |H_1,+\rangle, |E_1,-\rangle, |H_1,-\rangle\}$ where the ± sign refers to the spin of the electron. Moreover, the H_1 bands come from the Γ_8 states while the E_1 bands come from a combination of Γ_6 and Γ_8 states. Each 2×2 block can be expressed as

$$h(\vec{k}) = \varepsilon(\vec{k}) + \vec{\xi}(\vec{k}) \cdot \vec{\sigma} \tag{1.29}$$

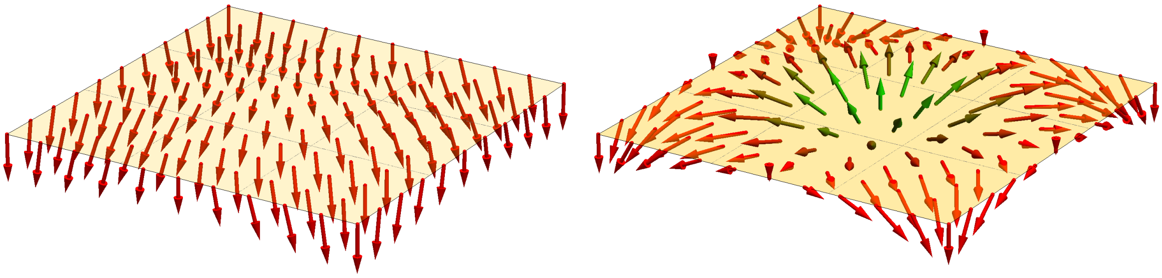

(a) Vanishing skyrmion number. (b) Skyrmion number $\nu = 1$.

Fig. 1.8 Vector plot of $\vec{\xi}(\vec{k})$ in the first Brillouin zone (yellow square). Γ point is in the middle. (a) Trivial regime: $m/(2B) = -4 < 0$. (b) Topological regime $0 < m/(2B) = 1.8 < 2$.

where $\vec{\sigma} = \{\sigma_x, \sigma_y, \sigma_z\}$ are the Pauli matrices,

$$\vec{\xi}(\vec{k}) = [A\sin(ak_x),\, A\sin(ak_y),\, m - 2B\,(2 - \cos(ak_x) - \cos(ak_y))] \tag{1.30}$$

$$\varepsilon(\vec{k}) = C - 2D\,(2 - \cos(ak_x) - \cos(ak_y))\,, \tag{1.31}$$

and A, B, C, D, m are parameters depending on the particular properties of the quantum well. Here a is the lattice constant. Note that $h^*(-\vec{k})$ is the time-reversal symmetric of $h(\vec{k})$.

The Hamiltonian (1.28) features gap closures at high symmetry points:

- at the Γ point ($\vec{k} = (0,0)$) when $m/(2B) = 0$;
- at the X and Y points ($\vec{k} = (\pi/a, 0)$ or $\vec{k} = (0, \pi/a)$ respectively) when $m/(2B) = 2$;
- at the M point ($\vec{k} = (\pi/a, \pi/a)$) when $m/(2B) = 4$.

Let us study how the vector $\vec{\xi}(\vec{k})$ behaves within the first Brillouin zone, depending on the parameter $m/(2B)$. In the regime $m/(2B) < 0$, the z-component of vector $\vec{\xi}$ has always the same sign as shown in Fig. 1.8a. By contrast, in the regime $0 < m/(2B) < 2$ the vector $\vec{\xi}$ behaves in a peculiar way (see Fig. 1.8b): it points to the north (or south) pole a the Γ point, points in the opposite direction at the zone boundaries and winds around the equatorial plane in the middle region. Such a peculiar structure is known as skyrmion and it is characterized by a non-vanishing topological number (skyrmion number) [40]

$$\nu = -\frac{1}{8\pi^2} \iint dk_x dk_y\, \vec{\xi} \cdot \left(\partial_x \vec{\xi} \times \partial_y \vec{\xi}\right)\,, \tag{1.32}$$

which basically counts the number of time $\vec{\xi}$ winds around the unit sphere over the Brillouin zone torus. This skyrmion number therefore represents a topological invariant which allows

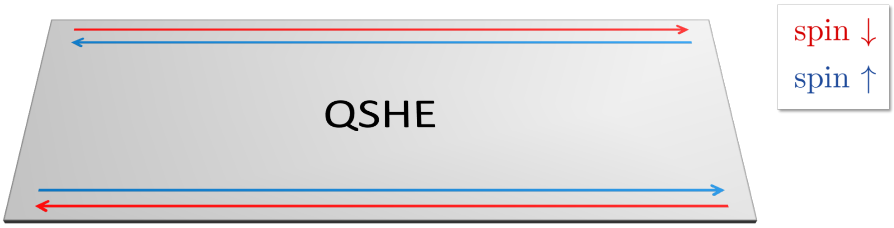

Fig. 1.9 Helical edge states in QSH effect. Different colors refer to different spin orientations.

us to distinguish between the two regimes $m/(2B) < 0$ ($\nu = 0$) and $0 < m/(2B) < 2$ ($\nu = 1$). Other regimes are not experimentally relevant. Note that the sign of $m/(2B)$ is related to sign of the energy difference between bands H_1 and E_1 at the Γ point which, in turn, depends on the band structure of the quantum well:

- if the HgTe region exceed a critical thickness $d > d_c \simeq 6.3nm$ (see Fig. 1.7a) the band structure is inverted (like in bulk HgTe) and $m/(2B) > 0$;
- otherwise the band structure is standard, like in bulk CdTe, and $m/(2B) < 0$ [40].

So far we have focused only on one 2×2 block, say the one associated with spin-up electrons (bands $|E_1, +\rangle$ and $|H_1, +\rangle$). Interestingly, in the context of quantum anomalous Hall effect, it is known that within such a two-band model the skyrmion number is actually related to the Chern number and thus to the Hall conductance [44, 40]

$$\sigma_{\mathrm{H}}^{(+)} = \frac{e^2}{h}\,\nu\,. \tag{1.33}$$

As for the spin-down block, which is related to the previous one by TRS, the Hall conductance is the opposite $\sigma_{\mathrm{H}}^{(-)} = -\sigma_{\mathrm{H}}^{(+)}$. In the end, the total Hall conductance always vanished (as expected in presence of TRS) but the spin-Hall conductance, defined as $\Delta\sigma_{\mathrm{H}} = \sigma_{\mathrm{H}}^{(+)} - \sigma_{\mathrm{H}}^{(-)}$, can indeed be finite.

Pulling all the threads together, the BHZ model proves that a CdTe/HgTe quantum well in the inverted regime (i.e. when the HgTe region is thicker than $d_c \simeq 6.3\,nm$) features a non-trivial topological invariant: a non-vanishing spin-Hall conductance $\Delta\sigma_{\mathrm{H}} = 2e^2/h$. This effect is called QSH effect and systems which feature it are usually called two-dimensional topological insulators (2DTIs). In analogy with quantum Hall physics, a non-zero spin-Hall conductance implies the existence of peculiar edge states at the boundary of the 2D bulk insulator. These edge states are called helical and consist of two counterpropagating 1D channels with opposite spin, as shown in Fig. 1.9. This peculiar relation between spin projection and electron momentum is known as spin-momentum locking [55].

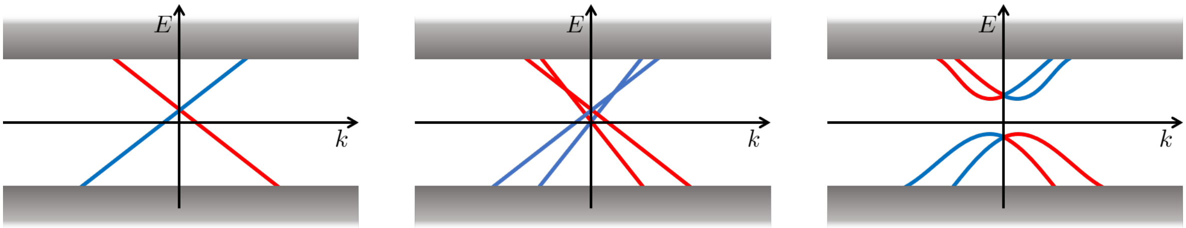

Fig. 1.10 Sketch of the linear dispersion relation, within the bulk gap, of helical modes on one edge. A single helical state (left) cannot be gapped out without violating Kramer's theorem. By contrast, a pair of Helical edge states (center) can be gapped out without violating Kramer's theorem (right).

The helical edges of QSH effect

An explicit solution for the helical edge states in QSH effect can be obtained by solving the BHZ model with an open boundary [55]. In particular, one can show their exponential localization at the edges of the sample as well as their linear dispersion around the Dirac point (see Fig. 1.10).

The counterpropagating nature of the helical states is in sharp contrast with the chirality of the edge states in IQH effect (see Fig. 1.6). Therefore, one may wonder if this poses a threat to the protection from backscattering. It turns out that single-particle elastic backscattering cannot occur as long as TRS is not broken. Kramer's theorem indeed states that, if $|\psi\rangle$ is an eigenstate of a system featuring a TRS which squares to $\mathcal{T}^2 = -1$, then $\mathcal{T}|\psi\rangle \neq e^{i\phi}|\psi\rangle$ is a different eigenstate with the same energy[7]. This guarantees the protection of the degeneracy at the Dirac point ($k = 0$), which cannot be lifted by any time-reversal-symmetric perturbation[8]. Note that this topological protection from backscattering holds only for a single helical state on each edge: every time one has an even number of helical states on the same edge, they can be fully gapped out without violating Kramer's theorem as sketched in Fig. 1.10.

Interestingly, in discussing the protection of the edge states, we encountered two of the main features of the symmetry class AII (see Table 1.1): TRS must square to -1 (otherwise Kramer's theorem does not hold) and we can only have either zero or one protected helical state on a single edge, a fact which reflects the $\mathbb{Z}_2$ nature of the topological invariant characterizing the QSH effect. This observation, far from being a coincidence, can be seen as a manifestation

---

[7] To prove the theorem one has to show that $\mathcal{T}|\psi\rangle \neq e^{i\phi}|\psi\rangle$ via proof by contradiction. Assuming that $\mathcal{T}|\psi\rangle = e^{i\phi}|\psi\rangle$, one would have

$$\mathcal{T}^2|\psi\rangle = \mathcal{T}\left(e^{i\phi}|\psi\rangle\right) = e^{-i\phi}e^{i\phi}|\psi\rangle$$

which in turn would imply $\mathcal{T}^2 = 1 \neq -1$.

[8] Note, however, that Kramers theorem does not impede transitions between counterpropagating electrons with different energies, i.e. inelastic backscattering. As a result, there are actually several mechanisms which can limit the helical edge conductance. See, e.g., Ref. [56].

of bulk-boundary correspondence: what happens on the edges is actually a manifestation of topological properties of the bulk!

The existence of edge states represents an important signature of the QSH effect which can be directly probed experimentally. The first experimental evidence of QSH physics [54] indeed consisted in a conductance measurement in a CdTe/HgTe quantum wells: in the inverted regime ($d > d_c$) a quantized conductance plateau within the bulk gap was observed, indicating the presence of gapless 1D states; moreover, such a conductance is highly suppressed by applying an external magnetic field which breaks TRS and hence the topological protection [54]. A few years later, the edge states in topological CdTe/HgTe quantum wells have been directly observed using a scanning SQUID which measured the tiny magnetic field created by edge currents [57].

In the last years, several other materials have been proposed and experimentally proved to display QSH effect. It is the case, for example, of InAs/GaSb quantum wells which, in principle, also allow changing the topology of the system by acting on external gates [58, 59]. QSH effect has been observed also in graphene (with enhanced SOC induced by deposition of magnetic adatoms) [60], silicene and 2D germanium [61]. One of the goals of the current research is to develop topological insulators with large gaps which allow for QSH effect at high temperature. In this respect, chemical functionalization and engineered external strain on tin film has proved to be quite effective [62]. Another option is represented by bismuthene: scanning tunneling spectroscopy detected a very large gap of $\sim 0.8\,eV$ as well as conducting edge state [63]. An exhaustive review of the experimental progress in 2DTIs is provided in Ref. [64].

1.4 Topology in one dimension

Topological non-trivial phases of matter are not restricted to 2D systems. In 1D there are indeed several SPT phases [65] described by non-vanishing topological invariants[9]. Bulk-boundary correspondence still holds and, instead of 1D gapless states at the edges of a topological 2D system, here one expects the existence of zero-energy modes localized at the two ends of a 1D topological system. Interestingly enough, these zero-energy states usually feature exotic properties, as it will be shown in Chapter 4.

The rest of the chapter will be devoted to the discussion of the so-called Kitaev chain, a 1D lattice model proposed by Alexei Kitaev in 2001 in Ref. [7]. This simple toy model features indeed many important virtues in the context of the present Thesis

- Its topological features emerge in an easy and intuitive fashion.

---

[9] Note, however, that without enforcing symmetries all the gapped 1D phases are topologically trivial [65].

- It predicts the existence of zero-energy Majorana modes in spinless 1D p-wave superconductors, systems which can be experimentally realized.
- It represents the ideal starting point to introduce parafermions, which will be the main subject of the last chapter of the thesis.

The following detailed discussion of the 1D Kitaev chain is largely inspired by the approach presented in Ref. [66].

1.4.1 A toy model: the 1D Kitaev chain

Let us consider a 1D chain of spinless fermions which can hop on a L-site open chain and exhibit p-wave superconductivity[10]. The Hamiltonian for such a model reads

$$H_K = -\mu \sum_{j=1}^{L} c_j^\dagger c_j + \frac{1}{2} \sum_{j=1}^{L-1} \left[-t\, c_j^\dagger c_{j+1} - \Delta\, c_j c_{j+1} \, + \mathrm{H.c.} \right] \tag{1.34}$$

where operator c_j ($c_j^\dagger$) annihilates (creates) an electron on site j. Here $t \geq 0$ is the nearest-neighbor hopping amplitude, μ is the chemical potential and $\Delta \geq 0$ is the p-wave superconducting pairing amplitude. For simplicity, the superconducting phase is set to 0.

The peculiar physics of this model can be most simply accessed by decomposing the spinless fermion c_j into a couple of so-called Majorana operators via

$$c_j = \frac{1}{2} \left(b_j + i a_j \right) . \tag{1.35}$$

The inverse relations

$$a_j = i(c_j^\dagger - c_j) \tag{1.36}$$

$$b_j = c_j^\dagger + c_j \tag{1.37}$$

show that, roughly speaking, these operators can be seen as the real (b_j) and the imaginary (a_j) part of a physical fermion. They satisfy the following anti-commutation relations

$$\{a_j, a_l\} = \{b_j, b_l\} = 2\delta_{i,l} \tag{1.38}$$

$$\{a_j, b_l\} = 0 \tag{1.39}$$

---

[10] Note that the standard s-wave superconductivity cannot be achieved with *spinless* fermions.

and they are Hermitian operators

$$a_j^\dagger = a_j \tag{1.40}$$

$$b_j^\dagger = b_j\,, \tag{1.41}$$

hence the name after the Italian physicist Ettore Majorana who, back in 1937, hypothesized the existence of fermions which are their own antiparticles[11]. The Hamiltonian H_K can be rewritten in terms of Majornas as

$$H_K = -\frac{\mu}{2}\sum_{j=1}^{L}\left(1 + i b_j a_j\right) - \frac{i}{4}\sum_{j=1}^{L-1}\left[(\Delta + t) b_j a_{j+1} + (\Delta - t)\, a_j b_{j+1}\right]\,, \tag{1.42}$$

and it becomes very simple in the two limiting cases, schematically depicted in Fig. 1.11.

- The so-called "trivial limit" with $t = \Delta = 0$ and $\mu < 0$. In this case the Hamiltonian simply reads
  $$H_K^{(\mathrm{triv})} = -\frac{\mu}{2}\sum_{j=1}^{L}\left(1 + i b_j a_j\right) \tag{1.43}$$
  and pairs Majoranas on the same site, as depicted in Fig. 1.11a.

- The so-called "topological limit" with $t = \Delta \neq 0$ and $\mu = 0$. Here the Hamiltonian
  $$H_K^{(\mathrm{topo})} = -\frac{t}{2}\sum_{j=1}^{L-1} i b_j a_{j+1}\,. \tag{1.44}$$
  pairs Majoranas on different sites and leaves two dangling Majoranas at the edges, as shown in Fig. 1.11b.

These two limiting cases are very different from each other. The former features a unique ground state corresponding to the vacuum of c_j fermions. By contrast, the latter features two degenerate ground states: the two unpaired Majoranas at the edges can be indeed combined into an ordinary – though highly non-local – fermion

$$f = \frac{1}{2}(a_1 + i b_L) \tag{1.45}$$

---

[11] As we will discuss in Chapter 4, the exchange statistics of zero-energy Majoranas is not fermionic since these excitations actually behave as non-Abelian anyons. Hence, in order to avoid any possible misunderstanding, in the present Thesis I will refer to operators a_i and b_j simply as "Majorana operators", "Majorana modes" or simply "Majoranas".

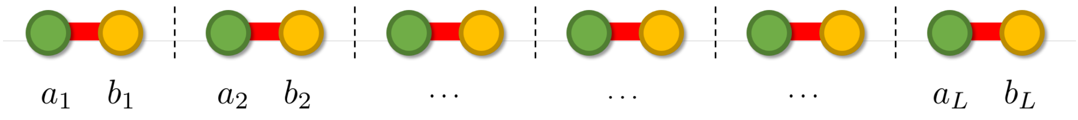

(a) Trivial limit

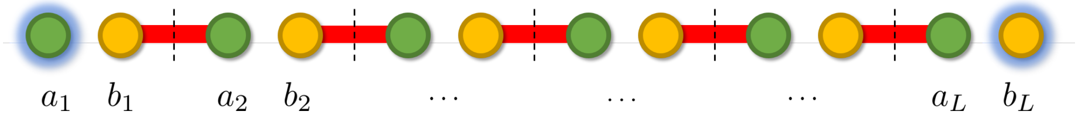

(b) Topological limit

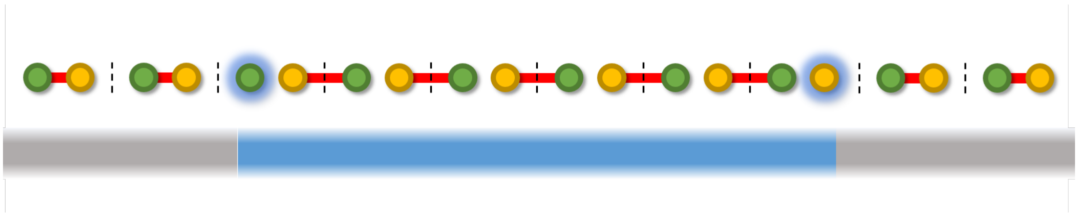

(c) Domain walls between phases

Fig. 1.11 (a) The trivial limit of the Kitaev chain in Eq. (1.43). (b) The topological limit in Eq. (1.44). Note the two dangling Majoranas at the edges highlighted with blue glow. (c) Dangling Majoranas appearing at domain walls between the topological phase (blue) and the trivial one (gray).

that commutes with the Hamiltonian

$$[f, H_K^{(\mathrm{topo})}] = 0\,.$$

The ground state $|0\rangle$, which satisfies $f|0\rangle = 0$, has therefore the same energy of $|1\rangle = f^\dagger|0\rangle$, which is another ground state with opposite fermion parity.

As the names suggest, the “topological limit” actually belongs to a SPT phase which is topologically distinct from the one containing the “trivial limit”. We prove this statement in Appendix A.3, where we demonstrate the phase diagram of the Kitaev chain:

- the topological gapped phase is present for $t > |\mu|$ and $\Delta \neq= 0$;
- the system is gapless[12] for $t = |\mu|$ or when $\Delta = 0$ and $t \geq |\mu|$;
- the system is in a trivial gapped phase otherwise.

The two dangling zero-energy Majoranas we just described can be therefore understood as the manifestation of bulk-edge correspondence in 1D. They indeed appear at the domain walls between topological and trivial regions, as shown in Fig. 1.11c (note that the fermionic vacuum can be seen as a trivial Kitaev chain in the limit $\mu \to -\infty$).

---

[12] in the thermodynamic limit.

1.4.2 Protection of zero energy Majorana modes

Zero-energy Majorana modes have topological origin and their existence is therefore expected to be protected from perturbations, just like the edge states of IQH or QSH effects. In this subsection, we will discuss this protection when a finite chemical potential μ drives the systems away from the topological sweet spot $\mu = 0$ and $t = \Delta \neq 0$. A very useful tool to characterize the system, which is extremely relevant also from an experimental point of view, is the so-called local fermionic spectral function $\mathcal{A}_j$ [32]. For a system in an eigenstate $H|\varphi\rangle = E_\varphi|\varphi\rangle$, $\mathcal{A}_j$ is defined as[13]

$$\begin{aligned}\mathcal{A}_j(\omega) &= \int e^{-i\omega\tau}\langle\varphi|\left\{c_j^\dagger(\tau), c_j(0)\right\}|\varphi\rangle\, d\tau \\ &= 2\pi\sum_{|n\rangle}\left[\delta(\omega+E_n-E_\varphi)|\langle n|c_j|\varphi\rangle|^2 + \delta(\omega-E_n+E_\varphi)|\langle n|c_j^\dagger|\varphi\rangle|^2\right]\end{aligned} \tag{1.46}$$

where the sum is over all the eigenstates $|n\rangle$ of the system (whose energy is denoted by E_n). In the following we will focus on the behavior of $\mathcal{A}_j(\omega)$ for energies within the bulk energy gap (EG), i.e. where Majorana edge modes live.

At the topological sweet spot (1.44), the local spectral function features two zero-energy peaks localized at the edges, signaling the presence of the zero-energy dangling Majoranas in Fig. 1.11b.

$$A_j(\omega) = \pi\,\delta(\omega)\left(\delta_{j,1}+\delta_{j,L}\right) \qquad \text{for } \omega \in \text{EG} \tag{1.47}$$

This can be easy verified by observing that the only non-vanishing matrix elements within the two-dimensional ground-state subspace are

$$|\langle 0|c_j|1\rangle|^2 = \frac{1}{4}\left(\delta_{j,1}+\delta_{j,L}\right) \tag{1.48}$$

where we used $|1\rangle = f^\dagger|0\rangle$ with f being the non-local fermion defined in terms of Majoranas in Eq. (1.45).

In order to study the effects of a finite chemical potential, it is useful to compute the integral of the local spectral function over the bulk EG

$$\mathbf{A}_j = \int_{\omega\in\text{EG}} \mathcal{A}_j(\omega)\, d\omega\,. \tag{1.49}$$

This quantity is plotted in Fig. 1.12a for decreasing values of the chemical potential, while $t = \Delta$ are kept fixed. Even if one moves away from the sweet spot ($\mu = 0$), the spectral weight associated with the two Majoranas is still localized at the two edges and features only an

---

[13] In the rest of the chapter we set $\hbar = 1$

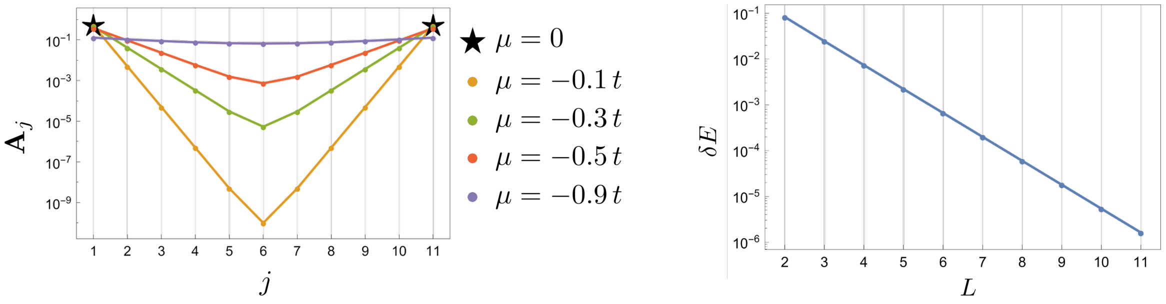

(a) Localization of zero-energy Majoranas (b) Topological protection of degeneracy

Fig. 1.12 Behavior of the open Kitaev chain away from the sweet spot. In (a) the local spectral weight $\mathbf{A}_j$ [units 2π] inside the energy gap is plotted for different values of the chemical potential μ (see the legend) whit $t = \Delta$. At the topological sweet spot $\mu = 0$, $\mathbf{A}_j$ is non-vanishing only at the edges (black stars). In (b) it is plotted the energy splitting δE [units t] between the ground state and the first excited state as a function of the system length L, with fixed parameters $\mu = 0.3t$ and $t = \Delta$. Both plots are obtained by exact numerical diagonalization.

exponentially suppressed leakage in the bulk of the system. Clearly, as μ approaches the critical value $\mu = -t$, the leakage becomes more and more relevant.

A finite overlap between the two edge modes leads to a splitting of the ground-state degeneracy. For a given choice of the parameters, the overlapping, and hence the splitting, is exponentially suppressed with the system size L. This behavior clearly emerges in Fig. 1.12b where we plotted the energy difference δE between the first two eigenstates of the system as a function of the chain length L.

In view of these results, we can state that the zero-energy Majorana modes are topologically protected in the sense that deviations from both an exact localization and an exact two-fold degeneracy are characterized by a finite and parameter-dependent decay length. In the thermodynamic limit ($L \to \infty$), as long as the Kitaev chain is in the topological regime, one always has exact zero-energy edge Majoranas.

1.4.3 Majoranas in experiments

The Kitaev chain wouldn't have been so successful if it there wasn't the possibility to experimentally realize systems with the same intriguing topological properties. In this concluding subsection, we will discuss how to devise a physical system whose Hamiltonian has the same topological properties of the Kitaev model. We will also give an overview on the experimental achievements obtained so far: clearly this is a huge topic and our one-page summary is basically intended to provide some useful literature suggestions.

Kitaev chain in real life

The goal is to find a realistic setup which could mimic the Kitaev chain Hamiltonian 1.34, i.e. a 1D spinless model with p-wave superconductivity. The task is far from being trivial and it involves different challenges. First of all, we need to find a way to freeze out half of the degrees of freedom of the electrons, in order to have system which could be effectively “spinless”. Moreover, intrinsic p-wave superconductors are extremely rare and almost impossible to have in 1D [66]. Interestingly enough, several ingenious schemes have been devised in order to overcome these issues. They usually rely on three ingredients: superconducting proximity effect, TRS breaking, and SOC.

In the following, we will briefly present a setup based on 1D quantum wires, which was proposed in 2010 by two seminal papers [67, 68] and sparked a successful experimental research, eventually leading to milestone achievements [8, 69, 70, 9]. The Hamiltonian of the proposed system reads

$$H = H_{\text{wire}} + H_{\text{sc}} \tag{1.50}$$

with

$$H_{\text{wire}} = \int dx\, \Psi^{\dagger} \left(-\frac{\partial_x^2}{2m} - \mu - i\alpha\sigma_y\partial_x + \zeta\sigma_z \right) \Psi \tag{1.51}$$

$$H_{\text{sc}} = \int dx \Delta \left[\psi_{\uparrow}\psi_{\downarrow} + h.c. \right] . \tag{1.52}$$

Here, $\Psi^{\dagger} = \left(\psi_{\uparrow}^{\dagger}, \psi_{\downarrow}^{\dagger} \right)$ where the operator $\psi_{\sigma}^{\dagger}$ adds to the wire an electron with effective mass m and spin σ (along the z-axis); μ is the chemical potential; α is the SOC strength (which favors the alignment of the spins in the y direction, depending on the sign of the momentum); ζ is an external Zeeman field along the z-direction; Δ is the proximity induced pairing from a conventional s-wave superconductor adjacent to the wire.

At first, let us focus on H_{wire} only, with the aim of understanding the effects of each term.

- The kinetic one clearly determines a dispersion relation with two spin-degenerate parabolic bands (see Fig. 1.13a).

- If only the SOC term is turned on ($\alpha \neq 0$, $\zeta = 0$), the two parabolas get spin-polarized along the y-direction and they split as shown in Fig. 1.13b.

- If only the Zeeman term is turned on ($\zeta \neq 0$, $\alpha = 0$), the two parabolas get spin-polarized along the z-direction and they split as shown in Fig. 1.13c.

- When both $\alpha \neq 0$ and $\zeta \neq 0$, the dispersion relation looks like the one in Fig. 1.13d. In order to develop some intuition about it, note that the SOC term is proportional to

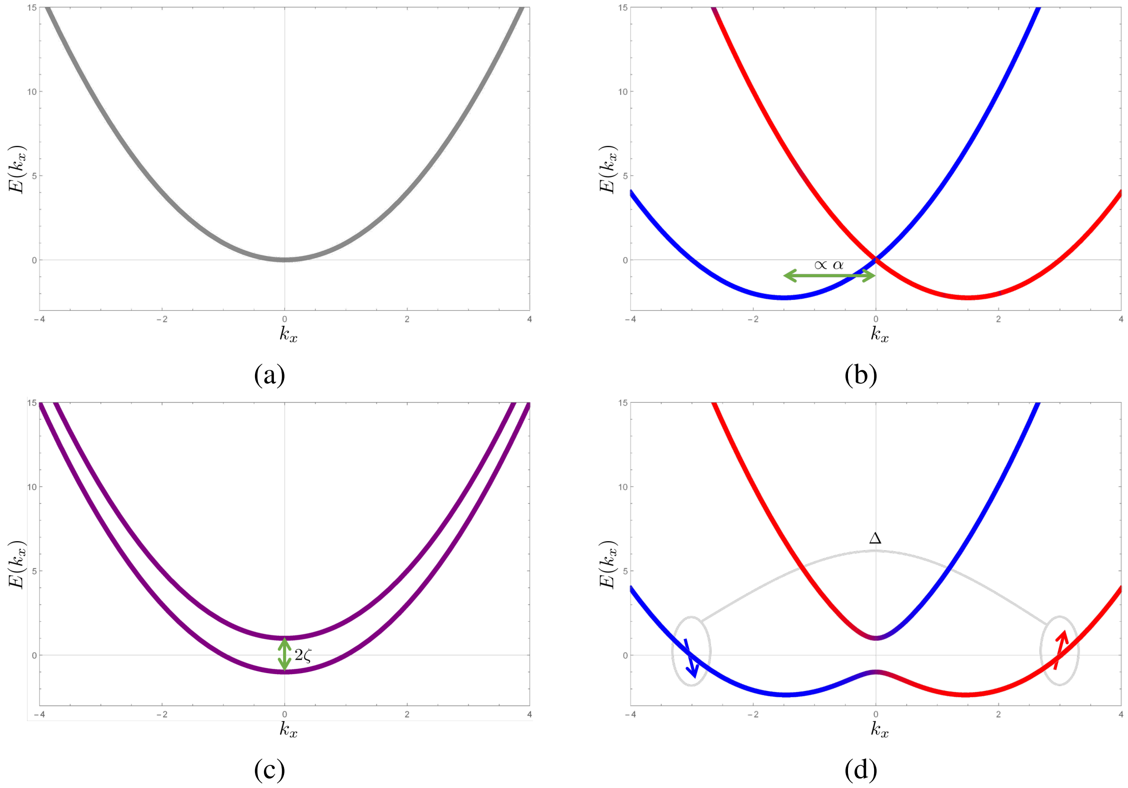

Fig. 1.13 Dispersion relations of a 1D quantum wire parallel to the x-direction: (a) with the kinetic term only; (b) in presence of SOC ($\alpha \neq 0$) along y-direction; (c) in presence of a Zeeman field ($\zeta \neq 0$) along z-direction; (d) in presence of both the aforementioned SOC and Zeeman field. Colors refer to spin polarization along the y-axis: red and blue stand for complete polarization [as qualitatively shown in panel (d)] while purple indicates no polarization along y.

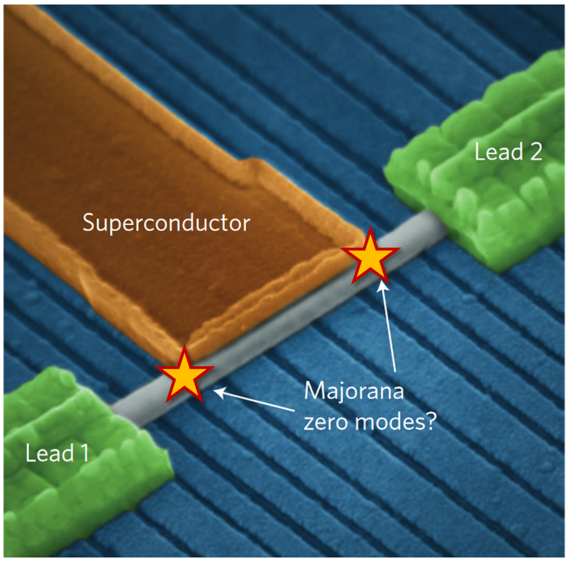

Fig. 1.14 Multi-terminal transport set-up used by the Kouwenhoven group to search for Majorana zero modes (stars) at both ends of a semiconducting InSb wire (gray) contacted to a superconductor (orange). Image taken from Ref. [6].

the momentum $|k_x|$ while the Zeeman splitting is momentum-independent: at large $|k_x|$ the dispersion will be dominate by SOC effects and it indeed looks like the one in Fig. 1.13(a); at small $|k_x| \sim 0$ the Zeeman splitting dominates instead and the dispersion relation acquires a gap proportional to ζ just like in Fig. 1.13(b)

If the chemical potential is tuned to $\mu \sim 0$, so that the Fermi level lies in the Zeeman-induced gap, the wire features only two gapless and quasi-helical 1D channels. Working at low temperature, the degrees of freedom of the higher band can be frozen out as desired. Moreover, the quasi-helical nature of the gapless channels do allow the superconductive pairing H_{sc}, inherited from a adjacent s-wave superconductor via proximity effect, to be effective (see Fig. 1.13d).

The Hamiltonian (1.50) has therefore all the ingredients needed to capture the physics of the Kitaev chain. Remarkably, one can show that by an appropriate tuning of the parameters the system can access a regime which connects smoothly with the topological phase of the Kitaev chain [71]. More precisely, the phase diagram of the wire in (1.50) is controlled by the topological criterion [66]

$$\zeta > \sqrt{\Delta^2 + \mu^2}\,. \tag{1.53}$$

If the magnetic field is high enough, the wire is in the topological phase and at its ends, where it is connected to the trivial one, zero-energy Majorana will appear (see Fig. 1.14).

Experimental realization

From the experimental point of view, the actual realization of this proposal posed many challenges. One has indeed to identify materials which feature a strong effective SOC, a large effective Zeeman energy and which are compatible with proximity-induced superconductivity. This represents a formidable task in material science. So far, the heavy-element semiconductors InAs and InSb have received considerable attention due to their strong SOC and the large Landé g-factor. Quantum semiconductor wires can be obtained in two different ways, via a top-down approach based on molecular-beam epitaxy (MBE) followed by etching or via a bottom-up scheme based on vapor-liquid-solid (VLS) growth mechanism [72]. The quality of interfaces between the wires and superconductors turns out to be crucial: the more smooth and clean the interfaces, the more effective the proximity-induced p-wave pairing.

If the realization of these hybrid systems is challenging, finding compelling evidence for the existence of Majorana zero modes can be even more complicated. The point is that most measurements come with a certain degree of ambiguity: even when the system is in the trivial phase, e.g. when the external magnetic field is not strong enough, fine-tuning some parameters can lead to experimental observations which resemble those expected for Majoranas!

The simplest experiments involve tunneling conductance measurements of the local density of states at the wire ends. Here Majoranas should appear as robust and quantized zero-energy peaks within the superconducting gap (see also Eq. (1.48)). The observation of a zero-bias peak in the topological regime was indeed the first experimental "evidence" for the presence of Majoranas back in 2012 [8]. Huge improvements in material science allowed for better samples and, in turn, to more impressive measurements which were actually able to probe also the quantization and the robustness of the peak [9]. Other possible measurements aiming at proving the existence of Majoranas include the study of Josephson current (which features 4π periodicity in presence of Majoranas) [73] as well as the relation between the ground-state degeneracy splitting and the wire length (which is expected to be exponentially suppressed as shown in Fig. 1.12b) [70].

The definite proof, however, will be the observation of a key feature of Majoranas which we haven't discussed yet: their non-Abelian statistics. This fundamental topic will be discussed in detail in Section 4.1, where we will also discuss the important connection between Majoranas and topological quantum computation. In this respect, however, experimental research is still ongoing. A nice review and outlook of experimental Majorana physics in superconductor-semiconductor hybrid systems can be found in Ref. [72].

Chapter 2

Interaction in 1D systems

In the previous chapter we considered only free-fermion systems. The presence of Coulomb interaction between electrons, however, is often unavoidable, raising the question to which degree topology and interactions coexist or compete. It has by now become clear that there is no general answer to this question and this topic is actually still a matter of ongoing research.

When it comes to IQH and QSH effects, it turns out that they do tolerate interactions as long as they do not spontaneously break symmetries or close the bulk gap. Therefore, chiral and helical edge states are still present and robust even in an interacting environment. Interestingly enough, however, the interaction between 1D channels makes their physics surprisingly richer.

The study of interaction effects in 1D systems will be one of the main topic of the present chapter, where we will review the Luttinger liquid model in the spinless and helical case. Peculiar 1D phenomena, such as charge fractionalization, will be also discussed both theoretically and experimentally. Eventually, we will also introduce the so-called electron quantum optics: an intriguing field where the interplay between topological edge states and interaction effects is extremely relevant[1].

2.1 Luttinger liquid theory in a nutshell

2.1.1 One dimensional systems are different

Inter-particle interactions characterize a large variety of physical systems and they can lead to intriguing behaviors which are not captured at all by non-interacting single-particle theories [74]. Noteworthy examples of these interaction-induced phenomena are the superfluidity of helium-3 [75, 76] (whose discovery earned D. M. Lee, D. D. Osheroff, R. C. Richardson and,

---

[1] In this chapter we set $\hbar = 1$

later, A. Leggett the Nobel Prize in Physics), the existence of Mott insulators [77], the Kondo effect [78] and the fractional quantum Hall effect [79, 80], just to name a few.

Yet remarkably, fermionic systems usually feature a regime called "Fermi liquid" in which they behave almost like a non-interacting Fermi gas, in spite of a Coulomb interaction energy comparable with the particles' kinetic energy. This behavior is successfully explained by the celebrated Fermi liquid theory, introduced by L. D. Landau in 1956 [81], which well describes normal metals. In a Fermi liquid, the low-energy excitations acquire a infinite lifetime and it is therefore possible to describe the whole systems as a collection of these well-defined and (almost) non-interacting fermionic quasiparticles.

Things are dramatically different in 1D [82–85]. The aforementioned quasiparticles are not well defined any more and the low-energy physics of a 1D interacting system has to be described in terms of collective and highly non-localized bosonic excitations. As a consequence, interactions in 1D have dramatic effects and many exotic phenomena occur, such as charge fractionalization [86–88, 5] and spin-charge separation [85, 83, 89] to name a few. When dealing with 1D interacting systems, the theory of choice is the so called Tomonaga-Luttinger model, which is a fixed point of the renormalization group (RG) flow, as nicely reviewed in Ref. [90]. A system described by this theory, which was developed by S. Tomonaga [91] and J. M. Luttinger [92] and later refined by Haldane [84, 85], is known as Luttinger liquid LL.

In the following, the LL model is presented, focusing on the aspects which are relevant and noteworthy in the context of the present thesis. For a more detailed and complete treatment the reader is referred to the many excellent reviews and books present in the literature [82, 83, 93, 94, 84, 85].

2.1.2 Spinless and helical Luttinger liquids

Let us consider a generic spinless 1D fermionic system, with length $l \to \infty$ and subject to PBC. Its Hamiltonian reads

$$H = H_0 + H_{\text{int}}\,, \tag{2.1}$$

where

$$H_0 = \int_{-\infty}^{+\infty} dx\; \psi^\dagger(x)\varepsilon(-i\partial_x)\psi(x) \tag{2.2}$$

is the free term associated with the dispersion relation $\varepsilon(k)$ and

$$H_{\text{int}} = \frac{1}{2}\iint_{-\infty}^{+\infty} dx\,dy\; \psi^\dagger(x)\psi^\dagger(y)V(y-x)\psi(y)\psi(x) \tag{2.3}$$

is a two-particle interaction term described by the potential $V(x-y)$.

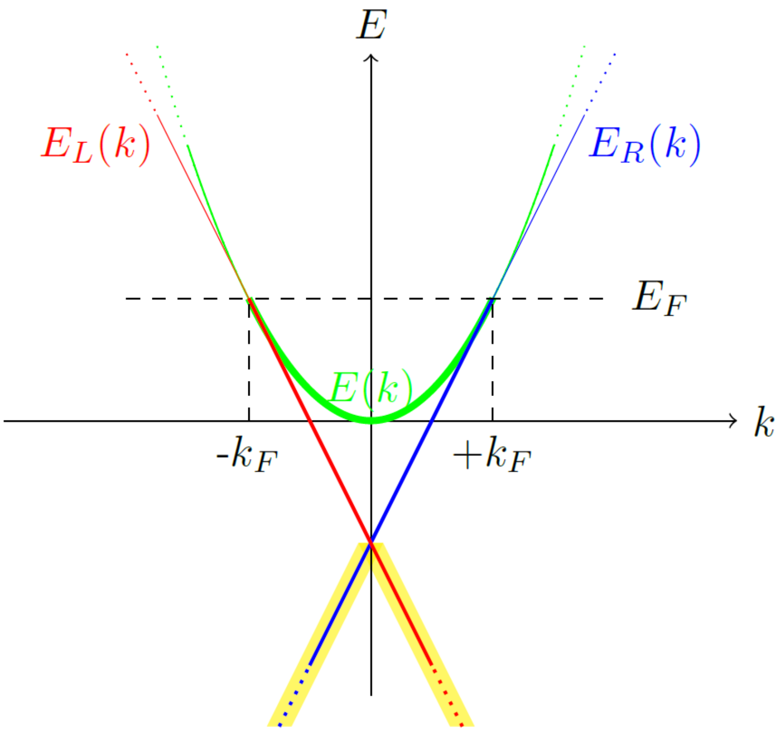

Fig. 2.1 Sketch of the two approximations at the very base of the LL theory: linearization of a generic dispersion relation (in green) around the Fermi points; extension of the linear branches (right-movers in blue, left-movers in red) from $k = -\infty$ to $k = +\infty$ by adding non-physical states (in yellow) which will form the Dirac sea.

The Luttinger liquid theory, which allows to conveniently deal with the interactions, relies on two main approximations. In particular, one has to

- linearize of the spectrum of H_0 around the two Fermi points at $k = \pm k_\mathrm{F}$;
- replace the Fermi sea with a Dirac sea, unbounded from below.

These approximations, which hold in the low-energy limit, are schematically shown in Fig. 2.1. As a result, we can identify two species of fermions: the right-movers (R) with positive group-velocity v_F and the left-movers (L) with opposite group velocity. Note that such a picture, obtained for spinless fermions, can be easily generalized to the helical systems introduced in section 1.3.1. Indeed, the spin-momentum locking simply consists in associating one of the two possible spin projections to each branch. In the following we will assume, for example, that electron on the R-branch (L-branch) have spin-up (spin-down).

Fermionic operators $\psi_r(x)^\dagger$ and $\psi_r(x)$ create and annihilate one electron at position x on the $r = R, L$ branch, respectively. The linearized non-interacting Hamiltonian can be thus expressed as

$$H_0 = v_{\mathrm{F}} \sum_{r=R,L} \vartheta_r \int_{-\infty}^{+\infty} dx\, \psi_r^\dagger(x)(-i\partial_x)\psi_r(x) \tag{2.4}$$

where $\vartheta_{R/L} = +/-1$.

Bosonization

The celebrated bosonization identity [93, 94] allows to express fermionic fields $\psi_r(x)$ in terms of bosonic degrees of freedom

$$\psi_r^\dagger(x) = \frac{F_r^\dagger}{\sqrt{2\pi a}}\, e^{-i\vartheta_r k_{\mathrm{F}} x}\, \exp[i\sqrt{2\pi}\phi_r(x)]\,. \tag{2.5}$$

Here, $v_{\mathrm{F}} a^{-1}$ is a high-energy cut-off, needed in view of the unboundedness of the two branches. More importantly, $\phi_r(x)$ is a bosonic field which obey the algebra

$$[\phi_r(x), \partial_y \phi_{r'}(y)] = -ir\delta_{r,r'} \frac{1}{\pi} \frac{a}{(x-y)^2 + a^2} \xrightarrow[a\to 0]{} -ir\delta_{r,r'}\delta(x-y)\,. \tag{2.6}$$

It can be conveniently expressed as (considering l finite)

$$\phi_r(x) = \sum_{q>0} \frac{i}{\sqrt{lq}} \left(e^{iq\vartheta_r x} b_{r,q} + e^{-iq\vartheta_r x} b_{r,q}^\dagger \right) e^{-aq/2} \tag{2.7}$$

where the bosonic operators $b_{r,q}^\dagger$, which obey

$$\left[b_{r,q}, b_{r',q'}\right] = 0 \tag{2.8}$$

$$\left[b_{r,q}^\dagger, b_{r',q'}\right] = \delta_{r,r'}\delta_{q,q'}\,, \tag{2.9}$$

have a nice and clear physical interpretation: $b_{r,q}^\dagger$ creates a coherent superposition of particle-hole excitations (hence the their bosonic nature[2]) with momentum $\vartheta_r q$ on the r-branch, i.e.

$$b_{r,q}^\dagger = \sqrt{\frac{2\pi}{ql}} \sum_k c_{r,(k+q)}^\dagger c_{r,k} \tag{2.10}$$

---

[2] Actually, in order to prove (2.8) and (2.9) it is also crucial that the spectrum is unbounded, i.e. that k ranges from $-\infty$ to $+\infty$ in Eq. (2.10)

where the fermionic operator $c^\dagger_{r,k}$ creates an electron with momentum $\vartheta_r k$ on the r-branch. Equation (2.7) shows that a^{-1} can be interpreted as an upper bound to the momentum of particle hole excitations.

Since the bosonic field $\phi_r(x)$ consists of particle hole excitations, it cannot clearly account for variation of the fermionic particle number on each branch. In other words, if N_r is the number operator of the r-branch[3], one has

$$\left[b^\dagger_{r,k}, N_{r'}\right] = 0\,. \tag{2.12}$$

As a consequence, another ingredient is needed in order to be able to relate $\phi_r(x)$ with a fermionic field: the Klein factor operators $F^\dagger_r$ which appear in (2.5). These unitary operators add one particle to the r-branch

$$\left[N_r, F^\dagger_{r'}\right] = \delta_{r,r'} F^\dagger_r \tag{2.13}$$

$$\left[F^\dagger_r, \phi_r(x)\right] = 0 \tag{2.14}$$

and ensure the anticommutation relation between fermionic fields

$$\left\{F^\dagger_r, F_{r'}\right\} = 2\delta_{r,r'} \tag{2.15}$$

$$\{F_r, F_{r'}\} = 0 \tag{2.16}$$

Note that Klein factors are often omitted in calculations because they drop out in particle number conserving expressions due to their unitarity.

An important result, which is crucial for the following, is that the fermionic particle density operator[4] has a very nice bosonic expression

$$\rho_r(x) =: \psi_r(x)^\dagger \psi_r(x) := \frac{N_r}{l} - \frac{r}{\sqrt{2\pi}} \partial_x \phi_r(x)\,. \tag{2.17}$$

It indeed consists of an constant term and of a fluctuating contribution described by the derivative of the bosonic fields.

---

[3] Note that, when considering a physical observable like N_r, one has to take into account for the infinite number of fictitious single-particle states introduced with the Dirac sea. This can be properly done by looking at normal ordered operator [93]

$$:N_r: = N_r - \langle N_r \rangle_\Omega \tag{2.11}$$

which basically consists in subtracting the expectation value of the operator on the ground state Ω of the system Hamiltonian (H_0 in Eq. (2.4) in the present case).

[4] See footnote 3 for the definition of the normal ordering $:\ldots:$.

Diagonalization of the Hamiltonian

In view of the bosonic description we have given so far, it is natural to distinguish two contributes to the free Hamiltonian (2.4): the former is associated with the bosonic excitations at fixed particle number while the latter, usually called zero-mode term $H_{0,N}$, exclusively depends on the particle numbers on each branch. One can indeed show that

$$\begin{aligned} H_0 &= \sum_r \sum_{q>0} v_{\mathrm{F}} q \, b^\dagger_{r,q} b_{r,q} + H_{0,N} \\ &= \frac{v_{\mathrm{F}}}{2} \sum_r \int dx \; :[\partial_x \phi_r(x)]^2: + H_{0,N} \, . \end{aligned} \tag{2.18}$$

In the following we will only focus on the bosonic part of the Hamiltonians. Note that, with respect to H_0, the bosonic fields $\phi_r(x,t)$ are chiral

$$\phi_r(x,t) = e^{iH_0 t} \phi_r(x,0) e^{-iH_0 t} = \phi_r(x - \vartheta_r v_{\mathrm{F}} t, 0) \tag{2.19}$$

They thus describe collective bosonic excitations which travels either to the left or to the right.

As for the interacting term (2.3), assuming a short-range potential, one can show that in general the only relevant contributions can be expressed in terms of density-density couplings [82]

$$H_{\mathrm{int}} \simeq H_4 + H_2 \tag{2.20}$$

where

$$\begin{aligned} H_4 &= \frac{g_4}{2} \sum_r \int dx \; :\rho_r(x)\rho_r(x): = \frac{g_4}{4\pi} \sum_r \int dx \; :[\partial_x \phi_r(x)]^2: \\ H_2 &= g_2 \int dx \; :\rho_R(x)\rho_L(x): = \frac{g_4}{2\pi} \int dx \; :\partial_x \phi_R(x) \partial_x \phi_L(x): \end{aligned} \tag{2.21}$$

Here the coupling constants g_4 (intra-branch) and g_2 (inter-branch) are named according to the so-called g-ology [82, 93, 94]. Note that, in the fermionic language, H_4 describe two-particle forward scattering within the same branch while H_2 describes forward scattering of two particles on different branches. It is important to note that, in general, it is possible to devise other interaction processes. One noteworthy example is the so-called two-particle Umklapp scattering, which describes the backscattering of two R electrons into two L electrons (and vice versa). Such a process is allowed by momentum conservation only at the Dirac point and, moreover, it is RG relevant only under special conditions. Nevertheless, it can play a crucial role in some exotic phenomena as we will briefly discuss in section 4.2.2.

The great advantage provided by bosonization is now clear: the interacting Hamiltonians H_2 and H_4, whose fermionic expressions consists of product of four fields, are quadratic in the bosons! Therefore, the whole Hamiltonian $H = H_0 + H_2 + H_4$ can be straightforwardly diagonalized by implementing a proper Bogoliubov transformation

$$\begin{cases} \beta_{+,q} = A_+ b_{R,q} - A_- b^\dagger_{L,q} \\ \beta^\dagger_{-,q} = A_+ b^\dagger_{L,q} - A_- b_{R,q} \end{cases} \Leftrightarrow \begin{cases} \phi_+(x) = A_+ \phi_R(x) - A_- \phi_L(x) \\ \phi_-(x) = A_+ \phi_L(x) - A_- \phi_R(x) \end{cases} \tag{2.22}$$

with

$$A_\eta = \frac{1}{2}\left(\frac{1}{\sqrt{K}} + \eta\sqrt{K}\right) \qquad (\eta = \pm 1) \tag{2.23}$$

and

$$K = \sqrt{\frac{2\pi v_{\mathrm{F}} - g_2 + g_4}{2\pi v_{\mathrm{F}} + g_2 + g_4}} \tag{2.24}$$

the so-called Luttinger parameter. The latter describes the density-density interaction strength: one has $K = 1$ in the non interacting case, while $K < 1$ ($K > 1$) in the presence of repulsive (attractive) interactions.

In terms of the new bosonic operators, the whole Hamiltonian reads

$$H = \frac{u}{2} \sum_{\eta=\pm} \int dx \; :[\partial_x \phi_\eta(x)]^2 := \sum_{\eta=\pm} \sum_{q>0} uq \, \beta^\dagger_{\eta,q} \beta_{\eta,q} \tag{2.25}$$

where

$$u = (2\pi)^{-1} \sqrt{(2\pi v_{\mathrm{F}} + g_4)^2 - g_2^2} \tag{2.26}$$

is the renormalized propagation velocity of the diagonal bosonic excitations. The new bosonic fields, when evolved with H, are indeed chiral and satisfy

$$\phi_\eta(x,t) = \phi_\eta(x - u\eta t, 0)\,. \tag{2.27}$$

They are clearly related to the operators $\beta_{\eta,q}$ by a relation analogue to (2.7)

$$\phi_\eta(x) = \sum_{q>0} \frac{i}{\sqrt{lq}} \left(e^{iq\eta x} \beta_{\eta,q} + e^{-iq\eta x} \beta^\dagger_{\eta,q}\right) e^{-iaq/2}\,. \tag{2.28}$$

A couple of observations, useful for the following chapter, are in order. First of all, note that, if $g_2 = g_4$, one has the simple relation $u = v_{\mathrm{F}} K^{-1}$. For the sake of simplicity, we will assume this relation throughout all the next chapter. By inspecting the Bogoliubov coefficients

A_η, it is easy to prove that

$$A_+^2 = 1 + A_-^2 \geq 1\,. \tag{2.29}$$

Finally, it is useful to derive the bosonic particle density ρ_η associated to the chiral excitations:

$$\begin{aligned}\rho_R(x,t)+\rho_L(x,t) &= \frac{1}{\sqrt{2\pi}}\partial_x\left[\phi_L(x,t)-\phi_R(x,t)\right] \\ &= \frac{1}{\sqrt{2\pi}}(A_+-A_-)\partial_x\left[\phi_-(x+ut,0)-\phi_+(x-ut,0)\right] \\ &= \underbrace{\left\{\sqrt{\frac{K}{2\pi}}\partial_x\phi_-(x+ut,0)\right\}}_{\rho_-(x,t)}+\underbrace{\left\{-\sqrt{\frac{K}{2\pi}}\partial_x\phi_+(x-ut,0)\right\}}_{\rho_+(x,t)}\end{aligned} \tag{2.30}$$

2.2 Charge fractionalization

As anticipated at the beginning of the chapter, interactions in 1D lead to some remarkable effects such as the fractionalizaton of the electron charge, anomalous tunneling behavior [95, 96], and the spin-charge separation [84, 83, 89]. In this section we will review the former, both theoretically and experimentally, exploiting the formalism of spinless LL introduced in the previous section.

2.2.1 Theory

The starting point is the bosonization identity (2.5) of the fermionic operator $\psi_r^\dagger(x)$ in presence of interactions. Implementing the Bogoliubov transformation 2.22, one has

$$\begin{aligned}\psi_r^\dagger(x,t) &= \frac{F_r^\dagger}{\sqrt{2\pi a}}\,e^{-i\vartheta_r k_F x}\,\exp[i\sqrt{2\pi}A_{\vartheta_r}\phi_+(x,t)+i\sqrt{2\pi}A_{-\vartheta_r}\phi_-(x,t)] \\ &= \frac{F_r^\dagger}{\sqrt{2\pi a}}\,e^{-i\vartheta_r k_F x}\,\exp[i\sqrt{2\pi}A_{\vartheta_r}\phi_+(x-ut,0)]\exp[i\sqrt{2\pi}A_{-\vartheta_r}\phi_-(x+ut,0)]\end{aligned} \tag{2.31}$$

where in the second line we exploited the chirality of the fields ϕ_η [see Eq. (2.27)]. Eq. (2.31) clearly shows that creating an electron on the r-branch corresponds to the simultaneous creation of bosonic excitations traveling in opposite directions. Importantly, the charge carried by each one of these excitations is just a fraction of the electron's one. The total particle density does indeed satisfy the following commutator[5]

$$\begin{aligned}\Big[\rho_R(x)+\rho_L(x),\exp[i\sqrt{2\pi}A_\pm\phi_\eta(y)]\Big] &= \Big[\rho_\eta(x),\exp[i\sqrt{2\pi}A_\pm\phi_\eta(y)\Big] \\ &= \sqrt{K}A_\pm\delta(x-y)\ \exp[i\sqrt{2\pi}A_\pm\phi_\eta(y)]\,.\end{aligned} \tag{2.33}$$

Therefore, if one electron is created on the r-branch, a fraction q_+ of its charge will travel in the r direction while the remaining fraction q_- will move in the opposite direction. These charge fractionalization factors are given by

$$q_+ = \sqrt{K}A_+ = \frac{1+K}{2} \geq \frac{1}{2} \quad \text{and} \quad q_- = \sqrt{K}A_- = \frac{1-K}{2} \leq \frac{1}{2} \tag{2.34}$$

and they depend only on the interaction strength. Note that in the non interacting limit $K=1$ one recovers $q_+=1$ and $q_-=0$ as expected. Interestingly, q_+ always satisfies $q_+ > 1/2$ meaning that the majority of the charge will always flow in the r direction.

As an important remark, note that the two counterpropagating fractional excitations are created by the *product* of the vertex operators displayed in Eq. (2.31): charge fractionalization is therefore a genuine many-body phenomenon and it is not the result of a trivial superposition of states where the electron moves either to the right or to the left.

Effects of non-interacting leads

The study of single-electron fractionalization after its injection into an interacting system with counterpropagating 1D channels will be one important topic of the next chapter [see in particular section 3.1]. It is important to underline, however, that fractionalization can arise also in a slightly different context, namely in presence of inhomogeneities of the interaction strength in a 1D system. This point is extremely relevant also from an experimental point of view since the measurement of many transport properties requires the presence of metallic leads which, being Fermi liquids, can be modeled as non-interacting systems [86, 87].

The effects of interaction inhomogeneity on 1D transport properties have been extensively studied in the context of DC electrical conductance [86, 87], thermal and energy transport [97, 98], out-of-equilibrium systems [99] and time-resolved dynamics of both charge [5, 100] and spin transport [18, 17, 101]. Here, I'll mainly focus on charge transport. In order to develop some intuition, let us consider a spinless LL with an interface between an interacting region to the left and a non-interacting region to the right. In a realistic sample the width of the junction is

---

[5] Here we used the identity

$$[A,e^B] = [A,B]e^B \tag{2.32}$$

which holds if $[[A,B],A] = [[A,B],B] = 0$ [93].

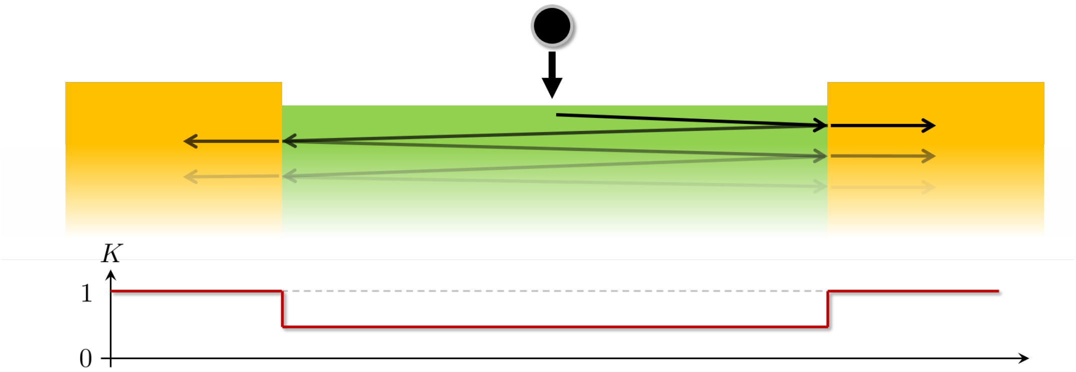

Fig. 2.2 Interacting 1D LL (green) coupled to two non-interacting leads (yellow). The Luttinger parameter K is not homogeneous and fractionalization occurs also at the interfaces. The black arrows show the multiple scattering events underwent by one of the fractional excitations created by the injection of an electron.

usually much larger than the Fermi wavelength, meaning that backscattering of single electron at the junction can be neglected. Let us focus on an excitation with charge Q impinging the interface from the interacting side and, therefore, traveling to the right at the renormalized velocity $u = K^{-1}v_{\mathrm{F}}$. After the scattering at the boundary, there will be a transmitted excitation with charge tQ traveling into the non-interacting part at velocity v_{F} and a reflected one, with charge rQ and traveling back to the left at velocity u. Conservation of charge and current (the latter due to the absence of single particle backscattering) leads to

$$\begin{cases} r+t=1 \\ Kt-r=1 \end{cases} \quad \Rightarrow \quad t=\frac{2}{1+K} \quad \text{and} \quad r=\frac{K-1}{K+1}\,. \tag{2.35}$$

One remarkable consequence of this result is that fractionalization phenomena cannot directly emerge in the DC regime [86, 87, 100, 17]. Suppose, in fact, that one R-electron is injected in the middle of an interacting 1D system connected to two non-interacting leads [see Fig. 2.2]. The two fractional excitations which are created will scatter many times at the two interfaces according to (2.35), eventually leading to a Fabry-Pérot-like pattern. If one computes the total charge which enters the right lead, the result reads

$$Q_R^{\mathrm{tot}} = \left[\frac{1+K}{2}+\frac{1-K}{2}r\right] t \sum_{n=0}^{\infty} r^{2n} = 1\,. \tag{2.36}$$

The R-electron we have injected is thus eventually entirely transmitted to the right: from a DC perspective, the interaction-induced fractionalization mechanism have no effect! Note that the

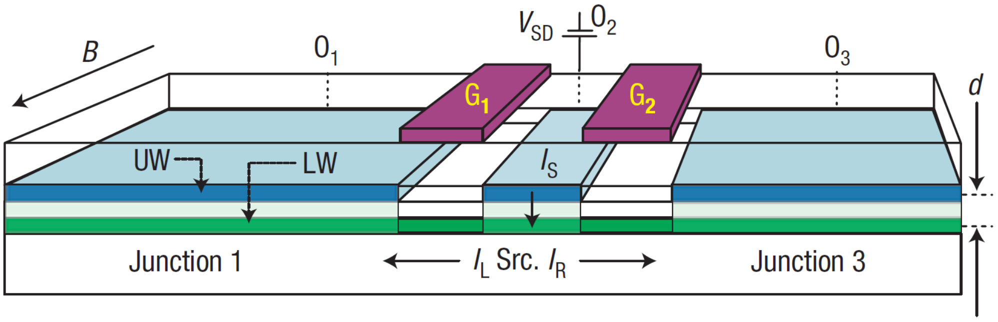

Fig. 2.3 Setup used by A. Yacoby and collaborators to provide the first evidence of charge fractionalization. Two quantum wires form on the cleaved-edge of an heterostructure. An electrical current I_s is injected from the upper wire into the lower one, where it fractionalizes.

same result is obtained considering the fate of one electron impinging the interacting region from the left lead: after many reflection it will be eventually entirely transmitted to the right.

In view of the result presented above, a *direct* study of fractionalization phenomena usually requires to go beyond the DC limit, considering either time-resolved or AC-based setups. A brief review of some experimental evidences of charge fractionalization will be presented in the following.

On a related note, it is possible to show that the DC electrical conductance of the whole system lead-LL-lead, sketched in Fig. 2.2, is independent on the Luttinger parameter K. This interesting result was derived in 1995 [86, 87] and explained the conductance measurements performed early the same year by S. Tarucha and collaborators [102]. The reason for this is again the effect of the leads and the scattering which happens at the interfaces. The conductance of the *sole* LL would have been indeed renormalized by K [103].

2.2.2 Experiments

The first experimental evidence of charge fractionalization was provided in 2008 by A. Yacoby's group [88]. Their setup, shown in Fig. 2.3, consists into a couple of adjacent wires obtained by means of the so-called cleaved-edge-overgrowth technique. The central region of the upper wire (UW in the picture) is biased and used to inject a DC current of electrons on the L-branch of the interacting lower wire (LW). Such a selective injection of L-electrons is achieved by the so-called momentum resolved tunneling: here an external magnetic field allows to shift and control the electrons' momentum, which is a well defined quantity in an highly non-local tunneling junction. The injected charge fractionalizes and eventually reaches the leads (named O_1 and O_3) where two steady electrical currents are measured. Crucially, the LW is not directly connected to the leads and electrons have to tunnel across two additional tunneling junctions

("Junction 1" and "Junction 3"). This clearly introduces backscattering at the junctions, thus replacing the transmission t in (2.35) with a different coefficient β[6]. As a result, the sum rule in (2.36) does not hold anymore and one can have a non-vanishing current in both the leads. The price to pay is that parameter β is not known.

In addition to the current asymmetry between the two leads

$$A_s = \frac{I_L - I_R}{I_s},$$

they measured also the DC conductance G between the two leads when no electron injection take place. As mentioned in the previous chapter, these two quantities are related to each other. In particular, using linear response theory and the LL model, one can show that the expression (2.34) for the charge fractionalization factors necessarily implies the relation [104]

$$G = A_s \frac{2e^2}{h}. \tag{2.37}$$

The validity of Eq. (2.37) have been successfully checked for different samples and different experimental conditions, thus proving indirectly the existence of charge fractionalization for the very first time.

Although remarkable and compelling, this experiment cannot provide a direct evidence of fractionalization because of its intrinsic DC nature. In this respect, the first direct observation of fractionalized wave packets is due to T. Fujisawa's group in 2014 [5]. They indeed developed a time-resolved detection scheme to probe the dynamics of charge packets in a spinless LL. The latter has been "artificially" realized by bringing two integer quantum Hall edge channels close to each other by means of a thin top gate. The setup is shown in Fig. 2.4a. The couple of edge states can be effectively described as an inhomogeneous LL (see Fig. 2.4b): when they are far apart from each other, inter-channel interaction vanishes (i.e. $g_2 \to 0$) leading to a non-interacting Luttinger parameter $K = 1$; by contrast, when they are on the two side of the thin metallic gate (in yellow), the two channel make up a interacting LL with $K < 1$. Note that backscattering between the two edge channels is strongly suppressed by the negative biased gate so that transport in the LL can be still considered ballistic.

A bunch of electrons (~ 150) is injected on one channel in the non-interacting region and moves chirally until it reaches the thin gate. Here, the inhomogeneity of K determines the Fabry-Pérot-like pattern of multiple reflections described in the previous section and precisely computed in [100]. Electrons packets which are reflected back in the left non-interacting region

---

[6] Parameter β effectively takes into account also for the backscattering events within the LW, which does not feature any kind of topological protection and, therefore, allows for ballistic transport only over very short distances.

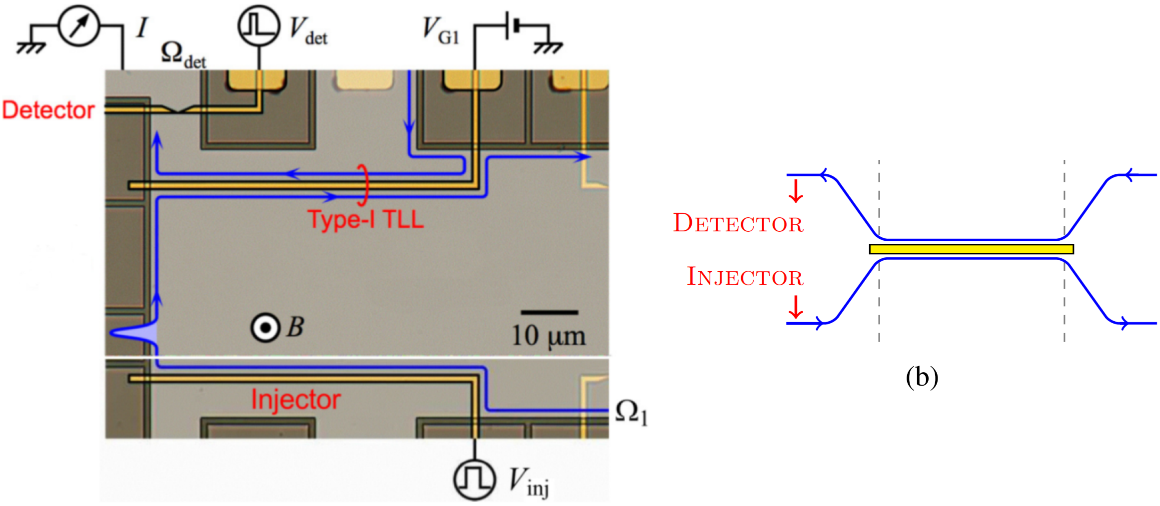

(a)

(b)

Fig. 2.4 (a) Experimental setup for the time-resolved measurement of charge fractionalization. Image adapted from [5]. (b) Sketch of the inhomogeneous artificial LL: two separated chiral edge state can be seen as a non-interacting LL; by contrast, when they are close enough to each other, interactions start to be relevant and the couple can be described as an interacting LL.

will eventually reach a QPC charge detector. The time width of the injected packet is around 1 *ns* and the high time resolution of the detector (tens of *ps*) allows to precisely measure the shape of the different fractionalized packets. The observed pattern is consistent with the charge fractionalization framework and with a Luttinger parameter $K \approx 0.92$[7].

It is important to underline that fractionalization-like phenomena, associated with the injection of a single electron, have been observed in 2015 [105] within the framework of the so-called electron quantum optics. This interesting and fast developing filed, as well as the mentioned experiment, will be discussed in Section 2.3.

2.2.3 Other fractionalization phenomena

Along with the charge, also other quantities can undergo fractionaliation in interacting 1D systems [106]. It is the case, for example, of the spin [107]: in this case the bosonic collective excitations which are created have a spin projection different from $\pm 1/2$. This intriguing phenomenon is more elusive than charge fractionalization and an experimental observation is still lacking to date. The reason lies in the fact that, in addition to a challenging time-resolved detection scheme [17], spin fractionalization also requires systems with peculiar spin properties and does not occur in ordinary interacting spinless or spinful quantum wires. In this respect,

---

[7] Such a weak interaction is due to the screening effects of the gate.

helical systems represent a promising platform [107, 17]. In Ref. [18] I proposed a setup based on the helical edge state of 2DTIs in a geometry inspired by Fujisawa's experiment: by exploiting the spin-momentum locking and the topological protection from backscattering, this setup would allow to create neutral excitations with fractionalized spin and to probe their signature by means of time-resolved electrical measurements only. The latest experimental developments in 2DTIs [108] might lead to a future observation of spin fractionalization.

Another interesting phenomenon is known as energy partitioning[8] [98]. The energy is indeed conserved during the tunneling process which injects particles into an interacting LL. Therefore, it makes perfect sense to ask how the injected energy is partitioned between the counterpropagating fractional excitations created in the LL. In Ref. [98], the authors showed that the energy behaves in a rather different way from the charge: the DC energy partitioning ratio p_η (between a right-moving and a left-moving energy flows) depends not only on the interaction strength in the LL K but also on the injection process. In particular, the limit of a local-injection differs quite significantly from the momentum-resolved tunneling limit (highly non-local injection). Moreover, they showed that the presence of leads does not prevent the direct observation of energy partitioning, even in the DC limit. This observation is directly related to the fact that thermal conductance measured a lead-LL-lead setup (see Fig. 2.2) does depend on the Luttinger parameter K [109, 97], in sharp contrast with the aforementioned electrical conductance.

In Chapter 3, in the context of a broad characterization of time-resolved single-electron injection into an interacting LL, I will also discuss the energy partitioning between the two counterpropagating fractional excitations which are created in the LL. In this respect, we will investigate the crossover between the local injection limit and the non-local regime, generalizing the DC findings of Ref. [98] and showing how they apply in the single-electron injection framework.

2.3 Electron quantum optics

The discovery of 2D topological states of matter, together with their protected 1D edge channels described in Chapter 1, has triggered a number of theoretical proposals and cutting-edge experiments. As a remarkable example, it has been realized that 1D ballistic systems are great candidates to realize electronic waveguides, where particles can propagate in a coherent way over long distances. This key observation represents one of the building blocks of the so-called electron quantum optics (EQO), an emerging and fast developing field which aims

---

[8] Here the word "partitioning" is preferred over "fractionalization" since, unlike charge and spin, there is no a "quantum of energy".

at transposing quantum optics setups in solid state devices where electrons play the role of photons.

Photons are long known to be extremely useful to study quantum effects such as entanglement, non-locality, quantum teleportation or quantum cryptography [110–113]. Needless to say, the possibility of reproducing these results in solid state devices is certainly appealing. Moreover, EQO comes with a key advantage over standard quantum optics: differently from photons[9], electrons do interact with each other (especially in 1D systems, as discussed before)! While strong interactions come with some drawbacks such as a shorter coherence time, they clearly allow for a richer phenomenology and for an additional tunability of the electrons' states. For example, the possibility of performing complex operations with flying electrons is very attractive from a quantum information point of view [115].

Electron quantum optics represents therefore an excellent example of interplay between topological systems and interactions in 1D. In analogy with conventional quantum optics, it relies on three main building blocks:

Conventional quantum optics		**Electron quantum optics**
Photon waveguide	⇔	1D topological edge states
Cohrent single photon sources	⇔	Coherent single electron sources
Beam splitter	⇔	Quantum point contact (QPC)

The experimental realization of EQO setups is far from being trivial as it requires a full mastering of very low temperatures, high quality sample fabrication and radio-frequency techniques. That said, the high interest in the topic and some important theoretical and experimental breakthroughs have already allowed for remarkable results and paved the way for the future development of EQO.

2.3.1 Single electron sources

As discussed before, one the most important goal of EQO is to control transport in 1D ballistic channel at the single-particle level. Over the last ten years, several on-demand single-electron sources (SESs) have been developed and successfully exploited in experiments. As an interesting aside, note that SESs play a central role also in metrology since they can link the ampere to the elementary charge and frequency [116].

---

[9] Several strategies, based on optical QED concepts, have actually been proposed to artificially introduce an interaction between photons. They turned out to be very challenging from an experimental point of view though [114].

Mesoscopic capacitor

An important example of SES is the so-called “mesoscopic capacitor”, developed in 2007 by G. Féve and collaborators [117]. Its physics relies on earlier work by M. Büttiker who theoretically investigated the quantum analogue of an RC circuit [118]. A mesoscopic capacitor consists of a small island of a 2DEG, isolated from the rest of the system by means of a QPC. The island dimensions are small enough so that it can be assimilated to a quantum dot (QD) with discrete energy levels. A DC voltage (V_{G} in Fig. 2.5) controls the transmission from the island to the rest of the 2DEG, which is driven in the integer quantum Hall regime by applying an orthogonal magnetic field. A second top gate is capacitively coupled to the dot and allows to shift the discrete spectrum of the QD via the AC voltage V_{exc}. Note that the top gate screen the Coulomb interaction in the dot region [117, 4].

The operating principle is sketched in Fig. 2.5. Starting from a situation where the uppermost occupied electron level is below the Fermi energy of the 2DEG (1), a sudden rise of V_{exc} brings it above the Fermi energy (2). After a time comparable with the level lifetime (tunable via the DC voltage V_{G}) the electron leaves the dot and is injected in the chiral edge channel. Then, restoring the top gate voltage to its initial value (3), the unoccupied energy level is brought below the Fermi energy and captures an electron from the edge channel (or, equivalently, it emits an hole). Fig. 2.5(b) shows time-resolved measurements of the injected current averaged over many periodic emission cycles: the exponential decay of the current, typical of RC circuits, reflects the exponential decay rate of the emission probability of electrons and holes. The relaxation time τ can be increased by reducing the transmission D of the QPC.

The mesoscopic capacitor is a tunable energy-resolved single electron source. Electrons are indeed injected with an energy ε_0 above the Fermi energy with an uncertainty given by the inverse lifetime τ^{-1}. Note that ε_0 is clearly bounded from above by the level spacing Δ of the QD spectrum. One of the limitations of mesoscopic capacitors as SESs is that it is only possible to inject one energy-resolved electron and one energy-resolved hole per cycle. Moreover, it is technically difficult to realize identical dots due to nano-lithography reliability: an important issue to deal with when interferometric experiments requiring more than one SES are considered [114].

Levitons

Another interesting method to realize a SES is to apply an ultra-short voltage pulse to a contact connected with the 1D channel of interest. According to finite frequency Büttiker quantum transport theory, this injects a number of particles which depends on the time integral of the

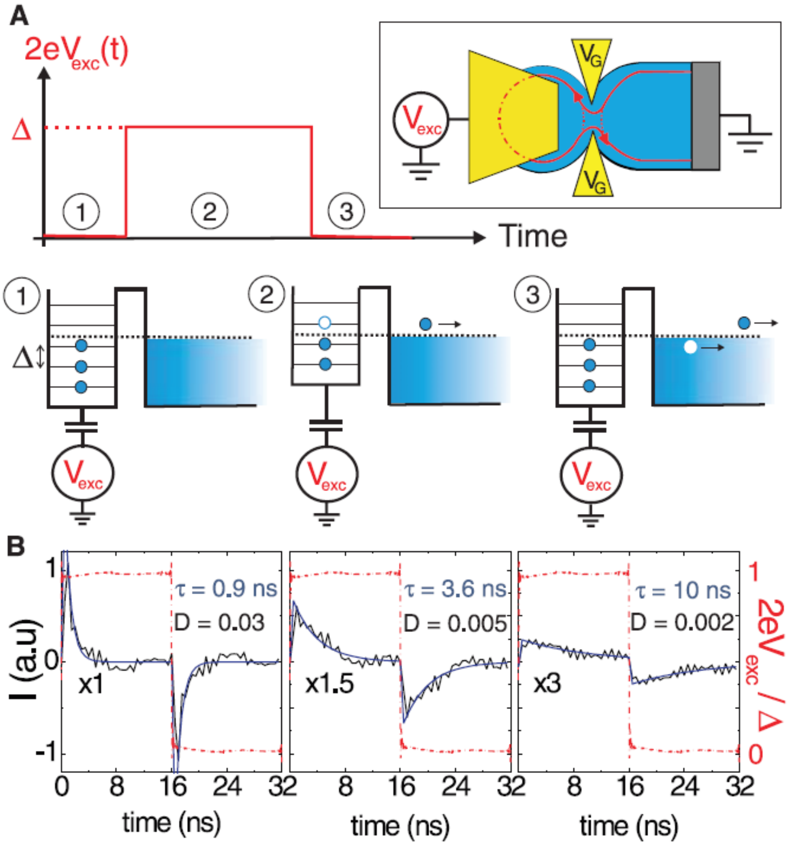

Fig. 2.5 (a) Sketch of a mesoscopic capacitor and of its operating principle. (b) Experimental plots of the top-gate potential V_{exc} (dashed red curves) and of the injected current (black) which is fitted well by an exponential decay (in blue). If the frequency of the driving is small enough, one electron and one hole are emitted per cycle. Image taken from Ref. [117].

voltage pulse as

$$n = \frac{e}{2\pi}\int dt\, V(t) . \qquad n \in \mathbb{N} \tag{2.38}$$

Injecting a single electron ($n = 1$) may thus seem an easy task to perform. The problem, however, is that the voltage pulse in general perturbs all the electrons of the Fermi sea and creates additional and unwanted neutral particle-hole excitations. Levitov and collaborators showed that this issue can be overcome by a clever choice of the pulse shape, namely a Lorentzian pulse [119]. It this case no extra neutral excitations are created and the single injected electron is called “leviton”. Note that this technique does not require any lithography processes, a great advantage from an experimental point of view [120]. Levitons are injected at the Fermi energy and lack of the energy-tunability provided by the mesoscopic capacitor. This point might also be seen as an advantage in terms of resilience against relaxation processes [114].

Other kind of SESs can be realized as well. They can rely, for instance, on dynamic semiconductor quantum dots [121] or on surface acoustic waves [122]. The interested reader is referred to Ref. [114], where SESs (and EQO in general) are nicely reviewed.

2.3.2 Interaction in electron-quantum optics

As discussed before, electron-electron interactions play a central role in EQO, both as a phenomenon to study and, eventually, as a tool to exploit. Within the integer quantum Hall framework, the appearance of interesting interaction effects require the presence at least of a couple of adjacent 1D channels. Indeed, as discussed in section 2.1.2, the presence of intra-channel interactions alone does not have huge consequences: if the inter-channel coupling g_2 is zero, the Luttinger parameter K in Eq. (2.24) is not affected at all by the intra-channel coupling g_4. The simplest setup to probe interaction effects in EQO is therefore based on a Hall bar at filling factor $\nu = 2$, which is characterized by two *co-propagating* 1D edge channels [123, 105, 124]. Although similar, the theoretical model which describes two *co-propagating* interacting channels is different from the one presented in Section 2.1.2, which holds for two *counterpropagating* channels. While a detailed review of the co-propagating model is beyond the scope of the present thesis, it is worth to briefly discuss its main predictions related to single-electron injections.

Suppose that one electron is injected into one of the two channels. This can be achieved for example with a mesoscopic capacitor which is coupled only with the outer 1D channel (see Fig. 2.6a). In the “strongly interacting” regime, which is the relevant one in experimental realizations [4], one can show that the injected electron splits up into a couple of collective excitations. They propagate in the same direction but with different velocities. Moreover,

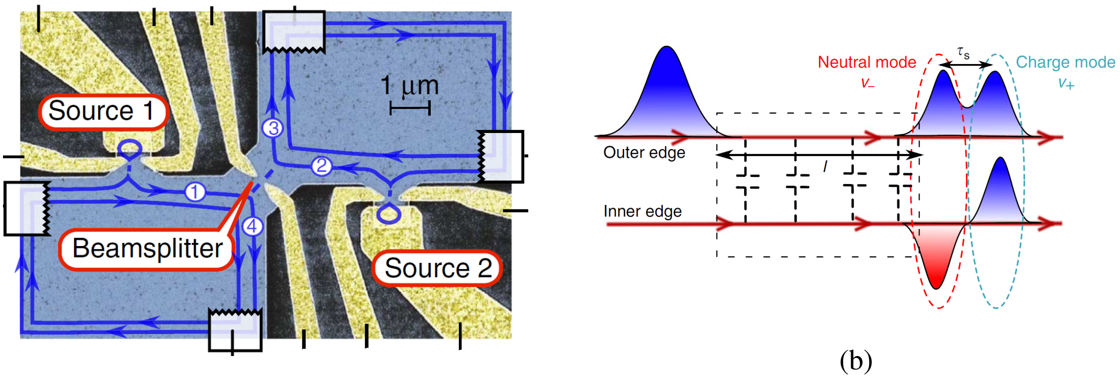

(a)

(b)

Fig. 2.6 (a) Experimental setup used to study interaction effects on single electrons injected from mesoscopic capacitors (“Sources”) into the outer edge channel of a Hall bar at filling factor $\nu = 2$. The coherence properties of the collective excitations created in each couple of co-propagating 1D channels are probed with an interferometric detection scheme (known as Hong-Ou-Mandel interferometer) realized with a QPC acting as beamsplitter. (b) Sketch of the splitting mechanism underwent by an electron injected on the outer channel. Because of inter-channel Coulomb interaction, the electron splits up into two co-propagating excitations: the fast one carries all the charge while the slower one is neutral. Both excitations involve the two channels. Images taken from Ref. [105].

the charge of the electron is carried only by the faster one, the slower being neutral. This is schematically shown in Fig. 2.6b. The properties of these excitations and their real-time dynamics have been extensively studied, both theoretically [123, 125, 126] and experimentally [124]. One of the main finding is that the splitting of the electron into two excitations leads to decoherence effects which, in turn, dramatically reduce the contrast in interferometric detection schemes [123, 124, 105].

Inspired by these interesting results, we studied for the first time the interaction effects after a single-electron injection into a 1D system consisting of two *counterpropagating* channels. A detailed characterization of the two fractional excitations which originated from the injection will constitute the main core of the next chapter, where our results [12, 13] are presented. Note that counterpropagating systems are actually relevant for EQO in at least two different ways. As nicely showed in Ref. [5], an “artificial” LL with counterpropagating and interacting channels can indeed be realized in a Hall bar at filling factor $\nu = 1$ by using a thin gate. Moreover, helical edge states of 2DTIs represent another ideal playground to perform EQO experiments: they are indeed topologically protected from backscattering, thus allowing for ballistic transport, and it is possible to take advantage of their spin-momentum locking to further enrich the EQO phenomenology [127–129]. In this respect, a recent experimental breakthrough in wet-etching techniques may pave the way for an actual implementation of EQO techniques in HgTe-based 2DTIs [108].

Chapter 3

Time-dependent evolution of interacting systems

In this chapter, we will present our original results about the time evolution of 1D interacting systems. In particular, we will focus on a single-electron injection into a 1D interacting system consisting of two topologically protected counterpropagating channels. This process, extremely relevant in the context of EQO, creates two fractional counterpropagating excitations whose properties are carefully analyzed. In this respect, we will present the findings detailed into two of our publications: Ref. [12] and Ref. [13].

The machinery we developed for the aforementioned tasks can be used to study also other out-of-equilibrium regimes of 1D systems, e. g. the one induced by a quantum quench. In this respect, we will also briefly present our results concerning the discovery of a universal feature of relaxation dynamics which follows an interaction quench in a LL. We refer to our original works in Ref. [14, 15] for a more detailed and comprehensive discussion[1].

3.1 Single electron injection in 1D interacting systems

As discussed in the previous chapter, single electron injection is one of the fundamental building block of EQO. In this section, we will focus in particular on the injection from a mesoscopic capacitor, a process which has been widely studied, both theoretically [125, 126] and experimentally [4, 105], in the context of Hall edge states at $\nu = 1$ (non interacting single-channel) and at $\nu = 2$ (a couple of *co-propagating* and interacting 1D channels). Here, however, we will focus, for the first time, on a single-electron injection into a couple of *counterpropagating* and interacting 1D ballistic channels.

---

[1] In this chapter we set $\hbar = 1$

3.1.1 Single electron injection

Let us begin by describing the simple model we will focus on. We consider a single electron level and a 1D interacting system consisting of two counterpropagating ballistic channels. The injection of a single electron into the 1D channels is made possible by a tunneling coupling between the two. The Hamiltonian of the whole system reads

$$H = H_{\mathrm{SL}} + H_{\mathrm{LL}} + H_{\mathrm{T}}\,. \tag{3.1}$$

The single level from which the injected electron originates is modeled as

$$H_{\mathrm{SL}} = \varepsilon_0 d^\dagger d\,, \tag{3.2}$$

with off-resonance energy $\varepsilon_0 > 0$ measured with respect to the Fermi energy E_{F} of the 1D systems. The latter is modeled as an interacting LL

$$H_{\mathrm{LL}} = \int_{-\infty}^{+\infty} dx\, \mathcal{H}(x,t) \tag{3.3}$$

where the Hamiltonian density

$$\mathcal{H}(x,t) = \frac{u}{2} \sum_{\eta=\pm} [\partial_x \phi_\eta (x - \eta u t)]^2 \tag{3.4}$$

is expressed in terms of the bosonic chiral modes ϕ_η, defined in section 2.1.2 [see Eq. (2.28)]. Electron tunneling from the resonant level into the right-moving branch of the 1D system is described by the tunneling Hamiltonian

$$H_T = \lambda \int_{-\infty}^{+\infty} dy\, w(y)\, \psi_R^\dagger(y) d + h.c.\,. \tag{3.5}$$

Here λ is the (small) tunneling amplitude while the function $w(y)$, whose properties will be discussed in the following, characterize the envelope of the tunneling region. Note that the choice of a tunneling Hamiltonian which involves only the R-channel allows to break the inversion symmetry and thus to study the differences between excitations moving in opposite directions.

Physical setups described by our model

Our simple model describes the physics of different experimental setups. One possibility is to consider a mesoscopic capacitor in a 2DTI, see Fig. 3.1a. Here a quantum dot could be

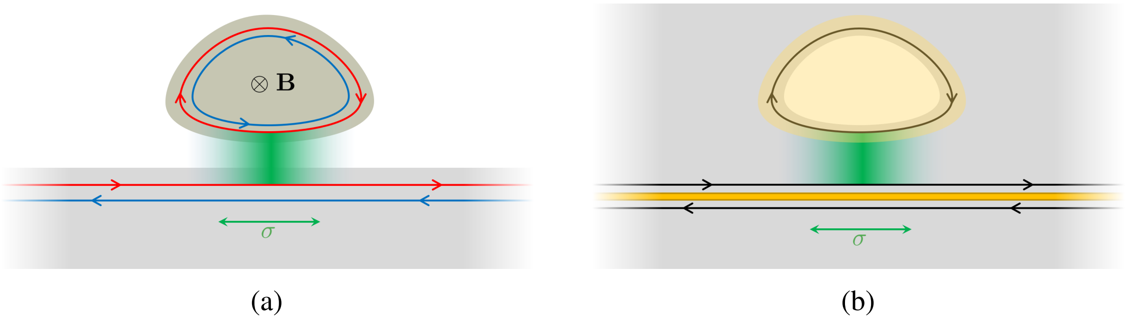

(a) (b)

Fig. 3.1 Possible setups described by our model. In (a), a QD pierced by a magnetic field in a 2DTI acts as SES which injects electrons on one spin-polarized channel of an helical edge state (different colors refer to different spin polarization). In (b), an analogous setup in a Hall bar (filling factor $\nu = 1$) with an anti-dot acting as a mesoscopic capacitor and injecting single electrons on the right moving channel of an effective counterporpagating system realized by implementing a thin gate (yellow).

realized by mean of wet-etching[2], separating an island from the rest of the 2DTI [127–130]. A capacitively coupled top gate is used to shift the discrete spectrum of the dot and it also highly suppresses the electron-electron interactions within the QD because of its screening effects[3]. Because of its finite dimension, the QD will have discrete single-particle levels that come in Kramers pairs. Spin degeneracy can be lifted by an external Zeeman field [127] in the island region. The uppermost occupied level in the dot will thus consist of one spin-polarized electron: acting on the top gate it can be brought at energy ε_0 above the E_F so that it will tunnel into the helical edge. If only spin-preserving tunneling is allowed, the electron is injected only into one channel, say the right-moving one, thus justifying the tunneling Hamiltonian considered in Eq. (3.5). Note that an anti-dot geometry might be used as well [135].

Another possibility consists in mimicking the setup used in Ref. [5] to detect charge fractionalization. A thin metallic gate is placed on a Hall bar at filling factor $\nu = 1$ so that, on each side of the gate, one chiral edge channel is present, see Fig. 3.1b. If the gate is thin enough so that electrons on opposite site interact, the whole system can be effectively described as a couple of interacting and counterpropagating 1D channels. An anti-dot, capacitively coupled with a top-gate, can be pierced on one side of the thin gate and act as a mesoscopic capacitor [136]. Note that the electron injection involves only one 1D channel, i.e. the one on the same side of the thin gate, thus achieving the selective tunneling considered in Eq. (3.5).

---

[2] In principle, if InAs/GaSb-based 2DTIs are used, one could also use metallic gates to shape the topological region.

[3] It has been experimentally shown (in Hall bars) that the charging energy contribution in a mesoscopic capacitor is very small [117, 4, 105, 131] thus explaining the success of non-interacting models usually considered in describing the QD region. It is worth noting that, in systems *without* a top gate, interactions between QDs and 1D channels can have strong effects [132–134].

Usually the tunneling Hamiltonian is assumed to be local. Here, however, we want to explore also the non-local injection regime. To this end, we consider an extended tunneling region of width σ (see Fig. 3.1): as we will see in Section 3.1.3, this allows for a richer phenomenology mainly due to the fact that, in a non-local tunneling event, the momentum of the injected electron can play an important role. A non-local injection is quantitatively described by the envelope function

$$w(y) = \xi(y)e^{ik_0y} = e^{ik_0y}\frac{1}{\sqrt{\pi}\sigma}\,e^{-\frac{y^2}{\sigma^2}} \tag{3.6}$$

consisting of a real Gaussian $\xi(y)$ and of a complex phase. Here $k_0 = k_{\mathrm{QD}} - k_{\mathrm{F}}$ is defined as the mismatch between the momentum of the electron which is about to tunnel from the quantum (anti-) dot (k_{QD}) and the Fermi momentum in the right-moving channel (k_{F}). In principle, k_0 can be tuned by means of additional gate voltages applied either to the QD or to the edge channels in order to shift their spectra with respect to each other [137–139]. Note that in the local-injection limit ($\sigma \to 0$) one has $w(y) \to \delta(y)$ and k_0 is completely irrelevant, as expected.

Description of the injection process

Here we model the single electron injection process. Let us assume that at time $t = 0$ the 1D system is in its ground state $|\Omega_N\rangle$ (zero temperature limit) with fixed particle number N. Its equilibrium density matrix reads $\hat{\rho}_{LL}(0) = |\Omega_N\rangle\langle\Omega_N|$. On the contrary, the single resonant level is initially occupied and described by the density matrix $\hat{\rho}_{QD}(0) = |1\rangle\langle 1|$.

Let O be a generic number-conserving operator that acts on the LL, such as, for example, the particle density. In the interaction picture, with respect to the tunneling Hamiltonian H_T, the time evolution average of $O(t)$ reads

$$\langle O(t)\rangle = \mathrm{Tr}\left\{O(t)\hat{\rho}(t)\right\}, \tag{3.7}$$

with the time dependent density matrix

$$\hat{\rho}(t) = U(t,0)\hat{\rho}(0)U^{\dagger}(t,0) \tag{3.8}$$

where ($\mathbb{T}$ denoting the time-ordering)

$$U(t,0) = \mathbb{T}\left[e^{-i\int_0^t dt' H_T(t')}\right] \tag{3.9}$$

$$\hat{\rho}(0) = \hat{\rho}_{LL}(0)\otimes\hat{\rho}_{QD}(0). \tag{3.10}$$

We are interested in the average variation of $O(t)$ induced by the tunneling process

$$\delta O(t) = \mathrm{Tr}\{O(t)\,[\hat{\rho}(t) - \hat{\rho}(0)]\}\,. \tag{3.11}$$

At lowest order in the tunneling one has

$$\begin{aligned}\delta O(t) = &\int_0^t dt_1 \int_0^{t_1} dt_2\ \mathrm{Tr}\{\hat{\rho}(0) H_T(t_2)\,[O(t), H_T(t_1)]\}_{1,N}\\ &+\int_0^t dt_1 \int_0^{t_1} dt_2\ \mathrm{Tr}\left\{\hat{\rho}(0) H_T(t_2)\left[O(t)^{\dagger}, H_T(t_1)\right]\right\}^*_{1,N}\end{aligned} \tag{3.12}$$

where the symbol $\mathrm{Tr}\{\dots\}_{1,N}$ denotes the trace over system's excitations with fixed particle numbers: one electron in the single level and N in the LL.

Being tunnel coupled with the LL, the resonant level acquire a finite lifetime $(2\gamma)^{-1}$ [4, 140]. Note that the energy broadening γ must be small, i.e. $0 < \gamma \ll \varepsilon_0$, so that the injection of a single electron is actually possible. In the following we will focus on this regime, known as "optimal" in the EQO community [4, 141]. In order to describe the discharge of the single level, we explicitely take into account its large-but-finite lifetime via the approximate correlator[4]

$$\langle d^{\dagger}(t_2) d(t_1)\rangle = \beta^*(t_2)\beta(t_1) \tag{3.13}$$

with

$$\beta(t) = e^{-i\varepsilon_0 t} e^{-\gamma t}. \tag{3.14}$$

Eq. (3.13) consists in a Markov approximation, already exploited in literature [126, 143]. The precise value of γ will be calculated microscopically in order to guarantee the conservation of the total injected charge[5]. Approximation (3.13) allows to express (3.12) as

$$\begin{aligned}\delta O(t) = |\lambda^2| \int_0^t dt_1 \int_0^{t_1} dt_2 \iint_{-\infty}^{+\infty} dy_1\, dy_2&\\ \Xi(t_1,y_1;t_2,y_2)\left[\mathcal{I}_{(O)}(t_1,y_1;t_2,y_2;t) + \mathcal{I}_{(O^{\dagger})}(t_1,y_1;t_2,y_2;t)^*\right]&\end{aligned} \tag{3.15}$$

---

[4] It is worth noting that, in the *non-interacting* case, it is possible to solve the problem at all orders in lambda without the need of such an approximation[142].

[5] Here, we have not considered energy-dependent corrections to the self energy of the single-level [144, 145] since, in the optimal regime, their effects can be neglected.

where

$$\Xi(t_1,y_1;t_2,y_2) = \beta(t_1)w(y_1)\beta(t_2)^*w(y_2)^* \tag{3.16}$$

$$\mathcal{I}_{(O)}(t_1,y_1;t_2,y_2;t) = \langle \psi_R(y_2,t_2)\left[O(t),\psi_R^\dagger(y_1,t_1)\right]\rangle_\Omega \tag{3.17}$$

and the average is performed over the LL ground state $|\Omega\rangle$.

Inverse lifetime

We now evaluate the inverse lifetime 2γ of the single resonant level. It is related to the time derivative of $P(t)$, the probability of transition from the dot to the edge channel, by

$$2\gamma = \lim_{t\to+\infty} \dot{P}(t)\,. \tag{3.18}$$

Recalling that the system is initially in a state with one electron in the dot and N electrons in the edge channels, the transition probability is given by the relation

$$P(t) = \mathrm{Tr}\{\langle N+1,0|\,\hat{\rho}(t)\,|N+1,0\rangle\}\,, \tag{3.19}$$

where $|N+1,0\rangle$ denotes the state with no electrons in the dot and $N+1$ electrons in the edge channels. The trace is calculated over the excitations of the system at fixed particle number. At lowest order in the tunneling one has

$$P(t) = |\lambda|^2 \iint_0^t dt_2dt_1 \iint_{-\infty}^{+\infty} dy_2dy_1\; e^{i\varepsilon_0(t_2-t_1)}\; w^*(y_2)w(y_1)\,\mathcal{G}(y_2,t_2;y_1,t_1)\,, \tag{3.20}$$

where we have introduced the fermionic correlator on the R-channel

$$\mathcal{G}(y_2,t_2;y_1,t_1) = \left\langle \psi_R(y_2,t_2)\psi_R^\dagger(y_1,t_1)\right\rangle_\Omega\,. \tag{3.21}$$

Using the identity in (B.15) and introducing the shorthand notations

$$z_\eta = x-\eta ut\,, \qquad z_i^\eta = y_i-\eta ut_i \qquad (i=1,2)\,, \tag{3.22}$$

the correlator $\mathcal{G}$ is expressed in terms of the bosonic Green function

$$G(\pm z) = \langle\phi_\mp(z)\phi_\mp(0)\rangle_\Omega - \langle\phi_\mp^2(0)\rangle_\Omega = \frac{1}{2\pi}\log\frac{a}{a\pm iz} \tag{3.23}$$

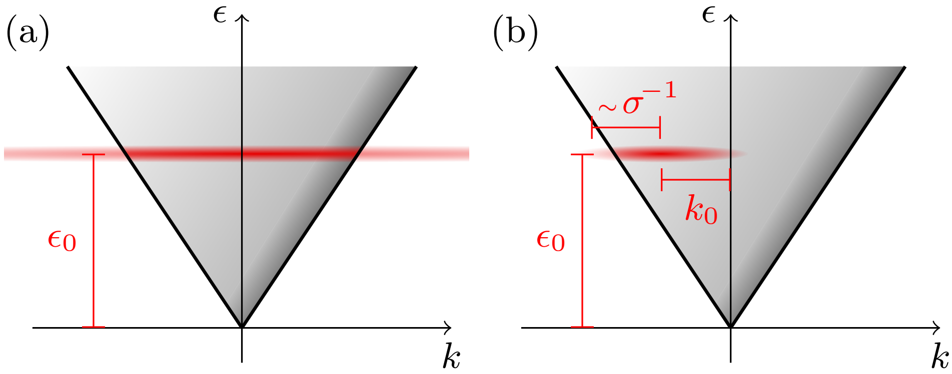

Fig. 3.2 Sketch of the overlap between the spectral function $\mathcal{A}_R(k,\varepsilon)$ (in gray) and $|\tilde{\xi}(k)|^2$ (in red). The latter is represented with a horizontal line at energy ε_0 since we are considering injection of an electron with well defined energy. Panel (a): local injection ($\sigma \to 0$). Panel (b): non-local injection ($\sigma \sim 2u\varepsilon_0^{-1}$) with a finite extension in k region for $|\tilde{\xi}(k)|^2$ centered around k_0.

as

$$\mathcal{G}(z_2^\pm; z_1^\pm) = \frac{1}{2\pi a}\, e^{2\pi A_+^2 G(z_1^+ - z_2^+)}\, e^{2\pi A_-^2 G(z_2^- - z_1^-)}\,. \tag{3.24}$$

Performing the time derivative one has (see Appendix B.1)

$$\gamma = \gamma_0 \frac{v_\mathrm{F}}{2\pi} \int dk\, \mathcal{A}_R(k,\varepsilon_0) \left|\tilde{\xi}(k_0 - k)\right|^2, \tag{3.25}$$

with

$$\gamma_0 = \frac{|\lambda|^2}{2v_\mathrm{F}}. \tag{3.26}$$

Here, $\tilde{\xi}(k)$ is the Fourier transform of the real envelope function $\xi(y)$ (see Eq. (3.6) and Eq. (B.5)) and thus $|\tilde{\xi}(k_0 - k)|^2$ is centered around $k = k_0$. The function

$$\mathcal{A}_R(k,\varepsilon > 0) = \frac{2\pi\, e^{-\varepsilon a/u}}{A_-^2 \Gamma^2(A_-^2)} \left(\frac{a}{2u}\right)^{2A_-^2} (\varepsilon + uk)^{A_-^2} (\varepsilon - uk)^{A_-^2 - 1}\, \theta(\varepsilon - u|k|), \tag{3.27}$$

is the spectral function of the right edge channel [82]. Recall that k and ε are defined as momentum and energy with respect to k_F and E_F respectively. Equation (3.25) has a clear physical interpretation: 2γ represents a tunneling rate and is proportional to the overlap between the spectral function $\mathcal{A}_R(k,\varepsilon_0)$ and the k “spectrum” of the injected electron, described by $|\tilde{\xi}(k_0 - k)|^2$. In Fig. 3.2 one can see this overlap in the energy and momentum space. The region where $\mathcal{A}_R(k,\varepsilon) \neq 0$ is filled in gray, showing that in the presence of e-e interactions the spectral function broadens and does not vanish away from the mass shell ($\varepsilon = uk$). The injected

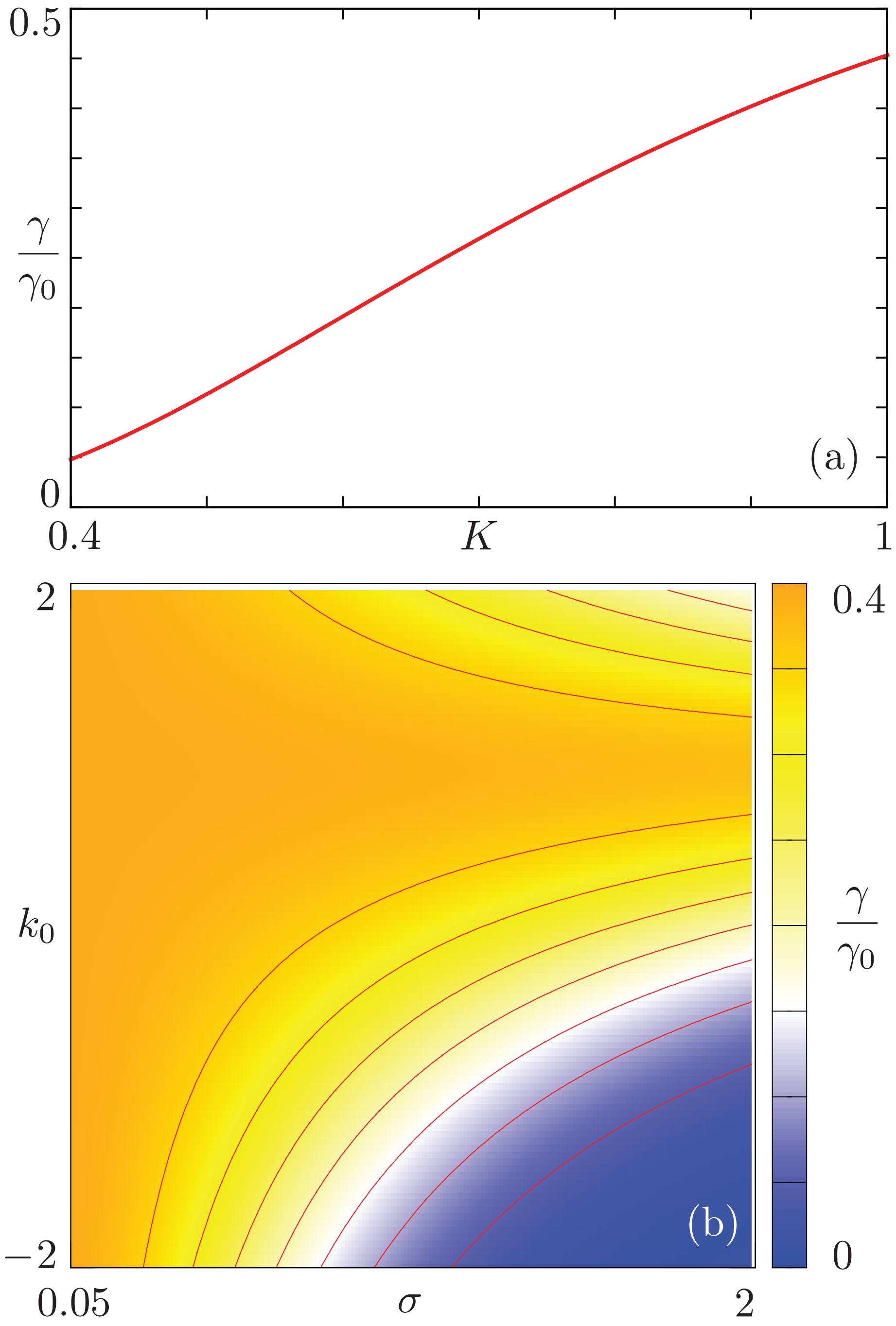

Fig. 3.3 Panel (a): ratio γ/γ_0 as a function of interaction strength K with $\bar{\sigma} = 0.9$ and $\bar{k}_0 = -1.2$. Panel (b): density plot of γ/γ_0 as a function of $\bar{\sigma}$ (x-axis) and $\bar{k}_0$ (y-axis) with $K = 0.6$. In both panels $a = 1/40 v_{\mathrm{F}} \varepsilon_0^{-1}$.

electron has a well defined energy $\varepsilon_0 > 0$ and thus the function $|\tilde{\xi}(k_0 - k)|^2$ is represented as a red horizontal line at ε_0, centered around $k = k_0$ with an extension of the order of σ^{-1}. Panel (a) refers to local injection: $\sigma \to 0$, with $|\tilde{\xi}(k_0 - k)|^2 \sim 1$. Here, the momentum k_0 is not relevant and the overlap is along the darker red line over the gray cone. In this limit the integral in Eq. (3.25) can be solved analytically, giving the local rate

$$\gamma^{loc} = K\gamma_0 \frac{\left(Ka\frac{\varepsilon_0}{v_{\mathrm{F}}}\right)^{2A_-^2}}{\Gamma(1+2A_-^2)} e^{-Ka\frac{\varepsilon_0}{v_{\mathrm{F}}}}, \tag{3.28}$$

Note that γ_0 in Eq. (3.26) represents the asymptotic value of $\gamma^{loc} < \gamma_0$ in the non interacting limit $K \to 1$.

Fig. 3.2(b) shows a non-local injection. Here, $|\tilde{\xi}(k_0 - k)|^2$ is centered around k_0, chosen in the figure to be negative, with a width $\sim \sigma^{-1}$. The overlap between the two functions is significantly smaller with respect to (a) and it further reduces as long as k_0 is pushed away from the gray cone. In addition, for a given interaction strength K, and momentum k_0, the overlap decreases as σ increases with the result $\gamma < \gamma^{loc} < \gamma_0$.

For convenience we introduce the dimensionless parameters

$$\bar{\sigma} = \frac{\sigma\varepsilon_0}{v_{\mathrm{F}}}, \quad \bar{k}_0 = \frac{k_0 v_{\mathrm{F}}}{\varepsilon_0}. \tag{3.29}$$

The dependence of the ratio γ/γ_0 on different parameters is reported in Fig. 3.3, where the relation $\gamma < \gamma_0$ clearly emerges. Panel (a) shows the suppression of the tunneling rate as the interaction strength increases, a well-known feature of LL. Parameter $\bar{k}_0$, considered in panel (b), does not affect γ as long as local-tunneling is concerned but becomes more and more relevant as $\bar{\sigma}$ increases. In particular, γ significantly diminishes when k_0 is pushed away from the momentum range where the spectral function $\mathcal{A}_R(k, \varepsilon_0)$ has finite values (see also Fig. 3.2).

3.1.2 Charge density and its fractionalization

Here we will use the result (3.15) to compute the time evolution of the charge density variation $\delta\rho(x,t)$, defined as in Eq. (3.11) with $O \equiv \rho$. Note that charge is measured in units of the electron's one so that charge density exactly equals particle density $\rho(x,t)$. The latter can be expressed in terms of chiral bosonic fields as

$$\rho(x,t) = -\sqrt{\frac{K}{2\pi}} \sum_\eta \eta\, \partial_x \phi_\eta \,. \tag{3.30}$$

As shown in Appendix B.2.1, the average factor $\mathcal{I}_{(O=\rho)}$ in Eq. (3.17) can be evaluated yielding

$$\mathcal{I}_{(\rho)} = \mathcal{I}_{(\rho^\dagger)} = \sum_{\eta=\pm 1} q_\eta \left[\frac{1}{\pi} \frac{a}{a^2 + (z_\eta - z_2^\eta)^2} \right] \mathcal{G}(y_2, t_2; y_1, t_1) \,, \tag{3.31}$$

where q_η are the charge fractionalization factors defined in (2.34), i.e.

$$q_\eta = \frac{1 + \eta K}{2} \,, \tag{3.32}$$

and $\mathcal{G}$ is the fermionic correlator (3.21). The charge density is then computed inserting $\mathcal{I}_\rho$ into the average (3.15). It results into the sum of two chiral contributions

$$\delta\rho(x,t) = \sum_\eta \delta\rho_\eta(z_\eta),$$

which can be expressed in terms of the bosonic correlators G in (3.23)

$$\begin{aligned} \delta\rho_\eta(z_\eta) = \frac{q_\eta |\lambda|^2}{\pi a} \,\mathrm{Re} \int_0^t dt_1 \int_0^{t_1} dt_2 \iint_{-\infty}^{+\infty} dy_2 \, dy_1 & \\ \Xi(t_1, y_1; t_2, y_2) \;\; \delta(z_\eta - z_2^\eta) \;\; e^{2\pi A_+^2 G(z_1^+ - z_2^+)} \; e^{2\pi A_-^2 G(z_2^- - z_1^-)} & . \end{aligned} \tag{3.33}$$

This important result will be the starting point for the study of the charge density profile of the two fractional excitations which travel in the LL after the single-electron injection. However, before addressing this topic [see section 3.1.4], let us focus here on the total charge associated with each one of the two fractional excitations.

Charge fractionalization

The total amount of injected charge that travels in a given direction ($\eta = \pm$) is

$$\mathcal{Q}_\eta = \int_{-\infty}^{+\infty} dx \, \delta\rho_\eta(x, t \to \infty). \tag{3.34}$$

This integral can be easily performed from Eq. (3.33) for $\delta\rho_\eta(z_\eta)$. One finds $\mathcal{Q}_\eta = q_\eta \mathcal{Q}$ where

$$\mathcal{Q} = |\lambda|^2 \int_0^\infty dt_1 \int_0^{t_1} dt_2 \iint_{-\infty}^{+\infty} dy_2 dy_1 \; [\Xi \mathcal{G} + h.c.] \tag{3.35}$$

represents the total amount of charge injected in the system. Note that the previous relation can be also written as

$$\mathcal{Q} = |\lambda|^2 \iint_0^{+\infty} dt_2 dt_1 \iint_{-\infty}^{+\infty} dy_2 dy_1 \; \Xi(t_1, y_1; t_2, y_2) \mathcal{G}(y_2, t_2; y_1, t_1) \,. \tag{3.36}$$

We thus recover the expression (2.34) for charge fractionalization factors

$$\frac{\mathcal{Q}_\eta}{\mathcal{Q}_+ + \mathcal{Q}_-} = q_\eta = \frac{1+\eta K}{2} \tag{3.37}$$

that depend *only* on the interaction strength K. This is not surprising giving the fact that charge fractionalization stems from an operator identity, see Eq. (2.31).

For $t \gg 1/(2\gamma)$ the QD level is empty and the total amount of injected charge $\mathcal{Q} = \mathcal{Q}_+ + \mathcal{Q}_-$ is expected to satisfy $\mathcal{Q} = 1$. It is indeed shown in Appendix B.2.2 that, as long as $\gamma \ll \varepsilon_0$, the condition $\mathcal{Q} = 1$ holds.

3.1.3 Energy density and its partitioning

The injected electron transfers into the helical edge not only charge but also energy. We then start focusing on the evaluation of the energy density [see Eq. (3.4)] variation, proceeding along the lines discussed in the previous subsection. Considering $\mathcal{I}_{(O=\mathcal{H})}$ in Eq. (3.17) and the commutator relation in Eq. (B.13) one can derive the following expression

$$\begin{aligned}\mathcal{I}_{\mathcal{H}} &= \sum_\eta \frac{u}{2}\left\langle \psi_R(y_2,t_2)\left[:(\partial_x\phi_\eta(z_\eta))^2:,\, \psi_R^\dagger(y_1,t_1)\right]\right\rangle_\Omega \\ &= -\sum_\eta \frac{u\eta A_\eta\sqrt{\pi}}{\sqrt{2}}\left(\frac{1}{\pi}\frac{a}{a^2+(z_\eta-z_1^\eta)^2}\right)\partial_x\left(\mathcal{M}_\eta^{(a)}+\mathcal{M}_\eta^{(b)}\right)\end{aligned} \tag{3.38}$$

with

$$\mathcal{M}_\eta^{(a)} = \left\langle \psi_R(y_2,t_2)\,\phi_\eta(z_\eta)\,\psi_R^\dagger(y_1,t_1)\right\rangle_\Omega \tag{3.39}$$

$$\mathcal{M}_\eta^{(b)} = \left\langle \psi_R(y_2,t_2)\,\psi_R^\dagger(y_1,t_1)\,\phi_\eta(z_\eta)\right\rangle_\Omega . \tag{3.40}$$

These average functions are evaluated in Appendix B.3 with the final result

$$\mathcal{I}_{\mathcal{H}} = u\sum_\eta A_\eta^2\,\mathcal{G}\left[i\frac{\eta}{2}\partial_{z_1^\eta}\left(\frac{1}{\pi}\frac{a}{a^2+(z_\eta-z_1^\eta)^2}\right)+\left(\frac{1}{\pi}\frac{a}{a^2+(z_\eta-z_1^\eta)^2}\right)\frac{1}{a+i\eta(z_\eta-z_2^\eta)}\right]. \tag{3.41}$$

This formula allows to express the total energy density profile $\delta\mathcal{H}(x,t)$ in Eq. (3.15) as a sum of the left and right moving contributions $\delta\mathcal{H}(x,t)=\sum_\eta \delta\mathcal{H}_\eta(z_\eta)$, with

$$\begin{aligned}\delta\mathcal{H}_\eta(z_\eta) = \frac{uA_\eta^2|\lambda|^2}{\pi a^2}\, \mathrm{Re}\int_0^t dt_1\int_0^{t_1} dt_2 \iint_{-\infty}^{+\infty} dy_2 dy_1\ \Xi(t_1,y_1;t_2,y_2) \\ \times\mathcal{G}(t_2,y_2;t_1,y_1)\left(\frac{a}{a+i\eta(z_\eta-z_2^\eta)}+i\frac{\eta a}{2}\partial_{z_1^\eta}\right)\delta(z_\eta-z_1^\eta).\end{aligned} \tag{3.42}$$

As for the charge, let us focus at first on the total amount of energy associated with each one of the two counterpropagating fractional excitations. The detailed study of the energy density profile from Eq. (3.42) will be discussed in section 3.1.5.

Energy partitioning

To analyze energy partitioning phenomena, we now focus on the total amount of energy that travels in a given direction once the injection is concluded

$$E_\eta = \int_{-\infty}^{+\infty} dx\, \delta\mathcal{H}_\eta(x,t\to\infty)\,. \tag{3.43}$$

Using the expression (3.42) for $\delta\mathcal{H}_\eta(x,t)$ one has

$$E_\eta = \frac{uA_\eta^2|\lambda|^2}{2\pi a^2}\int_0^{+\infty} dt_1\int_0^{t_1} dt_2 \iint_{-\infty}^{+\infty} dy_2 dy_1 \left[\Xi\ e^{2\pi G(z_1^+-z_2^+)g_\eta^+}\, e^{2\pi G(z_2^- -z_1^-)g_\eta^-}+h.c.\right]\,, \tag{3.44}$$

where $g_\eta^\pm = A_\pm^2+(1\pm\eta)/2$. The above expression can be conveniently represented in Fourier space (similarly to what has been done in Appendix B.1) as

$$\begin{aligned}E_\eta = \frac{KA_\eta^2\gamma_0}{2\pi}\left(\frac{Ka}{2v_\mathrm{F}}\right)^{2A_-^2}\frac{1}{\Gamma(g_\eta^-)\Gamma(g_\eta^+)}\int_0^{+\infty} d\varepsilon_+ \left|\tilde{\beta}(\varepsilon_+)\right|^2 e^{-K\frac{\varepsilon_+}{v_\mathrm{F}}} \\ \times\int_{-\varepsilon_+}^{+\varepsilon_+} d\varepsilon_-(\varepsilon_+ +\varepsilon_-)^{g_\eta^+-1}(\varepsilon_+ -\varepsilon_-)^{g_\eta^- -1}\left|\tilde{\xi}\,(k_0-\varepsilon_-/u)\right|^2.\end{aligned} \tag{3.45}$$

The key quantities to discuss are the energy partitioning factors defined as

$$p_\eta = \frac{E_\eta}{E_+ + E_-}\,. \tag{3.46}$$

They indeed represent the fraction of the total energy $E=E_+ + E_-$ that propagates in the direction $\eta=\pm$. Concerning the total contribution $E=E_+ + E_-$, we demonstrate in Appendix B.3.1 that $E=\varepsilon_0$ as long as $\gamma \ll \varepsilon_0$.

In the local injection limit $\tilde{\xi}(k) = 1$ one has (see Appendix B.3.1)

$$p_{\eta}^{loc} = \frac{A_{\eta}^{2}}{A_{-}^{2} + A_{+}^{2}} = \frac{(1+\eta K)^{2}}{2(K^{2}+1)}. \tag{3.47}$$

Namely, energy partitioning has a “universal” character, i.e. p_{η}^{loc} does not depend on injection parameters but *only* on interaction strength, in agreement with the partitioning of DC energy transport found in Ref. [98].

On the other hand, it can be shown that such universality breaks down as the width of the tunneling region increases. In order to quantitatively highlight this deviation we present below results for the right moving energy fraction p_{+} in Eq. (3.46), using the gaussian envelope $\xi(y)$ in (3.6).

Fig. 3.4 shows two representative cases of energy partitioning as a function of interaction strength. The local limit p_{+}^{loc} (3.47) is drawn with a solid red line. Panel (a), has $\bar{k}_0 = 0$, and shows deviations from the local limit as $\bar{\sigma}$ increases, with $0.5 < p_{+}(K) < p_{+}^{loc}(K)$. These deviations are even more striking for negative values of $\bar{k}_0$ as shown in panel (b) with $\bar{k}_0 = -1.2$. Here, it is even possible to achieve $p_{+}(K) < 0.5$ for a wide range of interaction strength (dot-dashed curve). This means that, due to interactions and non local tunneling, the energy of an electron, injected into the right branch, can travel mostly to the left while its charge still continues to move mainly to the right ($q_{+} > q_{-}$). Fig. 3.5 represents the cartoon of this charge and energy decoupling. To clarify the physical interpretation of this effect, we consider in Fig. 3.6 the energy partitioning factor p_{+} as a function of $\bar{\sigma}$ for different interaction strength. In panel (a) $\bar{k}_0 = 0$ while in panel (b) $\bar{k}_0 = -1.2$. For $\bar{\sigma} \to 0$ one recovers the “universal” behavior, while deviations from it become relevant as $\bar{\sigma}$ increases and reaches $\bar{\sigma} \gtrsim 1$. Comparing the two panels, note that these deviations emerge at smaller $\bar{\sigma}$ when $\bar{k}_0$ is significantly different from $\bar{k}_0 = 0$. This fact can be understood considering again the overlap between the spectral function $\mathcal{A}_R(\varepsilon, k)$ and the injected electron momentum “spectrum” $|\tilde{\xi}(k_0 - k)|^2$ represented as insets of the two main panels in Fig. 3.6. Here, we sketched two typical situations with the same interaction and momentum $\bar{k}_0$ as given in the main panel. Non-universal effects appear only when the red line does not cover the whole gray region, whose extension at $\varepsilon = \varepsilon_0$ is given by $2\varepsilon_0 K/v_{\mathrm{F}}$ (see Eq. (3.27)). Therefore, if one considers $\bar{k}_0 = 0$ (panel (a)) it is necessary $\bar{\sigma} \gtrsim K^{-1}$ in order to break the energy partitioning universality. By contrast, for a negative $\bar{k}_0 = -1.2$ (panel (b)), a smaller $\bar{\sigma}$ will be required since the overlap is already smaller. While discussing $\bar{\sigma}$, it worth noting that, for the two experimental realizations devised in subsection 3.1.1, one has the constraint $\bar{\sigma} \lesssim 2$ which stems from the requirement that the level spacing in the dot is less than ε_0.

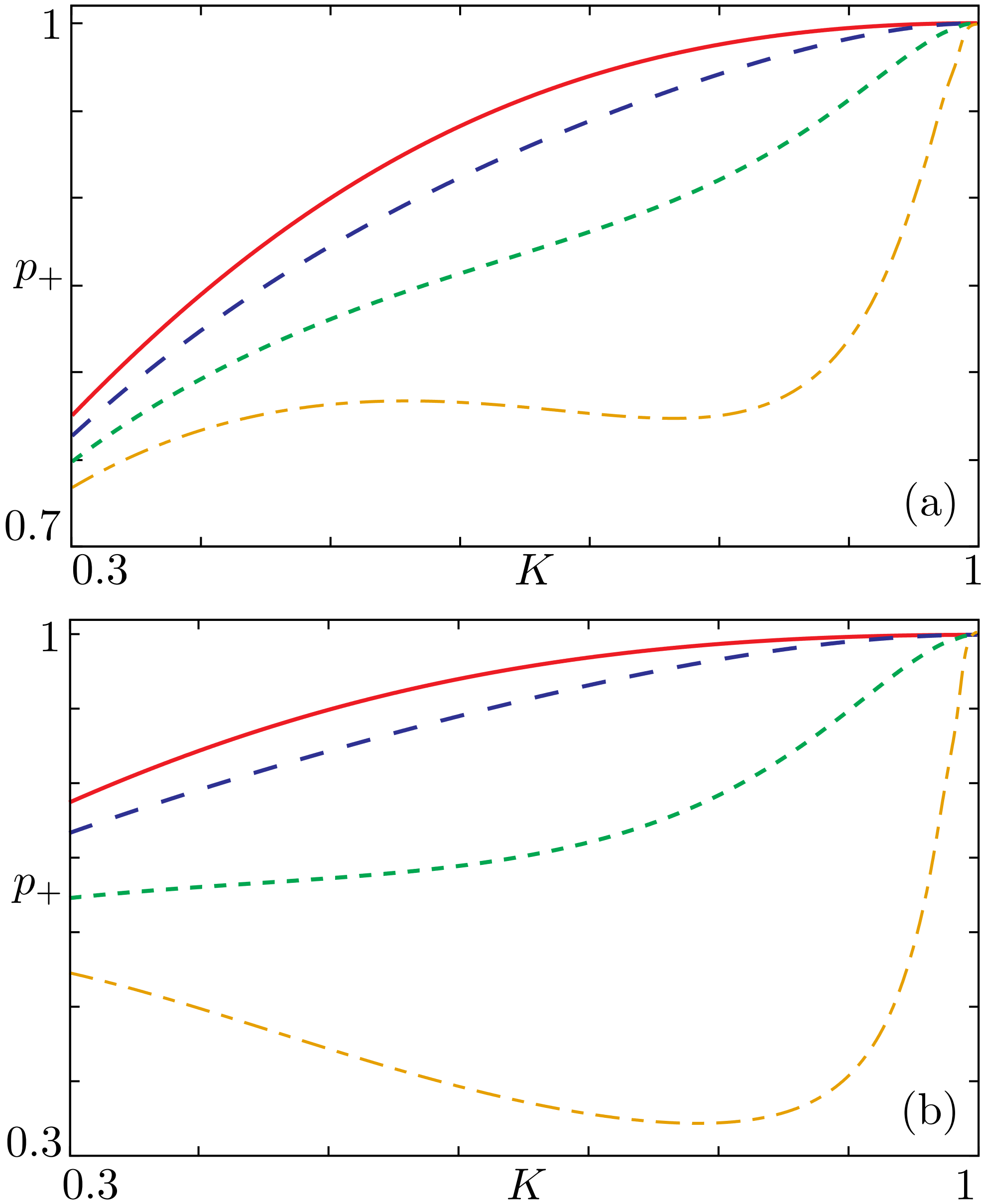

Fig. 3.4 Energy partitioning factor p_+ as a function of the interaction strength K. In panel (a) $\bar{k}_0 = 0$, with $\bar{\sigma} \to 0$ (solid red), $\bar{\sigma} = 2$ (dashed blue), $\bar{\sigma} = 3$ (dotted green) and $\bar{\sigma} = 3.75$ (dot dashed orange). Panel (b) shows $\bar{k}_0 = -1.2$ with $\sigma \to 0$ (solid red), $\bar{\sigma} = 0.9$ (dashed blue), $\bar{\sigma} = 1.5$ (dotted green) and $\bar{\sigma} = 1.95$ (dot dashed orange). Parameters: $\gamma_0 = 0.05\,\varepsilon_0$ and $a = 1/40 v_{\mathrm{F}} \varepsilon_0^{-1}$.

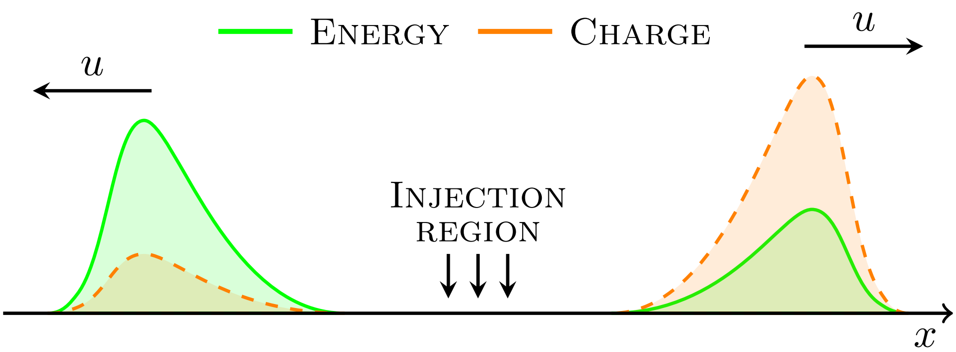

Fig. 3.5 Cartoon showing the strong direction separation of energy (solid green) and charge (dashed orange) for $K = 0.8$, $\bar{\sigma} = 1.95$ and $\bar{k}_0 = -1.2$. The majority of charge (80%) travels to the right while most of the energy (about 65%) moves to the left.

Note that all these deviations are much less pronounced (and then not shown) for $\bar{k}_0 > 0$ since even with extended tunneling, the transferred momentum lies near the right electron branch, leading to $p_+(K) > p_+^{loc}$. As a last comment, the non-interacting limit $K \to 1$ shows always $p_+ = 1$, regardless of all the other parameters. Energy partitioning is indeed a manifestation of e-e interactions and so, if they're absent, all the energy added to the system after an R-electron injection goes to the right.

Non-universal features of energy partitioning can thus play an important role when a non-local injection is concerned. In particular, it is possible to directly control the energy flow after a single electron injection, being able even to invert its direction with respect to the charge flow. The energy flow, and its partitioning, could be inspected by means of nanocalorimetric measurements [146, 147].

3.1.4 Charge density profile

We now focus on the local-injection limit $\xi(y) = \delta(y)$, in order to study interactions effects on the charge density profile. Integrating Eq. (3.33) one has

$$\delta\rho_\eta(x,t) = \frac{q_\eta|\lambda|^2}{2\pi a u} 2\mathrm{Re}\int_0^t dt_1 \int_0^{t_1} dt_2\, \beta^*(t_2)\beta(t_1)\, \delta(t_1 - t - \frac{\eta x}{u}) \left(\frac{a}{a + iu(t_2 - t_1)}\right)^{1+2A_-^2} . \tag{3.48}$$

We observe that, apart from the fractionalization factors q_η, the two chiral charge density packets share the same mirrored shape

$$\frac{\delta\rho_+(x,t)}{q_+} = \frac{\delta\rho_-(-x,t)}{q_-}. \tag{3.49}$$

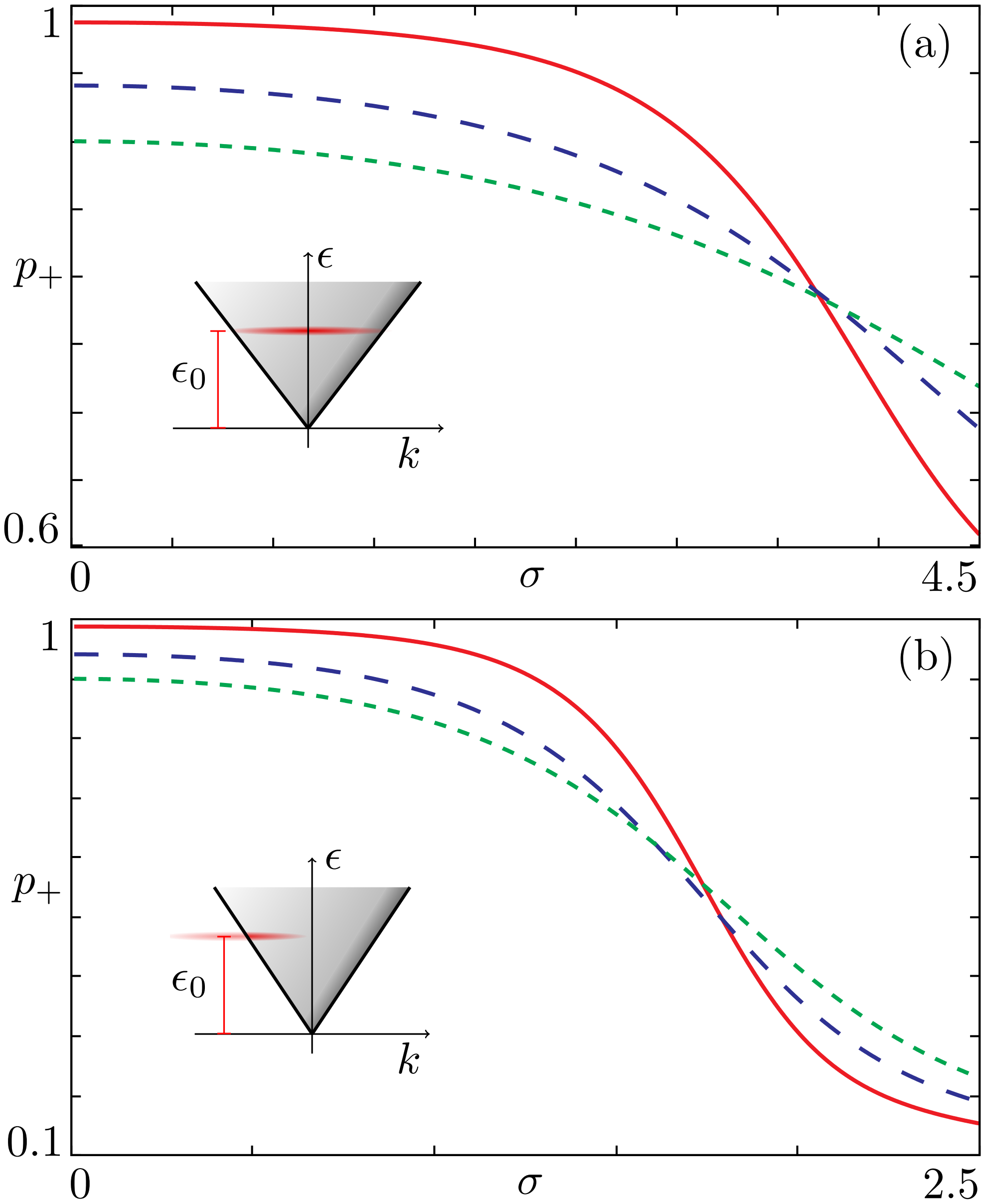

Fig. 3.6 Energy partitioning factor p_+ as a function of the tunneling region width $\bar{\sigma}$. Each line refers to different interaction parameter: $K = 0.8$ (solid red), $K = 0.6$ (dashed blue) and $K = 0.5$ (dotted green). In panel (a) $\bar{k}_0 = 0$ while panel (b) $\bar{k}_0 = -1.2$. The insets show the overlap, at the same interaction strength, between the edge spectral function (in gray) and the momentum "spectrum" of the injected electron (in red), along the lines of Fig. 3.2. The momentum $\bar{k}_0$ is the same of the hosting panel. Parameters: $\gamma_0 = 0.05\,\varepsilon_0$ and $\bar{a} = \frac{1}{40}v_\mathrm{F}\varepsilon_0^{-1}$.

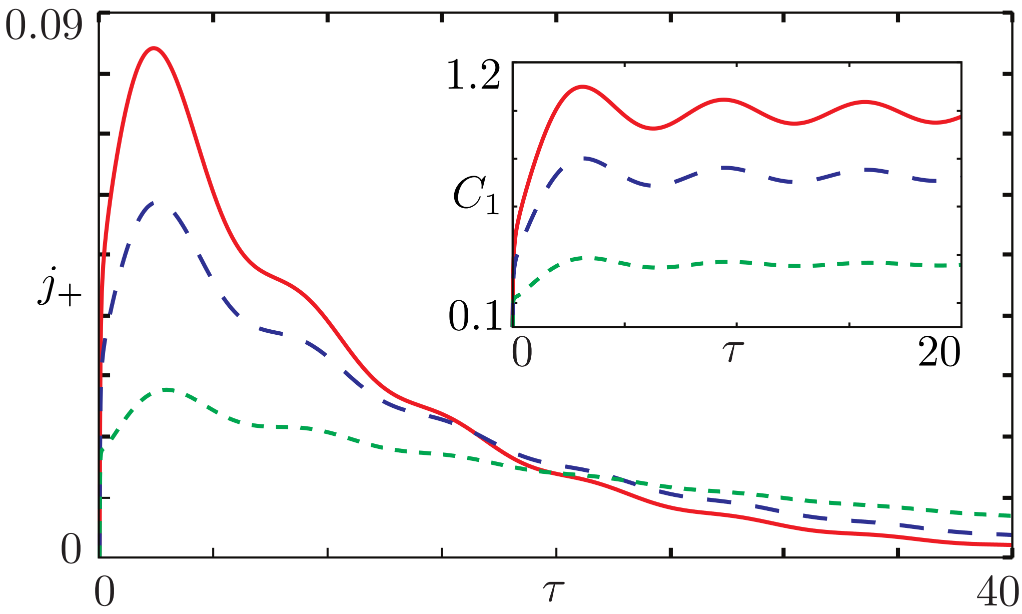

Fig. 3.7 Charge current $j_+(\tau)$ (in units of ε_0) flowing in the right direction through the detection point $x_D > 0$ as a function of time (in units of ε_0^{-1}). Different interaction strengths are considered: solid red line $K = 1$ (non-interacting case), dashed blue $K = 0.8$, and green dotted $K = 0.6$. The inset shows the function $C_1(\tau)$ with the same color coding. Parameters: $\gamma_0 = 0.05\ \varepsilon_0$ and $a = 1/40 v_F \varepsilon_0^{-1}$.

As a consequence, we can focus only on the right-moving packet ($\eta = +$). We analyze the corresponding charge current $j_+(\tau) = u\delta\rho_+(\tau)$ with $\tau = t - x_D/u$, flowing through a "detection" point $x_D > 0$ away from the injection region. The integral over t_1 in Eq. (3.48) can be easily performed yielding

$$j_+(\tau) = 2q_+\gamma_0\ \theta(\tau)\ \exp[-2\tau\gamma]\ \mathrm{Re}[C_1(\tau)]\ , \tag{3.50}$$

where ($m \in \mathbb{N}$)

$$C_m(\tau) = \frac{\varepsilon_0}{\pi}\left(\frac{v_F}{a\varepsilon_0}\right)^m \int_{-\tau}^{0} ds\, e^{-s\gamma} e^{is\varepsilon_0} \left(\frac{a v_F^{-1}}{a v_F^{-1} + isK^{-1}}\right)^{m+2A_-^2} . \tag{3.51}$$

First of all we note that, because of causality, $j_+(\tau) \neq 0$ only for $\tau > 0$, since an excitation created in $x = 0$ takes exactly a time x_D/u to reach the detection point. Another clear feature is the exponential decrease $e^{-2\gamma\tau}$ due to the QD single level inverse lifetime (2γ). The presence of the interacting helical Fermi sea is taken into account by the function $C_1(\tau)$[6]. Fig. 3.7 shows

---

[6] It is possible to show that, for $K = 1$ and in the limit $\varepsilon_0 \to +\infty$ (where one can actually forget about the Fermi sea), function $C_1(\tau)$ does not contribute to $j_+(\tau)$ since $\mathrm{Re}[C_1(\tau)] \sim 1$.

all these features. The decreasing exponential behavior is clearly visible as well as the increase of the QD level lifetime $(2\gamma)^{-1}$ as interactions strength increases. Function $C_1(\tau)$, plotted in the inset, is characterized by a global decrease, while increasing interaction strength. It also presents oscillations with a period given by $2\pi\varepsilon_0^{-1}$ and an amplitude damped by interactions. This fact is due to the smearing of the Fermi function, which weakens the effects of the Fermi sea.

Similar qualitative features are expected in the case of non-local injection, where however the pulse will be less localized. Although challenging, experimental detection of such fractional charge packets could be performed. High-resolution time-resolved measurements are indeed possible in quantum Hall bars, using a quantum point contact as a shutter on the ps scale [148, 149] that allows the study of charge packet profiles [5]. Different measurement schemes, based on Hong-Ou-Mandel interferometry [131, 105], have also been used to detect charge profiles.

3.1.5 Energy density profile

Along the lines of what we have done about the charge, here we discuss the energy density profile of the two fractional excitations. Again, we focus on the local-injection limit. By integrating Eq. (3.42) over space with $\xi(y) = \delta(y)$ one obtains

$$\begin{aligned}\delta\mathcal{H}_\eta(z_\eta) = \frac{A_\eta^2|\lambda|^2}{\pi a^2}\,\mathrm{Re}\int_0^t dt_1\int_0^{t_1} dt_2\;\beta^*(t_2)\beta(t_1)&\\ \times\left[\frac{a}{2ui}\left(\frac{a}{a+iu(t_2-t_1)}\right)^{2A_-^2+1}\partial_{t_1}\delta(t_1-t+\frac{\eta x}{u})\right.&\\ \left.+\left(\frac{a}{a+iu(t_2-t_1)}\right)^{2A_-^2+2}\delta(t_1-t+\frac{\eta x}{u})\right].&\end{aligned} \tag{3.52}$$

Similarly to charge, the two chiral energy density packets share the same mirrored shape as long as local-injection is concerned

$$\frac{\delta\mathcal{H}_+(x,t)}{A_+^2} = \frac{\delta\mathcal{H}_-(-x,t)}{A_-^2}. \tag{3.53}$$

We then focus on the right moving energy packet ($\eta = +$), by analyzing the instantaneous energy power $P_+(\tau) = u\,\delta\mathcal{H}_+(\tau)$ that flows through the "detection" point x_D. Integration of (3.52) over t_1 leads to ($\tau = t - x_D/u$)

$$P_+(\tau) = A_+^2\,\gamma_0\,\varepsilon_0\,\theta(\tau)\exp\left[-2\tau\gamma\right]\mathrm{Re}\left[C_{\mathcal{H}}(\tau)\right]\,, \tag{3.54}$$

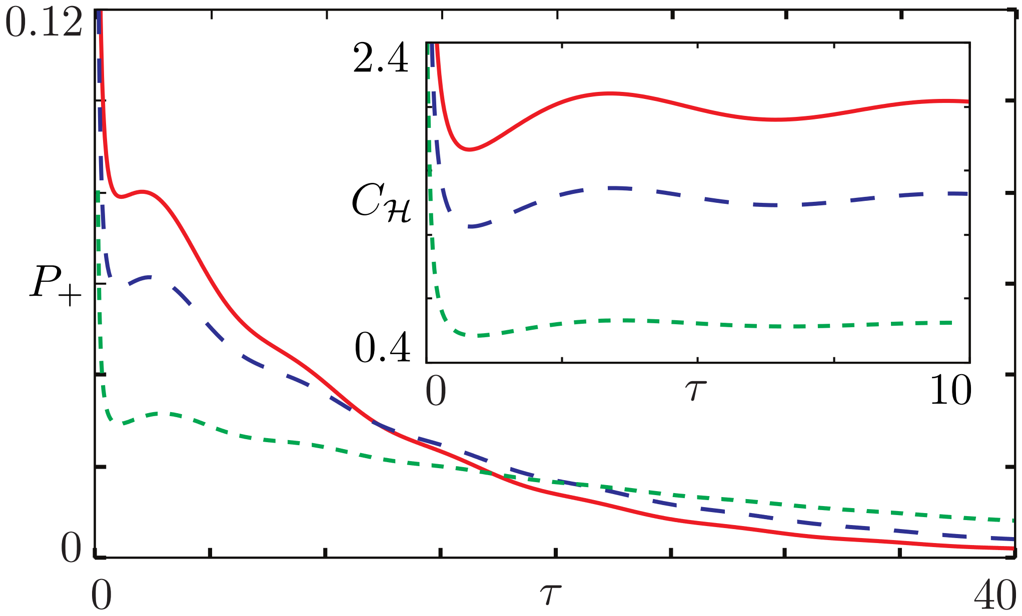

Fig. 3.8 Instant energy power $P_+(\tau)$ (in units of ε_0^2) flowing through the detection point $x_D > 0$ as a function of time τ (in units of ε_0^{-1}). Different interaction strengths are considered: solid red line ($K = 1$), dashed blue $K = 0.8$, and green dotted $K = 0.6$. Inset: function $C_{\mathcal{H}}(\tau)$ with the same color code for interactions. Parameters: $\gamma_0 = 0.05\ \varepsilon_0$ and $a = 1/40 v_F \varepsilon_0^{-1}$.

with

$$C_{\mathcal{H}}(\tau) = \frac{\varepsilon_0 - i\gamma}{\varepsilon_0} C_1(\tau) + \frac{1}{K}\left(1 - 2A_-^2\right) C_2(\tau) \tag{3.55}$$

and $C_m(\tau)$ ($m = 1, 2$) given in Eq. (3.51). In Fig. 3.8 the instantaneous energy power $P_+(\tau)$ is plotted as a function of time for different interaction strength. As for charge current, it reflects causality, ensured by $\theta(\tau)$, and the exponential decay related to the QD level inverse lifetime 2γ, with analogous behaviors. The function $C_{\mathcal{H}}(\tau)$ (plotted in the inset) features also a spike at $\tau = 0$, even in the non-interacting case, reflecting the sudden turning on of the injection process and the consequent excitation, at short times, of energy modes even higher than ε_0.

3.1.6 Single-electron coherence for local-injection

In the two previous subsections, we have demonstrated that in the local-injection limit the charge density profiles of the two counterpropagating excitations are mirror-shaped, differing only for a prefactor controlled by charge fractionalization [see Eq. (3.49)]. The same holds for the energy density profiles, as stated in Eq. (3.53).

However, in view of the highly asymmetric injection process (we are injecting one electron at energy ε_0 on the R-channel only), one may expect more striking differences between the two counterpropagating excitations. Such differences are indeed present and they clearly emerge when more involved quantities are analyzed, namely the momentum and energy distribution. As we will see in the following, these important properties can be derived from the so-called single-electron coherence.

The coherence properties at single-particle level are described by the single-electron coherence correlator [4, 141, 150]

$$\mathfrak{G}_r(s,t;\xi,z) = \left\langle \psi_r^\dagger\left(s-\frac{\xi}{2},t-\frac{z}{2}\right)\psi_r\left(s+\frac{\xi}{2},t+\frac{z}{2}\right)\right\rangle , \tag{3.56}$$

in analogy with Glauber's optical coherence [151–153]. Despite a close parallelism between electronic many-body systems and quantum optics, there are also important differences, one of them being that, even at equilibrium, the single-electron coherence does not vanish because of the presence of the Fermi sea. For this reason it is a standard procedure [4, 141, 150] to focus on its deviations from the equilibrium value $\mathfrak{G}_r^0$, and thus to consider $\delta\mathfrak{G}_r = \mathfrak{G}_r - \mathfrak{G}_r^0$. Our goal is to study the evolution of $\delta\mathfrak{G}_r$ after the electron injection, i.e. implement Eq. (3.12). A first result is that the single-electron coherence features the structure

$$\delta\mathfrak{G}_r(s,t;\xi,z) = g_r(s,t;\xi,z) + g_r^*(s,t;-\xi,-z) . \tag{3.57}$$

The detailed evaluation of functions g_r is shown in Appendix B.4.1, while here we focus on their dependence on space and time variables. First of all, it is clear that the s and t dependence must be retained since the system is not invariant under either space or time translations because of the injection process. Moreover, in presence of interactions the electron injected in the R-branch fractionalizes into two counterpropagating chiral excitations. In the long-time limit $t \gg \gamma^{-1}$, i.e. when the injection is over, they are spatially separated and they contribute independently to the single-electron coherence correlator. In Appendix B.4.1, we demonstrate that this is indeed the case: the functions g_r can be written as the sum of two chiral terms $g_{r,+}$ and $g_{r,-}$, the former propagating to the right and the latter to the left

$$g_r(s,t;\xi,z) = \sum_{\eta=\pm} g_{r,\eta}(s-\eta ut;\xi,z) . \tag{3.58}$$

This important relation allows us to separately study the dynamical properties of the two chiral fractional excitations. We find the following expression for functions $g_{r,\eta}$

$$\begin{aligned} g_{r,\eta}(x_\eta;\xi,z) = {} & \frac{|\lambda|^2}{(2\pi a)^2}\, \mathcal{C}_{r,\eta}(\xi,z)\, e^{i\vartheta_r k_{\mathrm{F}}\xi} \\ & \times \iint_0^{+\infty} \mathrm{d}t_1\, \mathrm{d}\tau\, e^{-2\gamma t_1} \mathcal{F}(\tau)\, \Upsilon_{r,\eta}(x_\eta,\zeta_\eta,t_1,\tau) , \end{aligned} \tag{3.59}$$

where $x_\eta = s - \eta ut$, $\zeta_\eta = \xi - \eta uz$ and

$$\mathcal{C}_{r,\eta}(\xi,z) = \left[\frac{a}{a - iuz + i\vartheta_r\xi}\right]^{A_+^2}\left[\frac{a}{a - iuz - i\vartheta_r\xi}\right]^{A_-^2}\frac{\zeta_\eta - ia\vartheta_r}{\zeta_\eta}\,, \tag{3.60a}$$

$$\mathcal{F}(\tau) = e^{-\gamma\tau - i\varepsilon_0\tau}\left[\frac{a}{a - iu\tau}\right]^{1+2A_-^2}\,, \tag{3.60b}$$

$$\begin{aligned}\Upsilon_{r,\eta}(x_\eta,\zeta_\eta,t_1,\tau) = &\left[\frac{a + i\eta(x_\eta + \zeta_\eta/2 + \eta ut_1)}{a + i\eta(x_\eta - \zeta_\eta/2 + \eta ut_1)}\right]^{\alpha_{r,\eta}} \\ &\times 2i\,\mathrm{Im}\left\{\left[\frac{a - i\eta(x_\eta - \zeta_\eta/2 + \eta u(t_1 + \tau))}{a - i\eta(x_\eta + \zeta_\eta/2 + \eta u(t_1 + \tau))}\right]^{\alpha_{r,\eta}}\right\}.\end{aligned} \tag{3.60c}$$

The exponents $\alpha_{r,\eta}$ are related to the A_η coefficients in by

$$\alpha_{R,\eta} = A_\eta^2\,, \quad \alpha_{L,\eta} = A_+A_-\,. \tag{3.61}$$

The factor $(\zeta_\eta - ia\vartheta_r)\zeta_\eta^{-1}$ in Eq. (3.60a) stems from the point-splitting procedure[7] [93] and ensures that the diagonal part of the single-electron coherence truly represents the electron particle density $\delta\rho_r(s,t) = \delta\mathfrak{G}_r(s,t,;0,0)$ (see Appendix B.4.2 for details). Eq. (3.59) will be the building blocks from which the energy and momentum distributions can be obtained.

3.1.7 Momentum distribution

The momentum distribution of the R and L branches is defined as the average variation [as in Eq. (3.12)] of the occupation number operator

$$n_r(k,t) = c_{r,k}^\dagger(t)c_{r,k}(t)\,, \tag{3.62}$$

where $c_{r,k}$ annihilates an electron with momentum k on the r-branch ($r = R,L$). Using the single-electron coherence, one can represent the occupation number variation as

$$\delta n_r(k,t) = \frac{1}{2\pi}\iint_{-\infty}^{+\infty} \mathrm{d}\xi\ \mathrm{d}s\, e^{-ik\xi}\delta\mathfrak{G}_r(s,t;\xi,0)\,. \tag{3.63}$$

In general, the momentum distribution $\delta n_r(k,t)$ has a temporal evolution [125, 124]. Focusing on the long-time limit $t \gg \gamma^{-1}$, however, the decoupling relation in Eq. (3.58) allows us to

---

[7] The insertion of the point-splitting factor only affects functions $g_{r,\eta}$ around the point $z = \xi = 0$. This does not change significantly the momentum and energy distribution in the region of interest.

express the momentum distribution as a sum of time-independent contributions

$$\delta n_r(k) = \sum_{\eta=\pm} \delta n_{r,\eta}(k)\,, \tag{3.64}$$

where each of the four terms

$$\delta n_{r,\eta}(k) = \frac{1}{\pi}\mathrm{Re}\left\{\iint_{-\infty}^{+\infty} \mathrm{d}\xi\ \mathrm{d}s\, e^{-ik\xi} g_{r,\eta}(s;\xi,0)\right\} \tag{3.65}$$

represents the momentum distribution of the r-branch electrons associated to the right ($\eta = +$) or the left ($\eta = -$) moving chiral excitation. Using Eq. (3.59) and conveniently shifting the variable s, each term can be written as

$$\begin{aligned}\delta n_{r,\eta}(k) = \frac{|\lambda|^2}{2\pi\gamma}\frac{1}{(2\pi a)^2}\mathrm{Re}&\left\{\int_0^{+\infty} \mathrm{d}\tau \mathcal{F}(\tau)\right.\\ &\times\left.\int_{-\infty}^{+\infty} \mathrm{d}\xi\, e^{-i(k-\vartheta_r k_{\mathrm{F}})\xi}\, \mathcal{C}_{r,\eta}(\xi,0)\int_{-\infty}^{+\infty} \mathrm{d}s\, \chi_{r,\eta}(s,\xi,\tau)\right\},\end{aligned} \tag{3.66}$$

with

$$\chi_{r,\eta}(s,\xi,\tau) = 2i\left[\frac{a+i\eta(s+\xi-\eta u\tau)}{a+i\eta(s-\eta u\tau)}\right]^{\alpha_{r,\eta}} \mathrm{Im}\left\{\left[\frac{a-i\eta s}{a-i\eta(s+\xi)}\right]^{\alpha_{r,\eta}}\right\}. \tag{3.67}$$

The time independence of the momentum distribution in the long time limit $t \gg \gamma^{-1}$ stems from the fact that our model does not take into account for spectrum non-linearities or equilibration mechanism that would induce a time evolution even on time scales greater than γ^{-1} [126, 154].

In order to clarify the meaning of the $\delta n_{r,\eta}(k)$ terms, is it useful to focus at first on the integrated quantities

$$\delta N_{r,\eta} = \int_{-\infty}^{+\infty} \delta n_{r,\eta}(k)\, dk\,, \tag{3.68}$$

which represent the excess number of electrons carried by each of the two chiral excitations in the r branch. A straightforward calculation leads to

$$\delta N_{R,+} = 1 + A_-^2 = 1 + \tfrac{1}{4}\left(K^{-1} + K - 2\right) \tag{3.69}$$

$$\delta N_{R,-} = -A_-^2 = -\tfrac{1}{4}\left(K^{-1} + K - 2\right) \tag{3.70}$$

$$\delta N_{L,\pm} = \mp A_+ A_- = \mp\tfrac{1}{4}\left(K^{-1} - K\right)\,. \tag{3.71}$$

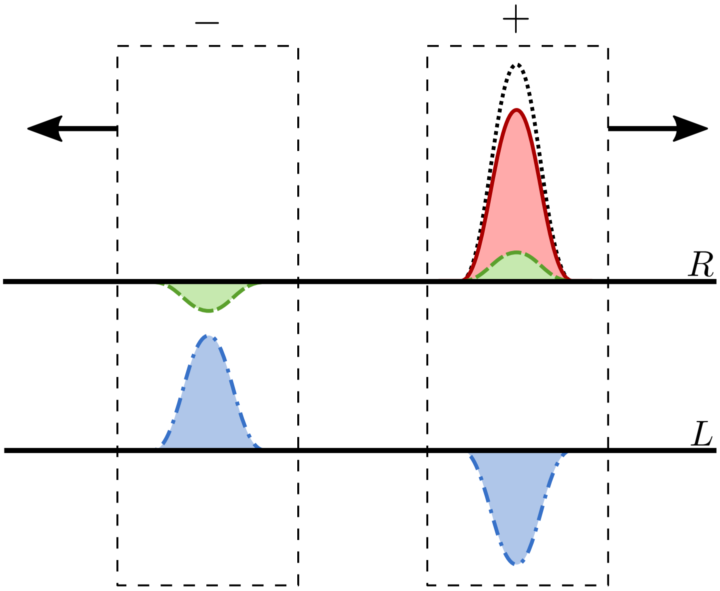

Fig. 3.9 Sketch of the fractionalization mechanism. The real-space structure of the counterpropagating fractional excitations (highlighted by the “$+$” and “$-$” rectangles) is shown, distinguishing between the contributions from the two branches, R and L.

The total charge (units of e) of each chiral excitation is thus

$$q_\eta = \sum_{r=R,L} \delta N_{r,\eta} = \frac{1+\eta K}{2}\,, \tag{3.72}$$

reproducing Eq. (3.37), i.e. the well-known charge fractionalization ratio. As a direct consequence of conservation of the electron number on each branch, which follows from the absence of backscattering, the following sum rules are also satisfied

$$\sum_{\eta=\pm} \delta N_{R,\eta} = 1\,, \quad \sum_{\eta=\pm} \delta N_{L,\eta} = 0\,. \tag{3.73}$$

In Fig. 3.9 we sketch the structure of the chiral excitations in position space. The left-moving excitation is made up of a negative packet R_- (in green) and a positive one L_- (in blue). By contrast, the right-moving excitation is made up of a negative packet L_+ (in blue) and a positive one R_+ (dotted line). According to Eq. (3.69), the latter can be regarded as the sum of a unit packet (in red), representing the injected electron, and a positive packet (in green) with opposite charge compared to R_-.

This scenario corresponds to the well-known fractionalization phenomenon, where the injected single-electron charge is split into counterpropagating fractional charges. However, being based on the integrated quantities (3.68), this picture is not able to describe the detailed structure of the many-body excitations created in the 1D conductor, and these types of information are crucial to give a proper characterization of the relaxation and decoherence mechanism due to the interplay of single-electron injection and electron interaction. Therefore, we go beyond this coarse description in the following by characterizing the many-body nature of the fractionalization phenomenon using the momentum-resolved contributions (3.66).

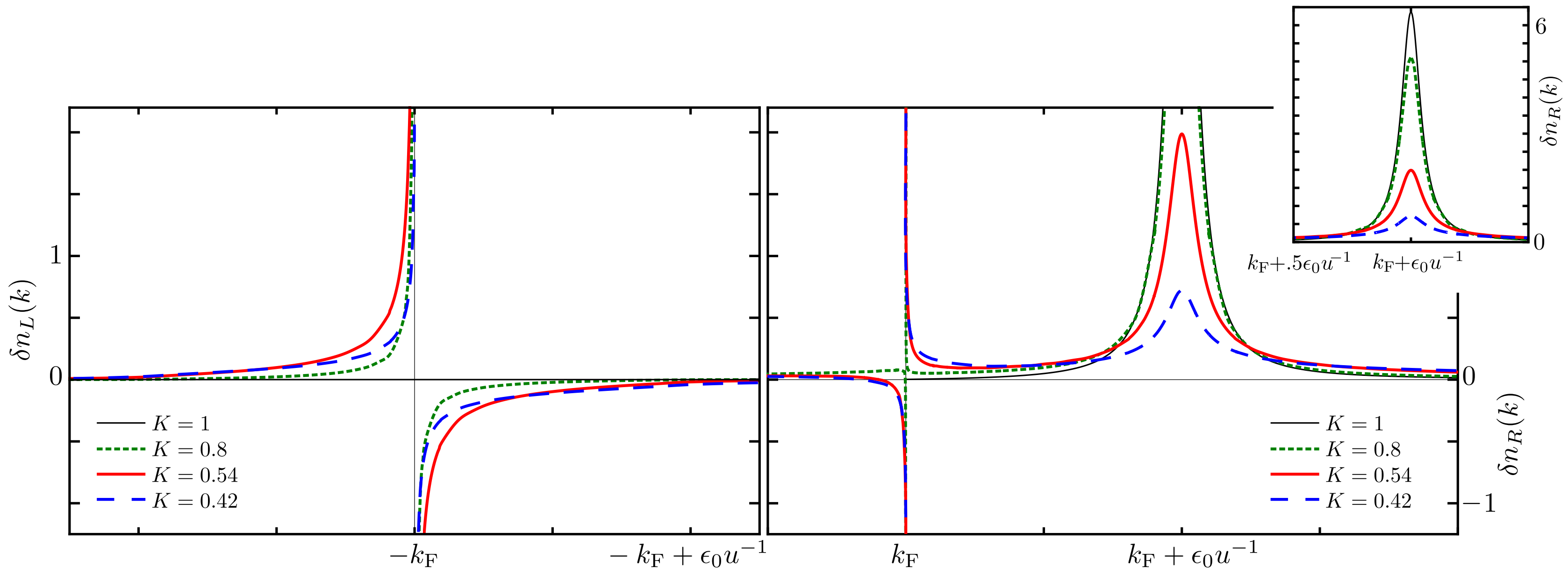

Fig. 3.10 Momentum distribution (in units of $u\varepsilon_0^{-1}$) of the L branch (left panel) and R branch (right panel) for different interaction strengths: $K = 0.8$ (green short-dashed line), 0.54 (red continuous line), 0.42 (blue long-dashed line) and 1 (thin black line). The inset focuses on the broadening of the peak centered in $k_F + \varepsilon_0 u^{-1}$ as the interaction strength increases. Parameters: $\varepsilon_0 a u^{-1} = 1/40$ and $\gamma = 0.05\varepsilon_0$.

At first, let us consider the noninteracting case $K = 1$. Here $A_+ = 1$, $A_- = 0$ and Eq. (3.66) readily reduces to:

$$\begin{aligned} \delta n_{R,+}(k) &= \theta(k - k_\mathrm{F}) \frac{v_\mathrm{F}\gamma/\pi}{\gamma^2 + [\varepsilon_0 - v_\mathrm{F}(k - k_\mathrm{F})]^2} \\ \delta n_{R_-} &= \delta n_{L,\pm} = 0. \end{aligned} \tag{3.74}$$

For $K = 1$ the right and left branches are two independent and chiral systems, so the electron injected on the R branch will just propagate to the right without affecting the L branch. The momentum distribution in Eq. (3.74) is a truncated Lorentzian [150, 155] of width γ, centered in $k = k_\mathrm{F} + \varepsilon_0 v_\mathrm{F}^{-1}$. In the limit $\gamma/\varepsilon_0 \to 0$ it becomes a delta function. It is worth noting that the Fermi sea remains a spectator as $\delta n_{R,+}(k) \neq 0$ only for $k > k_\mathrm{F}$. As we will see, this will no longer be true in presence of interactions.

In an interacting system the complete momentum distribution functions is obtained by numerically computing the integrals in Eq. (3.66). In Fig. 3.10 we plot $\delta n_L(k)$ (left panel) and $\delta n_R(k)$ (right panel) for different values of the interaction parameter K. Increasing the interaction strength, the peak around $k_\mathrm{F} + \varepsilon_0 u^{-1}$ (right panel) lowers and broadens while particle-hole contributions emerge around the Fermi points. In this respect, it is useful to consider the limit $k \to \pm k_\mathrm{F}$ where the momentum distributions $\delta n_{R/L}(k)$ exhibit a power-law behavior

$$\delta n_r(k) \simeq \frac{u}{\pi^2 \varepsilon_0} \left(\frac{\varepsilon_0 a}{u}\right)^{2A_-^2} \Gamma(1 - 2A_-^2)\, \mathcal{C}_r \,\mathrm{sgn}(k - \vartheta_r k_\mathrm{F}) \left| u \frac{k - \vartheta_r k_\mathrm{F}}{\varepsilon_0} \right|^{2A_-^2 - 1}, \tag{3.75}$$

with interaction-dependent coefficients

$$\mathcal{C}_R = \sin(2\pi A_-^2)\sin(\pi A_-^2) \tag{3.76a}$$

$$\mathcal{C}_L = -\sin^2(\pi A_+ A_-)\cos(\pi A_-^2)\,. \tag{3.76b}$$

Eq. (3.75) is demonstrated in Appendix B.5.1 and holds as long as $A_-^2 < 1/2$, i.e., when the interaction in not too strong ($K > 0.27$). In this case, the momentum distribution features a power-law divergence at the Fermi points $\pm k_\mathrm{F}$. This divergence is integrable, consistently with the fact that $\delta n_r(k)$ defines a probability density, and gets weaker as the interaction strength increases. Such a behavior can be understood as a manifestation of the well-known Anderson's orthogonality catastrophe [156, 157] We note that, as discussed in Appendix B.5.1, the exponent of the power-law behavior in Eq. (3.75) is robust with respect to the approximation made in Eq. (3.13).

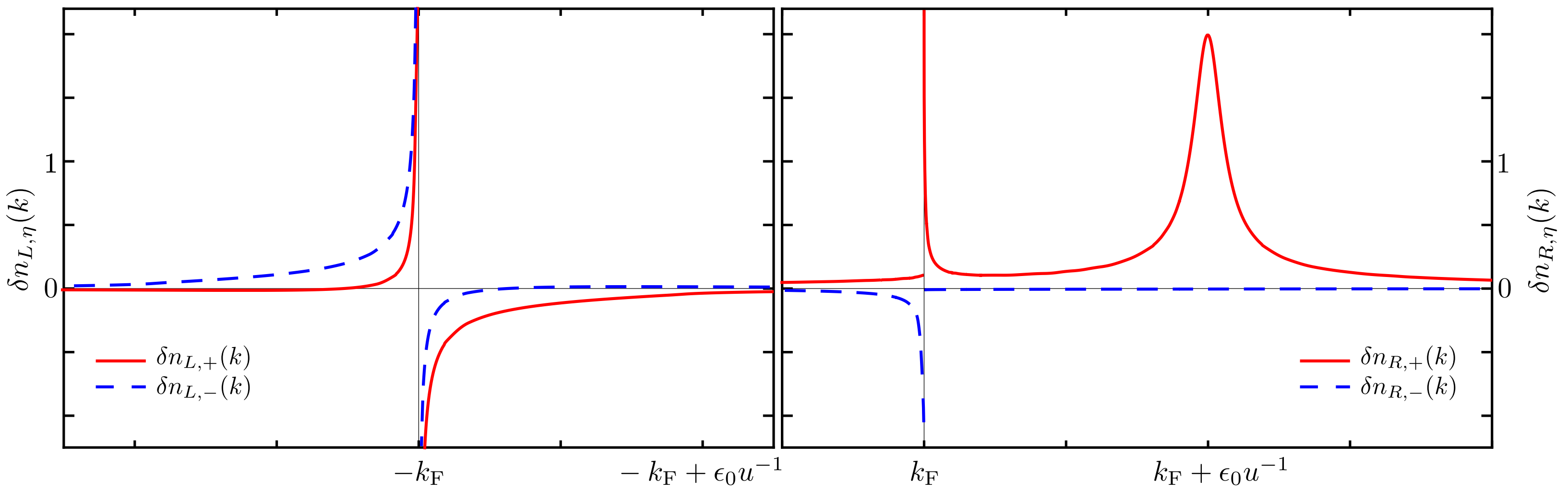

Fig. 3.11 Chiral components of the momentum distribution (in units of $u\varepsilon_0^{-1}$). The red continuous line refers to the momentum distribution of the chiral right moving excitation, i.e. $\delta n_{L,+}$ (left panel) and $\delta n_{R,+}$ (right panel). The dashed blue line refers to the momentum distribution of the chiral left moving excitation, i.e. $\delta n_{L,-}$ (left panel) and $\delta n_{R,-}$ (right panel). Parameters: $K = 0.54$, $\varepsilon_0 a u^{-1} = 1/40$ and $\gamma = 0.05\varepsilon_0$.

Quite interestingly, particle-hole pairs are much more relevant on the L branch than on the R one, as can be seen in Fig. 3.10. This means that excitations around the Fermi points are more important on the channel which is not tunnel-coupled to the single-electron emitter. This feature, which from a mathematical point of view emerges from Eqs. (3.76) where C_L is greater than C_R, can be interpreted by relying on the following picture of the interaction mechanism [83, 158]. We note that the intra-branch coupling g_4 alone simply renormalizes the Fermi velocity and does not modify the Luttinger parameter $K = 1$ (see Eq. (2.24) with $g_2 = 0$). Therefore, it is the inter-branch coupling g_2 which plays a fundamental role in the fractionalization mechanism. Since the injection is performed on the right branch, a first interaction process couples the injected electrons with momentum near $\varepsilon_0 u^{-1}$ to the left branch, thus creating particle-hole excitations around $-k_{\mathrm{F}}$. Then, a second process couples the excitations just created on the left branch to the right branch, exciting particle-hole pairs around $+k_{\mathrm{F}}$. The latter is thus a higher-order process compared to the creation of particle-hole pairs on the L branch. For weak interactions, this heuristic picture perfectly fits with the expression of the $\mathcal{C}_r$ coefficients. Indeed on can show that

$$\mathcal{C}_R = \tfrac{1}{8}\pi^2 (g_4 + 2\pi v_{\mathrm{F}})^{-4}\,(g_2)^4 + \mathrm{O}(g_2)^6 \tag{3.77}$$

$$\mathcal{C}_L = -\tfrac{1}{4}\pi^2 (g_4 + 2\pi v_{\mathrm{F}})^{-2}\,(g_2)^2 + \mathrm{O}(g_2)^4. \tag{3.78}$$

Having discussed the features of δn_R and δn_L for different interaction strengths, we can now analyze the chiral components of the momentum distribution. In Fig. 3.11, the four terms $\delta n_{r,\eta}$ are plotted for $K = 0.54$. Functions $\delta n_{L,\pm}$ are shown in the left panel, while $\delta n_{R,\pm}$ are plotted in the right one. Solid red lines refer to the chiral right-moving components ($\eta = +$) and the blue dashed ones to the chiral left-moving terms ($\eta = -$). Interestingly, it is possible to understand the features of these plots using the sketch in Fig. 3.9. The peak on $R+$ centered around $k_{\mathrm{F}} + \varepsilon_0 u^{-1}$ is indeed the remnant of the injected electron: it is related to the red packet in Fig. 3.9. As discussed above, the inter-branch interaction creates particle-hole pairs on the L-branch. However, because of the excess right-moving charge present on $R+$, the majority of the holes is "dragged" to the right (see the negative blue packet in Fig. 3.9). This explains the asymmetry between $\delta n_{L+}(k)$, rich in holes and larger for $k > -k_{\mathrm{F}}$, and $\delta n_{L-}(k)$, rich in particles and larger for $k < -k_{\mathrm{F}}$. Electron-hole pairs are also created on the R branch, but through a higher-order process and thus their impact on the R branch is reduced. Again, the excess left-moving charge on branch $L-$, represented by the positive blue packet in Fig. 3.9, drags the holes on the R branch to the left (green negative packet) and pushes particles to the right (green positive packet). As a consequence, $\delta n_{R,-}(k)$ basically contains only holes while $\delta n_{R,+}(k)$ features a particle component near the Fermi point, superimposed on the peak tails.

As a last comment, we note that the momentum distribution of the right-moving excitation (solid red lines) is very different from the left-moving one (dashed blue lines): the former features the peak around $k_{\mathrm{F}}+\varepsilon_0 u^{-1}$ while the latter has significant weight only around $-k_{\mathrm{F}}$. As shown in Eq. (3.49), this strong asymmetry is completely lost within a real-space description of the chiral excitations.

We would like to stress that it is possible in principle to experimentally access every contribution $\delta n_{r,\eta}(k)$. A detector placed to the right (left) of the injection point can in fact exclusively measure the properties of the chiral right (left) moving excitation $\eta=+$ ($\eta=-$). Moreover, we observed that the interesting features of the momentum distributions are centered around the Fermi points and around $k_{\mathrm{F}}+\varepsilon_0 u^{-1}$. Provided that $k_{\mathrm{F}} \gg \varepsilon_0 u^{-1}$, it is thus possible to easily distinguish between the contributions from the R and the L branches.

3.1.8 Energy distribution

In an interacting system, energy and momentum are not related through a simple dispersion relation and are independent quantities [83, 159]. Therefore, the energy distribution of the excitations provides complementary information to the already discussed momentum distribution. Here, we will focus on the following component of the local nonequilibrium spectral function integrated over time

$$\delta\mathcal{A}_r(\omega,x_p)=\frac{u}{2\pi}\iint_{-\infty}^{+\infty} dt\,dz\;\delta\mathfrak{G}_r(x_p,t;0,z)\,e^{i\omega z}\,. \tag{3.79}$$

Such a quantity has the great advantage to be directly related to a physical observable, namely the total charge transferred from the system to a tunnel coupled single empty level. It can be thus experimentally accessed via quantum dot spectroscopy [160, 158, 161]. Before explicitly computing $\delta\mathcal{A}_r$, it is worth discussing more in detail the aforementioned relation, in order to further clarify the meaning of Eq. (3.79) and to allow for a clearer interpretation of the results.

Let $H_p=\omega\, b^\dagger b$ be the Hamiltonian of a probe quantum dot, modeled as a single level with energy $\omega>0$. At position x_p, it is tunnel coupled to the r-branch of the system via

$$H_T^p=\left[\lambda_p\psi_r^\dagger(x_p)b+\mathrm{H.c.}\right]\,. \tag{3.80}$$

The current transferred from the system to the probe dot reads

$$I_r=ie\left[H_T^p,b^\dagger b\right]=ie\left[\lambda_p\psi_r^\dagger(x_p)b-\mathrm{H.c.}\right] \tag{3.81}$$

and, to the lowest order in the tunneling amplitude λ_p, its average value is given by

$$I_r(t) = i\int_{-\infty}^{t} \left\langle \left[H_{\mathrm{T}}^{p}(\tau), I_r(t)\right] \right\rangle d\tau. \tag{3.82}$$

We now assume that the single level is held empty, i.e. $\langle b^{\dagger} b\rangle = 0$, considering for example an additional stronger coupling with a drain at lower chemical potential [158]. Then, the total charge transferred from the system to the dot

$$q_r(\omega, x_p) = \int_{-\infty}^{+\infty} I_r(t)\, dt \tag{3.83}$$

can then be expressed as

$$q_r(\omega, x_p) = e|\lambda_p|^2 \iint_{-\infty}^{\infty} dt\, dz\, \mathfrak{G}_r(x_p, t; 0, z)\, e^{i\omega z}. \tag{3.84}$$

The variation of this quantity, induced by the electron injection, is thus directly related to the energy distribution defined in Eq. (3.79) via

$$\delta q_r(\omega, x_p) = 2\pi \frac{e|\lambda_p|^2}{u} \delta\mathcal{A}_r(\omega, x_p). \tag{3.85}$$

Since the energy is conserved in the tunneling process, it is clear that the function $\delta\mathcal{A}_r(\omega, x_p)$ represents the probability density of destroying an excitation with energy $\omega > 0$ by extracting an electron from the r branch at position x_p. Note that if the system is in its ground state (without the injected electron), no excitations can be destroyed and no charge can be transferred to the probe dot. As a consequence, the variation δq_r correspond to the total transferred charge q_r.

If the probe dot is positioned far away from the injection point, i.e. $|x_p| \gg u\gamma^{-1}$, the chiral excitations created by the electron injection will reach it only at large time $t \gg \gamma^{-1}$. In this limit, Eq. (3.58) holds and allows to distinguish between the contributions of each chiral excitation

$$\delta\mathcal{A}_r(\omega, x_p) \simeq \begin{cases} \delta\mathcal{A}_{r,+}(\omega) & x_p \gg u\gamma^{-1} \\ \delta\mathcal{A}_{r,-}(\omega) & x_p \ll -u\gamma^{-1} \end{cases}. \tag{3.86}$$

Here, the chiral energy distribution of the r branch does not depend on x_p and reads

$$\begin{aligned}\delta\mathcal{A}_{r,\eta}(\omega) &= \frac{u}{\pi}\,\mathrm{Re}\left\{\iint_{-\infty}^{+\infty} dt dz\, e^{i\omega z}\, g_{r,\eta}(ut;0,z)\right\}\\ &= \frac{|\lambda|^2}{2\pi\gamma}\frac{1}{(2\pi a)^2}\mathrm{Re}\left\{\int_0^{+\infty}\mathrm{d}\tau\mathcal{F}(\tau)\int_{-\infty}^{+\infty}\mathrm{d}z\, e^{i\omega z}\mathcal{C}_{r,\eta}(0,z)\int_{-\infty}^{+\infty}\mathrm{d}s\,\chi_{r,\eta}(s,-\eta uz,\tau)\right\}.\end{aligned} \tag{3.87}$$

It is also possible to define a total chiral energy distribution, summing with respect to branch index r

$$\delta\mathcal{A}_{\eta}(\omega) = \sum_{r=R,L}\delta\mathcal{A}_{r,\eta}(\omega)\,. \tag{3.88}$$

Fig. 3.12 shows the behavior of $\delta\mathcal{A}_{\pm}(\omega)$ obtained by using Eq. (3.88) and numerically evaluating Eq. (3.87). In analogy to the momentum distribution, the chiral right-moving component features a peak centered at $\omega = \varepsilon_0$ (the average energy of the injected electron) which lowers and broadens as the interaction increases. However, in this case, the broadening is highly asymmetric and tails increase only for energies $\omega < \varepsilon_0$. This behavior is a consequence of energy conservation: on average, the total energy transferred to the LL by the electron injection is ε_0 and it is therefore impossible to create more energetic excitations. Tails for $\omega > \varepsilon_0$ are indeed just a consequence of the finite level broadening γ. As the peak lowers, low-energy excitations appear near the Fermi energy both on $\delta\mathcal{A}_+$ (top panel) and $\delta\mathcal{A}_-$ (bottom panel), exhibiting a power law divergence at $\omega = 0$. Indeed, in the limit $\omega \to 0^+$ the total chiral energy distributions read

$$\delta\mathcal{A}_{\eta}(\omega) = \frac{1}{\pi^2\varepsilon_0}\left(\frac{\varepsilon_0 a}{u}\right)^{2A_-^2}\Gamma(1-2A_-^2)D\left(\frac{\omega}{\varepsilon_0}\right)^{2A_-^2-1}, \tag{3.89}$$

with

$$D = \sin^2(\pi A_+ A_-) + \sin^2(\pi A_-^2)\,. \tag{3.90}$$

Equation (3.89) is demonstrated in Appendix B.5.2 and holds as long as $A_-^2 < 1/2$ ($K > 0.27$). We observe that the divergence is integrable and features exactly the same exponents we already found in Eq. (3.75) for the momentum distribution. Once again, this exponent is robust with respect to the approximation in Eq. (3.13).

In Fig. 3.13 the contributions $\delta\mathcal{A}_{r,\eta}(\omega)$, associated with the $r = R$ and the $r = L$ branch for a given chirality η, are analyzed for a fixed interaction strength ($K = 0.54$). The peak centered around ε_0 is present only in $\delta\mathcal{A}_{R,+}$ (solid red line). Conversely, the majority of the low-energy excitations near the Fermi energy are hosted by the L branch. In this respect, note that $\delta\mathcal{A}_{L,+}$ and $\delta\mathcal{A}_{L,-}$ coincide in the energy range we considered and they are both represented with the long-dashed blue line. Note that also $\delta\mathcal{A}_{L,\eta}(\omega)$ are strongly suppressed above ε_0 as a

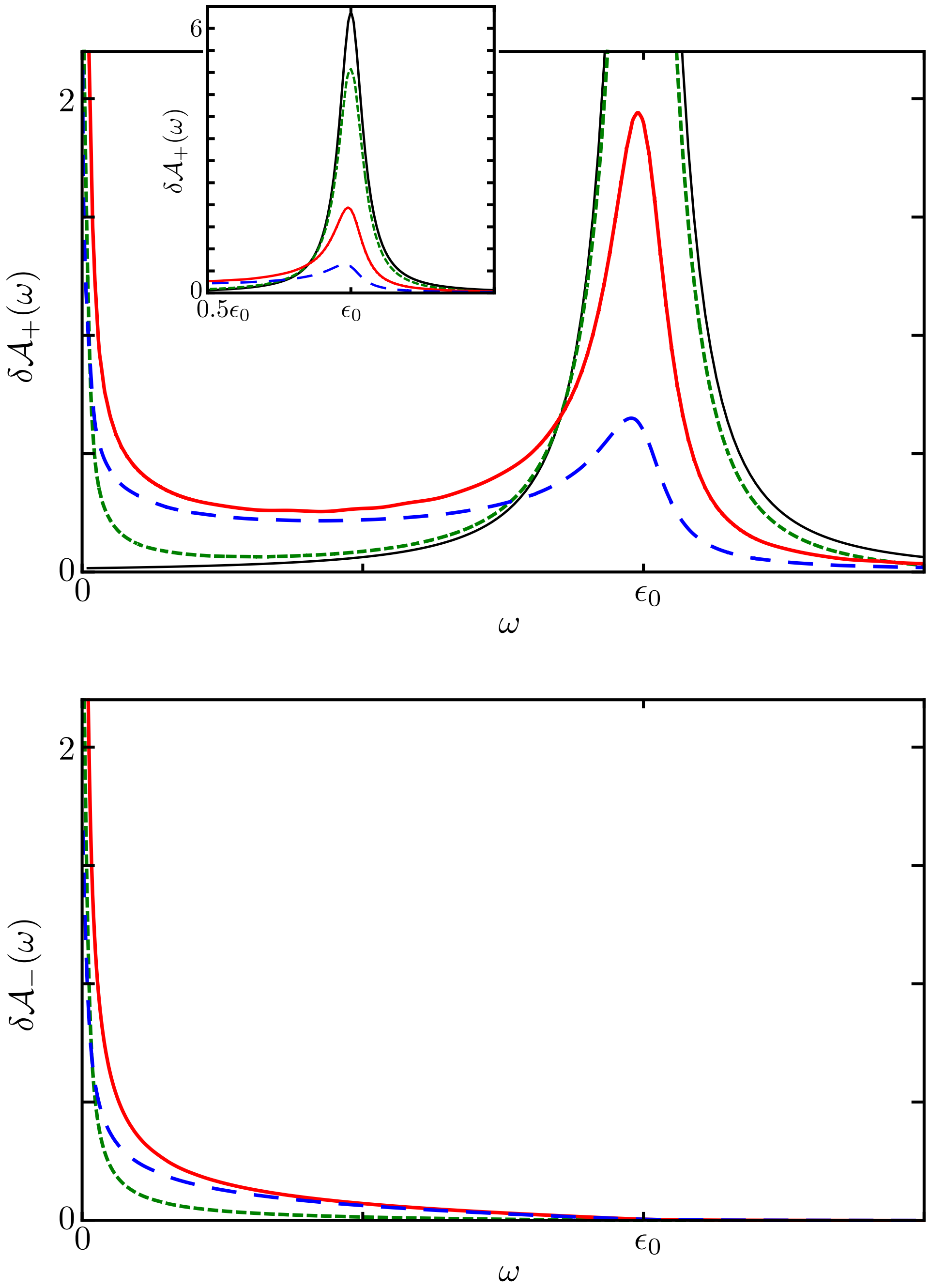

Fig. 3.12 Total chiral energy distribution $\delta\mathcal{A}_{\pm}(\omega)$ (in units of ε_0^{-1}) associated, respectively, with the chiral right-moving excitation $\delta\mathcal{A}_{+}$ (top panel) and the left-moving one $\delta\mathcal{A}_{-}$ (bottom panel). Different values of the interaction parameter K are considered: $K = 0.8$ (green short-dashed line), 0.54 (red continuous line), 0.42 (blue long-dashed line) and 1 (thin black line). The inset in the top panel is a zoom of the peak centered around $\omega = \varepsilon_0$. Parameters: $\varepsilon_0 a u^{-1} = 1/40$ and $\gamma = 0.05\varepsilon_0$.

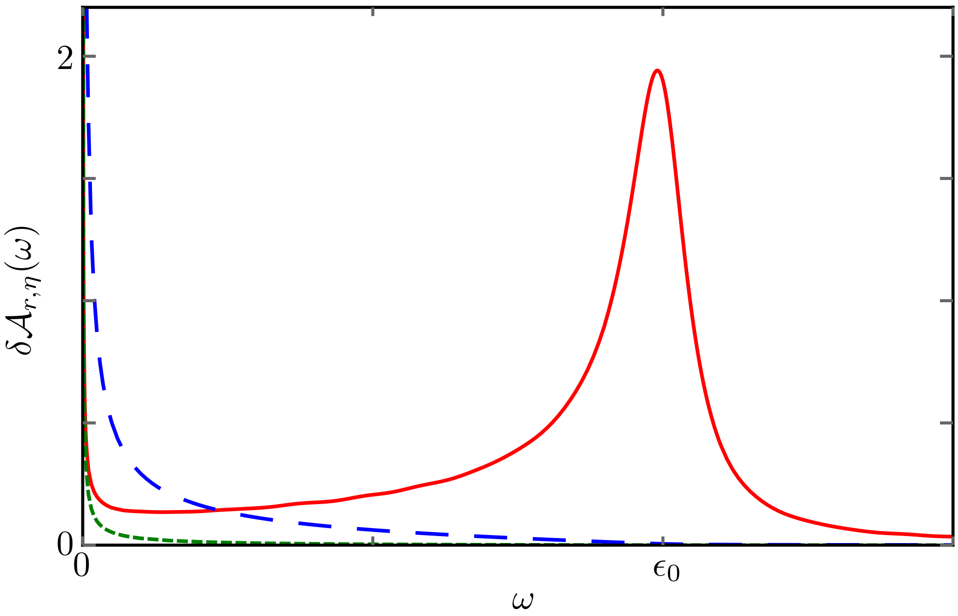

Fig. 3.13 Chiral energy distributions $\delta\mathcal{A}_{r,\eta}(\omega)$ in units of ε_0^{-1}. The solid red line refers to the $\delta\mathcal{A}_{R,+}$ contribution; the short-dashed green one refers to $\delta\mathcal{A}_{R,-}$. The long-dashed blue line refers to $\delta\mathcal{A}_{L,\pm}$. Parameters: $K = 0.54$, $\varepsilon_0 a u^{-1} = 1/40$ and $\gamma = 0.05\varepsilon_0$.

consequence of energy conservation. As discussed for the momentum distribution, the creation of low-energy excitations on the R branch comes from a higher-order process and it is thus less relevant. This can be clearly seen by observing the short-dashed green line representing $\delta\mathcal{A}_{R,-}$ as well as the behavior of $\delta\mathcal{A}_{R,+}$ (solid red line) near the Fermi energy.

3.2 Quantum quench of interaction

The injection of a single electron in a 1D system, which originates the fractional counterpropagating excitations we have studied so far, can be seen as a way to bring the 1D system out of equilibrium. Obviously, there are also many other protocols which allows to study non-equilibrium physics in 1D. Among them, the quantum quench of interactions is particularly relevant for the present thesis. It is indeed possible to adapt the machinery developed in the previous section to study how a sudden interaction quench affects the time-evolution of a LL focusing, for example, on its spectral function.

The parallel between interaction quenches in LL and the electron injection discussed before is strengthen also by the observation that the former can be also interpreted as a creation of an infinite superposition of fractional counterpropagating excitations [162, 163]. In this section we will demonstrate that this peculiar superposition of excitations has a remarkable universal signature, namely a power-law relaxation of observables $\propto t^2$ which does not depend on the details of the quench protocol! This intriguing result represents the core of our publications in Ref. [14, 15], to which we refer the reader for a more comprehensive and detailed discussion.

Quantum quenches: a short digest

Before diving into the model we considered, let us give a brief overview about quantum quenches. They consist in the rapid and controlled variation over time of one of the system parameters. Such a protocol, which clearly settles an out-of-equilibrium state with non-trivial time evolution, has recently known a widespread interest thanks to the dramatic experimental development in cold atomic system: indeed, their high degree of tunability and the isolation of the system from the environment make them the ideal platform to study quantum quenches[8].

When dealing with quenched systems, two important questions arise: do such systems eventually settle to a steady state? And if so, what does characterize their relaxation dynamics? Several theoretical studies [166–168] and experiments [169–171] have addressed such topics, showing that the answers strongly depend on the system considered. In this respect, integrable systems such as the LL model are particularity interesting to analyze: their large number of conserved quantities strongly constrain the post-quench dynamics and, as long as the system is isolate, it will retain a strong memory of the initial state. In particular, it has been conjectured that they eventually approach the so-called generalised Gibbs ensemble (GGE) [172, 173], whose associated density matrix is in general very different from the thermal one. Interestingly, the first analytical confirmation of such a conjecture did come from the study of quenched LL, see Ref. [174] and Appendix C.1, hence proving the usefulness of LL model as a tool to study also non-equilibrium 1D systems.

In the following we will answer to the second of the aforementioned questions, which is still open: what are the characteristics of the relaxation process which describe the system evolution of a quenched LL?

3.2.1 Sudden quench protocol

We consider an isolated 1D interacting system, consisting of two counterpropagating channels described by the LL model. We enforce periodic boundary conditions and consider the thermodynamic limit, i.e. the system size $L \to \infty$. The system is subject to the following quench protocol. For $t < 0$, the Luttinger parameter is $K_i < 1$ and the system Hamiltonian reads

$$H_i = \frac{u_i}{2} \sum_{\eta=\pm} \int_{-\infty}^{+\infty} \mathrm{d}x \; [\partial_x \phi_{i,\eta}(x)]^2 \,, \tag{3.91}$$

---

[8] It is worth noting that quench-like protocols have been recently investigated also in solid-state devices [164, 165]

where the chiral bosonic fields $\phi_{i,\eta}(x)$ propagate at velocity $u_i = v_\mathrm{F} K_i^{-1}$.

$$\phi_{i,\eta}(x,t) = \phi_{i,\eta}(x - \eta u_i t, 0) \qquad (t < 0). \tag{3.92}$$

The system is initially described by a thermal equilibrium density matrix (here we assume $k_B = 1$)

$$\hat{\rho}_{eq} = \frac{e^{-H_i/T}}{Z} \tag{3.93}$$

where $Z = \mathrm{Tr}\{e^{-H_i/T}\}$ is the partition function and T is the temperature[9].

At $t = 0$ the interaction is suddenly quenched from $K_i \to K_f < 1$, resulting in a sudden switch of the Hamiltonian $H_i \to H_f$. The latter reads

$$H_f = \frac{u_f}{2} \sum_{\eta=\pm} \int_{-\infty}^{+\infty} \mathrm{d}x \, \left[\partial_x \phi_{f,\eta}(x)\right]^2 . \tag{3.94}$$

Here the new bosonic fields $\phi_{f,\eta}$ are chiral for $t > 0$ and propagates with the new renormalized velocity $u_f = v_\mathrm{F} K_f^{-1}$:

$$\phi_{f,\eta}(x,t) = \phi_{f,\eta}(x - \eta u_f t, 0) \qquad (t > 0). \tag{3.95}$$

It is crucial for what follows to clearly establish the relations between the different bosonic fields at play (we recall that $\vartheta_{R/L} = +/-1$)

- The fields $\phi_{i,\eta}$ diagonalize the Hamiltonian H_i with Luttinger parameter K_i and they are thus chiral for $t < 0$. Following Eq. (2.22), it is possible to relate them with the non interacting boson fields ϕ_r via

$$\phi_r(x) = \sum_{\eta=\pm} B_{(\eta\vartheta_r)} \phi_{i,\eta}(x) \qquad \text{with } B_\pm = \frac{1}{2}\left[\frac{1}{\sqrt{K_i}} \pm \sqrt{K_i}\right]. \tag{3.96}$$

- Along the same line, the fields $\phi_{f,\eta}$ diagonalize the Hamiltonian H_f with Luttinger parameter K_f and they are thus chiral for $t > 0$. They are relate to ϕ_r via

$$\phi_r(x,t) = \sum_{\eta=\pm} A_{(\eta\vartheta_r)} \phi_{f,\eta}(x,t) \quad \text{with} \quad A_\pm = \frac{1}{2}\left[\sqrt{\frac{1}{K_f}} \pm \sqrt{K_f}\right]. \tag{3.97}$$

---

[9] Such a situation can be realized by coupling, at a very early time, the system with a thermal bath at temperature T, then letting the system thermalize and eventually disconnecting the bath.

- By combining (3.96) and (3.96), it is possible to directly relate $\phi_{f,\eta}$ and $\phi_{i,\eta}$ via

$$\phi_{f,\eta}(x,t) = \sum_{\ell=\pm} \theta_{(\ell\eta)} \phi_{i,\ell}(x,t) \quad \text{with} \quad \theta_{\pm} = \frac{1}{2}\left[\sqrt{\frac{K_f}{K_i}} \pm \sqrt{\frac{K_i}{K_f}}\right] . \tag{3.98}$$

The relation between the different Bogoliubov coefficients is

$$B_{\pm} = A_{\pm}\theta_{+} + A_{\mp}\theta_{-} . \tag{3.99}$$

Note that the non-quenched case ($K_i = K_f$) is represented by $\theta_- = 0$, $\theta_+ = 1$ and $A_{\pm} = B_{\pm}$.

3.2.2 Quench-induced entanglement

If we are only interested in the dynamics of the system for $t \geq 0$, we can regard the sudden interaction quench just as a way to initialize the system at $t = 0$ in a particular out-of-equilibrium state of the Hamiltonian H_f, described by a non-equilibrium density matrix $\hat{\rho}_{NE}$. In this subsection, we will study the properties of $\hat{\rho}_{NE}$ from a post-quench perspective.

For the sake of simplicity, in this subsection we focus on the zero-temperature limit. This allows to readily identify the density matrix with $\hat{\rho}_{NE} = |\Omega_i\rangle\langle\Omega_i|$, i.e. with the ground state of the initial Hamiltonian H_i. This state is defined by the property of being annihilated by every "initial" bosonic operator $\beta^{(i)}_{\eta,q}$

$$\beta^{(i)}_{\eta,q}|\Omega_i\rangle = 0 , \quad \forall \eta = \pm,\ q > 0 . \tag{3.100}$$

Here we have denoted by $\beta^{(i)}_{\eta,q}$ ($\beta^{(f)}_{\eta,q}$) the bosonic operators related to the bosonic field $\phi_{i,\eta}$ ($\phi_{f,\eta}$) by Eq. (2.28). Interestingly, the condition in Eq. (3.100) is satisfied by the state [163, 162]

$$|\psi_{NE}\rangle = \mathfrak{N} \exp\left[\frac{\theta_-}{\theta_+} \sum_{q>0} \left(\beta^{(f)}_{+,q}\right)^{\dagger} \left(\beta^{(f)}_{-,q}\right)^{\dagger}\right] |\Omega_f\rangle \tag{3.101}$$

where $\mathfrak{N}$ is a normalization factor and Ω_f is the ground state of H_f. Indeed, using (3.98), one has

$$\begin{aligned} \beta^{(i)}_{\eta,q}|\psi_{NE}\rangle = \mathfrak{N} \left(\theta_+ \beta^{(f)}_{\eta,q} - \theta_- \left(\beta^{(f)}_{-\eta,q}\right)^{\dagger}\right) \exp\left[\frac{\theta_-}{\theta_+} \left(\beta^{(f)}_{+,q}\right)^{\dagger} \left(\beta^{(f)}_{-,q}\right)^{\dagger}\right] \\ \times \prod_{p\neq q} \exp\left[\frac{\theta_-}{\theta_+} \sum_{q>0} \left(\beta^{(f)}_{+,p}\right)^{\dagger} \left(\beta^{(f)}_{-,p}\right)^{\dagger}\right] |\Omega_f\rangle \end{aligned} \tag{3.102}$$

which vanishes because

$$\begin{aligned}
&\theta_+ \beta^{(f)}_{\eta,q} \exp\left[\frac{\theta_-}{\theta_+}\left(\beta^{(f)}_{+,q}\right)^\dagger \left(\beta^{(f)}_{-,q}\right)^\dagger\right]|\Omega_f\rangle \\
&= \sum_{n\geq 1} \frac{1}{n!}\left(1+\beta^{(f)\dagger}_{\eta,q}\beta^{(f)}_{\eta,q}\right)\frac{\theta_-^n}{\theta_+^{n-1}}\left(\beta^{(f)}_{\eta,q}\right)^{\dagger(n-1)}\left(\beta^{(f)}_{-\eta,q}\right)^{\dagger(n)}|\Omega_f\rangle \\
&= \theta_-\left(\beta^{(f)}_{-\eta,q}\right)^\dagger \exp\left[\frac{\theta_-}{\theta_+}\left(\beta^{(f)}_{+,q}\right)^\dagger \left(\beta^{(f)}_{-,q}\right)^\dagger\right]|\Omega_f\rangle
\end{aligned} \tag{3.103}$$

A sudden interaction quench can be seen as a way to initialize the system in a highly non-trivial state. The latter consists of a superposition of couples of counterpropagating and entangled excitations which originate from every point of the system at $t = 0$. In the following we will show a remarkable signature of this entangled state, namely a universal relaxation behavior in the non-equilibrium spectral function of the system and in its transport properties.

3.2.3 Quenched bosonic and fermionic correlators

In this subsection we will discuss the local lesser fermionic Green function of the 1D channel

$$\mathcal{G}^<_r(z,t,\bar{t}) \equiv i\left\langle \psi^\dagger_r(z,\bar{t})\psi_r(z,t)\right\rangle_{eq} = \frac{i}{2\pi a}\left\langle e^{i\sqrt{2\pi}\phi_r(z,\bar{t})}e^{-i\sqrt{2\pi}\phi_r(z,t)}\right\rangle_{eq}, \tag{3.104}$$

at the generic position z. Here, the brackets $\langle\ldots\rangle_{eq}$ denotes a quantum average performed on the initial thermal density matrix $\hat{\rho}_{eq}$ and the last bosonic expression is obtained using the bosonization identity (2.5). The first step to evaluate the Green function is to compute the time evolution of the free bosonic fields $\phi_r(z,t)$. It crucially depends on whether the operators are evaluated before or after the quench. Indeed, using Eqs. (3.96) and (3.97) one can write

$$\phi_r(z,t) = \begin{cases} A_{\vartheta_r}\phi_{f,+}(z-u_f t,0)+A_{-\vartheta_r}\phi_{f,-}(z+u_f t,0) & t>0 \\ B_{\vartheta_r}\phi_{i,+}(z-u_i t,0)+B_{-\vartheta_r}\phi_{i,-}(z+u_i t,0) & t<0 \end{cases}, \tag{3.105}$$

having exploited the proper chirality properties of Eq. (3.92) and Eq. (3.95).

Note that, since space translational invariance is not broken by the quench protocol, the Green function will not depend on the generic position z. On the other hand, due to the breaking of time translational invariance, it will feature four different time regimes depending on the positive (p) or negative (n) sign of t and $\bar{t}$. One can thus write

$$\mathcal{G}_r^<(t,\bar{t}) = \begin{cases} \mathcal{G}_r^{nn}(t,\bar{t}) & t<0,\ \bar{t}<0 \\ \mathcal{G}_r^{pn}(t,\bar{t}) & t>0,\ \bar{t}<0 \\ \mathcal{G}_r^{np}(t,\bar{t}) & t<0,\ \bar{t}>0 \\ \mathcal{G}_r^{pp}(t,\bar{t}) & t>0,\ \bar{t}>0 \end{cases} \tag{3.106}$$

Note that the average in (3.104) is with respect to the initial state, meaning that the only known correlator is [82]

$$\begin{aligned} \mathfrak{C}_\eta(x) &\equiv \langle \phi_{i,\eta}(x,0)\phi_{i,\eta}(0,0)\rangle_{eq} - \langle \phi_{i,\eta}^2(0,0)\rangle_{eq} \\ &= \frac{1}{2\pi}\ln\frac{\left|\Gamma(1+T\omega_i^{-1}-iT\eta x u_i^{-1})\right|^2}{\Gamma(1+T\omega_i^{-1})^2} + \frac{1}{2\pi}\ln\left(\frac{1}{1-i\eta x a^{-1}}\right). \end{aligned} \tag{3.107}$$

In order to compute the functions appearing in (3.106), one has therefore to express everything in terms of $\mathfrak{C}_\eta(x)$, a task which can be performed by exploit the canonical transformations (3.96 - 3.98) and the chiral evolutions (3.92) and (3.95). The explicit expressions for each function appearing in (3.106) are reported in Appendix C.2.1.

The most important function is $\mathcal{G}_r^{pp}$. As we will see, it is indeed the only one responsible for the presence of the universal features which characterise the post-quench relaxation dynamics. Moreover, it is the only one controlling the transport properties after the quench. It is therefore worth to analyse it in details, highlighting the physical origin of its peculiar quench-induced features. To this end, it is useful to rewrite it in terms of correlation functions between the final chiral bosonic fields. One thus has

$$\begin{aligned} \mathcal{G}_r^{pp}(t,\bar{t}) &= \frac{i}{2\pi a}\exp\left\{\pi\left[A_{\vartheta_r}^2 D_{+,+}(t,t-\bar{t}) + A_{-\vartheta_r}^2 D_{-,-}(t,t-\bar{t})\right.\right. \\ &\quad \left.\left. + 2A_+A_-D_{+,-}(t,t-\bar{t})\right]\right\}, \end{aligned} \tag{3.108}$$

with

$$\begin{aligned} D_{\alpha,\beta}(t,\tau) &\equiv 2\langle\phi_{f,\alpha}(0,t-\tau)\phi_{f,\beta}(0,t)\rangle_{eq} - \langle\phi_{f,\alpha}(0,t-\tau)\phi_{f,\beta}(0,t-\tau)\rangle_{eq} \\ &\quad -\langle\phi_{f,\alpha}(0,t)\phi_{f,\beta}(0,t)\rangle_{eq}. \end{aligned} \tag{3.109}$$

Here $\alpha,\beta=\pm$ and the time difference should satisfy $\tau\equiv t-\bar{t}<t$. One can identify two contributions

$$D_{\alpha,\beta}(t,\tau) = D_{\alpha,\beta}^{(0)}(t,\tau) + \Delta D_{\alpha,\beta}(t,\tau), \tag{3.110}$$

with $D^{(0)}_{\alpha,\beta}(t,\tau)$ the zero-temperature contribution and $\Delta D_{\alpha,\beta}(t,\tau)$ the corrections due to the finite-temperature of the initial state. In particular, one obtains (see Appendix C.2.1)

$$D^{(0)}_{\alpha,\alpha}(\tau) = \sum_{\eta=\pm} \frac{\theta_\eta^2}{\pi} \log \frac{1}{1 - i\eta\omega_f\tau}, \tag{3.111}$$

$$\Delta D_{\alpha,\alpha}(\tau) = \frac{\theta_+^2 + \theta_-^2}{\pi} \log \frac{|\Gamma(1 + T\omega_i^{-1} + iT\Lambda\tau)|^2}{\Gamma^2(1 + T\omega_i^{-1})}, \tag{3.112}$$

$$D^{(0)}_{\alpha,-\alpha}(t,\tau) = \frac{\theta_+\theta_-}{2\pi} \log \frac{[1 + 4\omega_f^2(t-\tau)^2](1 + 4\omega_f^2 t^2)}{[1 + \omega_f^2(2t-\tau)^2]^2}, \tag{3.113}$$

$$\Delta D_{\alpha,-\alpha}(t,\tau) = \frac{2\theta_+\theta_-}{\pi} \log \frac{|\Gamma(1 + T\omega_i^{-1} - iT\Lambda(2t-\tau))|^2}{|\Gamma(1 + T\omega_i^{-1} + 2iT\Lambda(t-\tau))||\Gamma(1 + T\omega_i^{-1} + 2iT\Lambda t)|}, \tag{3.114}$$

with the cut-off frequencies $\omega_f = u_f a^{-1}$, $\omega_i = u_i a^{-1}$ and

$$\Lambda = \frac{K_i}{K_f}. \tag{3.115}$$

As a general feature, we note that auto-correlators ($\alpha = \beta$) only depend on the time difference τ and not on t. By contrast, cross-correlators ($\alpha = -\beta$) feature a full dependence on both t and τ. Note that the fact that cross-correlators are finite is a direct consequence of the highly entangled state induced by the quench and described, in the $T = 0$ limit, in subsection 3.2.2: at thermal equilibrium, chiral fields $\phi_{f,\eta}(x,t)$ would have been completely decoupled leading to a vanishing cross-correlator. This fact is obviously confirmed by observing that, without a quantum quench, one has $\theta_- = 0$ which kills the whole $D_{\alpha,-\alpha}(t,\tau)$.

We now want to study the dependence on t of the cross-correlators when $t \gg \tau$. Functions $D_{\alpha,-\alpha}$ are plotted in Fig. 3.14 for different temperatures, showing a power-law behavior $\propto t^{-2}$. A careful asymptotic analysis, carried on in Appendix C.3.1, gives indeed

$$D_{\alpha,-\alpha}(t,\tau) \approx \frac{\theta_+\theta_-}{\pi} \begin{cases} 2(T\Lambda\tau)^2\Gamma(1, 1 + T\omega_i^{-1}) - \left(\frac{\tau}{2t}\right)^2 & \tau \ll t \ll (\Lambda T)^{-1} \\ 2T\omega_i^{-1}\left(\frac{\tau}{2t}\right)^2 & \tau \ll (\Lambda T)^{-1} \ll t \end{cases} \tag{3.116}$$

in perfect agreement with the plots. As one can see there are two different regimes, both featuring a power-law decay $\propto t^{-2}$ but with different prefactors. For long time $t \gg (\Lambda T)^{-1}$ the cross-correlator is positive and proportional to the temperature. By contrast, when finite temperature effects have not kicked in yet, i.e. at shorter time $t \ll (\Lambda T)^{-1}$, the prefactor of the t^{-2} decay is negative and temperature-independent.

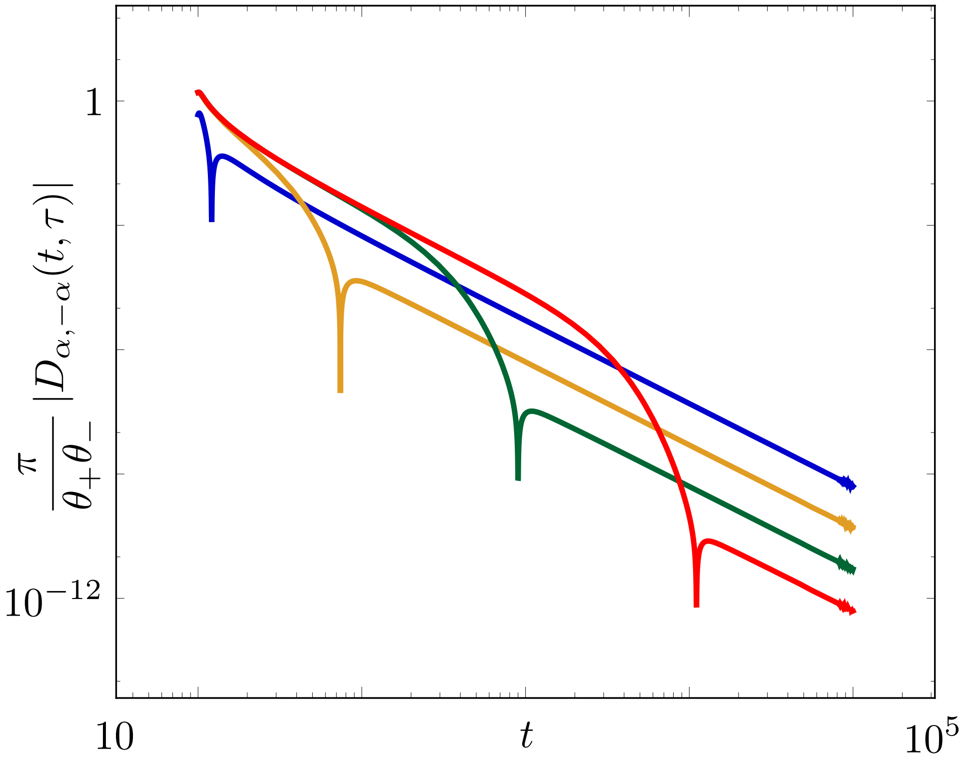

Fig. 3.14 Plot of the full cross-correlator $\frac{\pi}{\theta_+\theta_-}|D_{\alpha,-\alpha}(t,\tau)|$ as a function of time t for different temperatures: $T = 10^{-4}$ (red), $T = 10^{-3}$ (green), $T = 10^{-2}$ (yellow), $T = 10^{-1}$ (blue). Here, $\tau = 10$, $K_i = 0.9$, $K_f = 0.6$, time units ω_f^{-1} and temperature units ω_i.

3.2.4 Non-equilibrium spectral function

To fully characterise the effects of the quench, we now focus on the local (lesser) non-equilibrium spectral function. This is a key quantity to inspect the presence of universal features in the relaxation dynamics, as well as an important ingredient to evaluate observable transport properties. The local non-equilibrium spectral function is defined as [175]

$$\mathcal{A}_r^<(\omega,t) \equiv \frac{-i}{2\pi}\int_{-\infty}^{\infty} e^{i\omega\tau}\, G_r^<(t,t-\tau)\, d\tau. \tag{3.117}$$

Our task is to investigate its time evolution after the quench, i.e. for $t > 0$. Since the integration range over τ extends to $+\infty$, the calculation of the above expression requires to distinguish between two different regimes of the Green function:

$$\begin{aligned}\mathcal{A}_r^<(\omega,t) &= \mathcal{A}_r^{pp}(\omega,t) + \mathcal{A}_r^{pn}(\omega,t)\\ &= \frac{-i}{2\pi}\int_{-\infty}^{t} e^{i\omega\tau}\,\mathcal{G}_r^{pp}(t,t-\tau)\, d\tau + \frac{-i}{2\pi}\int_{t}^{\infty} e^{i\omega\tau}\,\mathcal{G}_r^{pn}(t,t-\tau)\, d\tau.\end{aligned} \tag{3.118}$$

Equation (3.118) is exact and suitable for numerical investigation, using Eq. (C.8) and (C.9). It is possible, however, to devise helpful analytical limits and expansions.

Steady state

The non-equilibrium local spectral function finite steady state $\bar{\mathcal{A}}_r(\omega) \equiv \lim_{t\to\infty} \mathcal{A}_r^<(\omega,t)$ is given by

$$\begin{aligned}\bar{\mathcal{A}}_r(\omega) &= \frac{-i}{2\pi}\int_{-\infty}^{+\infty} e^{i\omega\tau} \lim_{t\to\infty} \mathcal{G}_r^{pp}(t,t-\tau)\, d\tau \\ &= \frac{a^{-1}}{(2\pi)^2}\int_{-\infty}^{\infty} e^{i\omega\tau} \left(\frac{1}{1-i\omega_f\tau}\right)^{\nu_-}\left(\frac{1}{1+i\omega_f\tau}\right)^{\nu_+}\left[\frac{|\Gamma(1+T\omega_i^{-1}+iT\Lambda\tau)|^2}{\Gamma^2(1+T\omega_i^{-1})}\right]^{\nu_++\nu_-} \mathrm{d}\tau,\end{aligned} \tag{3.119}$$

with

$$\nu_\pm = \theta_\mp^2(A_+^2 + A_-^2). \tag{3.120}$$

An extensive study of the effects of interaction quenches on the steady state limit of the spectral function can be found in our publications Ref. [19] and Ref. [20]. There, we also discuss the momentum dependence of the spectral function and how the transport properties, such as energy partitioning, are affected in the steady state.

Transient dynamics of the non-equilibrium spectral function

The analysis of $\mathcal{A}_r^{pp}$ is more tricky. The key observation is that the integrand $e^{i\omega\tau}\mathcal{G}_r^{pp}(t,t-\tau)$ contributes to $\mathcal{A}_r^{pp}(\omega,t)$ only in two distinct regions: near $\tau \sim 0$ and close to the boundary of the integration domain $\tau \sim t$. These are indeed the regions where the non-analytical points of the Green function are located, see Appendix C.2.1. In the region in between, i.e. for $0 < \tau < t$, the integrand is a smooth and slowly varying function multiplied by an oscillating phase $e^{i\omega\tau}$. Therefore, it does not contribute to the integral in the long time limit $t \gg \omega^{-1}$ and one simply has

$$\mathcal{A}_r^{pp}(\omega,t) \approx \mathcal{A}_r^{(1)}(\omega,t) + \mathcal{A}_r^{(2)}(\omega,t), \tag{3.121}$$

where the former term stems from an expansion of the integrand for $\tau \to 0$ and the latter from an expansion for $\tau \to t$.

The behaviour of $\mathcal{A}_r^{(1)}(\omega,t)$ is controlled by the bosonic cross-correlators: using (3.116) one can thus obtain the asymptotic expansion

$$\mathcal{A}_r^{(1)}(\omega,t) = \bar{\mathcal{A}}_r(\omega) - \kappa(t)\,\gamma\,\frac{\partial_\omega^2 \bar{\mathcal{A}}_r(\omega)}{t^2} + O\left(\frac{1}{t}\right)^3 \tag{3.122}$$

	$t \ll (\Lambda T)^{-1}$	$t \gg (\Lambda T)^{-1}$
Universal:	t^{-2}	t^{-2}
Non-universal:	$e^{i\omega t}\, t^{-\xi}$	$e^{i\omega t}\ \exp\left[-2\pi\Lambda T t\right]^{\nu_+ + \nu_-}$
		$e^{i\omega t}\ \exp\left[-2\pi\Lambda T t\right]^{\xi}$
	$e^{i\omega t \frac{u_i+u_f}{u_i}}\ t^{-\nu_-}$	$e^{i\omega t \frac{u_i+u_f}{u_i}}\ \exp\left[-2\pi\Lambda T t\right]^{\nu_- - 2\gamma}$

Table 3.1 Summary of the terms contributing to the transient dynamics of $\delta\mathcal{A}_r(\omega,t)$ defined in (C.3.3). Here we reported only the dominant time dependence of each term. Their full expressions can be found in Eq. (3.122) and in Appendix C.3.2.

where $\gamma = -A_+ A_- \theta_+ \theta_-$ and

$$\kappa(t) = \begin{cases} -\frac{1}{2} & t \ll (\Lambda T)^{-1} \\ T\omega_i^{-1} & t \gg (\Lambda T)^{-1} \end{cases} \tag{3.123}$$

distinguishes between the two regimes of $D_{\alpha,-\alpha}$. Interestingly, $\mathcal{A}_r^{(1)}(\omega,t)$ features a universal power-law relaxation $\propto t^{-2}$ in both regimes. The behaviour of $\mathcal{A}_r^{(2)}(\omega,t)$ and $\mathcal{A}_r^{pn}(\omega,t)$ is rather different: as detailed in Appendix C.3.2, they feature a non-universal power-law decay in the $t \ll (\Lambda T)^{-1}$ regime which is subsequently killed by a fast exponential decay for $t \gg (\Lambda T)^{-1}$. In the end, the transient dynamics of the whole non-equilibrium spectral function

$$\delta\mathcal{A}_r(\omega,t) \equiv \mathcal{A}_r^{<}(\omega,t) - \bar{\mathcal{A}}_r(\omega) \tag{3.124}$$

features two regimes, each one consisting of a sum of different terms whose dominant time dependence is summarized in Table 3.1. The quench-dependent exponents which appear in the non-universal terms are carefully analyzed in Appendix C.3.3.

- At short times ($t \ll (\Lambda T)^{-1}$) a oscillating non-universal power law decay with exponent either $\xi = \nu_+ + \nu_- - 2\gamma$ or ν_- (both lesser than 2) is present and dominates the relaxation dynamics, masking the universal features induced by the finite cross-correlators.
- For sufficiently long times($t \gg (\Lambda T)^{-1}$) the situation drastically changes: temperature effects kick in and the non-universal power laws are killed by fast exponential decays. As a result the non-equilibrium spectral function display a very clear universal t^{-2} relaxation.

The latter is a remarkable feature, since in general one would have expected exponential behaviors for all fermionic correlation functions at finite temperature. Note that at $T = 0$, the

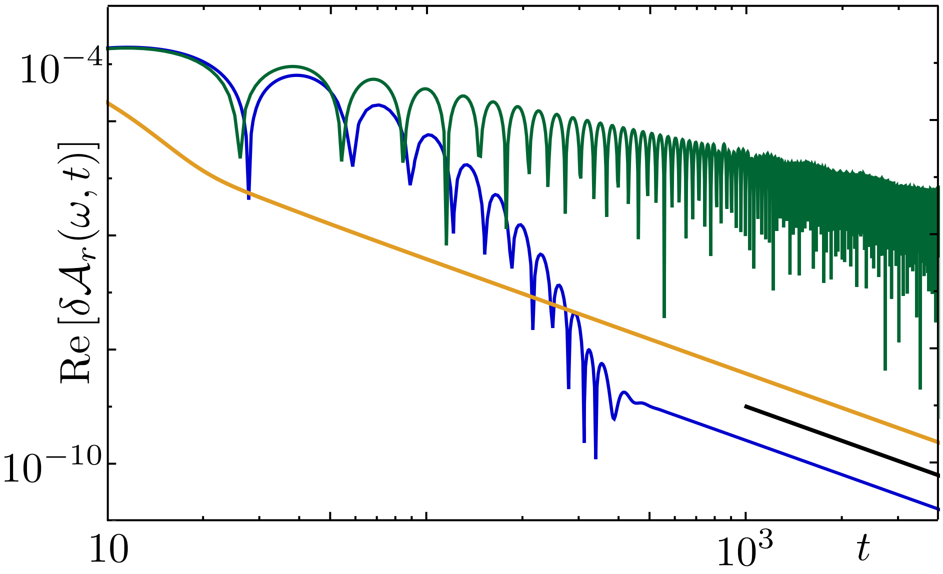

Fig. 3.15 Plot of the real part of $\delta A_r(\omega,t) = A_r^<(\omega,t) - \bar{A}_r(\omega)$ (units v_f^{-1}) as a function of time for different temperatures: $T = 10^{-1}$ (orange), $T = 10^{-2}$ (blue), $T = 0$ (green). Black line show a power-law decay $\propto t^2$. Here $\omega = 0.1\omega_f$, $K_i = 0.9$, $K_f = 0.6$, time units ω_f^{-1} and temperature units ω_i. We have included the zero temperature case (green curve) to underline the difference with the finite temperature case.

regime $t \gg (\Lambda T)^{-1}$ is never reached: the non-equilibrium spectral function always features non-universal power laws $\propto t^{-\xi}$ which completely mask the $\propto t^{-2}$ behavior.

All features described so far can be seen in Fig. 3.15, where the real and the imaginary part of the transient spectral function $\delta A_r(\omega,t)$ are evaluated numerically from Eq. (3.118) for different temperatures. Notice that we have also inserted the zero temperature case (green line) to better clarify how it differs from the finite temperature case. Once the exponential decay of the non-universal contributions sets in, around $t \sim 5(\Lambda T)^{-1}$, the universal decay $\propto t^{-2}$ clearly emerges in the real part of $\delta A_r(\omega,t)$.

In Ref. [14, 15] we demonstrate that the appearance of this remarkable universal relaxation characterizes also the transport properties. In particular we computed the time-dependence of both the charge and the energy currents which flow from an external probe to the quenched system via a weak-tunneling coupling. In view of their close relation to the spectral function (a relation emerged also in Section 3.1), these observables feature a qualitatively similar relaxation: a competition between the universal decay $\propto t^{-2}$ and non-universal terms, the latter being eventually killed by finite-temperature effects [14, 15].

Chapter 4

Fermionizing parafermions

This chapter is devoted to parafermions, i.e. non-Abelian anyons which generalize the Majoranas introduced in the first chapter. After a general introduction about Abelian and non-Abelian anyons in 2 dimensional systems, the focus will be on the reasons why it is both possible and interesting to go beyond Majoranas. Exploiting the Clock model generalization of the Ising chain, $\mathbb{Z}_p$ parafermions will be introduced along with their main properties. A brief discussion of the existing proposal for systems which can host parafermions will eventually lead to the last and main important section of the chapter. Here we will describe the original and exact mapping which we developed in order to directly relate chains of $\mathbb{Z}_4$ parafermions and chains of spinful fermions [16]. This will allow studying how the peculiar parafermionic properties previously discussed emerges at the level of interacting electrons[1].

4.1 Anyons

It is well known that in 3 spatial dimensions particles can be either fermions or bosons, depending on their exchange statistics: a many-body bosonic wave function is completely symmetric with respect to the exchange of two particles while a fermionic one is completely antisymmetric. Interestingly enough, a much wider variety of behaviors are possible in 2 spatial dimension, as pointed out for the first time in Ref. [176] in 1977. Particles which are neither fermions nor bosons have been named anyons [177].

4.1.1 Two indistinguishable particles

In order to highlight the differences between the three-dimensional case and the two dimensional one, let us focus at first on two indistinguishable particles at positions $\vec{r}_1 \neq \vec{r}_2$. The configuration

---

[1] In this chapter we set $\hbar = 1$

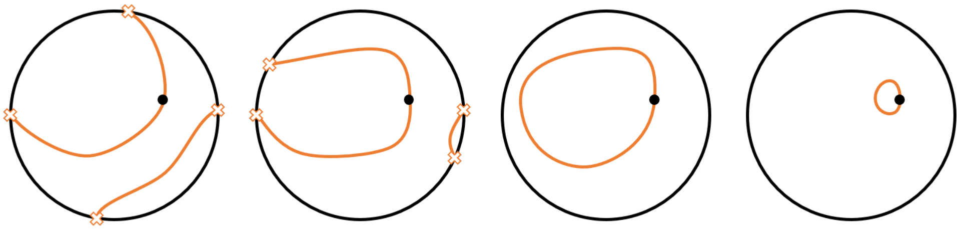

(a) Paths belonging to the direct class.

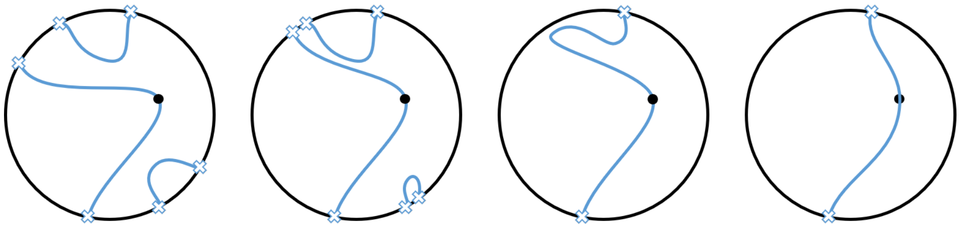

(b) Paths belonging to the exchange class.

Fig. 4.1 First homotopy group of the configuration space for two particles in 3 spatial dimensions: sketch of the two possible classes of closed loops (with fixed radius) on C_3. The circle represents half a sphere, viewed from above, whose opposite points on the boundary are identified (and marked with crosses).

of the system can be described in terms of the center of mass $\vec{R} = (\vec{r}_1 + \vec{r}_2)/2$ and the relative coordinate $\vec{r} = \vec{r}_1 - \vec{r}_2 \neq 0$. The former does not play any role in the exchange of the particles and we can therefore safely forget about it in what follows. Note that, since the two particles are indistinguishable, points $\vec{r}$ and $-\vec{r}$ must be identified with each other. As a result, the configuration space of the relative coordinate is given by $C_d = (\mathbb{R}^d - \vec{0})/\mathbb{Z}_2$ with $d = 2, 3$.

Suppose that at time t_i the two indistinguishable particles are at positions $\vec{r}_{1i} \neq \vec{r}_{2i}$, i.e. the system is initially at point $\vec{r}_i \in C_d$. The physics of the system can be studied by means of the path integral approach which, in turn, requires to take into account all the possible paths in configuration space which connects $\vec{r}_i$ with a final point $\vec{r}_f$. To this end, it is important to study the properties of these paths and, in particular, the existence of different classes of paths. In mathematical terms, this task is known as computing the first homotopy group Π_1 of the configuration space C_d [178].

Focusing at first on $d = 3$, it turns out that there are only two distinct classes of paths in C_3: mathematically $\Pi_1(C_3) = \mathbb{Z}_2$. Here distinct means that paths belonging to different classes cannot be continuously deformed into each other. In order to develop some intuition, it is useful to restrict our analysis to closed loops with a fixed[2] $|\vec{r}|$. The configuration space

---

[2] Note that, if $|\vec{r}|$ varies along the closed path, is it possible to continuously deform it into another path with fixed $|\vec{r}|$ belonging to the same class.

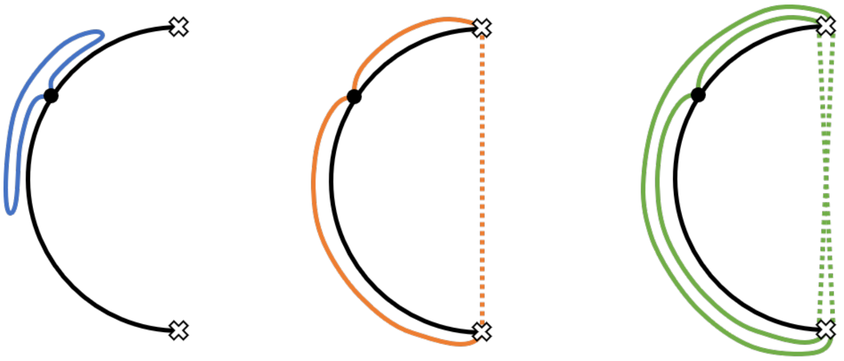

Fig. 4.2 First homotopy group of the configuration space for two particles in 2 spatial dimensions. Three different classes of closed paths (with fixed radius) with different winding number: 0, 1 and 2.

becomes, therefore, half a sphere with the additional prescription that opposite points on the boundary (the diameter) are identified. This allows to easily visualize the closed paths looking at the half sphere from above, see Fig. 4.1. The direct class consists of all the loops which can be continuously shrunk to a single point, i.e. to the trivial path where the two particles do not move at all [see Fig. 4.1a]. By contrast, the so-called exchange class consists of all the remaining loops, which are associated with an exchange of the two particles: the path connects two antipodal points $\vec{r}_i$ and $-\vec{r}_i$ [see Fig. 4.1b]. When the "trajectories" of two particles in $3+1$ dimensions are considered, it only matters whether at the end the two particles are exchanged or not: it does not matter at all how complicated these trajectories are in between the initial and the final point. This statement is directly related to the fact that all knots in 4 dimensions are trivial, i.e. they can always be untied.

The situation is completely different when $d = 2$. The first homotopy group is now $\Pi_1(C_2) = \mathbb{Z}$, meaning that paths can be subdivided into infinite classes X_ν, which can be labelled by an integer number ν. Again, for ease of visualization, let us focus on closed path with fixed $|\vec{r}|$. The configuration space becomes half of a circumference, whose two endpoints are identified with each other. By looking at Fig. 4.2, it is easy to convince ourself that loops can be classified based on their winding number ν around the circumference. As a result, specifying only whether a path exchanges two particles or not is not enough: one must also specify how many times the two particles wind around each other. Along the lines of the previous paragraph, this finding can be related to the fact that, as everybody experienced, it is indeed possible to tie knots in $2+1$ dimensions.

In order to see how these interesting results are related to physics, let us compute the quantum amplitude between the initial state at time t_i and a state at time t_f, both lying at the same point in the configuration space $\vec{r}_i$. If $d=3$, one has

$$\langle \vec{r}_i(t_i)|\vec{r}_i(t_f)\rangle = \sum_{\gamma\in D} e^{iS[\gamma]} + e^{i\theta}\sum_{\gamma\in E} e^{iS[\gamma]} \tag{4.1}$$

where we distinguished between closed paths γ belonging either to the direct (D) or the exchange (E) class. Here $S[\gamma]$ is the action computed along γ. Note that, since the two classes are completely decoupled, we are able to introduce the phase $e^{i\theta}$ which simply means adding a harmless constant to the action $S[\gamma]$ when $\gamma\in E$. Such a phase, however, is not arbitrary because composition rules must be satisfied: two concatenated paths, each one belonging to the E class, clearly gives a path which belongs to the D class. This means $e^{i2\theta}=1$ and therefore $e^{i\theta}=\pm 1$. Particles whose physics is described using the $+1$ are bosons, the others are fermions. By contrast, if $d=2$ one has

$$\langle \vec{r}_i(t_i)|\vec{r}_i(t_f)\rangle = \sum_{\nu\in\mathbb{Z}} \left[e^{i\theta_\nu} \sum_{\gamma\in X_\nu} e^{iS[\gamma]} \right] . \tag{4.2}$$

When paths are concatenated, winding numbers clearly sum up. This poses a constrain on the phases $e^{i\theta_\nu}e^{i\theta_\mu}=e^{i\theta_{\nu+\mu}}$ which implies $\theta_\nu=\nu\theta$. Interestingly enough, the angle θ remains arbitrary: in two spatial dimensions, one can therefore have bosons $\theta=0$, fermions $\theta=\pi$ but also everything in between, i.e. anyons!

4.1.2 Permutation and braiding groups

The above arguments can obviously be extended to N indistinguishable particles. For $d=3$, one can show that the disconnected classes of closed paths in the configuration space correspond to the possible ways to permute N objects. These permutations, along with their method of composition, yield the so-called symmetric group S_N. The problem of associate a complex phase to each class, consistently with the compositions rules, is equivalent to find the one-dimensional unitary representations of S_N. For $N=2$ we have already shown that there are only two possibilities. As expected, the same holds in general since there are only two 1D unitary representations of S_N:

- the trivial one, which associate the phase $+1$ to every permutation;
- the alternating one, which associated either $+1$ or -1 depending on the parity of the number of exchanges.

Particles which behave accordingly to the trivial (alternating) 1D representation of S_N are bosons (fermions).

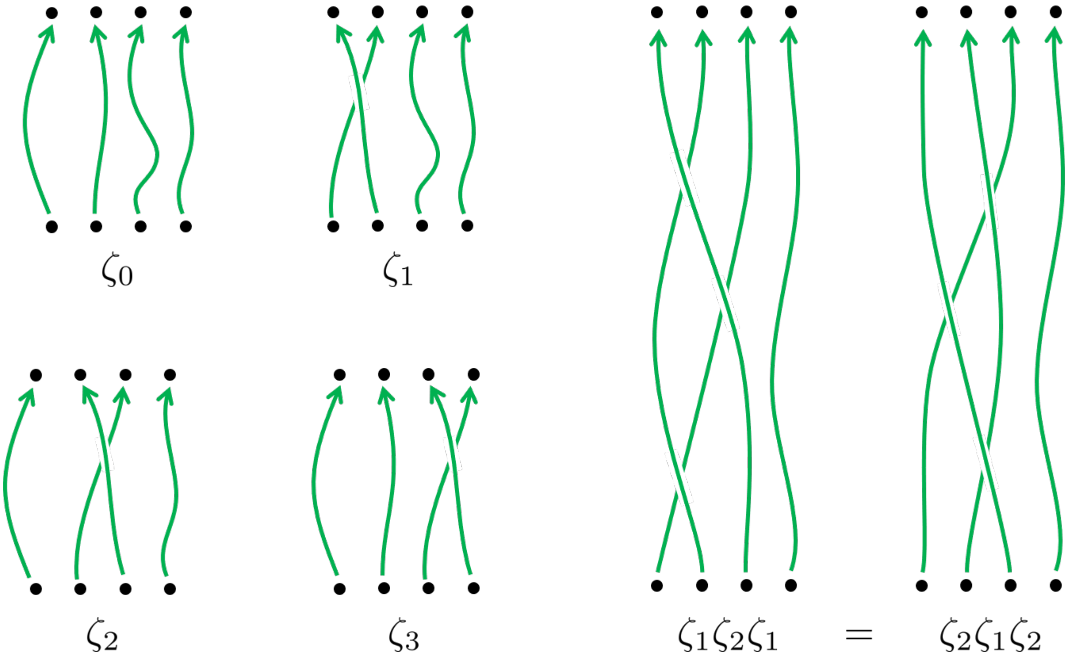

Fig. 4.3 The identity ζ_0 and the three generators ζ_i of the braid group B_4. On the right, the Yang-Baxter relation shown pictorially.

For $d = 2$, closed paths are classified based on the way particles' trajectories interweave with each other in a 3D space-time. If $N = 2$, as we have seen, the classification simply counts how many times the two trajectories twist around each other. In general, equivalence classes of interweavings are called braids. Together with their composition method, they yield the so-called braid group B_N. Counterclockwise exchanges of neighbor[3] particles form the generators ζ_i of this group. Group inversion is given by the clockwise exchange $(\zeta_i)^{-1}$ while the identity, i.e. no exchanges, is denoted by $\zeta_0 = (\zeta_i)(\zeta_i)^{-1}$. There are two defining relations satisfied by the group generators

$$\zeta_i\zeta_j = \zeta_j\zeta_i \qquad \text{for } |i-j| > 1 \tag{4.3}$$

$$\zeta_j\zeta_{j+1}\zeta_j = \zeta_{j+1}\zeta_j\zeta_{j+1} \tag{4.4}$$

which can easily checked pictorially using Fig. 4.3. Eq. (4.3) represent a far-commutativity relation while Eq. (4.4) is known as Yang-Baxter relation. In order to determine the possible behaviors of particles in two spatial dimensions, one has to find the unitary representations of B_N. Focusing at first on 1D representations, it turns out that the situation is the same we encountered for B_2: there is an infinite number of 1D representations which consist in associating the complex phase $e^{i\theta}$ to each generator, with θ arbitrary.

---

[3] Some arbitrary ordering rule has to be defined.

Being $U(1)$ an Abelian group, anyons associated with 1D representations of B_N are called Abelian anyons. Interestingly enough, it is possible to conceive even more exotic particles which behave accordingly to higher dimensional representations of B_N. These particles, whose existence requires that the system exhibits some degeneracy, are called non-Abelian anyons [179, 178]. By braiding two or more of these particles, the quantum state of the systems does not pick only a complex phase but it undergoes a unitary transformation within the degenerate subspace!

4.1.3 Majoranas as an example of non-Abelian anyons

In the previous subsection, we showed that particles in a 2D space can behave not only as fermions or bosons but also as anyons. It is important to stress, however, that a low dimensional confinement is a necessary condition for the existence of anyons but it is clearly not sufficient: for example, the physical degrees of freedom in a standard 2DEG (two-dimensional electron gas) are fermionic!

Remarkably enough, the Majorana modes introduced in the first chapter do behave as non-Abelian anyons. A convenient way to study their exchange statistic, easily generalizable to parafermions, will be discussed in Section 4.2.1. Here, however, we want to present an intuitive argument following Ref. [180]. To this end, let us consider two generic Majorana operators (which might be a_i and/or b_j) and conveniently call them γ_1 and γ_2. As explained in Sec. 1.4.2, they obey the defining properties

$$\gamma_1 = \gamma_1^\dagger \qquad \gamma_2 = \gamma_2^\dagger \tag{4.5}$$

$$\gamma_i^2 = 1 \tag{4.6}$$

$$\{\gamma_1, \gamma_2\} = 0\,. \tag{4.7}$$

Moreover, it is possible to combine them to build a fermionic operator

$$\mathtt{f} = \frac{1}{2}(\gamma_1 + i\gamma_2) \tag{4.8}$$

which clearly satisfy $\{\mathtt{f}^\dagger, \mathtt{f}\} = 1$ and allows to define a fermion number

$$n_{\mathtt{f}} = \mathtt{f}^\dagger \mathtt{f} = \frac{1}{2}(1 + i\gamma_2\gamma_1)\,. \tag{4.9}$$

The goal now is to build a braiding operator $U_{1,2}$ which exchange the two Majoranas. It must obey the following constraints:

- $U_{1,2}\,\gamma_i\,U_{1,2}^{-1}$ must be a Majorana operators, i.e. it must obey properties (4.5), (4.6), and (4.7);

- the fermion parity must be conserved, i.e. $[n_\mathtt{f}, U_{1,2}] = 0$.

As a result, the only possibilities are [180]:

$$U_{1,2}\,\gamma_1\,U_{1,2}^{-1} = \mp\gamma_2 \tag{4.10}$$

$$U_{1,2}\,\gamma_2\,U_{1,2}^{-1} = \pm\gamma_1\,, \tag{4.11}$$

where the freedom in choosing the overall sign stems from the possibility to associate $U_{1,2}$ either with a clockwise or a counterclockwise exchange. The unitary operator which generates this transformation (with $\gamma_1 \mapsto -\gamma_2$ and $\gamma_2 \mapsto \gamma_1$) is

$$U_{1,2} \propto \frac{1}{\sqrt{2}}(1+\gamma_1\gamma_2) = (1-n_\mathtt{f})e^{-i\frac{\pi}{4}} + n_\mathtt{f}\,e^{i\frac{\pi}{4}} \tag{4.12}$$

This operator clearly induces a non-trivial unitary transformation within the subspace spanned by the two eigenstates of $n_\mathtt{f}|n\rangle = n|n\rangle$:

$$U_{1,2}\,(\alpha|0\rangle + \beta|1\rangle) = \left(\alpha e^{-i\frac{\pi}{4}}|0\rangle + \beta e^{i\frac{\pi}{4}}|1\rangle\right). \tag{4.13}$$

It is therefore possible to change the quantum state[4] of a system just by braiding two Majoranas.

Note that, if other Majoranas γ_i are present, the generic braiding operator $U_{i,i+1}$ will satisfy both far commutativity and the Yang-Baxter relation, thus proving to be a legit 2D representation of the braiding group.

At this point, one may wonder how braid can be implemented within a 1D wire. A simple way out is to actually consider a 2D network of wires, whose simplest example is the so-called T-junction [71, 26]. As shown in Fig. 4.4, it is possible to successfully braid the edge modes by locally controlling the parameters in the wires and tuning them either in the trivial or topological phase. Many other protocols have been devised as well [181]. Their experimental implementation, however, represents a formidable ongoing challenge [8, 69, 70, 9].

The last years have been characterized by huge experimental efforts aiming at the observation of anyons, the reason being their twofold importance. In fact, in addition to their intrinsic value in the framework of fundamental physics, non-Abelian anyons also represent an extremely promising platform to perform the so-called topological quantum computation

---

[4] In reality, states like the one considered in Eq. (4.13) are not physical since their fermion parity is not defined. In order to avoid cat states, real implementation of the braiding protocol must consists of at least two couples of Majoranas [10].

Fig. 4.4 Simple braiding scheme for a couple of Majornas by exploiting a T-junction. Majornas are moved by locally tuning the wires either in the topological (dark blue) or trivial (light blue) phase.

(TQC) [10, 180]. The key feature of TQC, i.e. the possibility to minimize decoherence at the hardware level, will be briefly discussed in the following subsection.

4.1.4 Non-Abelian anyons and topological quantum computation

The birth of quantum computation dates back to the ’80s, when people started realizing that a computer able to operate coherently on quantum states can be much more powerful than a standard classical computer [182–185, 10]. Some many-body quantum Hamiltonian, for example, can be simulated exponentially faster on a quantum computer than on a classical one [183]. The interest in quantum computation is not confined within the physicists community: the celebrated Shor quantum algorithm for integer factorization, for instance, is extremely relevant for encryption and cryptography [186].

At the most elementary level, quantum computation consists of three steps: the initialization of the system, its unitary evolution under a Hamiltonian $H(t)$, and the measure of the output. In this sense, the Hamiltonian can be seen as the software program which is run. In complete analogy with a classical computer, a versatile and programmable quantum computer must consist of many small building blocks, which can be accessed and manipulated individually. These fundamental blocks are called qubits[5]: while a classical bit can be either 0 or 1, a qubit is a quantum-mechanical two-state system that can be in any of the infinitely many superpositions $\alpha|0\rangle+\beta|1\rangle$. The state of a n-qubit system is therefore a vector in a 2^n-dimensional Hilbert space. The elementary unitary operations performed on qubits are called quantum gates, in analogy with the logic gates used in classical computation.

The biggest issue in building a working computer is represented by errors, which inevitably happen during any kind of computation. Error correction schemes play therefore a key role, both for classical and quantum computers. In the former case, they’re based on repeatedly checking information against redundant copies of it. In a quantum computer, the task is more complicated. A measurement at some intermediate stage of a calculation, in order to see if some

---

[5] Note that it is also possible to conceive systems based on qudit, i.e. d-state systems with d not too large: this will be the case for parafermions [187].

errors have occurred, would cause the wave function collapse and ruin the whole calculation. Moreover, while in a classical computer errors are represented by discrete bit flip, quantum information is much more fragile and subject to continuous errors (e.g. the change of a phase in a state superposition). Despite this difficulty, many clever error correction schemes have been devised for quantum computers [188]. On a practical way, however, one has to take into account that also these schemes may be noisy, meaning that errors can occur even during error correction [188]. In the end, quantum computation can be performed only if the error rate on single operations is kept extremely low.

From a practical point of view, errors can be roughly divided into two categories [10]:

- errors occurring when qubits are simply storing information (i.e. when they act as a quantum memory);
- errors occurring when qubits are processed with quantum gates (e.g. when a quantum state is rotated by 90.01° instead of 90°).

Interestingly enough, topological quantum computation is protected from errors of both kinds. Let us think, for example, about non-local Majorana qubits. Here the information is stored in couples of topologically protected edge Majoranas modes. Any local perturbation has no nontrivial matrix elements within the ground state subspace, meaning that this kind of quantum memories are rather immune from decoherence. Moreover, protected quantum gates can be build by exploiting the adiabatic braiding of non-Abelian anyons: the outcome of these unitary operation depends only on the topology of the trajectories of the anyons and does not depend on the particular geometry or dynamics.

One of the biggest challenges faced by TQC is to find non-Abelian anyons whose braiding properties are rich enough such that all the necessary quantum gates can be performed by exploiting braiding. Unfortunately, this is not the case of Majoranas-based qubit. They would indeed require a whole set of non-protected gates in order to be able to perform universal quantum computation, i.e. to perform computations which cannot be efficiently simulated also by classical computers [10, 71, 187]. This implies by no means that Majoranas are useless for quantum computation: it is still possible to exploit part of their topological robustness and devise convenient platforms to efficiently implement non-protected gates and error correction schemes [189, 190]. It makes sense, however, to seek for more complicated non-Abelian anyons, with richer braiding properties. The study of parafermions, a generalization of Majoranas, heads in this direction and will constitute the topic of the following sections.

4.2 Parafermions, a generalization of Majoranas

Majoranas are extremely interesting to study and promising for their potential applications. However, as underlined in the previous section, their braiding properties are not complex enough to allow for universal computation. One may therefore wonder if it is possible to conceive other kinds of non-Abelian anyons, which generalize Majoranas and are computationally more powerful. A positive answer is provided by the so-called parafermions which will be the central subject of what follows.

4.2.1 Clock models as a convenient way to generalize Majoranas

A convenient way to generalize Majoranas is to look at first at their spin-model counterpart. It is indeed well known [191, 7, 192, 11] that a Jordan-Wigner transformation allows establishing a mapping between the spinless fermions, which make up the Kitaev chain, and bosonic Ising spins. In particular, by considering the non-local mapping

$$a_j = \left(\prod_{k=1}^{j-1} \sigma_k^x\right) \sigma_j^z \tag{4.14}$$

$$b_j = -i a_j \sigma_j^x = -i \left(\prod_{k=1}^{j-1} \sigma_k^x\right) \sigma_j^z \sigma_j^x \tag{4.15}$$

between Majorana operators a_j and b_j and Pauli matrices on site j, the Kitaev Hamiltonian on a open chain [see Eq. (1.42)] is mapped onto a transverse-field Ising model

$$\begin{aligned} H_K &= -iJ \sum_{j=1}^{L-1} b_j a_{j+1} - if \sum_{j=1}^{L} a_j b_j &(4.16)\\ &= -J \sum_{j=1}^{L-1} \sigma_j^z \sigma_{j+1}^z - f \sum_{j=1}^{L} \sigma_j^x \,. &(4.17)\end{aligned}$$

Before moving on and introducing parafermions, one important remark is in order. Although the two chains clearly share the same spectrum, their topological properties are rather different. This is due to the fact that the mapping in Eq. (4.14) and (4.15) is non-local: operators which are local in terms of Majorana can feature a highly non-local expression in terms of spins and vice-versa. In particular, one can easily show that the non-trivial topological phase of the Kitaev chain ($J > f$) maps to the topologically-trivial ferromagnetic phase of the Ising model. While they both feature an exact two-fold degeneracy at the sweet-spot ($f = 0$ and $J \neq 0$), their properties are indeed different: in the Kitaev chain the degeneracy is protected and due to the presence of dangling Majoranas localized at the two edges of the system; in the Ising chain the degeneracy stems from the spin-flip $\mathbb{Z}_2$ symmetry which is spontaneously broken and it is characterized by a bulk local order parameter, i.e. the magnetization along z, $\langle \sigma_j^z \rangle$.

Although topologically trivial, working with the Ising chain is very convenient when it comes to devise possible generalizations. In particular, a straightforward idea is to replace the two-state Ising spin variables and the $\mathbb{Z}_2$ symmetry of the model with p-state variables and $\mathbb{Z}_p$ symmetry. The subsequent step would be to exploit the generalization of the mapping in Eq. (4.14) and (4.15) in order to go back from the generalized spin-model to a topological model with generalized Majoranas. This procedure has proven effective and the operators which generalize Majoranas, which we are going to call α_j and β_j, are named $\mathbb{Z}_p$ parafermions [11, 193]. Let us now present in detail the procedure we have just sketched. The single-site σ^z operator measures the spin and generalizes to

$$\sigma^z = \begin{pmatrix} 1 & 0 \\ 0 & -1 \end{pmatrix} \quad \Longrightarrow \quad \sigma = \begin{pmatrix} 1 & & & & \\ & \omega & & & \\ & & \omega^2 & & \\ & & & \cdots & \\ & & & & \omega^{p-1} \end{pmatrix} \tag{4.18}$$

with $\omega = e^{i\frac{2\pi}{p}}$. Along the same lines, the single-site operator σ^x, which cycles the spin, generalizes to the "shift" operator

$$\sigma^x = \begin{pmatrix} 0 & 1 \\ 1 & 0 \end{pmatrix} \quad \Longrightarrow \quad \tau = \begin{pmatrix} 0 & 0 & 0 & \dots & 1 \\ 1 & 0 & 0 & \dots & 0 \\ 0 & 1 & 0 & \dots & 0 \\ \dots & \dots & \dots & \dots & 0 \\ 0 & 0 & 0 & 1 & 0 \end{pmatrix} . \tag{4.19}$$

These operators obey the on-site algebra

$$\sigma_j^p = \tau_j^p = 1 \,, \qquad \sigma_j \tau_j = \omega \tau_j \sigma_j \tag{4.20}$$

and commutes on different sites, e.g. $\sigma_j \tau_k = \tau_k \sigma_j$ for $j \neq k$. The generalization of the transverse-field Ising model

$$H_{\text{CM}} = -J \sum_{j=1}^{L-1} \left(e^{i\phi} \sigma_{j+1}^\dagger \sigma_j + H.c. \right) - f \sum_{j=1}^{L} \left(e^{i\theta} \tau_j^\dagger + H.c. \right) \tag{4.21}$$

is known as Clock model.

The $\mathbb{Z}_2$ spin-filp symmetry featured by the Ising model is promoted here to a $\mathbb{Z}_p$ symmetry. The presence of parameters ϕ and θ make the phase diagram of the model more complicated than the simple one of the Ising model [11, 194, 195]. In the following, however, we will mainly focus on the simple case $\phi = \theta = 0$ known as the p-state Potts model [196]. It exhibits a self-dual critical phase transition at $J = f$, separating ordered ($J > f$) and disordered ($f > J$) phases. At the sweet-spot $f = 0$, the Pott model features a p-fold degeneracy throughout all the spectrum, which indicates the spontaneously breaking of the $\mathbb{Z}_p$ symmetry. Each ground state can be identified by the local order parameter $\langle \sigma_j \rangle$, which generalize the magnetization of the Ising model.

We are now in a position to implement the generalization of the mapping in Eq. (4.14) and (4.15), rewriting the Hamiltonian in terms of parafermions [193]

$$\alpha_j = \left(\prod_{k=1}^{j-1} \tau_k \right) \sigma_j \tag{4.22}$$

$$\beta_j = \iota \, \alpha_j \tau_j = \iota \left(\prod_{k=1}^{j-1} \tau_k \right) \sigma_j \tau_j \tag{4.23}$$

Where $\iota = e^{-i\pi/p}(-1)^p$. These operators obey the parafermionic algebra

$$\alpha_j^p = \beta_j^p = 1 \qquad \alpha_j \beta_k = \omega \beta_k \alpha_j \quad (\text{with } k \geq j) \tag{4.24}$$

$$\alpha_j^\dagger \alpha_j = \beta_j^\dagger \beta_j = 1 \tag{4.25}$$

The Potts model Hamiltoinan thus becomes

$$H = -J \sum_{j=1}^{L-1} \left(\iota^* \beta_j \alpha_{j+1}^\dagger + H.c. \right) - f \sum_{j=1}^{L} \left(\iota^* \alpha_j \beta_j^\dagger + H.c. \right) . \tag{4.26}$$

This model looks like a direct generalization of the Kitaev chain and features similar characteristics. In particular, at the sweet spot $f = 0$ and $J \neq 0$ there are two dangling parafermions α_1 and β_L which commute with the Hamiltonian. Remarkably, they do not commute with the $\mathbb{Z}_p$ symmetry of the Hamiltonian and are therefore responsible for a p-fold degeneracy throughout all the spectrum. Operators α_1 and β_L are therefore topologically protected zero-energy edge modes.

Braiding of $\mathbb{Z}_p$ parafermions

Now that $\mathbb{Z}_p$ parafermions have been introduced, one can study their braiding properties in order to highlight their advantages over Majoranas (which can be thought as $\mathbb{Z}_2$ parafermions). To this end, one has to identify which representations of the braid group are compatible with parafermions' algebra. We consider a chain of $2L$ uncoupled parafermions $(\alpha_1, \beta_1, \alpha_2, \ldots, \beta_L)$ and seek for the set of unitary operations which can be performed by braiding them. It turns out to be convenient to relabel the parafermion operators as

$$\begin{aligned} \alpha_j &= \gamma_{2j-1} \\ \beta_j &= \gamma_{2j} \end{aligned} \tag{4.27}$$

This allow to readily define the so-called parity operators as

$$\Gamma_j = \omega^{\frac{p+1}{2}} \gamma_j \gamma_{j+1}^\dagger \,. \tag{4.28}$$

and prove that they obey [187]

$$\Gamma_j^p = 1 \tag{4.29}$$
$$\left[\Gamma_j, \Gamma_k\right] = 0 \qquad \text{if } |j-k| > 1 \tag{4.30}$$
$$\Gamma_j \Gamma_k = \omega^{\operatorname{sgn}(k-j)} \Gamma_k \Gamma_j \qquad \text{if } |j-k| = 1 \,. \tag{4.31}$$

These operators clearly satisfy far-commutativity (see Eq. (4.3)) and therefore represent the building blocks of the unitary representation U_j of the braid group generators which exchange γ_j and γ_{j+1}. In particular one has

$$U_j = \frac{1}{\sqrt{p}} \sum_{m \in \mathbb{Z}_p} c_m \, \Gamma_j^m \,. \tag{4.32}$$

Note that the overall parity is conserved by these braid operators as expected

$$[U_j, \sum_{k=1}^{L} \Gamma_{2k}] = 0 \qquad \forall j \tag{4.33}$$

Constraints on the coefficients c_m are imposed by requiring unitarity $U_j U_j^\dagger = 1$ and the Yang-Baxter relation (see Eq. (4.4)). A family of $2p$ solutions for arbitrary p can be found [187]

$$c_m = \omega^{\pm \frac{m(m+2r+p)}{2}} \,, \tag{4.34}$$

with $r \in \mathbb{Z}_p$. The presence of $\pm$ simply stems from the fact that we are free to associate U_j either to clockwise or anti-clockwise exchanges. It is instructive to check that for Majoranas ($p = 2$) one get $c_0 = 1$, $c_1 = \pm i$, consistently with Eq. (4.12).

While being computationally way more powerful with respect to Majoranas (especially when p is an odd prime number), one can show that $\mathbb{Z}_p$ are still not enough to perform universal quantum computation [187]. It is worth noting, however, that it is possible to generate even more exotic kinds of anyons by letting $\mathbb{Z}_p$ parafermions interact with each other: a 2D lattice of $\mathbb{Z}_3$ parafermion, for example, can give rise to the so-called “Fibonacci” anyons which are eventually capable of universal topologically quantum computation [194, 197].

4.2.2 Proposed system which could host parafermions

The richer braiding properties of parafermions come with an obvious drawback: their greater complexity makes it harder to find physical systems which can actually host parafermions. In view of their commutation relation (4.24), for instance, it is likely that strongly correlated systems with non-trivial emergent degrees of freedom are needed. Moreover, it has been shown in Ref. [198, 199] that is not possible to have parafermions which are fully topologically protected in strictly 1D systems.

In spite of these difficulties, there are several proposals of systems which can host zero-energy modes obeying parafermionic algebra. While a precise and detailed description of the different setups is beyond the scope of the present subsection, it is useful to provide a list of the main ideas which have been put forward.

- Several proposals are based on 2DTI-superconductor hybrid structures [200–202]. Here $\mathbb{Z}_4$ parafermions emerge as a result of the interplay between two gapping mechanisms of the helical QSH edge states. One is provided by the proximity-induced superconductivity, the second is actually what differentiates the various proposals: in Ref. [200], they consider two-particle Umklapp backscattering within a single helical edge state; in Ref. [201] the gap is opened thanks to a spin impurity coupled with the helical edge; in [202], they considered two-particle scattering processes between two helical edge states brought close together by an extended constriction of the QSH bar. In all these proposals, the presence of electron-electron interaction is a crucial ingredient.

- Other proposals rely on interacting 1D quantum wires [203–205]. In Ref. [204], for example, two strongly interacting Rashba wires are coupled with a conventional s-wave superconductor: here $\mathbb{Z}_3$ parafermions appear at the wires’ ends because of the interplay between two types of induced superconductive pairing, intrawire and interwire. Note that (strong) electron-electron interaction is necessary also for this kind of proposals.

- Another important class of proposals is based on hybrid system consisting of fractional quantum Hall bars (which also feature 1D edge states) coupled with superconductors. The main difference with respect to the other proposals is that, here, the 1D edge channels are intrinsically embedded into a 2D environment, consisting of a strongly interacting quantum liquid. Depending on the filling factor of the fractional quantum Hall bar, different kind of parafermions can arise. For example, $\mathbb{Z}_{2m}$ parafermions are considered in [181, 206], while $\mathbb{Z}_3$ parafermion arise in Ref. [207].

Although useful and interesting, these approaches all rely on effective low-energy field theories. Therefore one may wonder if it is possible to find an exact mapping between chains of $\mathbb{Z}_p$ parafermions and fermions on a lattice. This would allow studying exact microscopic fermionic models, discussing how the peculiar features of parafermions arise there and highlighting the difference with the approaches based on bosonization. Moreover, a fermionic model which generalize the Kitaev chain may be the starting point for studying parafermion-related physics with cold-atoms setup. The existence and the properties of an exact mapping between parafermions and fermions will be the central topic of the following section, which constitutes the original content of this chapter.

4.3 Parafermions in 1D fermionic lattices

In this section, we will present our results, published in Ref. [16][6]. The starting point of the analysis is a one-dimensional open chain of $\mathbb{Z}_4$-parafermions. At each site $i \in \{1,\dots,L\}$, there are two parafermionic operators α_i and β_i which obey the defining properties in Eq. (4.24) and (4.25).

4.3.1 From Fock parafermions to fermions

To relate these operators to physical electrons, we study how they act on the states of the system. The fact that $\alpha_i^4 = 1 = \beta_i^4$ implies that each lattice site can be associated with four different states, and that the application of the operators α_i and β_i cycles through those states. This notion can be made more precise by associating a Fock space to the parafermionic operators via the introduction of "Fock parafermions" (FPF) [210]. The latter are described by creation ($d_j^\dagger$) and annihilation (d_j) operators, which allow us to express α_i and β_i as

$$\alpha_j = d_j + d_j^{\dagger 3}, \quad \beta_j = e^{i\pi/4}(d_j i^{N_j} + d_j^{\dagger 3}), \tag{4.35}$$

---

[6] Note that a similar topic has been discussed also by two contemporary papers, in Ref. [208, 209]: the findings discussed in these references are consistent with our results where they overlap.

where

$$N_j = \sum_{m=0}^{3} d_j^{\dagger m} d_j^m \tag{4.36}$$

is the number operator for FPF whose four integer eigenvalues run from 0 to 3. These relations show that both α_j and β_j reduce the number of FPFs on site j by one modulo 4. The parafermionic algebra of α_i and β_i is handed down to the FPFs in their commutations relations,

$$d_l d_j = i\, d_j d_l, \quad d_l^\dagger d_j = -i\, d_j d_l^\dagger \quad \text{for } l < j, \tag{4.37}$$

$$d_j^{\dagger m} d_j^m + d_j^{\dagger(4-m)} d_j^{4-m} = 1 \quad \text{for } m = 1,2,3. \tag{4.38}$$

Moreover, on a given site $d_j^4 = 0$. The key idea of our mapping to electrons is to identify the four-dimensional parafermionic Fock space with the Fock space of spin-$1/2$ fermions.

As a first step, we focus on a single site with FPF annihilation operator d and fermionic operators $c_{\uparrow,\downarrow}$. Denoting the FPF basis by

$$\{|0\rangle, |1\rangle, |2\rangle, |3\rangle\}, \tag{4.39}$$

where $|n\rangle$ are the eigenstates of the FPF number operator N with eigenvalue n, we can for instance identify these states with the fermionic basis

$$\left\{|E\rangle,\ c_\uparrow^\dagger|E\rangle,\ ic_\uparrow^\dagger c_\downarrow^\dagger|E\rangle,\ -ic_\downarrow^\dagger|E\rangle\right\}, \tag{4.40}$$

where $|E\rangle$ denotes the vacuum state, $c_\sigma|E\rangle = 0$. For this choice of basis, one finds the representation (see Appendix D)

$$d = c_\downarrow^\dagger c_\uparrow c_\downarrow - c_\uparrow^\dagger c_\downarrow^\dagger c_\downarrow + ic_\uparrow^\dagger c_\uparrow c_\downarrow + c_\uparrow, \tag{4.41}$$

which automatically satisfies the algebra of Eq. (D.2). Clearly, different choices of the fermionic basis (D.4) lead to different expressions for d. The mapping (4.41), however, is particularly useful because d has a well-defined fermionic parity. This will simplify the extension of the mapping from a single site to a chain, to which we turn now.

The well-known Jordan-Wigner transformation maps spin-$1/2$ chains to fermionic chains by the introduction of string factors. A similar technique can be employed to map parafermionic chains to electronic chains, e.g., by defining

$$d_j = i^{\sum_{p<j}\left(N_p + 2n_{p\uparrow} + 2n_{p\downarrow}\right)} \left(c_{j\uparrow} - c_{j\uparrow}n_{j\downarrow} - c_{j\uparrow}^\dagger n_{j\downarrow} + ic_{j\downarrow}n_{j\uparrow}\right) \tag{4.42}$$

where $n_{j\sigma} = c^\dagger_{j\sigma} c_{j\sigma}$. The FPF number operator has the fermionic representation

$$N_p = n_{p\uparrow} - 2n_{p\uparrow} n_{p\downarrow} + 3n_{p\downarrow} \,. \tag{4.43}$$

The string factor cancels the fermionic anticommutation factors of $-1 = i^2$ while adding the factors of $\pm i$ required for parafermions. The fact that d_j has odd fermion parity ensures that every parafermionic operator conserving the number of FPFs modulo 4 is transformed into a fermionic operator *without* string factors. To see this, consider a generic operator D which involves FPF operators on m adjacent lattice sites

$$D = d_j^{\dagger\alpha_0} d_j^{\beta_0} \;\dots\; d_{j+m}^{\dagger\alpha_m} d_{j+m}^{\beta_m}. \tag{4.44}$$

where $\alpha_k, \beta_k \in \{0,1,2,3\}$. Its fermionic expression factorizes into a form

$$D = i^{\sum_{p<j} \left[\sum_{i=0}^{m} (\beta_i - \alpha_i)\right] \left(N_p + 2n_{p\uparrow} + 2n_{p\downarrow}\right)} \, C$$

with an operator C containing, up to prefactors, only fermion operators on sites $j, \dots, j+m$. Requiring that D conserves the total number of FPFs modulo 4 then implies

$$\sum_{i=0}^{m} (\beta_i - \alpha_i) = 0 \;(\mathrm{mod}\; 4) \,,$$

so the string factor cancels. This remarkable result is at the heart of the locality of our mapping between parafermion chain Hamiltonians and electronic systems.

4.3.2 Mapping of the Hamiltonian

In the remainder of the chapter, we will focus on the $\mathbb{Z}_4$-parafermionic Hamiltonian at the topological sweet spot

$$\begin{aligned} H_J &= -J \sum_{j=1}^{L-1} e^{i\frac{\pi}{4}} \; \beta_j \alpha^\dagger_{j+1} \; + \mathrm{h.c.} \\ &= -J \sum_{j=1}^{L-1} i \left(d_j d^3_{j+1} i^{N_j} + d_j^{\dagger 3} d^3_{j+1} + d_j d^\dagger_{j+1} i^{N_j} + d_j^{\dagger 3} d^\dagger_{j+1} \right) + \mathrm{h.c.} \end{aligned} \tag{4.45}$$

defined on a L-site open chain. This Hamiltonian can be readily obtained from the Pott model in Eq. (4.26) by considering $f = 0$. It features two dangling parafermions, α_1 and β_L, which commute with the Hamiltonian and induce an exact and topologically protected 4-fold degeneracy throughout the entire spectrum. The $\mathbb{Z}_4$ symmetry $\mathcal{Z}$ featured by this Hamiltonian is clearly associate with the conservation of the total number of FPFs modulo 4

$$\mathcal{Z} = i^{\sum_j N_j} . \tag{4.46}$$

The mapping (4.42) allows us to translate the Hamiltonian (4.45) to a local fermionic Hamiltonian

$$H_J = H^{(2)} + H^{(4)} + H^{(6)}, \tag{4.47}$$

with

$$H^{(2)} = -J \sum_{\sigma,j} \left[c^{\dagger}_{\sigma,j} c_{\sigma,j+1} - i\, c^{\dagger}_{-\sigma,j} c^{\dagger}_{\sigma,j+1} \right] + h.c., \tag{4.48}$$

$$\begin{aligned} H^{(4)} = -J \sum_{\sigma,j} \Big[& c^{\dagger}_{\sigma,j} c_{\sigma,j+1} \left(-n_{-\sigma,j} - n_{-\sigma,j+1} \right) + c^{\dagger}_{\sigma,j} c_{-\sigma,j+1}\, i \left(n_{-\sigma,j} + n_{\sigma,j+1} \right) \\ & + c^{\dagger}_{-\sigma,j} c^{\dagger}_{\sigma,j+1}\, i \left(n_{\sigma,j} + n_{-\sigma,j+1} \right) + c^{\dagger}_{\sigma,j} c^{\dagger}_{\sigma,j+1} \left(n_{-\sigma,j} - n_{-\sigma,j+1} \right) \Big] + h.c., \end{aligned} \tag{4.49}$$

$$H^{(6)} = -J \sum_{j} \left[-2i\, c^{\dagger}_{\sigma,j} c_{-\sigma,j+1} \left(n_{-\sigma,j} n_{\sigma,j+1} \right) - 2i\, c^{\dagger}_{-\sigma,j} c^{\dagger}_{\sigma,j+1} \left(n_{\sigma,j} n_{-\sigma,j+1} \right) \right] + h.c.. \tag{4.50}$$

In the fermionic language, H_J consists of superconducting pairing and hopping terms with and without spin-flip, locally weighted by the fermion occupation numbers on the lattice sites. Note that the Hamiltonian H_J is time-reversal invariant.

The mapping we have developed allows to express parafermionic operators in terms of electrons. The zero-energy parafermionic modes, in particular, have the following fermionic expression:

$$\begin{aligned} \alpha_1 &= i c_{1\downarrow} n_{1\uparrow} - c^{\dagger}_{1\uparrow} n_{1\downarrow} + c_{1\uparrow}(1 - n_{1\downarrow}) + i c^{\dagger}_{1\downarrow}(1 - n_{1\uparrow}) \\ \beta_L &= e^{i\pi/4} \, (-i)^{\sum_{j=1}^{L-1} N_j} \left[i c^{\dagger}_{L\uparrow} n_{L\downarrow} + i c_{L\uparrow}(1 - n_{L\downarrow}) - i c^{\dagger}_{L\downarrow}(1 - n_{L\uparrow}) - i c_{L\downarrow} n_{L\uparrow} \right]. \end{aligned} \tag{4.51}$$

These equations represent an important result, namely the explicit expression of combinations of fermionic operators that satisfy the parafermionic algebra and that commute with the fermionic Hamiltonian H_J.

An important question concerns the locality and topological protection of the zero-energy states of the fermionic Hamiltonian. Although α_1 and β_L are localized at the edge in the parafermionic language, one of the corresponding fermionized operators (in our case β_L) inevitably contains a non-local string factor. This string factor is not associated with a density of states (see below), but allows the edge mode to "feel" what happens in the bulk. The non-locality hence challenges the *topological* protection of the fourfold ground state degeneracy in the fermionic model. As we will discuss in the next section, it indeed turns out that only a twofold degeneracy is topologically protected. Remarkably, the non-locality of β_L does not prevent us from finding local operators on either edge of the fermionic chain that cycle through the four degenerate ground states (see Appendix E).

4.3.3 Topological properties of the fermionic chain

In the parafermionic language, the model in Eq. (4.45) represents a topological phase [11, 211, 194] in which the spectrum exhibits a topologically protected fourfold degeneracy that cannot be lifted by local parafermionic perturbations. It is natural to ask if the same holds also for the corresponding fermionic chain, since it is well known that the presence of string factors can change the topological properties of the system. It is the case of the Kitaev chain and the Ising model discussed in section 4.2.1.

In this respect, it is instructive to study the symmetries featured by the fermionic model in Eq. (4.48-4.50). The $\mathbb{Z}_4$ symmetry of the parafermionic Hamiltonian in Eq. (4.45) can be expressed in terms of fermions as $\mathcal{Z} = i^{\sum_j [(n_{j\uparrow}+n_{j\downarrow})^2+2n_{j\downarrow}]}$. Its square corresponds to the usual $\mathbb{Z}_2$ fermion parity $\mathcal{P} = \mathcal{Z}^2 = (-1)^{\sum_j (n_{j\uparrow}+n_{j\downarrow})}$. Interestingly, the local operator $M_j = i\gamma_{\uparrow,j}\gamma_{\downarrow,j}$, where $\gamma_{\sigma,j} = c^\dagger_{\sigma,j} + c_{\sigma,j}$ are Majorana operators, commutes with the Hamiltonian but anticommutes with the $\mathbb{Z}_4$ symmetry $\{M_j, \mathcal{Z}\} = 0$. It can be therefore identified as a $\mathbb{Z}_2$ local order operator, associated with the $\mathbb{Z}_2$ symmetry $\mathcal{S}_B = e^{-i\frac{\pi}{4}} 2^{-\frac{1}{2}}\ \mathcal{Z} + h.c.$ which is spontaneously broken and satisfies $[\mathcal{S}_B, H_J] = \{\mathcal{S}_B, M_j\} = 0$. This local order parameter thus differentiates the four degenerate ground states into two pairs and the degeneracy between them can be split by a local perturbation containing any of the M_j. A concrete example of such a perturbation is a magnetic field along the y axis

$$H_y = B_y \sum_{i=1}^{L} i\left(c^\dagger_{j,\uparrow} c_{j,\downarrow} - c^\dagger_{j,\downarrow} c_{j,\uparrow}\right) = B_y \sum_{i=1}^{L} \tfrac{1}{2}\left(M_j + i\eta_{\uparrow,j}\eta_{\downarrow,j}\right) \tag{4.52}$$

where $\eta_{\sigma,j} = i(c^\dagger_{\sigma,j} - c_{\sigma,j})$ are the other Majorana operators. Our DMRG simulations indeed confirm that even a small field B_y reduces the fourfold degeneracy to a doublet of twofold (almost) degenerate states, with an energy difference which scales linearly with the system size L, as showed in Appendix E.

On the other hand, the fourfold degeneracy is protected against other local perturbations, including in particular a magnetic field in the (x,z)-plane or a chemical potential: our DMRG calculations indicate that the lifting induced by these perturbations is exponentially suppressed in the system length, see Appenidx E. The protection of the degeneracy against some of these perturbations becomes apparent in the parafermionic language. Both the chemical potential and the magnetic field along the z axis conserve the total number of FPF modulo 4 and they thus feature a local expression also in terms of parafermions.Our findings are consistent with the results of Ref. [198, 199, 212] in that the fully topologically protected part of the degeneracy (the part that cannot be lifted by symmetry-breaking local perturbations) is only twofold.

4.3.4 Phase diagram

Being an exactly solvable model, H_J allowed us to derive important analytical results such as the existence of the local order parameter M_j and the expression of the zero-energy parafermions in Eq. (4.51). The price we payed for this exact solvability is the rather complicated form of H_J in the fermionic basis, which in particular includes three-body interactions. Instead of searching for fine-tuned models that might realize Eq. (4.48-4.50), we view this model as one representative of a much larger class of systems realizing parafermionic physics at low energies. In this spirit, the specific model H_J is not only crucial in that it allows us to fully understand the physics beyond any low-energy approximations, but also as a controlled starting point around which we now explore topologically equivalent models by smooth deformations of the Hamiltonian. As long as the gap is not closed, the system remains in the same topological phase and will feature the same topological properties. In particular, we consider the much more generic Hamiltonian

$$\bar{H}(U,V) = H^{(2)} + U\left[V\left(H^{(4)} + H^{(6)}\right) + (1-V)\bar{H}^{(4)}\right] \tag{4.53}$$

where the parameter U weights all interacting terms and V allows to smoothly transform the three-body terms into simpler two-body terms with

$$\begin{aligned}\bar{H}^{(4)} = -J\sum_{\sigma,j}\Big[& c^{\dagger}_{\sigma,j}c_{\sigma,j+1}\left(-n_{-\sigma,j} - n_{-\sigma,j+1}\right)\\ &+ c^{\dagger}_{\sigma,j}c^{\dagger}_{\sigma,j+1}\left(n_{-\sigma,j} - n_{-\sigma,j+1}\right)\Big] + h.c.\end{aligned} \tag{4.54}$$

DMRG simulations on a chain with 16 sites reveal a gap closure in the region $U \sim 0.5-0.7$, see Fig. 4.5. This defines two different phases: a “strongly interacting” (SI) one on the right and a “weakly interacting” (WI) one on the left. The original Hamiltonian H_J [triangle in Fig. 4.5] belongs to the SI phase and can be continuously deformed into $H_A = \bar{H}(1,0)$ [square] – an Hamiltonian in the $\mathbb{Z}_4$ parafermionic phase *without* three-body interactions. Note that, away from the exactly solvable point H_J, Hamiltonians $\bar{H}$ in the SI phase feature an exact four-fold degeneracy (through out all the spectrum) only in the $L \to \infty$ limit.

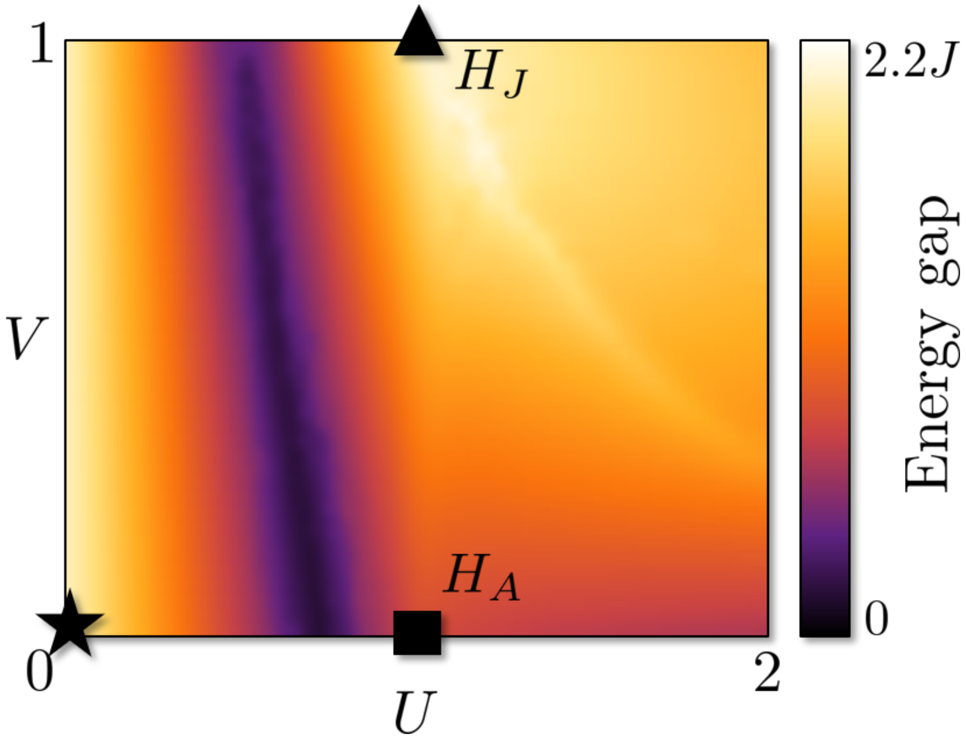

Fig. 4.5 Energy gap [units J] of $\bar{H}(U,V)$ as a function of U and V. Triangle, square and star correspond to H_J, H_A and $H^{(2)}$ respectively. DMRG simulations on 16 sites.

Our numerics thus show that parafermionic physics can already be generated from occupation-dependent hopping and pairing terms. Experimentally, such conditional terms can be realized if, e.g., the hopping involves intermediate virtual states whose energies are tuned by the interaction. Somewhat simpler density-dependent hoppings have already been engineered in cold-atomic systems [213–215]. On more general grounds, however, any not strictly local interaction gives rise to occupation-dependent hoppings and pairings [216–218]. It would be most desirable to identify (quasi-)one-dimensional systems in which these occupation-dependent terms are of appreciable size – a challenging goal for future research that will also benefit from investigating the stability of the parafermionic phase under further modifications of the Hamiltonian.

4.3.5 Fermionic spectral function

In analogy with what we have discussed for the Kitaev chain (see section 1.4.2), a crucial (albeit not conclusive) signature of topological phases is the appearance of a zero-energy density of states at the ends of the topological chain. In general, the spin-averaged fermionic local spectral

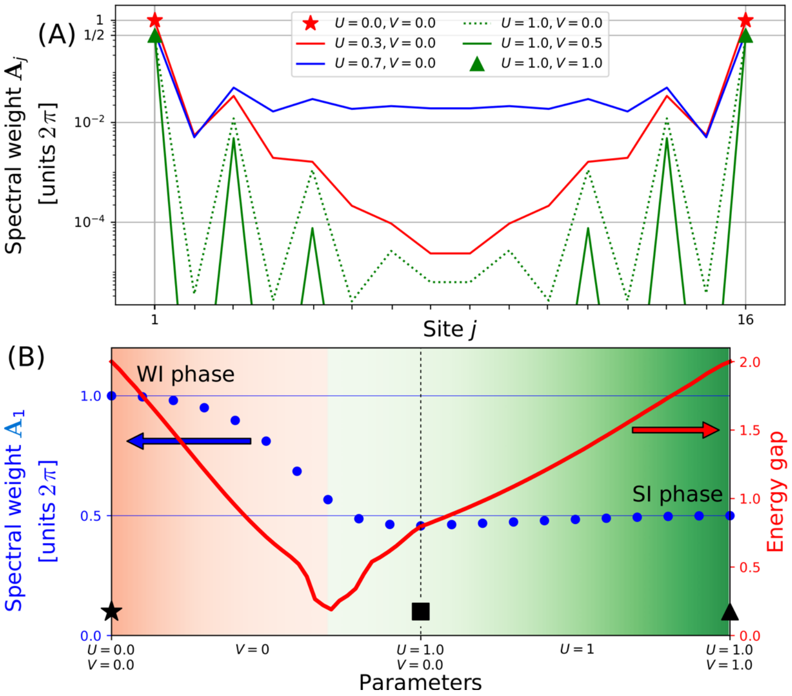

Fig. 4.6 (A): $\mathbf{A}_j$ for different points in the (U,V) parameter space. Green plots feature a dependence on the parity of the site j. (B): $\mathbf{A}_1$ (blue dots) along the straight paths in parameter space connecting $H^{(2)}$ [star], H_A [square] and H_J [triangle]. The energy gap [units J] is shown in red to help identifying the phase transition (here around $U \sim 0.7$) between the WI phase (red fade) and the SI one (green fade). DMRG simulations on 16 sites.

function at zero temperature reads

$$\begin{aligned}\mathcal{A}_j(\omega) = 2\pi \sum_{\sigma,|\varphi\rangle} \Big[& \delta(\omega - E_\varphi + E_{\mathrm{GS}})\, |\langle\varphi|c^\dagger_{j\sigma}|\mathrm{GS}\rangle|^2 \\ & + \delta(\omega + E_\varphi - E_{\mathrm{GS}})\, \left|\langle\varphi|c_{j\sigma}|\mathrm{GS}\rangle\right|^2 \Big]\end{aligned} \tag{4.55}$$

where $|\varphi\rangle$ are the eigenstates of the Hamiltonian with energies E_φ and $|\mathrm{GS}\rangle$ is the ground state the system is in[7].

At first, we focus on the exactly solvable Hamiltonian H_J. Denoting its four ground states with fixed FPF number m (modulo 4) by $|\psi_m\rangle$, one has that (see appendix E)

$$\sum_m |\langle\psi_m|c_{j\sigma}|\psi_l\rangle|^2 = \left(\delta_{j,1} + \delta_{j,L}\right)\frac{1}{8} \qquad [H = H_J] \tag{4.56}$$

---

[7] For the numerical computation of the spectral function in presence of degeneracy, we select the ground state with odd fermion parity and with the lower expectation value of M_1. Different choices would not have modified the results we presented though.

for $l \in \{0,1,2,3\}$ and $\sigma = \uparrow,\downarrow$. The same holds true for the creation operators. Focusing on energies below the gap, this immediately leads to a zero-energy peak $\mathcal{A}_{1,L}(\omega) = \pi\delta(\omega)$ localized at the edges and to a vanishing spectral weight in the bulk, $\mathcal{A}_j(\omega) = 0$ for $j \in \{2,\dots,L-1\}$. This result is confirmed by DMRG simulations which also allowed us to move away from the exactly solvable point. In particular, in Fig. 4.6 we plot the spin-averaged spectral function integrated over the energy gap (EG) $\mathbf{A}_j = \int_{EG} \mathcal{A}_j(\omega)\, d\omega$ for different Hamiltonians. Interestingly, the spectral weight is robust with respect to variations of the parameters U and V as long as the system remains in the SI phase. The fermionic edge density of state remains indeed trapped at the edges and features only an exponentially suppressed leakage into the bulk. This is clearly displayed in Fig. 4.6 A. Note that the spectral weight within the gap has proven to be robust also with respect to other kind of small perturbations such as magnetic fields (along *every* direction) and chemical potential.

Fig. 4.5 shows that a pronounced reduction of the interaction strength U eventually leads to a phase transition, located where the gap closes (in a finite system the gap reaches a minimum but remains finite). At this point the low-energy spectral weight is spread all over the chain, as testified by the blue plot in Fig. 4.6 A computed for $U = 0.7$ and $V = 0$. Once the system enters the WI phase, the spectral weight localizes again at the edges but with an important difference: as clearly shown in Fig. 4.6 B, the low-energy spectral weight in the WI phase is twice the one in the SI one. The reason is that the WI phase features two couples of zero-energy Majoranas instead of a single pair of parafermions. The non-interacting and exactly solvable Hamiltonian $H^{(2)}$ [red star in Fig. 4.5], which belongs to the WI phase, can indeed be expressed as two decoupled Kitaev chains with 4 dangling edge Majoranas:

$$H^{(2)} = -Ji \sum_{j=1}^{L-1} \left[\tau_{\downarrow,j}\, \chi_{\downarrow,j+1} + \tau_{\uparrow,j}\, \chi_{\uparrow,j+1} \right] \tag{4.57}$$

where $\tau_{\sigma,j} = (\gamma_{-\sigma,j} + \eta_{\sigma,j})/\sqrt{2}$ and $\chi_{\sigma,j} = (\gamma_{\sigma,j} - \eta_{-\sigma,j})/\sqrt{2}$. Moreover, it is possible to show that the four ground states of $H^{(2)}$ satisfy (see Appendix E)

$$\sum_m |\langle \phi_m | c_{j\sigma} | \phi_l \rangle|^2 = \left(\delta_{j,1} + \delta_{j,L} \right) \frac{1}{4} \qquad [H = H^{(2)}], \tag{4.58}$$

for $l \in \{0,1,2,3\}$ and $\sigma = \uparrow,\downarrow$. The same holds true for the creation operator. This leads to a peak $\mathcal{A}_{1,L}(\omega) = 2\pi\delta(\omega)$ whose weight is exactly twice the one found in the SI phase.

The zero-energy peak in the local spectral function, localized at the edges and with weight π in a system with a time-reversal symmetric Hamiltonian provides therefore a robust signature of the SI phase and allows to distinguish between the presence of its $\mathbb{Z}_4$ parafermionic modes and the two couples of Majoranas featured by the WI phase. The existence of the phase transition between SI and WI underlines once more that inter-particle interactions play a crucial role for the emergence of zero-energy parafermions, as discussed also in Ref. [205, 203, 204, 201].

Conclusions and outlook

In this thesis, we have explored the interplay between topology and interaction effects in 1D systems, from two different perspectives. In Chapter 3, we studied how a single-electron injection is affected by the presence of electron-electron interactions between the topological 1D edge channels in IQH and QSH effects. In Chapter 4 we studied the properties of the zero modes which arise in a topological interacting fermionic chain, obtained from a $\mathbb{Z}_4$ parafermion Hamiltonian via an exact mapping.

Summary of the main results on the "time-dependent evolution of interacting systems" [Chapter 3]

The injection of a single electron into an interacting 1D system is one of the building blocks of EQO and it has been already studied in the context of a couple of *co-propagating* 1D channels. In this thesis, we carefully analyzed the characteristics of the two fractional excitations, created by interactions, after a single-electron injection into the right-moving channel of a *counter-propagating* system. Such a process can be engineered in EQO setups based on either IQH or QSH bars. By using the LL model, we analytically studied the charge, momentum and energy properties of the fractional excitations, obtaining the main results summarized below.

- Because of the electron-electron interactions, the charge and the energy of the injected electron fractionalize between the two counterpropagating excitations. The charge fractionalization ratio depends only on the interaction strength while the energy partitioning ratio is strongly affected by other parameters as well: the width of the tunneling region, the energy and the momentum of the injected electron. Charge and energy flows are therefore decoupled and could be tuned separately.
- Real-space study in the local injection limit showed that the two fractional excitations have mirror-shaped charge and density profiles. Important additional insights on their properties is provided by the study of their momentum and energy distributions. The former clearly shows that the injected electron loses its single-particle nature by creating many particle-hole pairs. Interestingly, these are mostly excited within the channel not

directly tunnel-coupled to the single-electron source. The creation of particle-hole pairs is clearly associated with an energy relaxation process. The energy distribution of the system features indeed a Lorentzian-shaped peak around the injection energy which is lowered by the interactions while a relaxation tail appears between the peak and the Fermi energy.

As an aside, we also showed that similar techniques can be used to study the time-resolved dynamics of a LL brought out-of-equilibrium by a quantum quench of the interaction strength. Remarkably, we analytically identified and explained the emergence of a peculiar relaxation behavior. with the following characteristics.

- In the long-time limit, the non-equilibrium spectral function of the quenched system relaxes towards a steady value following a universal power law decay $\propto t^{-2}$. This exponent is independent of the initial and final interaction strengths. This can be seen as a robust signature of the quench-induced entanglement between counterpropagating bosonic fields.
- This universal power law decay is robust with respect to finite temperature effects, which actually greatly enhance its visibility by killing other non-universal contributions. This is quite remarkable since usually all the power law behaviors appearing in fermionic correlators are eventually destroyed by finite temperature effects.

Summary of the main results of the "fermionization of parafermions" [Chapter 4]

Parafermions are non-Abelian anyons which intriguingly generalize Majoranas and are extremely relevant for TQC. Majorana zero modes nicely appear at the edge of the Kitaev chain, a toy-model consisting of non-interacting spinless fermions on a 1D lattice in a topological superconductive phase. Our goal was to generalize such a model, aiming at building an interacting fermionic chain which features zero modes with $\mathbb{Z}_4$ parafermionic algebra. To this end, we first developed an exact mapping between fermions and parafermions on 1D lattices; then we applied it to a well-known parafermionic Hamiltonian in a topological phase. We eventually discussed the interesting properties of the fermionic Hamiltonians we obtained. Our main results are summarized below.

- It is possible to find an exact mapping between spinful fermions and $\mathbb{Z}_4$ parafermions on a 1D lattice. Despite the mapping's intrinsic non-locality, we showed that certain local parafermionic operators (conserving the total number of Fock parafermions modulo 4) can be mapped onto local fermionic operators. This allows for the systematic construction of nearest-neighbor Hamiltonians in interacting fermionic lattice systems which feature zero-energy parafermionic modes.

- An exactly solvable fermionic Hamiltonian is provided, thus making possible to find an exact fermionic expression for its zero-energy parafermionic modes. Fermionic properties of its four-fold degenerate ground states are also discussed. The original $\mathbb{Z}_4$ symmetry of the parafermionic model emerges also in the fermionic one, although with a crucial difference: the latter features a $\mathbb{Z}_2$ spontaneously broken symmetry which challenges the full topological protection of the parafermionic zero-energy modes.
- We identified an entire phase which contains the exactly solvable model mentioned above as well as other simpler interacting Hamiltonians. These are more suitable for numerical and experimental investigation while retaining the same topological properties we are interested in. In this respect, we showed that the local fermionic spectral function is a good quantity in order to distinguish between this interesting phase and another weakly interacting phase where, instead of parafermions, there are two couples of less exotic Majorana zero modes.

Outlook

Having carefully discussed the properties of the fractional counterpropagating excitations originated after a single-electron injection, it would be interesting to properly devise experimental setups where their properties can be probed and even exploited. In this respect, a very recent experimental breakthrough in the fabrication of QSH bars (in HgTe quantum wells) might be extremely interesting and promising [108]. Another intriguing extension of our work is to consider different types of single electron sources, focusing for example on levitons injection. In this respect our work has already triggered subsequent research, see for example Ref. [219].

As for the study of parafermions, extension of the present work could investigate more profoundly the relationship between our model and the ones relying on effective low-energy field theories. In particular, it would be extremely interesting to understand how one of the flagship properties of parafermions, their exchange statistics, emerges in our system and in other models. Moreover, it would be interesting to extend our exact mapping also to chains of generic $\mathbb{Z}_p$ parafermions.

Appendix A

Topology

A.1 Why the Chern number has to be an integer?

Here we want to give an intuition why the Chern number appearing in Eq. (1.17) has to be an integer. Let us assume that the whole torus can be subdivided into two different patches, P and $\mathcal{T}^2 - P$, so that inside each one of them the phase of the eigenstates is smooth and single valued. On the boundary ∂P between the patches, however, the phase associate with every eigenstate $|n_0(\vec{k})\rangle$ is clearly discontinuous

$$\lim_{\vec{k}\to\vec{k}_0} |n_0(\vec{k})\rangle = e^{i\xi(\vec{k}_0)} \lim_{\vec{p}\to\vec{k}_0} |n_0(\vec{p})\rangle \tag{A.1}$$

with $\vec{k} \in (\mathcal{T}^2 - P)$, $\vec{p} \in P$, $\vec{k}_0 \in \partial P$. Here $\zeta(\vec{k}_0)$ is the gauge transformation on the boundary which relates the gauge choices made in the two patches. At this point, Stokes theorem can be safely applied within P and $\mathcal{T}^2 - P$ and one obtains

$$\begin{aligned} \int_{\mathcal{T}^2} \vec{\nabla} \times \vec{\mathcal{A}}_{n_0}(\vec{k}) \cdot d\vec{k} &= \int_{\mathcal{T}^2 - P} \vec{\nabla} \times \vec{\mathcal{A}}_{n_0}(\vec{k}) \cdot d\vec{k} + \int_{P} \vec{\nabla} \times \vec{\mathcal{A}}_{n_0}(\vec{k}) \cdot d\vec{k} \\ &= \oint_{\partial P} \vec{\nabla}\xi(\vec{k}) \cdot d\vec{k} \; = 2\pi\, n \quad n \in \mathbb{Z}\,. \end{aligned} \tag{A.2}$$

In the second line we observed that the line integral of $\vec{\nabla}\xi$ basically counts the winding number (times 2π) of the gauge transformation on the boundary between the two patches. For more details, we refer to the literature, e.g. Ref. [40].

A.2 The TKNN formula

Here we want to briefly review the seminal TKNN result in Eq. (1.18), highlighting the key points of its derivation. For a more detailed discussion we refer to the original paper in Ref. [41] as well as to other reviews, e. g. Ref. [39, 31].

Let us consider a square lattice placed in an orthogonal uniform magnetic field. The first issue to deal with is to understand the fate of the Brillouin zone. Its existence indeed relies on the translational invariance of the lattice which, however, is broken when we fix a gauge to explicitly express the vector potential. The interplay between lattice and magnetic effects leads to a surprisingly rich physics, which is very sensitive to the magnetic flux Φ which threads the Brillouin zone. It turns out that, when Φ is a rational[1] of the unit flux $\Phi_0 = h/e$,

$$\Phi = \frac{p}{q}\Phi_0 \,, \tag{A.3}$$

it is possible to define a magnetic version of the Brillouin zone, i.e. it is possible to identify two translation operators T_1^q and T_2 which commutes between each other and allows to label the energy eigenstates of the Hamiltonian $H|\vec{k}\rangle = E(\vec{k})|\vec{k}\rangle$ as [31, 220, 41]

$$T_1^q|\vec{k}\rangle = e^{iqk_1a}\,|\vec{k}\rangle \qquad T_2|\vec{k}\rangle = e^{ik_2a}\,|\vec{k}\rangle \,. \tag{A.4}$$

Here $\vec{k} = (k_1, k_2)$ can be seen as a generalization of the crystal momentum and lives in the *magnetic* Brillouin zone (mBZ)

$$-\frac{\pi}{qa} < k_1 \leq \frac{\pi}{qa} \quad \text{and} \quad -\frac{\pi}{a} < k_2 \leq \frac{\pi}{a} \,. \tag{A.5}$$

Despite being smaller than the standard Brillouin zone[2], it is still a 2D torus and it allows to use all the machinery based on the Bloch theorem.

An explicit expression for the electrical conductivity of a system can be readily obtained using the linear response theory and, in particular, the Kubo formula [221, 32]. The electrical conductivity describes current response of the system when an external electrical field is applied. Since the latter couples to the current density in the Hamiltonian, the Hall conductivity should be determined by current-current correlators. Indeed, the Kubo formula reads [31]

$$\sigma_{xy} = i\hbar A^{-1} \sum_{|\varphi\rangle \neq |\psi_0\rangle} \frac{\langle\psi_0|J_y|\varphi\rangle\langle\varphi|J_x|\psi_0\rangle - \langle\psi_0|J_x|\varphi\rangle\langle\varphi|J_y|\psi_0\rangle}{(E_0 - E_\varphi)^2} \tag{A.6}$$

---

[1] Behavior for irrational values can be deduced by taking an appropriate limit [41].

[2] Being q times smaller, the spectrum in presence of magnetic field will split up into q different bands.

where A is the system surface while $|\psi_0\rangle$ and $|\varphi\rangle$ represent the many-body ground state and excited states respectively. When the system is non-interacting, the many-body wave functions can be written as a tensor product of single-particle states $|u_\alpha(\vec{k})\rangle$, labeled by the band index α and by the momentum $\vec{k}$ which lives in the magnetic Brillouin zone. This gives

$$\sigma_{xy} = i\hbar A^{-1} \sum_{\substack{E_\alpha(\vec{k})<E_\mathrm{F} \\ E_\beta(\vec{k}')>E_\mathrm{F}}} \frac{\langle u_\alpha(\vec{k})|J_y|u_\beta(\vec{k}')\rangle\langle u_\beta(\vec{k}')|J_x|u_\alpha(\vec{k})\rangle - \langle u_\alpha(\vec{k})|J_x|u_\beta(\vec{k}')\rangle\langle u_\beta(\vec{k}')|J_y|u_\alpha(\vec{k})\rangle}{(E_\alpha(\vec{k})-E_\beta(\vec{k}'))^2}\,. \tag{A.7}$$

where E_F is the Fermi energy lying in the gap of the system. Plugging in the expression of the current in terms of the group velocity

$$\vec{J} = \frac{e}{\hbar}\frac{\partial H}{\partial \vec{k}}\,, \tag{A.8}$$

one eventually obtains[3]

$$\sigma_{xy} = i\frac{e^2}{\hbar}\frac{1}{(2\pi)^2}\sum_{E_\alpha>E_\mathrm{F}}\int_{\mathrm{mBZ}} d^2k\, \left[\langle\partial_{k_y}u_\alpha(\vec{k})|\partial_{k_x}u_\alpha(\vec{k})\rangle - \langle\partial_{k_x}u_\alpha(\vec{k})|\partial_{k_y}u_\alpha(\vec{k})\rangle\right] \tag{A.9}$$

Remarkably, the square bracket in the RHS is exactly the Berry curvature defined in Eq. (1.13) for the band α. Since the mBZ is a 2D torus, Eq. (1.17) holds and allows to readily prove the relation in Eq. (1.18) between Hall conductance and Chern number.

A.3 Phase diagram of Kitaev chain

Here we will discuss the phase diagram of the Kitaev chain, following an approach which closely parallels the ones used before for the QSH effect [66]. We start by imposing PBC on the Kitaev model, thereby wrapping the chain into a closed loop. This gives us access to the bulk property of the chain and allows to work in momentum space. The Kitaev Hamiltonian

---

[3] Here, one has to exploit the identity

$$\langle u_\alpha(\vec{k})|\partial_{k_i}H|u_\beta(\vec{k}')\rangle = (E_\alpha(\vec{k})-E_\beta(\vec{k}'))\langle\partial_{k_i}u_\alpha(\vec{k})|u_\beta(\vec{k}')\rangle$$

($i = x, y$) and the completeness relation

$$\sum_{E_\beta(\vec{k}')>E_\mathrm{F}} |u_\beta(\vec{k}')\rangle\langle u_\beta(\vec{k}')| = 1 - \sum_{E_\alpha(\vec{k})<E_\mathrm{F}} |u_\alpha(\vec{k})\rangle\langle u_\alpha(\vec{k})|$$

can be conveniently rewritten in the standard Bogoliubov-de Gennes from as

$$H_K = \frac{1}{2} \sum_{k \in \mathrm{BZ}} C_k^\dagger \mathcal{H}_k C_k \tag{A.10}$$

where $C_k^\dagger = \left(c_k^\dagger, c_{-k} \right)$ and

$$\mathcal{H}_k = \begin{pmatrix} \varepsilon_k & \tilde{\Delta}_k^* \\ \tilde{\Delta}_k & -\varepsilon_k \end{pmatrix} . \tag{A.11}$$

Here $\varepsilon_k = -t\cos(k) - \mu$ is the kinetic energy and $\tilde{\Delta}_k = -i\Delta\sin(k)$ is the Fourier-transformed superconducting pairing potential. The Hamiltonian can be easily diagonalized (neglecting a constant term)

$$H_K = \sum_{k \in \mathrm{BZ}} E_{\mathrm{bulk}}(k)\, p_k^\dagger p_k \tag{A.12}$$

where the quasiparticle operators p_k read

$$p_k = -i \frac{\sqrt{E_{\mathrm{bulk}}(k) + \varepsilon_k}}{\sqrt{2E_{\mathrm{bulk}}(k)}} \left[c_k + \frac{E_{\mathrm{bulk}}(k) - \varepsilon_k}{\tilde{\Delta}_k} c_{-k}^\dagger \right] \tag{A.13}$$

and the energy of the bulk excitations reads

$$E_{\mathrm{bulk}}(k) = \sqrt{\varepsilon_k^2 + |\tilde{\Delta}_k|^2} . \tag{A.14}$$

Zero-energy bulk excitations are possible only when $\mu = \pm t$ (at $k = \pi$ or $k = 0$ respectively) or when $\Delta = 0$ and $t \geq |\mu|$ (at $k = \cos^{-1}(-\mu/t)$). It is therefore possible to distinguish three different gapped regions in the parameter space, separated by gap closures.

- The first one, for $\mu < t$, contains the "trivial limit" in Eq. (1.43) as well as the trivial fermion vacuum (when $\mu \to -\infty$).
- The second one, for $t > |\mu|$ and $\Delta \neq 0$, contains the "topological limit" in Eq. (1.44).
- The third one, for $\mu > t$, is related to the first one by a particle-hole transformation: they share the same properties and we can thus focus only on the first one.

Once the gapped phases have been found, we are left with the identification of a topological invariant. To this end, note that the 2×2 Hermitian matrix $\mathcal{H}_k$ can be written as

$$\mathcal{H}_k = \vec{h}(k) \cdot \vec{\sigma} \tag{A.15}$$

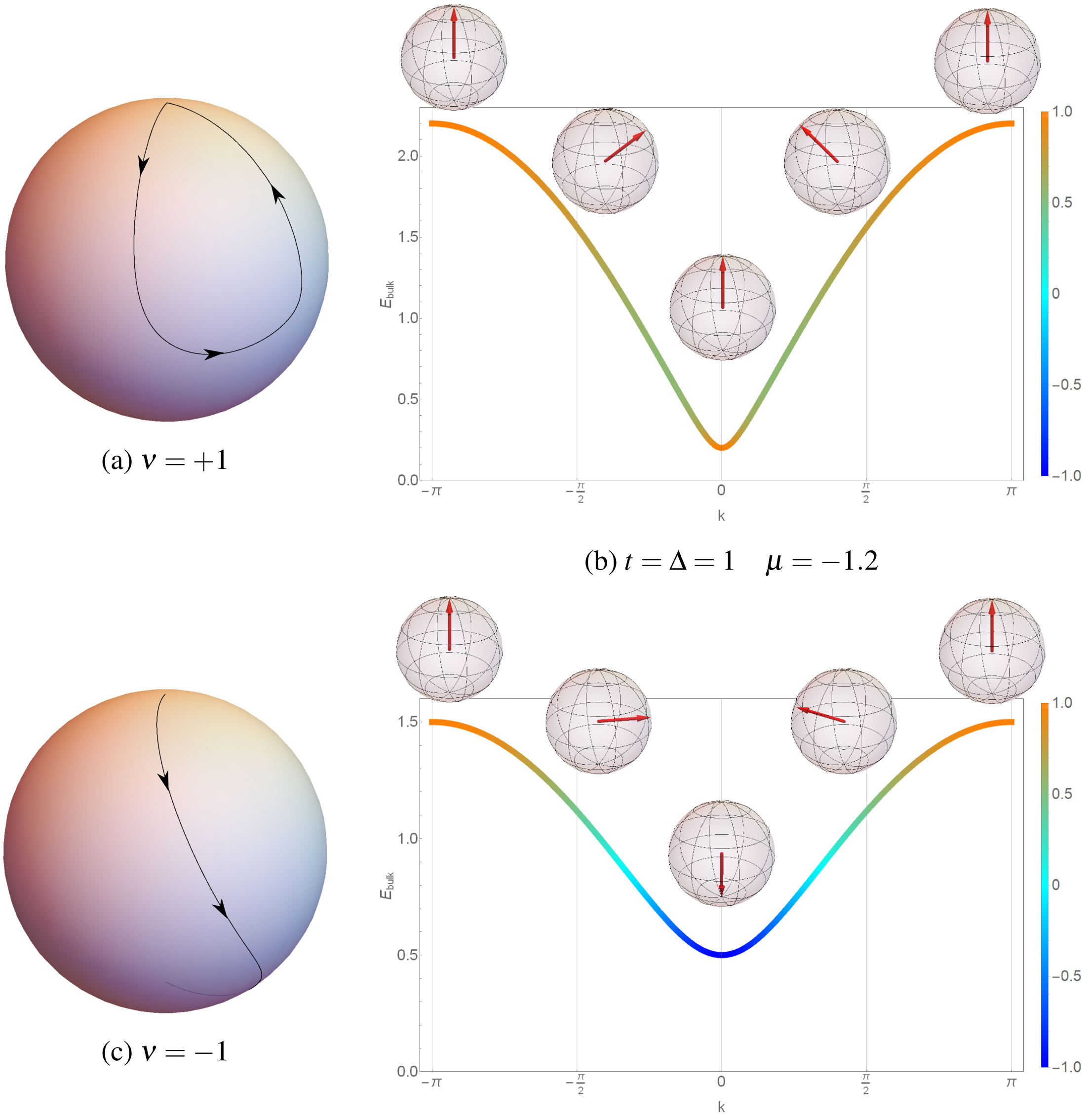

(a) $\nu = +1$

(b) $t = \Delta = 1 \quad \mu = -1.2$

(c) $\nu = -1$

(d) $t = \Delta = 1 \quad \mu = -0.5$

Fig. A.1 In (a) and (c), examples of two trajectories of vector $\hat{h}(k)$ on the unit sphere when k is swept on half of the BZ: in the first case the Hamiltonian is in the trivial phase, in the second case it is in the topological one. In (b) and (d) the energy of bulk excitations $E_{\mathrm{bulk}}(k)$ is plotted over the BZ. The colors display the z component $\hat{h}_z(k)$, ranging from -1 (blue) to $+1$ (orange). Sketches of the unit vector $\hat{h}(k)$ (in red) inside the unit sphere are also provided. In (b) the system is in the trivial gapped phase while in (c) it is in the topological one. The exact values of the parameters used to generate the plots are reported in the sub-captions.

where $\vec{\sigma} = (\sigma_x, \sigma_y, \sigma_z)$ is the vector of Pauli matrices and $\vec{h}(k)$ is a three-dimensional vector. Even for a rather general (translational invariant) Hamiltonian, the structure of $\vec{h}(k)$ is not completely arbitrary since the relation $(C^\dagger_{-k})^{\mathrm{T}} = \sigma_x C_k$ implies

$$h_{x,y}(k) = -h_{x,y}(-k) \qquad h_z(k) = h_z(-k)\,. \tag{A.16}$$

Therefore, it suffices to study $\vec{h}(k)$ in the interval $0 \leq k \leq \pi$ since, on the other half of the BZ, the value of the vector follows from the constraints in Eq. (A.16). Within a given gapped region, the vector $\vec{h}(k)$ cannot be zero and it is therefore possible to define a unit vector $\hat{h}(k) = \vec{h}(k)/|\vec{h}(k)|$ which provides a map between the BZ and the unit sphere. Because of Eq. (A.16), there are strong constraints at $k = 0$ and $k = \pi$: here the unit vector $\hat{h}$ can either point to the north or the south pole

$$\hat{h}(0) = s_0 \hat{\mathbf{z}} \qquad \hat{h}(\pi) = s_\pi \hat{\mathbf{z}} \tag{A.17}$$

depending on the sign of the kinetic energy (measured with respect to the Fermi level) at $k = 0$ (s_0) and $k = \pi$ (s_π). When k is swept between $k = 0$ and $k = \pi$, two topologically different trajectories are possible depending on the relative sign $\nu = s_0 s_\pi$:

- if $\nu = +1$, the unit vector begins and ends up at the same pole, see Fig. A.1a;
- if $\nu = -1$, the unit vector ends up at the opposite pole, see Fig. A.1c.

These two trajectories cannot be continuously deformed into each other and the only way to change the sign of ν is to go through a gap closure, resulting in $\hat{h}(k)$ being ill-defined at a certain point of the BZ.

We have therefore successfully identified the $\mathbb{Z}_2$ topological invariant ν, which allows to distinguish between a topological and a trivial phase. In particular, the one which contains the fermion vacuum is topologically trivial ($t < |\mu|$) while the other is topological ($t > |\mu|$ and $\Delta \geq 0$). Fig. A.1b and A.1d help in summarizing the results of this appendix. They show the gapped bulk spectrum $E_{\mathrm{bulk}}(k)$ and the behavior of the unit vector $\hat{h}(k)$ across the BZ for two different Hamiltonians: one belonging to the trivial phase (Fig. A.1b) and the other to the topological phase (Fig. A.1d). The spectrum is qualitatively analogous but the analysis of the unit vector over the whole BZ shows a profound (and indeed topological) difference between the two cases: in Fig. A.1d the unit vectors performs a twist over the BZ while in Fig. A.1b it does not.

Appendix B

Single electron injection into interacting systems

B.1 Inverse lifetime of the single resonant level

In this Appendix we explicitly calculate the inverse lifetime 2γ defined in Eq. (3.18). Let us start from the result in Eq. (3.20), which can be rewritten in the following form

$$
\begin{aligned}
P(t) = 2|\lambda|^2 \mathrm{Re} \int_0^t dt_1 \int_0^{t_1} dt_2 \iint_{-\infty}^{+\infty} dy_1 dy_2 \, e^{i\varepsilon_0 (t_2 - t_1)} \\
\times w^*(y_2) w(y_1) \mathcal{G}(y_2, t_2; y_1, t_1) \, .
\end{aligned}
\tag{B.1}
$$

It is now straightforward to perform the time derivative, obtaining

$$
\begin{aligned}
\dot{P}(t) = 2|\lambda|^2 \mathrm{Re} \int_0^t dt_2 \iint_{-\infty}^{+\infty} dy_1 dy_2 \, e^{i\varepsilon_0 (t_2 - t)} \\
\times w^*(y_2) w(y_1) \mathcal{G}(y_2, t_2; y_1, t) \, .
\end{aligned}
\tag{B.2}
$$

We now express this quantity in Fourier representation. First, considering [222]

$$
e^{2\pi g G(z)} = \frac{1}{\Gamma(g)} \left(\frac{a}{u} \right)^g \int_0^{+\infty} dE \, E^{g-1} e^{-i\frac{Ez}{u}} e^{-\frac{Ea}{u}} \, ,
\tag{B.3}
$$

the fermionic function $\mathcal{G}$ in Eq. (B.2) becomes

$$
\begin{aligned}
\mathcal{G} = \frac{1}{2\pi a} \frac{1}{\Gamma(A_-^2)\Gamma(A_+^2)} \left(\frac{a}{u} \right)^{1+2A_-^2} \iint_0^{+\infty} dE_1 dE_2 \\
\times E_1^{A_-^2} E_2^{A_-^2 - 1} e^{-a\frac{E_1+E_2}{u}} e^{-it_2(E_1+E_2)} \, e^{it(E_1+E_2)} e^{-iy_2\frac{E_2-E_1}{u}} e^{iy_1\frac{E_2-E_1}{u}} \, .
\end{aligned}
\tag{B.4}
$$

Then, we introduce the Fourier transform of $w(y)$

$$\tilde{w}(k) = \int_{-\infty}^{+\infty} dy\, w(y)\, e^{iky} = \int_{-\infty}^{+\infty} dy\, \xi(y)\, e^{iy(k+k_0)} = \tilde{\xi}(k+k_0)\,. \tag{B.5}$$

Using (B.4) and (B.5) in (B.2) we obtain

$$\begin{aligned}\dot{P}(t) = {} & \frac{|\lambda|^2}{\pi u}\frac{1}{\Gamma(A_+^2)\Gamma(A_-^2)}\left(\frac{a}{2u}\right)^{2A_-^2}\int_0^{+\infty} d\varepsilon \int_{-\varepsilon}^{+\varepsilon} dE \\ & \times \left|\tilde{w}(-Eu^{-1})\right|^2 (\varepsilon+E)^{A_-^2}(\varepsilon-E)^{A_-^2-1} e^{-\frac{\varepsilon a}{u}} \mathrm{Re}\int_0^t ds\, e^{-i(\varepsilon_0-\varepsilon)s}\,.\end{aligned} \tag{B.6}$$

Recalling the definition (3.18) and using

$$\mathrm{Re}\int_0^{+\infty} ds\, e^{-i(\varepsilon_0-\varepsilon)s} = \pi\delta(\varepsilon_0-\varepsilon)\,, \tag{B.7}$$

we find

$$\gamma = \frac{\gamma_0 K}{A_-^2\Gamma^2(A_-^2)} e^{-\frac{\varepsilon_0 a}{u}} \left(\frac{a\varepsilon_0}{2u}\right)^{2A_-^2} \int_{-1}^{+1} d\chi \left|\tilde{w}\left(-\frac{\varepsilon_0\chi}{u}\right)\right|^2 (1+\chi)^{A_-^2}(1-\chi)^{A_-^2-1}\,, \tag{B.8}$$

with $\gamma_0 = |\lambda|^2/(2v_\mathrm{F})$. Eq. (3.25) is thus proved by using the expression in Eq. (3.27) for the spectral function and Eq. (B.5). Note that when $\tilde{\xi}(k) = 1$ (local tunneling), the above integral can be evaluated analytically, yielding

$$\int_{-1}^{+1} d\chi\, (1+\chi)^{A_-^2}(1-\chi)^{A_-^2-1} = 2^{2A_-^2}\int_0^1 dx \frac{x^{A_-^2}}{(1-x)^{1-A_-^2}} = 2^{2A_-^2}\frac{A_-^2\Gamma^2(A_-^2)}{\Gamma(1+2A_-^2)}\,.$$

This result leads to Eq. (3.28) which holds in the case of local injection with $\sigma \to 0$.

B.2 Charge properties of wavepackets

B.2.1 Calculation of $\mathcal{I}_\rho$

This Appendix is devoted to the evaluation of the average function

$$\mathcal{I}_\rho = \left\langle \psi_R(y_2,t_2)\left[\rho(x,t), \psi_R^\dagger(y_1,t_1)\right]\right\rangle_\Omega\,, \tag{B.9}$$

defined in Eq. (15) and necessary in order to compute the density variation $\delta\rho(x,t)$ in Eq. (3.15). Let us start with the commutator in (B.9), which can be written in terms of chiral fields as

$$\left[\rho(x,t),\psi_R^\dagger(y_1,t_1)\right]=-\sqrt{\frac{K}{2\pi}}\sum_\eta\eta\left[\partial_x\phi_\eta(z_\eta),\psi_R^\dagger(y_1,t_1)\right], \tag{B.10}$$

with $z_\eta=x-\eta ut$. Using the bosonized expression (2.5) with (2.22) one has

$$\left[\partial_x\phi_\eta(z_\eta),\psi_R^\dagger(y_1,t_1)\right]=\frac{1}{\sqrt{2\pi a}}\left[\partial_x\phi_\eta(z_\eta),e^{i\sqrt{2\pi}\left(A_+\phi_+(z_1^+)+A_-\phi_-(z_1^-)\right)}\right] \tag{B.11}$$

with the boson fields satisfying c-number commutation relations [93, 94]

$$\left[\partial_x\phi_\eta(x),\phi_{\eta'}(y)\right]=i\eta\,\delta_{\eta,\eta'}\frac{1}{\pi}\frac{a}{a^2+(x-y)^2}. \tag{B.12}$$

This allows to use the Baker Hausdorff relation [93] among two operators A and B (with a c-number commutator) $\left[A,e^B\right]=[A,B]\,e^B$, getting to

$$\left[\partial_x\phi_\eta(z_\eta),\psi_R^\dagger(y_1,t_1)\right]=-\eta A_\eta\sqrt{2\pi}\left(\frac{1}{\pi}\frac{a}{a^2+(z_\eta-z_1^\eta)^2}\right)\psi_R^\dagger(y_1,t_1)\,. \tag{B.13}$$

Then, using Eq. (3.30), we obtain

$$\left[\rho(x,t),\psi_R^\dagger(y_1,t_1)\right]=\sum_\eta q_\eta\left[\frac{1}{\pi}\frac{a}{a^2+(z_\eta-z_2^\eta)^2}\right]\psi_R^\dagger(y_1,t_1)\,. \tag{B.14}$$

The average function $\mathcal{I}_\rho$ in Eq. (B.9) is then given by

$$\mathcal{I}_\rho=\sum_{\eta=\pm1}q_\eta\left[\frac{1}{\pi}\frac{a}{a^2+(z_\eta-z_2^\eta)^2}\right]\langle\psi_R(y_2,t_2)\psi_R^\dagger(y_1,t_1)\rangle_\Omega$$

As a final step the fermionic Green function $\mathcal{G}=\langle\psi_R(y_2,t_2)\psi_R^\dagger(y_1,t_1)\rangle_\Omega$, is expressed using the identity [93]

$$\left\langle e^{-i\alpha\phi_\eta(x)}e^{i\alpha\phi_\eta(y)}\right\rangle_\Omega=\exp\left[\alpha^2G(-\eta(x-y))\right], \tag{B.15}$$

with G the bosonic Green function defined in Eq. (3.23). In writing Eq. (3.33), we exploit the fact that a is the smallest length scale and it is thus possible to approximate

$$\frac{1}{\pi}\frac{a}{a^2+(z_\eta-z_2^\eta)^2}\to\delta(z_\eta-z_2^\eta). \tag{B.16}$$

B.2.2 Calculation of the total charge $\mathcal{Q}$

In this Appendix we calculate the total amount of charge injected in the edge channels, starting from the expression given in Eq. (3.36). Let us first introduce the Fourier transform of the funcion $\beta(t)$:

$$\tilde{\beta}(E) = \int_0^{+\infty} dt \beta(t) e^{iEt} = \frac{1}{i(E-\varepsilon_0)+\gamma} \,. \tag{B.17}$$

Taking advantage of the integral representation (B.3), we write $\mathcal{Q}$ as a double integral over energies:

$$\begin{aligned} \mathcal{Q} = & \frac{|\lambda|^2}{2\pi a} \frac{1}{\Gamma(A_-^2)\Gamma(A_+^2)} \left(\frac{a}{u}\right)^{1+2A_-^2} \\ & \times \iint_0^{+\infty} dE_1 dE_2 \, E_1^{A_-^2} E_2^{A_-^2-1} \left| \tilde{w}\left(\frac{E_2-E_1}{u}\right)\right|^2 \left|\tilde{\beta}(E_1+E_2)\right|^2 e^{-a\frac{E_1+E_2}{u}} . \end{aligned} \tag{B.18}$$

Moreover, since the energy level of the dot is well defined ($\gamma \ll \varepsilon_0$), the following approximation on the function $\tilde{\beta}(E)$ can be used:

$$\left|\tilde{\beta}(E)\right|^2 = \frac{1}{\gamma^2+(E-\varepsilon_0)^2} \to \frac{\pi}{\gamma}\, \delta(E-\varepsilon_0) \,. \tag{B.19}$$

Inserting this δ-function in Eq. (B.18) we are left with a single integral

$$\mathcal{Q} = \frac{K\gamma_0}{\gamma} e^{-a\frac{\varepsilon_0}{u}} \frac{1}{A_-^2 \Gamma^2(A_-^2)} \left(\frac{a\varepsilon_0}{2u}\right)^{2A_-^2} \int_{-1}^{+1} d\chi \, (1+\chi)^{A_-^2} (1-\chi)^{A_-^2-1} \left|\tilde{w}\left(-\varepsilon_0 \chi u^{-1}\right)\right|^2 , \tag{B.20}$$

with $\gamma_0 = |\lambda|^2/(2v_{\mathrm{F}})$. Recalling the expression of γ found in (B.8), we conclude that $\mathcal{Q} = 1$.

B.3 Energy properties of wavepackets

Here we evaluate the average function

$$\mathcal{I}_{\mathcal{H}} = \left\langle \psi_R(y_2,t_2) \left[\mathcal{H}(x,t), \psi_R^\dagger(y_1,t_1)\right] \right\rangle_\Omega \tag{B.21}$$

demonstrating the validity of Eq. (3.41), necessary in order to evaluate the energy density fluctuations $\delta\mathcal{H}(x,t)$. In particular we have to compute functions $\mathcal{M}_\eta^{(a/b)}$, introduced in Eq.

(3.38). Focusing on $\mathcal{M}_\eta^{(a)}$ we get

$$\begin{aligned} \mathcal{M}_\eta^{(a)} &= \left\langle \psi_R(y_2,t_2)\,\phi_\eta(z_\eta)\,\psi_R^\dagger(y_1,t_1) \right\rangle_\Omega \\ &= -\frac{i}{2\pi a}\left\langle e^{-i\sqrt{2\pi}A_{-\eta}\phi_{-\eta}(z_2^{-\eta})} e^{i\sqrt{2\pi}A_{-\eta}\phi_{-\eta}(z_1^{-\eta})} \right\rangle_\Omega \\ &\quad \times \partial_\nu \left\langle e^{-i\sqrt{2\pi}A_\eta\phi_\eta(z_2^\eta)}\; e^{i\nu\phi_\eta(z_\eta)}\; e^{i\sqrt{2\pi}A_\eta\phi_\eta(z_1^\eta)} \right\rangle_\Omega \Big|_{\nu=0} \end{aligned} \tag{B.22}$$

where we have used Eq. (2.5) and the identity

$$\phi_\eta(x,t) = -i\partial_\nu e^{i\nu\phi_\eta(x,t)}\big|_{\nu=0}. \tag{B.23}$$

By means of the Baker-Hausdorff identity, one can rewrite

$$\mathcal{M}_\eta^{(a)}(z_\eta,z_2^\pm,z_1^\pm) = -iA_\eta\sqrt{2\pi}\,\mathcal{G}(z_2^\pm,z_1^\pm)\;\left(G\left(\eta z_\eta-\eta z_2^\eta\right)-G\left(\eta z_1^\eta-\eta z_\eta\right)\right) \tag{B.24}$$

where the bosonic Green function G and the fermionic correlation function $\mathcal{G}$ have been defined in Eq. (3.23) and in Eq. (3.24) respectively. It is easy to show that $\mathcal{M}_\eta^{(b)}$ has the same expression apart from a different sign in the argument of the second bosonic Green function. As a result one has

$$\begin{aligned} \mathcal{M}_\eta^{(a)} + \mathcal{M}_\eta^{(b)} &= -iA_\eta\sqrt{2\pi}\,\mathcal{G}(z_2^\pm,z_1^\pm) \\ &\quad \times \left[2G\left(\eta z_\eta-\eta z_2^\eta\right)-G\left(\eta z_\eta-\eta z_1^\eta\right)-G\left(\eta z_1^\eta-\eta z_\eta\right)\right]. \end{aligned} \tag{B.25}$$

Eq. (3.41) can now be readily obtained simply taking the derivative of functions G.

B.3.1 Behavior of E_η

In this Appendix we present details on the energy E_η that travels in the η direction. Such quantity, defined in Eq. (3.43) is expressed as in Eq. (3.45).

Let us start to discuss the total energy $E = E_+ + E_-$. In the limit $\gamma \ll \varepsilon_0$ we can approximate $|\tilde{\beta}(\varepsilon_+)|^2 \to \delta(\varepsilon_+-\varepsilon_0)\,\pi/\gamma$, see Eq. (B.19), writing

$$\begin{aligned} E_\eta = \frac{K\gamma_0}{2\gamma}\left(\frac{K\bar{a}}{2\varepsilon_0}\right)^{2A_-^2} \frac{A_\eta^2}{\Gamma(g_\eta^-)\Gamma(g_\eta^+)}\, e^{-K\bar{a}}\int_{-\varepsilon_0}^{+\varepsilon_0} d\varepsilon_- \\ (\varepsilon_0+\varepsilon_-)^{g_\eta^+-1}(\varepsilon_0-\varepsilon_-)^{g_\eta^--1}\,|\tilde{w}(-\varepsilon_-/u)|^2. \end{aligned} \tag{B.26}$$

Recalling that $g_\eta^\pm = A_\pm^2 + (1 \pm \eta)/2$, one then has

$$
\begin{aligned}
E = \varepsilon_0 \frac{K\gamma_0}{\gamma} \left(\frac{K\bar{a}}{2} \right)^{2A_-^2} \frac{1}{A_-^2 \Gamma^2(A_-^2)} \, e^{-K\bar{a}} \\
\int_{-1}^{+1} d\chi \, (1+\chi)^{A_-^2} (1-\chi)^{A_-^2 - 1} \left| \tilde{w} \left(-\varepsilon_0 \chi u^{-1} \right) \right|^2 .
\end{aligned}
\tag{B.27}
$$

By comparing this result with the behavior of the total charge $\mathcal{Q}$ in Eq. (B.20) we can conclude that $E = \varepsilon_0 \mathcal{Q} = \varepsilon_0$, since $\mathcal{Q} = 1$. The "universal" limit present for local injection ($\tilde{\xi}(k) \to 1$) and given in Eq. (3.47) is recovered using in Eq. (3.45) the relation

$$
\int_{-\varepsilon_+}^{+\varepsilon_+} d\varepsilon_- \, \frac{(\varepsilon_+ + \varepsilon_-)^{g_\eta^+ - 1} (\varepsilon_+ - \varepsilon_-)^{g_\eta^- - 1}}{\Gamma(g_\eta^-)\Gamma(g_\eta^+)} = \frac{(2\varepsilon_+)^{1+2A_-^2}}{\Gamma(2+2A_-^2)} \, . \tag{B.28}
$$

We therefore have that $E_\eta = A_\eta^2 \mathcal{E}$ with

$$
\mathcal{E} = \frac{K\gamma_0}{\pi} \left(\frac{K\bar{a}}{\varepsilon_0} \right)^{2A_-^2} \frac{1}{\Gamma(2+2A_-^2)} \int_0^\infty d\varepsilon_+ \, \varepsilon_+^{1+2A_-^2} \left| \tilde{\beta}(\varepsilon_+) \right|^2 e^{-K\bar{a} \frac{\varepsilon_+}{\varepsilon_0}} \tag{B.29}
$$

independent of η. Such an expression immediately allows to recover the energy partitioning factors p_η^{loc} given in Eq. (3.47).

B.4 Calculation of the single electron coherence

B.4.1 Single-electron coherence

In this Appendix we give the details on the calculation of the single-electron coherence $\mathfrak{G}_r(s,t;\xi,z)$ in Eq. (3.56). The starting point is Eq. (3.12) together with the bosonization identity (2.5). Denote with $O_r(s,t;\xi,z)$ the operator in the average (3.56). It has the property that $O_r^\dagger(s,t;\xi,z) = O_r(s,t;-\xi,-z)$. Then Eq. (3.57) immediately follows from Eq. (3.12) with

$$g_r(s,t;\xi,z) = |\lambda|^2 \int_0^t \mathrm{d}t_2 \int_0^{t_2} \mathrm{d}t_1\, e^{-\gamma(t_2+t_1)-i\varepsilon_0(t_2-t_1)} \mathfrak{C}_r(t_1,s,t,\xi,z,t_2)\,, \tag{B.30}$$

where $\mathfrak{C}_r = \mathfrak{C}_r^{(1)} - \mathfrak{C}_r^{(2)}$ and

$$\mathfrak{C}_r^{(1)} = \Big\langle \psi_R(0,t_1) O_r(s,t;\xi,z) \psi_R^\dagger(0,t_2) \Big\rangle_\Omega\,, \tag{B.31a}$$

$$\mathfrak{C}_r^{(2)} = \Big\langle \psi_R(0,t_1) \psi_R^\dagger(0,t_2) O_r(s,t;\xi,z) \Big\rangle_\Omega\,. \tag{B.31b}$$

Here, $\langle \ldots \rangle_\Omega$ denotes the ground state average. Let us focus on $\mathfrak{C}_r^{(1)}$. First, the fermion fields are rewritten in terms of the chiral fields with the bosonization identity and Eq. (2.22), so that the time evolution becomes chiral. Introducing the shorthand notations $x_\eta = s - \eta u t$ and $\zeta_\eta = \xi - \eta u z$ we have:

$$\begin{aligned}
\mathfrak{C}_r^{(1)} = {} & \frac{e^{i\vartheta_r k_\mathrm{F} \xi}}{(2\pi a)^2} \prod_{\eta=\pm} \Big\langle e^{-i\sqrt{2\pi} A_\eta \phi_\eta(-\eta u t_1)} e^{i\sqrt{2\pi} A_{\vartheta_r \eta} \phi_\eta(x_\eta - \zeta_\eta/2)} \\
& \qquad \times e^{-i\sqrt{2\pi} A_{\vartheta_r \eta} \phi_\eta(x_\eta + \zeta_\eta/2)} e^{i\sqrt{2\pi} A_\eta \phi_\eta(-\eta u t_2)} \Big\rangle_\Omega \qquad (\mathrm{B.32}) \\
= {} & \frac{e^{i\vartheta_r k_\mathrm{F} \xi}}{(2\pi a)^2} \prod_{\eta=\pm} e^{2\pi A_\eta^2 G_\eta(\eta u (t_2 - t_1))} e^{2\pi A_{\vartheta_r \eta}^2 G_\eta(-\zeta_\eta)} \\
& \qquad \times e^{2\pi A_\eta A_{\vartheta_r \eta} G_\eta(-\eta u t_1 - x_\eta + \zeta_\eta/2)} e^{-2\pi A_\eta A_{\vartheta_r \eta} G_\eta(-\eta u t_1 - x_\eta - \zeta_\eta/2)} \\
& \qquad \times e^{-2\pi A_\eta A_{\vartheta_r \eta} G_\eta(x_\eta - \zeta_\eta/2 + \eta u t_2)} e^{2\pi A_\eta A_{\vartheta_r \eta} G_\eta(x_\eta + \zeta_\eta/2 + \eta u t_2)}\,. \qquad (\mathrm{B.33})
\end{aligned}$$

The average (B.32) has been evaluated by using the identity [93]

$$\Big\langle e^{O_1} \ldots e^{O_n} \Big\rangle = e^{\frac{1}{2}\sum_{j=1}^n \langle O_j^2 \rangle} e^{\sum_{i<j} \langle O_i O_j \rangle}\,, \tag{B.34}$$

with $n=4$, and the bosonic Green functions

$$G_\eta(x)=\langle\phi_\eta(x)\phi_\eta(0)\rangle_\Omega-\langle\phi_\eta^2(0)\rangle_\Omega=\frac{1}{2\pi}\ln\frac{a}{a-i\eta x}\,. \tag{B.35}$$

Substituting Eq. (B.35) into Eq. (B.33) we find

$$\begin{aligned}\mathfrak{C}_r^{(1)}=&\frac{e^{i\vartheta_r k_{\mathrm{F}}\xi}}{(2\pi a)^2}\left[\frac{a}{a-iuz+i\vartheta_r\xi}\right]^{A_+^2}\left[\frac{a}{a-iuz-i\vartheta_r\xi}\right]^{A_-^2}\\&\times\left[\frac{a}{a-iu(t_2-t_1)}\right]^{1+2A_-^2}\prod_{\eta=\pm}\Omega_{r,\eta}^{(1)}(x_\eta,\zeta_\eta,t_1,t_2)\,,\end{aligned} \tag{B.36}$$

with

$$\begin{aligned}\Omega_{r,\eta}^{(1)}(x_\eta,\zeta_\eta,t_1,t_2)=&\left[\frac{a+i\eta(x_\eta+\zeta_\eta/2+\eta ut_1)}{a+i\eta(x_\eta-\zeta_\eta/2+\eta ut_1)}\right]^{\alpha_{r,\eta}}\\&\times\left[\frac{a-i\eta(x_\eta-\zeta_\eta/2+\eta ut_2)}{a-i\eta(x_\eta+\zeta_\eta/2+\eta ut_2)}\right]^{\alpha_{r,\eta}}\,.\end{aligned} \tag{B.37}$$

The exponents $\alpha_{r,\eta}$ are defined in Eq. (3.61). The correlator $\mathfrak{C}_r^{(2)}$ has the same structure as Eq. (B.36) but with different functions $\Omega_{r,\eta}^{(2)}$, which are readily obtained from $\Omega_{r,\eta}^{(1)}$ by taking the complex conjugate of all the factors containing t_2.

The functions $\Omega_{r,+}^{(1,2)}$ and $\Omega_{r,-}^{(1,2)}$ correspond to the right and left moving packets respectively. Therefore their overlap becomes negligible in the long-time limit $t\gg\gamma^{-1}$ (i.e. when the injection is over). In order to further clarify this point, let us focus on Eq. (B.37). The main features of functions $\Omega_{r,\eta}^{(1,2)}$, with respect to the s variable, lie in the regions around their zeros and poles; everywhere else they are not significantly different from 1. If the time t is much greater then all the other variables, the poles and zeros of $\Omega_{r,+}^{(1,2)}$ are well separated from those of $\Omega_{r,-}^{(1,2)}$ and the product in Eq. (B.36) can be thus converted into a sum

$$\prod_{\eta=\pm}\Omega_{r,\eta}^{(1,2)}(x_\eta,\zeta_\eta,t_1,t_2)=\sum_{\eta=\pm}\Omega_{r,\eta}^{(1,2)}(x_\eta,\zeta_\eta,t_1,t_2)-1\,. \tag{B.38}$$

A similar decomposition has been used also in Ref. [126], where electron injection into interacting co-propagating channels is considered. Note that the condition $t\gg t_1,t_2$ is equivalent to $t\gg\gamma^{-1}$ because of the exponential suppression factor $e^{-\gamma(t_1+t_2)}$ present in (B.30). As for variables ξ and z, a restriction of their integration domain such that they satisfy $|\xi|,|uz|\gg ut$ introduces uncertainties of the order of $(ut)^{-1}$ and t^{-1} in the momentum and energy distribution respectively. In the long time limit one has $t\gg\gamma^{-1}\gg\varepsilon_0^{-1}$ and these uncertainty thus become negligible. Eq. (B.38) shows the separation of the two chiral contributions and the structure in Eq. (3.58) is proven.

Finally, the correlator $\mathfrak{C}_r = \mathfrak{C}_r^{(1)} - \mathfrak{C}_r^{(2)}$ reads

$$\mathfrak{C}_r = \frac{e^{i\vartheta_r k_{\mathrm{F}}\xi}}{(2\pi a)^2}\left[\frac{a}{a-iuz+i\vartheta_r\xi}\right]^{A_+^2}\left[\frac{a}{a-iuz-i\vartheta_r\xi}\right]^{A_-^2} \\ \times\left[\frac{a}{a-iu(t_2-t_1)}\right]^{1+2A_-^2}\sum_{\eta=\pm}\Upsilon_{r,\eta}(x_\eta,\zeta_\eta,t_1,t_2)\,, \tag{B.39}$$

where $\Upsilon_{r,\eta} = \Omega_{r,\eta}^{(1)} - \Omega_{r,\eta}^{(2)}$. In order to obtain Eq. (3.59) it is necessary to replace $t_2 = \tau + t_1$, performing the limit $t \to \infty$ and inserting the point-splitting term which is discussed in the next Appendix.

B.4.2 Point splitting procedure

In this Appendix we discuss the point splitting procedure. As explained in the main text, this procedure results in the insertion of the multiplicative factor $(\zeta_\eta - ia\vartheta_r)\zeta_\eta^{-1}$ in the function $\mathcal{C}_{r,\eta}(\xi,z)$, see Eq. (3.60a). In the following we show that it ensures the correct representation of the excess particle density $\delta\rho_r$ in terms of the single electron coherence

$$\delta\rho_r(s,t) = \delta\mathfrak{G}_r(s,t;0,0)\,. \tag{B.40}$$

We emphasize that this additional factor modifies the functions $g_{r,\eta}$ only near $\zeta_\eta = 0$. Therefore the energy and momentum distribution will be affected by the point splitting procedure only for high energies/momenta, i.e. far away from the region we are interested in.

The excess particle density on the r,η channel can be obtained by computing the following bosonic expression directly

$$\delta\rho_{r,\eta}(s,t) \equiv -\frac{\vartheta_r A_{\eta\vartheta_r}}{\sqrt{2\pi}}\,\delta\left[\partial_s\phi_\eta(s-\eta ut)\right] = \eta\vartheta_r A_\eta A_{\eta\vartheta_r} \\ \times\frac{|\lambda|^2}{\pi a}\mathrm{Re}\int_0^t \mathrm{d}t_2\int_0^{t_2}\mathrm{d}t_1 e^{-\gamma(t_1+t_2)-i\varepsilon_0(t_2-t_1)} \\ \times\left[\frac{a}{a-iu(t_2-t_1)}\right]^{1+2A_-^2}\frac{a/\pi}{a^2+[s-\eta u(t-t_2)]^2}\,. \tag{B.41}$$

This expression is consistent with the total injected charge given in Eq. (3.73). Here, we show that the same result is obtained using the relation in Eq. (B.40) and the expressions summarized in Eqs. (3.57-3.60c). In fact, considering the limit of $g_{r,\eta}(s,t;\xi,z)$ for $(\xi,z) \to (0,0)$, a straightforward expansion of the functions $\Upsilon_{r,\eta}$ leads to

$$\begin{aligned}\lim_{\zeta_\eta\to 0} g_{r,\eta}(s,t;\zeta_\eta) = & \frac{|\lambda|^2}{(2\pi a)^2}\int_0^t \mathrm{d}t_2 \int_0^{t_2} \mathrm{d}t_1 e^{-\gamma(t_1+t_2)} e^{-i\varepsilon_0(t_2-t_1)} \left[\frac{a}{a-iu(t_2-t_1)}\right]^{1+2A_-^2} \\ & \times \lim_{\zeta_\eta\to 0}\frac{\zeta_\eta - ia\vartheta_r}{\zeta_\eta}\left[\frac{2ia\eta\alpha_{r,\eta}\zeta_\eta}{a^2+(s-\eta u(t-t_2))^2} + \mathrm{O}(\zeta_\eta^2)\right] = \\ = & \frac{|\lambda|^2}{2\pi a}\eta\vartheta_r\alpha_{r,\eta}\int_0^t \mathrm{d}t_2 \int_0^{t_2}\mathrm{d}t_1 e^{-\gamma(t_1+t_2)} e^{-i\varepsilon_0(t_2-t_1)} \\ & \times \left[\frac{a}{a-iu(t_2-t_1)}\right]^{1+2A_-^2} \frac{a/\pi}{a^2+[s-\eta u(t-t_2)]^2}\,. \end{aligned} \tag{B.42}$$

Then Eq. (B.41) is recovered by taking into account the contribution of $g_r^*(s,t;-\zeta_\eta)$ and recalling that $\alpha_{r,\eta} = A_\eta A_{\eta\vartheta_r}$. Note that without the insertion of the point-splitting factor, the above limit would have been zero.

B.5 Scaling of the energy and momentum distributions

B.5.1 Momentum distribution

In this Appendix we derive the scaling behavior in Eq. (3.75) of the momentum distribution near the Fermi points $\pm k_\mathrm{F}$. Four contributions need to be evaluated, but the calculation is very similar for each of them. First, we note that the behavior of functions $\delta n_{R/L,\eta}(k)$ for k around $\pm k_\mathrm{F}$ is determined by large values of ξ in the Fourier transform in Eq. (3.66). Therefore we can safely neglect the cutoff a with respect to ξ as long as the integrals converge. In particular, for $A_-^2 < 1/2$, one has from Eq. (3.60a)

$$\mathcal{C}_{r,\eta}(\xi,0) = \frac{a}{i\vartheta_r\xi}\left[\frac{a^2}{a^2+\xi^2}\right]^{A_-^2} \to \frac{a^{1+2A_-^2}}{i\vartheta_r\xi}|\xi|^{-2A_-^2}\,. \tag{B.43}$$

Let us now focus on $\delta n_{R,-}(k\approx k_\mathrm{F})$. The integral over the s variable in Eq. (3.67) can be written, in the limit $a\to 0$, as

$$\int_{-\infty}^{+\infty}\chi_{R,-}(s,\xi,\tau)\,\mathrm{d}s = -2i\xi\sin(\pi A_-^2)J(\xi,\tau)\,, \tag{B.44}$$

with

$$J(\xi,\tau)=\int_0^1 \mathrm{d}x\left|\frac{x}{x-1}\,\frac{x-1-u\tau\xi^{-1}}{x-u\tau\xi^{-1}}\right|^{A_-^2} \\ \times\left[\theta(u\tau-\xi x)\theta(\xi x-\xi-u\tau)e^{i\pi A_-^2}+\theta(\xi x-u\tau)\theta(-\xi x+\xi+u\tau)e^{-i\pi A_-^2}\right]. \quad \text{(B.45)}$$

Now, for large ξ it is consistent to neglect $u\tau$ with respect to ξ, obtaining

$$J(\xi,\tau)\approx J_0(\xi)=\theta(-\xi)e^{i\pi A_-^2}+\theta(\xi)e^{-i\pi A_-^2}=e^{-i\pi A_-^2\,\mathrm{sgn}(\xi)}. \quad \text{(B.46)}$$

Inserting Eqs. (B.43), (B.44) and (B.46) into Eq. (3.66), one finds

$$\delta n_{R,-}(k)\approx-\frac{|\lambda|^2}{2\pi\gamma}\,\frac{a^{2A_-^2}\sin(\pi A_-^2)}{2\pi^2 a}\mathrm{Re}\left\{\int_0^{+\infty}\mathrm{d}\tau\,\mathcal{F}(\tau) \\ \times\int_{-\infty}^{+\infty}\mathrm{d}\xi\,\frac{e^{-i(k-k_\mathrm{F})\xi}}{|\xi|^{2A_-^2}}e^{-i\pi A_-^2\,\mathrm{sgn}(\xi)}\right\}. \quad \text{(B.47)}$$

Interestingly, the τ-independence of $J_0(\xi)$ allows to compute the integral over ξ without the need to know the function $\mathcal{F}(\tau)$

$$\int_{-\infty}^{+\infty}\mathrm{d}\xi\,\frac{e^{-i(k-k_\mathrm{F})\xi}}{|\xi|^{2A_-^2}}e^{-i\pi A_-^2\,\mathrm{sgn}(\xi)}= \\ =2\Gamma(1-2A_-^2)\sin(2\pi A_-^2)|k-k_\mathrm{F}|^{2A_-^2-1}\theta(k_\mathrm{F}-k). \quad \text{(B.48)}$$

As a result, the power-law exponent $2A_-^2-1$ is robust with respect to the approximation made in Eq. (3.13), which only affects the expression of $\mathcal{F}(\tau)$.

The final step is to evaluate the real part of the integral over τ. This can be done by exploiting the Fourier representation[223, 222]

$$\left(\frac{a}{a-iu\tau}\right)^g=\frac{1}{\Gamma(g)}\left(\frac{a}{u}\right)^g\int_0^{+\infty}\mathrm{d}E\,E^{g-1}e^{iE\tau}e^{-Ea/u} \quad \text{(B.49)}$$

and leads to (for $\gamma\ll\varepsilon_0$):

$$\mathrm{Re}\left\{\int_0^{+\infty}\mathrm{d}\tau\,\mathcal{F}(\tau)\right\}=\frac{2\pi a\gamma}{|\lambda|^2}. \quad \text{(B.50)}$$

Then one obtains

$$\delta n_{R,-}(k \approx k_{\mathrm{F}}) \approx -\frac{a^{2A_-^2}}{\pi^2}\Gamma(1-2A_-^2)\sin(\pi A_-^2)\sin(2\pi A_-^2) \\ \times |k-k_{\mathrm{F}}|^{2A_-^2-1}\theta(k_{\mathrm{F}}-k)\,. \tag{B.51}$$

The term $\delta n_{R,+}(k \approx k_{\mathrm{F}})$ follows in a similar way

$$\delta n_{R,+}(k \approx k_{\mathrm{F}}) \approx \frac{a^{2A_-^2}}{\pi^2}\Gamma(1-2A_-^2)\sin(\pi A_-^2)\sin(2\pi A_-^2) \\ \times |k-k_{\mathrm{F}}|^{2A_-^2-1}\theta(k-k_{\mathrm{F}})\,. \tag{B.52}$$

Thus the formula for $\delta n_R(k)$ in Eq. (3.75) is proven by combining the last two equations. The calculation for $\delta n_L(k \approx -k_{\mathrm{F}})$ is similar to the one presented above, the only substantial difference being the exponents of the functions $\chi_{L,\eta}$, which are responsible for a different result when computing the integral over ξ. Let us consider for example the contribution $\delta n_{L,-}$. We have

$$\int_{-\infty}^{+\infty} \chi_{L,-}(s,\xi,\tau)\,\mathrm{d}s = -2i\xi\sin(\pi A_+A_-)\bar{J}(\xi,\tau)\,, \tag{B.53}$$

where $\bar{J}$ is identical to Eq. (B.45) except for the exponent which now is A_+A_- instead of A_-^2. Therefore, the asymptotic form of $\bar{J}(\xi,\tau)$ is $\bar{J}_0(\xi) = e^{-i\pi A_+A_-\mathrm{sgn}(\xi)}$. Similar expressions hold for $\delta n_{L,+}$. Inserting these expressions, together with Eq. (B.43), in Eq. (3.66) one obtains

$$\delta n_{L,-}(k \approx -k_{\mathrm{F}}) \approx -\frac{a^{2A_-^2}}{\pi^2}\Gamma(1-2A_-^2)\sin(\pi A_+A_-)|k+k_{\mathrm{F}}|^{2A_-^2-1} \\ \times \{\sin[\pi(A_+A_-+A_-^2)]\theta(-k-k_{\mathrm{F}})+\sin[\pi(A_-^2-A_+A_-)]\theta(k+k_{\mathrm{F}})\}\,, \tag{B.54a}$$

$$\delta n_{L,+}(k \approx -k_{\mathrm{F}}) \approx \frac{a^{2A_-^2}}{\pi^2}\Gamma(1-2A_-^2)\sin(\pi A_+A_-)|k+k_{\mathrm{F}}|^{2A_-^2-1} \\ \times \{\sin[\pi(A_+A_-+A_-^2)]\theta(k+k_{\mathrm{F}})+\sin[\pi(A_-^2-A_+A_-)]\theta(-k-k_{\mathrm{F}})\}\,. \tag{B.54b}$$

The formula for $\delta n_L(k)$ in Eq. (3.75) follows from the last two expressions.

B.5.2 Energy distribution

In this Appendix we evaluate the expression in Eq. (3.89) of the energy distribution for small ω. In particular, we focus on the term $\delta\mathcal{A}_{R,-}$ in Eq. (3.87). The other contributions can be evaluated in the same way. First of all, we note that the behavior of function $\delta\mathcal{A}_{R,-}$ at small ω is described by large z in the Fourier transform in Eq. (3.87). One then has

$$\mathcal{C}_{R,-}(0,z) = \left[\frac{a}{a-iuz}\right]^{1+2A_-^2} \to \frac{ia^{1+2A_-^2}}{zu^{1+2A_-^2}} \frac{e^{i\pi A_-^2 \operatorname{sign}(z)}}{|z|^{2A_-^2}}. \tag{B.55}$$

Moreover, in complete analogy with the previous Appendix, the integral over s in Eq. (3.87) can be expressed as

$$\int_{-\infty}^{+\infty} \chi_{R,-}(s,uz,\tau)\,\mathrm{d}s = -2iuz\sin(\pi A_-^2)J(uz,\tau)\,, \tag{B.56}$$

where function J and its asymptotic expression are provided in Eqs. (B.45) and (B.46) respectively. Next, substituting these expressions in Eq. (3.87), one obtains

$$\delta\mathcal{A}_{R,-}(\omega) \approx \frac{|\lambda|^2}{2\pi\gamma}\frac{\sin(\pi A_-^2)}{2\pi^2 a}\mathrm{Re}\left\{\int_0^{+\infty}\mathrm{d}\tau\,\mathcal{F}(\tau)\left(\frac{a}{u}\right)^{2A_-^2}\int_{-\infty}^{+\infty}\mathrm{d}z\,\frac{e^{i\omega z}}{|z|^{2A_-^2}}\right\}. \tag{B.57}$$

The integral over z yields

$$\int_{-\infty}^{+\infty}\mathrm{d}z\,\frac{e^{i\omega z}}{|z|^{2A_-^2}} = 2\Gamma(1-2A_-^2)\sin(\pi A_-^2)\,\omega^{2A_-^2-1}. \tag{B.58}$$

Finally, using Eq. (B.50), one finds ($\omega > 0$)

$$\delta\mathcal{A}_{R,-}(\omega\approx 0) \approx \left(\frac{a}{u}\right)^{2A_-^2}\frac{\Gamma(1-2A_-^2)}{\pi^2}\sin^2(\pi A_-^2)\,\omega^{2A_-^2-1}. \tag{B.59}$$

The result for $\delta\mathcal{A}_{R,+}(\omega)$ is exactly the same, while for the L-channel we also find $\delta\mathcal{A}_{L,+}(\omega) = \delta\mathcal{A}_{L,-}(\omega)$, with

$$\delta\mathcal{A}_{L,-}(\omega\approx 0) \approx \left(\frac{a}{u}\right)^{2A_-^2}\frac{\Gamma(1-2A_-^2)}{\pi^2}\sin^2(\pi A_+ A_-)\,\omega^{2A_-^2-1}. \tag{B.60}$$

Combining the last two results we readily arrive at Eq. (3.89).

Appendix C

Quantum quenches in LL

C.1 The generalized Gibbs ensemble

Here we want to briefly show how to build the so-called generalized Gibbs ensemble (GGE) reached by a LL in the thermodynamic limit[1]. Since the diagonalized LL Hamiltonian H in Eq. 2.25 is quadratic in the bosons $\beta_{\eta,q}$, the occupation numbers of each mode are conserved by the unitary evolution of the system

$$\left[H, \beta^\dagger_{\eta,q}\beta_{\eta,q}\right] = 0\,. \tag{C.1}$$

These constraints strongly influence the time evolution of the system and it has been conjectured [172] (and analytically demonstrated [174]) that it eventually reach a steady state described by the GGE density matrix

$$\hat{\rho}_{\mathrm{GGE}} = \frac{1}{Z_{\mathrm{GGE}}} e^{-\sum_{\eta,q}\lambda_{\eta,q}\beta^\dagger_{\eta,q}\beta_{\eta,q}} \tag{C.2}$$

whit $Z_{\mathrm{GGE}} = \mathrm{Tr}\left[\exp\left(-\sum_{\eta,q}\lambda_{\eta,q}\beta^\dagger_{\eta,q}\beta_{\eta,q}\right)\right]$. The Lagrange multipliers $\lambda_{\eta,q}$ are determined by imposing that the integral of motions $\beta^\dagger_{\eta,q}\beta_{\eta,q}$ are equal to their initial (i) value,

$$\langle \beta^\dagger_{\eta,q}\beta_{\eta,q}\rangle_i = \langle \beta^\dagger_{\eta,q}\beta_{\eta,q}\rangle_{\mathrm{GGE}} = \frac{1}{e^{\lambda_{\eta,q}} - 1}\,. \tag{C.3}$$

It is worth it to underline that the result (C.2) can be obtained by maximizing the von Neumann entropy $S = -\mathrm{Tr}[\hat{\rho}\log\hat{\rho}]$ subject to the constraints imposed by the conservation of the integral of motions [172, 224]. Moreover, note that if in a system the only two conserved quantities are the total energy and the total number of particles, the GGE density matrix in

---

[1] A system with finite size features finite recurrence times and thus will not reach a steady state.

(C.2) reduces to the standard equilibrium Gibbs grand canonical ensemble. For more details, we remind to the literature [174, 172, 168, 173, 224].

C.2 Quenched fermionic and bosonic correlators

C.2.1 Fermionic green functions

Here we compute and express the four different regimes of the lesser local green function in Eq. 3.106. If both time arguments are negative (n), the Green function is not affected by the subsequent quench and it thus reduces to the standard equilibrium result

$$\mathcal{G}_r^{nn}(t,\bar{t}) = \frac{i}{2\pi a} \exp\left[2\pi\left(B_+^2 + B_-^2\right)\mathfrak{C}_+\left(u_i(t-\bar{t})\right)\right] \qquad (t,\bar{t}<0). \tag{C.4}$$

Here, we have introduced the equal time bosonic correlator

$$\mathfrak{C}_+(x) \equiv \langle \phi_{i,+}(x,0)\phi_{i,+}(0,0)\rangle_{eq} - \langle \phi_{i,+}^2(0,0)\rangle_{eq} \tag{C.5}$$

whose expectation value on the initial thermal state is [82]

$$\mathfrak{C}_+(x) = \frac{1}{2\pi}\ln\frac{\left|\Gamma(1+T\omega_i^{-1} - iTxu_i^{-1})\right|^2}{\Gamma(1+T\omega_i^{-1})^2} + \frac{1}{2\pi}\ln\left(\frac{1}{1-ixa^{-1}}\right), \tag{C.6}$$

with $\Gamma(z)$ the Euler Gamma function and $\omega_i = u_i a^{-1}$ a cut-off frequency. Note that, being a local correlator, one has $\mathfrak{C}_+(x) = \mathfrak{C}_-(-x)$ where

$$\mathfrak{C}_-(x) \equiv \langle \phi_{i,-}(x,0)\phi_{i,-}(0,0)\rangle_{eq} - \langle \phi_{i,-}^2(0,0)\rangle_{eq}\,. \tag{C.7}$$

It is worth to notice that $\mathcal{G}_r^{nn}(t,\bar{t})$ depends only on the time difference $\tau = t-\bar{t}$. By contrast, if $t>0$ and $\bar{t}<0$ one has

$$\begin{aligned}\mathcal{G}_r^{pn}(t,\bar{t}) = \frac{i}{2\pi a}\exp\Big[&2\pi\,\theta_+(B_+A_+ + B_-A_-)\,\mathfrak{C}_+(u_i(t-\bar{t}) + (u_f-u_i)t) \\ &+2\pi\,\theta_-(B_+A_- + B_-A_+)\,\mathfrak{C}_+(u_i(t-\bar{t}) - (u_f+u_i)t) \\ &+2\pi A_+A_-\theta_+\theta_-(\mathfrak{C}_+(2u_ft) + \mathfrak{C}_+(-2u_ft))\Big].\end{aligned} \tag{C.8}$$

The opposite regime ($t<0$, $\bar{t}>0$) can be easily obtained by exploiting $\mathcal{G}_r^{np}(t,\bar{t}) = -\mathcal{G}_r^{pn}(\bar{t},t)^*$.

Finally, the fourth regime, when both t and $\bar{t}$ are positive, is the most interesting one and can be expressed as

$$\begin{aligned}\mathcal{G}_r^{pp}(t,\bar{t}) = \frac{i}{2\pi a}\exp\Big[&2\pi\,\theta_+^2(A_+^2+A_-^2)\,\mathfrak{C}_+(-u_f(t-\bar{t}))+2\pi\,\theta_-^2(A_+^2+A_-^2)\,\mathfrak{C}_+(u_f(t-\bar{t}))\\&+2\pi A_-A_+\theta_+\theta_-(\mathfrak{C}_+(u_f(t+\bar{t}))+\mathfrak{C}_+(-u_f(t+\bar{t})))\\&-2\pi A_-A_+\theta_+\theta_-(\mathfrak{C}_+(u_ft)+\mathfrak{C}_+(-u_ft)+\mathfrak{C}_+(2u_f\bar{t})+\mathfrak{C}_+(-2u_f\bar{t}))\Big].\end{aligned} \tag{C.9}$$

Analytical structure

The expressions (C.4), (C.8), and (C.9) in terms of the bosonic correlator (C.6) allows to study their analytical structure. Focusing for simplicity on the zero-temperature limit one can easily show that each term

$$e^{2\pi\alpha\mathfrak{C}(x)} = \left(\frac{1}{1-ixa^{-1}}\right)^{\alpha} \tag{C.10}$$

has a branch point in $x=0$. Using the notation $\bar{t}=t-\tau$ we can thus conclude that

- $\mathcal{G}_r^{pp}(t,t-\tau)$ has branch points in $\tau\simeq 0$, t, $2t$ and $t\simeq 0$.
- $\mathcal{G}_r^{pn}(t,t-\tau)$ has branch points in $\tau\simeq t\frac{u_i+u_f}{u_i}$, $t\frac{u_i-u_f}{u_i}$ and $t\simeq 0$.
- $\mathcal{G}_r^{nn}(t,t-\tau)$ has branch points in $\tau\simeq 0$.

C.3 Asymptotic analysis of quench-induced dynamics

C.3.1 Bosonic correlators

To properly study the relaxation dynamics of the quenched system, it is useful to derive asymptotic expressions for the bosonic cross-correlator $D_{\alpha,-\alpha}(t,\tau)$ (see Eq. (3.113) and Eq. (3.114)). For the zero-temperature contribution of $D^{(0)}_{\alpha,-\alpha}(t,\tau)$ the relevant time scale is τ and for $t\gg\tau$ one finds

$$D^{(0)}_{\alpha,-\alpha}(t,\tau) = -\frac{\theta_+\theta_-}{\pi}\left(\frac{\tau}{2t}\right)^2+O\left(\frac{\tau}{t}\right)^3. \tag{C.11}$$

Inspecting the temperature-dependent term $\Delta D_{\alpha,-\alpha}(t,\tau)$, an additional time scale $(\Lambda T)^{-1}$ emerges and two different regimes of the gamma functions, present in Eq. (3.114), have to be

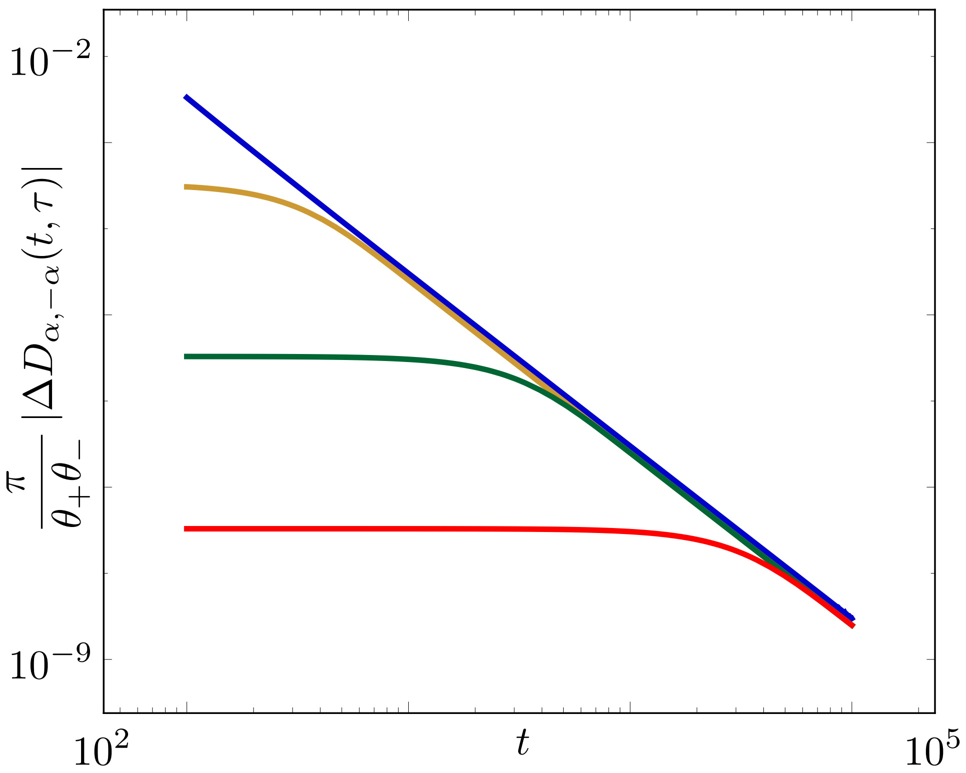

Fig. C.1 Plot of $\frac{\pi}{\theta_+\theta_-}|\Delta D_{\alpha,-\alpha}(t,\tau)|$ as a function of time t for different temperatures: $T=10^{-4}$ (red), $T=10^{-3}$ (green), $T=10^{-2}$ (yellow), $T=10^{-1}$ (blue). Here, $\tau=10$, $K_i=0.9$, $K_f=0.6$, time units ω_f^{-1} and temperature units ω_i.

considered

$$\left|\Gamma(1+T\omega_i^{-1}+iT\Lambda t)\right|^2 \approx \begin{cases} 2\pi(T\Lambda t)^{1+2T\omega_i^{-1}}e^{-\pi T\Lambda t} & t\gg(\Lambda T)^{-1} \\ \Gamma^2(1+T\omega_i^{-1})\left[1-(T\Lambda t)^2\Gamma(1,1+T\omega_i^{-1})\right] & t\ll(\Lambda T)^{-1} \end{cases}, \tag{C.12}$$

where $\Gamma(n,z)$ is the n-th order polygamma function.

Inserting Eq. (C.12) in the expression (3.114) for $\Delta D_{\alpha,-\alpha}(t,\tau)$ and considering the reasonable temperature regime $T\ll\omega_i$, one obtains the leading terms

$$\Delta D_{\alpha,-\alpha}(t,\tau)\approx\frac{\theta_+\theta_-}{\pi}\begin{cases} 2(T\Lambda\tau)^2\Gamma(1,1+T\omega_i^{-1}) & \tau\ll t\ll(\Lambda T)^{-1} \\ (1+2T\omega_i^{-1})\left(\frac{\tau}{2t}\right)^2 & \tau\ll(\Lambda T)^{-1}\ll t \end{cases}. \tag{C.13}$$

The validity of this asymptotic expansion is confirmed in Fig. C.1, where we have numerically evaluated $\Delta D_{\alpha,-\alpha}(t,\tau)$ as a function of time t for different temperatures and at fixed τ. At short time $t\ll(\Lambda T)^{-1}$ the thermal component of the cross-correlator saturates to a time-independent value, while a power law decay $\propto t^{-2}$ is evident for $t\gg(\Lambda T)^{-1}$, in accordance with Eq. (C.13).

By combining the asymptotic expressions (C.11) and (C.13) one eventually get the complete asymptotic expression (3.116) for $D_{\alpha,-\alpha}(t,\tau)$.

C.3.2 Non-equilibrium spectral function

Here we discuss the asymptotic expansion of the non-equilibrium spectral functions.

Function $\mathcal{A}_r^{(2)}$

In order to study $\mathcal{A}_r^{(2)}(\omega,t)$, it is useful to introduce $z=t-\tau$ and expand the integrand retaining only the leading term in z/t. The result reads

$$\mathcal{A}_r^{(2)}(\omega,t) = \frac{e^{i\omega t}}{a}\,\frac{\left|\Gamma(1+T\omega_i^{-1}+2iT\Lambda t)\right|^{4\gamma}\left|\Gamma(1+T\omega_i^{-1}+iT\Lambda t)\right|^{2(\nu_++\nu_--4\gamma)}}{(\omega_f t)^{\nu_++\nu_--2\gamma}}\, f(T,\omega), \tag{C.14}$$

with

$$f(T,\omega) = \frac{1}{(2\pi)^2 4^\gamma}\left[\Gamma(1+T\omega_i^{-1})\right]^{-2(\nu_++\nu_-)}\int_0^\infty dz\, e^{-i\omega z}\left[\frac{\left|\Gamma(1+T\omega_i^{-1}+2iT\Lambda z)\right|^4}{1+4\omega_f^2 z^2}\right]^\gamma. \tag{C.15}$$

Using Eq. (C.12), one can identify two asymptotic regimes

$$\begin{aligned}\mathcal{A}_r^{(2)}(\omega,t) &\approx \frac{f(T,\omega)}{a}\, e^{i\omega t}(\omega_f t)^{-\xi}\\ &\times\begin{cases}\left[\Gamma^2(1+T\omega_i^{-1})\right]^\xi & t\ll(\Lambda T)^{-1}\\ \left[2^{4\gamma}(2\pi)^{2\xi}(T\Lambda t)^{\xi(1+2T\omega_i^{-1})}\right]e^{-2\pi T\Lambda t(\nu_++\nu_-)} & t\gg(\Lambda T)^{-1},\end{cases}\end{aligned} \tag{C.16}$$

with

$$\xi = \nu_+ + \nu_- - 2\gamma. \tag{C.17}$$

a non-universal exponent encoding the strength of the interaction quench. The first regime, for $t\ll(\Lambda T)^{-1}$, is a typical interaction-dependent power law. On the other hand, for $t\gg(\Lambda T)^{-1}$, a fast exponential decay kicks in and kills $\mathcal{A}_r^{(2)}(\omega,t)$ in the long-time limit.

Function $\mathcal{A}_r^{pn}$

The asymptotic behaviour of $\mathcal{A}_r^{pn}(\omega,t)$, defined in Eq. (3.118), can be computed along the lines of $\mathcal{A}_r^{pp}(\omega,t)$. In this case, the integrand contributes only for $\tau\sim t$ (integration boundary) and $\tau \sim t(u_i+u_f)u_i^{-1}$. One can show that

$$\mathcal{A}_r^{pn}(\omega,t) = \mathcal{A}_r^{(3)}(\omega,t) + \mathcal{A}_r^{(4)}(\omega,t), \tag{C.18}$$

where the contribution stemming from the expansion for $\tau \to t$ is given by

$$\begin{aligned}\mathcal{A}_r^{(3)}(\omega,t) \approx & \left\{ \frac{i^{\nu_- - \nu_+}}{u_f[\Gamma(1+T\omega_i^{-1})]^{2\xi}(2\pi)^2} \right\} e^{i\omega t}\,(\omega_f t)^{-\xi} \\ & \times \begin{cases} 2^{-2\gamma}\,\Gamma(1+T\omega_i^{-1})^{2\xi} & t \ll (\Lambda T)^{-1} \\ \left[(T\Lambda t)^{(1+2T\omega_i^{-1})\xi}\,(2\pi)^{\xi-2\gamma}2^{2\gamma T\omega_i^{-1}}\right] e^{-\pi T\Lambda t\xi} & t \gg (\Lambda T)^{-1} \end{cases}\end{aligned} \tag{C.19}$$

while the one for $\tau \to t(u_i+u_f)u_i^{-1}$ is given by

$$\begin{aligned}\mathcal{A}_r^{(4)}(\omega,t) \approx & \left\{ \frac{(-i)^{\nu_- - 2\gamma} j(\omega)}{a(2\pi)^2[\Gamma(1+T\omega_i^{-1})]^{2\xi}} \right\} e^{i\omega t\left(1+\frac{u_f}{u_i}\right)}\,(2\omega_f t)^{-\nu_-} \\ & \times \begin{cases} \Gamma(1+T\omega_i^{-1})^{2\nu_- - 4\gamma} & t \ll (\Lambda T)^{-1} \\ [2\pi(T\Lambda t)^{(1+T\omega_i^{-1})}]^{(\nu_- - 2\gamma)}\,e^{-\pi T\Lambda t(\nu_- - 2\gamma)} & t \gg (\Lambda T)^{-1} \end{cases}.\end{aligned} \tag{C.20}$$

where function $j(\omega)$ reads

$$j(\omega) = \int_{-\infty}^{\infty} dz e^{i\omega z}\left(\frac{1}{1+i\omega_f z}\right)^{\nu_+ - 2\gamma} \left|\Gamma(1+T\omega_i^{-1}+iT\Lambda z)\right|^{\nu_+ - 2\gamma}. \tag{C.21}$$

As one can see, $\mathcal{A}_r^{pn}(\omega,t)$ qualitatively behaves like $\mathcal{A}_r^{(2)}(\omega,t)$. There is a regime $t \ll (\Lambda T)^{-1}$ where it features non-universal power-law decays. Here one can show that, for direct quenches ($K_f < K_i$) $\xi < \nu_-$, while for inverse quenches ($K_f > K_i$) the opposite holds (see Sec. C.3.3). In any case, when temperature effects kick in at long times $t \gg (\Lambda T)^{-1}$, both power laws are killed by a fast and non-universal exponential decay.

C.3.3 Quench-dependent exponents

In studying the behavior of the transient of the non-equilibrium spectral $\delta A_r(\omega,t)$, defined in , we encountered several quench-dependent exponents. Here we will give their explicit expressions in terms of K_i and K_f and study their behavior. In particular one has

$$\nu_+ = \frac{(K_f - K_i)^2(1+K_f^2)}{8K_f^2 K_i} \geq 0 \tag{C.22}$$

$$\nu_- = \frac{(K_f + K_i)^2(1+K_f^2)}{8K_f^2 K_i} \geq 1 \tag{C.23}$$

$$\nu_- - 2\gamma = \frac{(K_i + K_f)(1+K_i K_f)}{4K_i K_f} \geq 1 \tag{C.24}$$

$$\xi = \frac{K_f^4 + 3K_f^2(1+K_i^2) + K_i^2}{3K_f^2 K_i} \geq 1\,. \tag{C.25}$$

By looking at Table 3.1, it is clear that in the regime $t \ll (\Lambda T)^{-1}$ there is a competition between three power laws: the universal one t^{-2} and the two non-universal ones $t^{-\xi}$ and $t^{-\nu_-}$. In order to identify the leading term in the decay, it is useful to plot ξ as well as

$$\xi - \nu_- = \frac{(K_i^2+1) - (K_f^2+1)}{4K_i K_f} \tag{C.26}$$

for reasonable quenches, i.e. for $0.5 < K_i, K_f < 1$ [225]. Fig. C.2a shows that $\xi \geq 1$ does not dramatically exceed 1. Fig. C.2b shows that the difference vanishes along the non-quench line $K_i = K_f$: in the lower triangle where $K_i > K_f$ the quenches are direct and the dominant exponent is ξ. By contrast, in the upper triangle (inverse quenches) the dominant exponent is ν_-. Note that, in any case, the difference between the exponent is rather small and it is likely that both of them have to be taken into account to properly describe the transient of the spectral function.

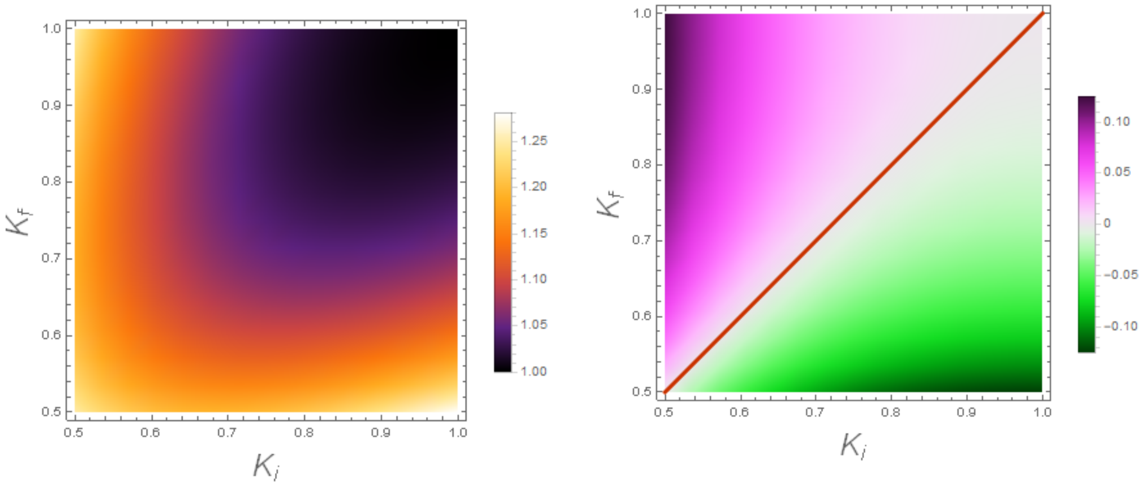

(a) Values of the non-universal exponent $\xi(K_i, K_f)$.

(b) Function $\xi(K_i, K_f) - \nu_-(K_i, K_f)$, which vanishes along the red line $K_i = K_f$

Fig. C.2 Study of the non-universal exponents ξ and ν_-.

Appendix D

Mapping from parafermions to fermions

Here we want to describe in details the procedure which allows to derive the full-lattice mapping between FPFs and fermions, stated in Eq. (4.42) of the fourth chapter. First of all, it is worth noting that the parafermionic algebra of α_i and β_i is handed down to the FPFs in their properties:

$$d_l d_j = i\, d_j d_l, \quad d_l^\dagger d_j = -i\, d_j d_l^\dagger \quad \text{for } l < j, \tag{D.1}$$

$$d_j^{\dagger m} d_j^m + d_j^{4-m} d_j^{\dagger(4-m)} = 1 \quad \text{for } m = 1,2,3 \tag{D.2}$$

$$d_j^4 = 0 \quad \forall j. \tag{D.3}$$

As stated in the fourth chapter, the key idea of our mapping to electrons is to identify the single-site four-dimensional parafermionic Fock space with the Fock space of spin-$1/2$ fermions. We thus focus on a single site with FPF annihilation operator d and fermionic operators $c_{\uparrow,\downarrow}$. A natural choice of a FPF basis is $\{|0\rangle, |1\rangle, |2\rangle, |3\rangle\}$, where $|n\rangle$ are the eigenstates of the FPF number operator N with eigenvalue n. As for the fermions, we can for instance choose the basis

$$\left\{|E\rangle,\, c_\uparrow^\dagger|E\rangle,\, ic_\uparrow^\dagger c_\downarrow^\dagger|E\rangle,\, -ic_\downarrow^\dagger|E\rangle\right\}, \tag{D.4}$$

where $|E\rangle$ denotes the vacuum state, $c_\sigma|E\rangle = 0$. The identification between these two bases induces the mapping in Eq. (4.41) of the fourth chapter,

$$d = c_\downarrow^\dagger c_\uparrow c_\downarrow - c_\uparrow^\dagger c_\downarrow^\dagger c_\downarrow + ic_\uparrow^\dagger c_\uparrow c_\downarrow + c_\uparrow\,, \tag{D.5}$$

which automatically satisfies the algebra of Eq. (D.2) and Eq. (D.3). In order to demonstrate the validity of the mapping in Eq. (D.5), we note that the action of the FPF annihilation operator d on the basis states $|n\rangle$ is known by construction and reads $d|n\rangle = |n-1\rangle$ for $n = 1,2,3$ and $d|0\rangle = 0$. Its fermionic counterpart must behave in the same way when applied to the corresponding four fermionic basis states $|f_n\rangle$. Using the projectors on these states, one has

$$\begin{aligned} d &= 0|f_0\rangle\langle f_0| + c_\uparrow|f_1\rangle\langle f_1| - ic_\uparrow|f_2\rangle\langle f_2| - c_\uparrow^\dagger|f_3\rangle\langle f_3| \\ &= c_\uparrow(1-n_\downarrow)(n_\uparrow) - ic_\uparrow(n_\uparrow n_\downarrow) - c_\uparrow^\dagger(1-n_\uparrow)n_\downarrow \\ &= c_\uparrow + c_\downarrow^\dagger c_\uparrow c_\downarrow + ic_\uparrow^\dagger c_\uparrow c_\downarrow - c_\uparrow^\dagger c_\downarrow^\dagger c_\downarrow , \end{aligned} \tag{D.6}$$

which corresponds to Eq. (4.41). This relation can be inverted, resulting in

$$c_\uparrow = d - d^\dagger d^2 - d^{\dagger 3} d^2 , \tag{D.7}$$

$$c_\downarrow = -id^3 - id^\dagger d^2 + id^{\dagger 2} d^3 \,. \tag{D.8}$$

The next step is to extend this mapping over the full lattice. As pointed out in Ref. [210], an FPF annihilation operator on site j can be built as

$$d_j = i^{\sum_{p<j} N_p} \underbrace{\mathbb{I}\otimes\cdots\otimes\mathbb{I}}_{j-1} \otimes d \otimes \underbrace{\mathbb{I}\otimes\cdots\otimes\mathbb{I}}_{L-j} \tag{D.9}$$

where $N_p = d_p^\dagger d_p + d_p^{\dagger 2} d_p^2 + d_p^{\dagger 3} d_p^3$ is the FPF number operator on site p and the $\mathbb{I}$ are identity operators on a single site. This construction ensures that the FPF commutator algebra in Eq. (D.1) is fulfilled. As for the fermions, one uses the standard Jordan-Wigner strings,

$$c_{j\sigma} = (-1)^{\sum_\sigma \sum_{p<j} n_{p\sigma}} \underbrace{\mathbb{I}\otimes\cdots\otimes\mathbb{I}}_{j-1} \otimes c_\sigma \otimes \underbrace{\mathbb{I}\otimes\cdots\otimes\mathbb{I}}_{L-j} \tag{D.10}$$

where $n_{p\sigma} = c_{p\sigma}^\dagger c_{p\sigma}$ is the number of fermions with spin σ on site p. Combining the above equations, one readily obtains the full lattice mapping

$$d_j = i^{\sum_{p<j}(N_p + 2n_{p\uparrow} + 2n_{p\downarrow})} \left(c_{j\downarrow}^\dagger c_{j\uparrow} c_{j\downarrow} + c_{j\uparrow} - c_{j\uparrow}^\dagger c_{j\downarrow}^\dagger c_{j\downarrow} + ic_{j\uparrow}^\dagger c_{j\uparrow} c_{j\downarrow} \right) \tag{D.11}$$

$$c_{j\uparrow} = i^{\sum_{p<j}(-N_p + 2n_{p\uparrow} + 2n_{p\downarrow})} \left[d_j - d_j^\dagger d_j^2 - (-1)^{\sum_{p<j} N_p}\, d_j^{\dagger 3} d_j^2 \right] \tag{D.12}$$

$$c_{j\downarrow} = i^{\sum_{p<j}(-N_p + 2n_{p\uparrow} + 2n_{p\downarrow})} (-i) \left[(-1)^{\sum_{p<j} N_p}\, d_j^3 + d_j^\dagger d_j^2 - d_j^{\dagger 2} d_j^3 \right] . \tag{D.13}$$

Interestingly, as stated in the main text, because of the definite odd fermion parity of Eq. (D.11) every parafermionic operators D which conserves the number of FPFs modulo 4 is transformed into a fermionic operator C *without* string factors. To see this, consider a generic operator D which involves FPF operators on m adjacent lattice sites

$$D = d_j^{\dagger \alpha_0} d_j^{\beta_0} \, \dots \, d_{j+m}^{\dagger \alpha_m} d_{j+m}^{\beta_m}. \tag{D.14}$$

where $\alpha_k, \beta_k \in \{0,1,2,3\}$. Using the mapping in Eq. (D.11), its fermionic expression factorizes into a form

$$D = i^{\sum_{p<j} \left[\sum_{i=0}^{m} (\beta_i - \alpha_i)\right] \left(N_p + 2n_{p\uparrow} + 2n_{p\downarrow}\right)} \, C, \tag{D.15}$$

with the operator C containing, up to prefactors, only fermion operators on sites $j, \dots, j+m$. Requiring that D conserves the total number of FPFs modulo 4 then implies

$$\sum_{i=0}^{m} (\beta_i - \alpha_i) = 0 \pmod 4, \tag{D.16}$$

so the string factor cancels. This remarkable result is at the heart of the locality of our mapping between parafermion chain Hamiltonians and electronic systems.

Appendix E

Fermionic description of the exactly solvable model

E.1 Fermionic ground states

In this section we focus on the properties of the four degenerate fermionic ground states of H_J, defined in Eq. (4.26) of the fourth chapter. Following Ref. [226], the ground states $|\psi_m\rangle$ of H_J (where $m = 0, \ldots, 3$ is the number of FPF modulo 4) can be expressed as

$$|\psi_m\rangle = \frac{1}{\sqrt{4^{L-1}}} \sum_{\substack{\{n_j\} \text{ such that} \\ \sum_j n_j = m \pmod 4}} \bigotimes_{j=1}^{L} |n_j\rangle \tag{E.1}$$

where $|n_j\rangle$ is the single-site state with n_j FPF. The proof of Eq. (E.1) is obtained by introducing the operator

$$\xi_j = \frac{1}{\sqrt{2}} \left[d_j i^{N_j} + d_j^{\dagger 3} - i \left(d_{j+1} + d_{j+1}^{\dagger 3} \right) \right] \tag{E.2}$$

which allows to write the Hamiltonian as

$$H_J = -2J(L-1) + 2J \sum_{j=1}^{L-1} \xi_j^\dagger \xi_j \, , \tag{E.3}$$

where the second term is non-negative. A state is a ground state if $\xi_j |\psi\rangle = 0 \; \forall j$, a condition which is fulfilled by Eq. (E.1). Note that excited states can be obtained from the ground states $|\psi_m\rangle$ by applying $\xi_j^\dagger$. The energy gap between the ground states and the first excited states is $2J$.

Our mapping allows us to express these ground states in terms of fermions: one simply has to replace each FPF single-site state $|n_j\rangle$ with the corresponding fermionic one, which we will call $|f_{n_j}\rangle$. This will allow us to directly study some interesting fermionic properties of the ground states. In the following, the integer indexes of $|\psi_m\rangle$ and $|f_n\rangle$ are always understood modulo 4.

E.2 Fermionic edge operators

The goal here is to show that, despite the intrinsic non-locality of β_L (see Eq. (4.51) in the fourth chapter), it is still possible to find *local* operators at either edge of the fermionic chain that cycle through the four degenerate ground states $|\psi_m\rangle$.

If we focus on the left edge ($j = 1$), it is easy to show that the parafermionic operator a_1 actually does the job. Indeed, being on the first site of the chain, its fermionic expression has no string factors (see Eq. (4.51) in the fourth chapter). Moreover, it decreases by one the number of FPF modulo 4 on the first chain site. Therefore, one has for all ground states,

$$\alpha_1|\psi_m\rangle = |\psi_{m-1}\rangle \tag{E.4}$$

Things are more complicated at the right edge ($j = L$), where one has to take care of string factors. For notational convenience, let us introduce the following state of a fermionic chain with S sites

$$|b_m^S\rangle = \frac{1}{\sqrt{4^{S-1}}} \sum_{\substack{\{n_j\} \text{ such that} \\ \sum_j n_j = m \ (\mathrm{mod}\ 4)}} \bigotimes_{j=1}^{S} |f_{n_j}\rangle\,. \tag{E.5}$$

This allows us to express the four ground states as

$$|\psi_m\rangle = \frac{1}{2}\Big(|b_0^{L-1}\rangle \otimes |f_m\rangle + |b_1^{L-1}\rangle \otimes |f_{m-1}\rangle + |b_2^{L-1}\rangle \otimes |f_{m-2}\rangle + |b_3^{L-1}\rangle \otimes |f_{m-3}\rangle\Big) \tag{E.6}$$

In view of the chosen fermionic basis (see Eq. (D.4)), the state $|b_m^{L-1}\rangle$ contains an even or an odd number of fermionic operators acting on the empty chain, depending on whether m is even or odd, respectively. As a consequence, in order to be able to cycle between the four ground states, a local fermionic edge operator γ_L must satisfy

$$\gamma_L \left(\bigotimes_{j=1}^{L-1} \mathbb{I}\right) \otimes |f_m\rangle = (-1)^{m-1} \left(\bigotimes_{j=1}^{L-1} \mathbb{I}\right) \otimes |f_{m-1}\rangle\,. \tag{E.7}$$

It is easy to show that

$$\gamma_L = c^{\dagger}_{L\uparrow} n_{L\downarrow} - i c_{L\downarrow} n_{L\uparrow} + c_{L\uparrow}(1 - n_{L\downarrow}) + i c^{\dagger}_{L\downarrow}(1 - n_{L\uparrow}) \tag{E.8}$$

satisfies the above condition and thus represents a fermionic edge operator which cycles between the four ground states

$$\gamma_L |\psi_m\rangle = |\psi_{m-1}\rangle \tag{E.9}$$

E.3 Effects of local fermionic perturbations

Here we compute, using DMRG simulations, the effects of some local fermionic perturbations on the 4-fold degeneracy of the ground states. At first, we focus on a magnetic field along the y axis (see Eq. (4.52) in the fourth chapter)

$$H_y = B_y \sum_{j=1}^{L} i \left(c^{\dagger}_{j,\downarrow} c_{j,\uparrow} - c^{\dagger}_{j,\uparrow} c_{j,\downarrow} \right) = B_y \sum_{i=1}^{L} \left(M_j + i \eta_{\uparrow,j} \eta_{\downarrow,j} \right) \tag{E.10}$$

which explicitly contains the local order parameter M_j and it is therefore expected to split the 4 ground states into two doublets. They are separated by energy ΔE_y which grows linearly with the system size, as shown in Fig. E.1. The saturation around $\Delta E_y \sim 2J$ is due to the presence of the bulk gap.

By contrast, magnetic fields in the (x,z)-plane and chemical potential terms

$$H_z = B_z \sum_{j,\sigma} \sigma\, c^{\dagger}_{\sigma,j} c_{\sigma,j} \tag{E.11}$$

$$H_x = B_x \sum_{j} c^{\dagger}_{j,\downarrow} c_{j,\uparrow} + h.c. \tag{E.12}$$

$$H_\mu = \mu \sum_{j,\sigma} c^{\dagger}_{\sigma,j} c_{\sigma,j} \tag{E.13}$$

lead to a degeneracy lifting which is exponentially suppressed with the system length L. This is clearly shown in Fig. E.2 where we display the energy splitting ΔE_μ between the ground state and the fourth eigenstate of the system when a chemical potential term H_μ is added to H_J. The energy splittings ΔE_z and ΔE_x (due to H_z and H_x respectively) happen to be the same as ΔE_μ.

Interestingly, both H_μ and H_z, conserve the total number of FPF modulo 4 and they thus feature a local expression also in terms of parafermions: neglecting an inessential constant

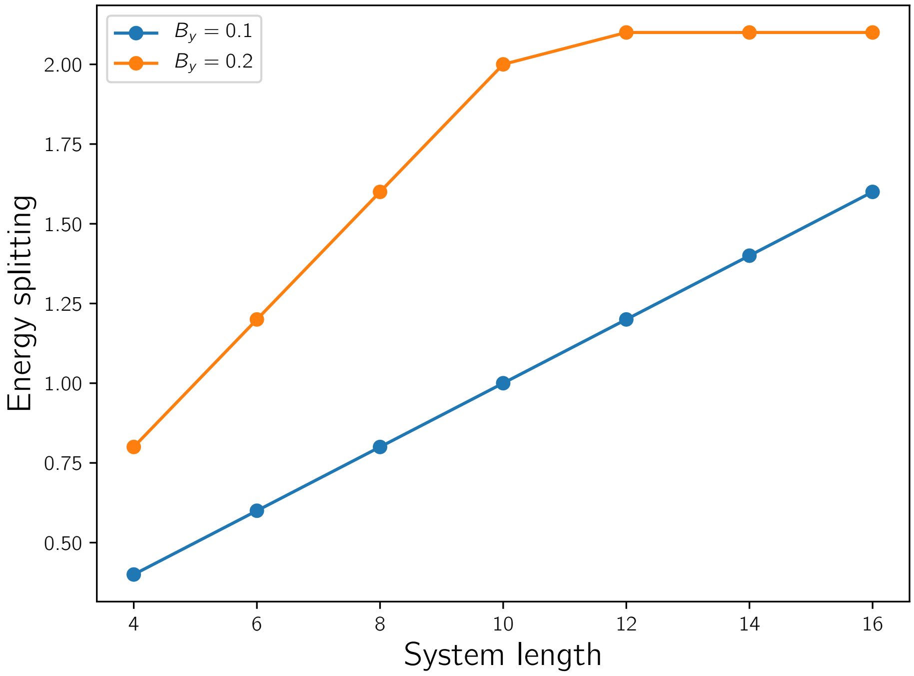

Fig. E.1 Lifting of the ground-state degeneracy ΔE_y [units J] for Hamiltonian $H_J + H_y$, as a function of system length L for different values of B_y [units J].

term, one has indeed

$$H_f = -\sum_{j,\sigma}(\mu+\sigma B_z)\, c^\dagger_{\sigma,j} c_{\sigma,j} \sim \sum_j e^{i\frac{\pi}{4}} \frac{B_z - i\mu}{2} a^\dagger_j b_j + h.c.. \tag{E.14}$$

Therefore it is clear that they cannot lift the four-fold degeneracy in an infinite system. Moreover, note that the $H = H_J + H_f$ correspond to well known nearest-neighbor four-state clock model [11, 211, 194] which features full topological protection for small B_z and μ.

E.4 Fermionic spectral function

In this section we are going to compute analytically the fermionic spectral function for the two exactly solvable models presented in the main text: H_J [see Eq. (4.47)] which belongs to the SI phase and $H^{(2)}$ [see Eq. (4.48)] which belongs to the WI phase.

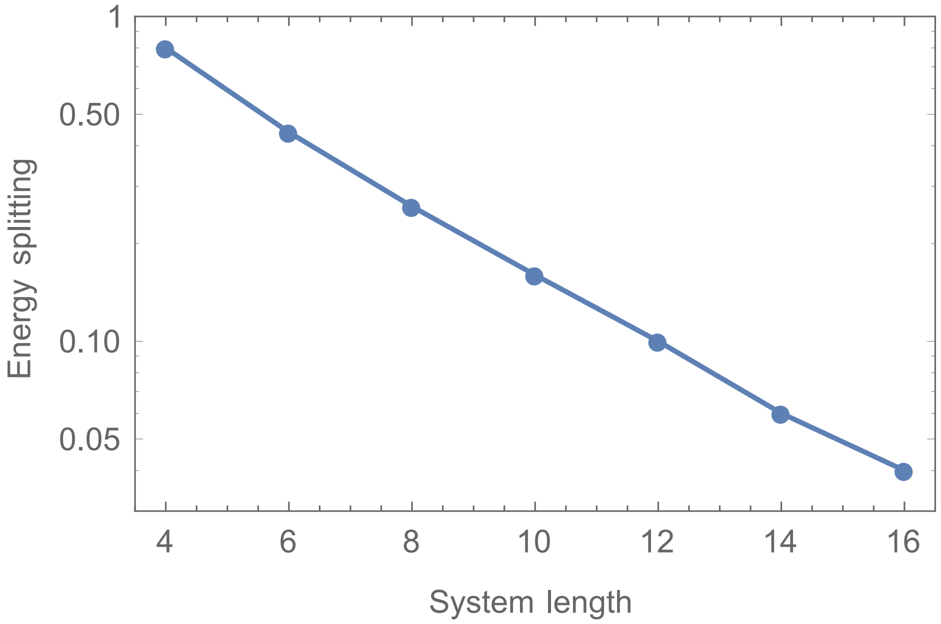

Fig. E.2 Liftings of the ground state degeneracy ΔE_μ [units J] as a function of system length L. Here we choose $\mu = 1.6J$

E.4.1 Hamiltonian H_J

Let us consider the Hamiltonian H_J which contains exact parafermionic edge states. Here we will prove that, despite string factors, its fermionic spectral function is non-vanishing only at the edges of the chain, where it has the universal prefactor $1/4$. To this end, we observe that the only non-vanishing matrix elements of the fermionic annihilation operators on a single site are

$$\begin{aligned} \langle f_0|c_\uparrow|f_1\rangle &= 1\,, \qquad & \langle f_3|c_\uparrow|f_2\rangle &= -1\,, \\ \langle f_1|c_\downarrow|f_2\rangle &= -i\,, \qquad & \langle f_0|c_\downarrow|f_3\rangle &= -i\,. \end{aligned} \tag{E.15}$$

This, together with the expression for the ground states in Eq. (E.6), allows to prove by direct calculation

$$\begin{aligned} |\langle\psi_{m\pm1}|c_{L\sigma}|\psi_m\rangle|^2 &= \frac{1}{16}\,, \\ |\langle\psi_m|c_{L\sigma}|\psi_m\rangle|^2 = |\langle\psi_{m+2}|c_{L\sigma}|\psi_m\rangle|^2 &= 0\,. \end{aligned} \tag{E.16}$$

The same argument applies for the left edge of the chain ($j = 1$), since the ground states can be equivalently expressed also as

$$|\psi_m\rangle = \frac{1}{2}\Big(|f_m\rangle \otimes |b_0^{L-1}\rangle + |f_{m-1}\rangle \otimes |b_1^{L-1}\rangle + |f_{m-2}\rangle \otimes |b_2^{L-1}\rangle + |f_{m-3}\rangle \otimes |b_3^{L-1}\rangle\Big). \quad \text{(E.17)}$$

This leads us to

$$\sum_l |\langle \psi_l | c_{j\sigma} | \psi_m\rangle|^2 = \frac{1}{8} \qquad \text{for } j = 1, L. \quad \text{(E.18)}$$

Let us now consider a bulk site $k \notin \{1, L\}$ and prove that the matrix elements of $c_{k\sigma}$ between the ground states are zero. The key observation is that $|\psi_m\rangle$ can also be expressed as

$$\begin{aligned} |\psi_m\rangle = \frac{1}{4}\sum_{a=0}^{3} \Big(&|b_a^{k-1}\rangle \otimes |f_m\rangle \otimes |b_{-a}^{L-k}\rangle + |b_a^{k-1}\rangle \otimes |f_{m-1}\rangle \otimes |b_{1-a}^{L-k}\rangle \\ &+ |b_a^{k-1}\rangle \otimes |f_{m-2}\rangle \otimes |b_{2-a}^{L-k}\rangle + |b_a^{k-1}\rangle \otimes |f_{m-3}\rangle \otimes |b_{3-a}^{L-k}\rangle\Big). \end{aligned} \quad \text{(E.19)}$$

Since a is not fixed, the matrix elements reads

$$\begin{aligned} &\langle \psi_{m\pm1} | c_{k\sigma} | \psi_m\rangle \propto \sum_{a=0}^{3} (-1)^a = 0, \\ &|\langle \psi_m | c_{k\sigma} | \psi_m\rangle|^2 = |\langle \psi_{m+2} | c_{k\sigma} | \psi_m\rangle|^2 = 0 \end{aligned} \quad \text{(E.20)}$$

with the factor $(-1)^a$ stemming from the anticommutation of $c_{k\sigma}$ with the fermionic operators contained in $|b_a^{k-1}\rangle$. Since the above results hold also for the fermionic creation operators $c_{j\sigma}^\dagger$, the properties of the spectral function discussed in the main text are proved.

E.4.2 Hamiltonian $H^{(2)}$

Here we focus on the non-interacting Hamiltonian $H^{(2)}$ (see Eq. (4.48)) which consists of two uncoupled Majorana chains

$$H^{(2)} = -Ji \sum_{j=1}^{L-1} \left[\tau_{\downarrow,j}\chi_{\downarrow,j+1} + \tau_{\uparrow,j}\chi_{\uparrow,j+1}\right] \quad \text{(E.21)}$$

with

$$\chi_{\sigma,j} = \frac{1}{\sqrt{2}}\left[c_{\sigma,j}^\dagger + c_{\sigma,j} - i\left(c_{-\sigma,j}^\dagger + c_{-\sigma,j}\right)\right] \quad \text{(E.22)}$$

$$\tau_{\sigma,j} = \frac{1}{\sqrt{2}}\left[c_{-\sigma,j}^\dagger + c_{-\sigma,j} + i\left(c_{\sigma,j}^\dagger - c_{\sigma,j}\right)\right]. \quad \text{(E.23)}$$

It is possible to define two non-local fermionic operators

$$\mathtt{f}_\sigma = \frac{1}{2}\left(\tau_{\sigma,L} + i\chi_{\sigma,1}\right) \tag{E.24}$$

which commute with $H^{(2)}$ and allows to label the four ground states of the system

$$|\phi_0\rangle,\ |\phi_1\rangle = \mathtt{f}_\downarrow^\dagger|\phi_0\rangle,\ |\phi_2\rangle = \mathtt{f}_\uparrow^\dagger\mathtt{f}_\downarrow^\dagger|\phi_0\rangle,\ |\phi_3\rangle = \mathtt{f}_\uparrow^\dagger|\phi_0\rangle \tag{E.25}$$

where here $|\phi_0\rangle$ is the ground state of $H^{(2)}$ annihilated by both $\mathtt{f}_\sigma$ ($\sigma =\uparrow,\downarrow$). Given the expression in Eq. (E.22)-(E.25), one can immediately show that

$$\sum_{m=0}^{3}|\langle\phi_m|c_{j,\sigma}^\dagger|\phi_n\rangle|^2 = \sum_{m=0}^{3}|\langle\phi_m|c_{j,\sigma}|\phi_n\rangle|^2 = \left(\delta_{j,1}+\delta_{j,L}\right)\frac{1}{4} \tag{E.26}$$

for all $n = 0,1,2,3$ and σ, thus proving Eq. (4.58) in the main text.

References

[1] K. v. Klitzing, G. Dorda, and M. Pepper. New method for high-accuracy determination of the fine-structure constant based on quantized hall resistance. *Phys. Rev. Lett.*, 45:494–497, Aug 1980.

[2] R. B. Laughlin. Quantized hall conductivity in two dimensions. *Phys. Rev. B*, 23:5632–5633, May 1981.

[3] B. I. Halperin. Quantized hall conductance, current-carrying edge states, and the existence of extended states in a two-dimensional disordered potential. *Phys. Rev. B*, 25:2185–2190, Feb 1982.

[4] Erwann Bocquillon, Vincent Freulon, François D. Parmentier, Jean-Marc Berroir, Bernard Plaçais, Claire Wahl, Jérome Rech, Thibaut Jonckheere, Thierry Martin, Charles Grenier, Dario Ferraro, Pascal Degiovanni, and Gwendal Fève. Electron quantum optics in ballistic chiral conductors. *Annalen der Physik*, 526(1-2):1–30, Dec 2013.

[5] H. Kamata, N. Kumada, M. Hashisaka, K. Muraki, and T. Fujisawa. Fractionalized wave packets from an artificial tomonaga–luttinger liquid. *Nature Nanotechnology*, 9(3):177–181, Feb 2014.

[6] Jason Alicea. Majorana modes materialize. *Nature Nanotechnology*, 8(9):623–624, Sep 2013.

[7] A. Yu. Kitaev. Unpaired Majorana fermions in quantum wires. *Phys. Usp.*, 44:131, 2001.

[8] V. Mourik, K. Zuo, S. M. Frolov, S. R. Plissard, E. P. A. M. Bakkers, and L. P. Kouwenhoven. Signatures of Majorana fermions in hybrid superconductor-semiconductor nanowire devices. *Science*, 336:1003, 2012.

[9] Hao Zhang, Chun-Xiao Liu, Sasa Gazibegovic, Di Xu, John A. Logan, Guanzhong Wang, Nick van Loo, Jouri D. S. Bommer, Michiel W. A. de Moor, Diana Car, Roy L. M. Op het Veld, Petrus J. van Veldhoven, Sebastian Koelling, Marcel A. Verheijen, Mihir Pendharkar, Daniel J. Pennachio, Borzoyeh Shojaei, Joon Sue Lee, Chris J. Palmstrøm, Erik P. A. M. Bakkers, S. Das Sarma, and Leo P. Kouwenhoven. Quantized majorana conductance. *Nature*, 556(7699):74–79, Mar 2018.

[10] Chetan Nayak, Steven H. Simon, Ady Stern, Michael Freedman, and Sankar Das Sarma. Non-Abelian anyons and topological quantum computation. *Rev. Mod. Phys.*, 80:1083, 2008.

[11] Paul Fendley. Parafermionic edge zero modes in Z_n-invariant spin chains. *J. Stat. Mech.*, 2012(11):P11020, 2012.

[12] Alessio Calzona, Matteo Acciai, Matteo Carrega, Fabio Cavaliere, and Maura Sassetti. Time-resolved energy dynamics after single electron injection into an interacting helical liquid. *Phys. Rev. B*, 94:035404, Jul 2016.

[13] Matteo Acciai, Alessio Calzona, Giacomo Dolcetto, Thomas L. Schmidt, and Maura Sassetti. Charge and energy fractionalization mechanism in one-dimensional channels. *Phys. Rev. B*, 96:075144, Aug 2017.

[14] Alessio Calzona, Filippo Maria Gambetta, Fabio Cavaliere, Matteo Carrega, and Maura Sassetti. Quench-induced entanglement and relaxation dynamics in luttinger liquids. *Phys. Rev. B*, 96:085423, Aug 2017.

[15] Alessio Calzona, Filippo Maria Gambetta, Matteo Carrega, Fabio Cavaliere, Thomas L. Schmidt, and Maura Sassetti. Universal scaling of quench-induced correlations in a one-dimensional channel at finite temperature. *SciPost Phys.*, 4:23, 2018.

[16] A. Calzona, T. Meng, M. Sassetti, and T. L. Schmidt. Z4 parafermions in one-dimensional fermionic lattices. *ArXiv e-prints*, February 2018.

[17] A. Calzona, M. Carrega, G. Dolcetto, and M. Sassetti. Transient dynamics of spin-polarized injection in helical luttinger liquids. *Physica E: Low-dimensional Systems and Nanostructures*, 74:630–636, Nov 2015.

[18] Alessio Calzona, Matteo Carrega, Giacomo Dolcetto, and Maura Sassetti. Time-resolved pure spin fractionalization and spin-charge separation in helical luttinger liquid based devices. *Phys. Rev. B*, 92:195414, Nov 2015.

[19] Alessio Calzona, Filippo Maria Gambetta, Matteo Carrega, Fabio Cavaliere, and Maura Sassetti. Nonequilibrium effects on charge and energy partitioning after an interaction quench. *Phys. Rev. B*, 95:085101, Feb 2017.

[20] A. Calzona, F. M. Gambetta, M. Carrega, F. Cavaliere, and M. Sassetti. Asymmetries in the spectral density of an interaction-quenched luttinger liquid. *Journal of Physics: Conference Series*, 969(1):012140, 2018.

[21] Wikipedia. Seven Bridges of Königsberg. https://en.wikipedia.org/wiki/Seven_Bridges_of_K%C3%B6nigsberg, 2018. Accessed: 4 July 2018.

[22] J M Kosterlitz and D J Thouless. Ordering, metastability and phase transitions in two-dimensional systems. *Journal of Physics C: Solid State Physics*, 6(7):1181, 1973.

[23] J M Kosterlitz. The critical properties of the two-dimensional xy model. *Journal of Physics C: Solid State Physics*, 7(6):1046, 1974.

[24] F. D. M. Haldane. Model for a quantum hall effect without landau levels: Condensed-matter realization of the "parity anomaly". *Phys. Rev. Lett.*, 61:2015–2018, Oct 1988.

[25] A.Yu. Kitaev. Fault-tolerant quantum computation by anyons. *Ann. Phys.*, 303(1):2 – 30, 2003.

[26] David Aasen, Michael Hell, Ryan V. Mishmash, Andrew Higginbotham, Jeroen Danon, Martin Leijnse, Thomas S. Jespersen, Joshua A. Folk, Charles M. Marcus, Karsten Flensberg, and Jason Alicea. Milestones toward majorana-based quantum computing. *Phys. Rev. X*, 6:031016, Aug 2016.

[27] Shuichi Murakami. Phase transition between the quantum spin hall and insulator phases in 3d: emergence of a topological gapless phase. *New Journal of Physics*, 9(9):356, 2007.

[28] Ching-Kai Chiu, Jeffrey C. Y. Teo, Andreas P. Schnyder, and Shinsei Ryu. Classification of topological quantum matter with symmetries. *Rev. Mod. Phys.*, 88:035005, Aug 2016.

[29] Kai-Yu Yang, Yuan-Ming Lu, and Ying Ran. Quantum hall effects in a weyl semimetal: Possible application in pyrochlore iridates. *Phys. Rev. B*, 84:075129, Aug 2011.

[30] Su-Yang Xu, Chang Liu, Satya K. Kushwaha, Raman Sankar, Jason W. Krizan, Ilya Belopolski, Madhab Neupane, Guang Bian, Nasser Alidoust, Tay-Rong Chang, Horng-Tay Jeng, Cheng-Yi Huang, Wei-Feng Tsai, Hsin Lin, Pavel P. Shibayev, Fang-Cheng Chou, Robert J. Cava, and M. Zahid Hasan. Observation of fermi arc surface states in a topological metal. *Science*, 347(6219):294–298, 2015.

[31] D. Tong. Lectures on the Quantum Hall Effect. *ArXiv e-prints*, June 2016.

[32] G. Giuliani and G. Vignale. *Quantum Theory of the Electron Liquid*. Cambridge University Press, 2008.

[33] M. Büttiker. Absence of backscattering in the quantum hall effect in multiprobe conductors. *Phys. Rev. B*, 38:9375–9389, Nov 1988.

[34] Joseph Avron, Daniel Osadchy, and Ruedi Seiler. A topological look at the quantum hall effect. *Physics Today*, 56:38, 2003.

[35] Richard E. Prange and Steven M. Girvin, editors. *The Quantum Hall Effect*. Springer New York, 1990.

[36] X.G. Wen. *Quantum Field Theory of Many-Body Systems: From the Origin of Sound to an Origin of Light and Electrons*. Oxford Graduate Texts. OUP Oxford, 2007.

[37] Daijiro Yoshioka. *The Quantum Hall Effect (Springer Series in Solid-State Sciences)*. Springer, 2010.

[38] M. V. Berry. Quantal phase factors accompanying adiabatic changes. *Proceedings of the Royal Society of London A: Mathematical, Physical and Engineering Sciences*, 392(1802):45–57, 1984.

[39] B. Andrei Bernevig. *Topological Insulators and Topological Superconductors*. Princeton University Press, 2013.

[40] B. Andrei Bernevig, Taylor L. Hughes, and Shou-Cheng Zhang. Quantum spin hall effect and topological phase transition in hgte quantum wells. *Science*, 314(5806):1757–1761, 2006.

[41] D. J. Thouless, M. Kohmoto, M. P. Nightingale, and M. den Nijs. Quantized hall conductance in a two-dimensional periodic potential. *Phys. Rev. Lett.*, 49:405–408, Aug 1982.

[42] Douglas R. Hofstadter. Energy levels and wave functions of bloch electrons in rational and irrational magnetic fields. *Phys. Rev. B*, 14:2239–2249, Sep 1976.

[43] C. R. Dean, L. Wang, P. Maher, C. Forsythe, F. Ghahari, Y. Gao, J. Katoch, M. Ishigami, P. Moon, M. Koshino, T. Taniguchi, K. Watanabe, K. L. Shepard, J. Hone, and P. Kim. Hofstadter's butterfly and the fractal quantum hall effect in moiré superlattices. *Nature*, 497(7451):598–602, May 2013.

[44] Xiao-Liang Qi, Yong-Shi Wu, and Shou-Cheng Zhang. Topological quantization of the spin hall effect in two-dimensional paramagnetic semiconductors. *Phys. Rev. B*, 74:085308, Aug 2006.

[45] Preden Roulleau, F. Portier, P. Roche, A. Cavanna, G. Faini, U. Gennser, and D. Mailly. Direct measurement of the coherence length of edge states in the integer quantum hall regime. *Physical Review Letters*, 100(12), Mar 2008.

[46] Liang Fu and C. L. Kane. Time reversal polarization and a Z_2 adiabatic spin pump. *Phys. Rev. B*, 74:195312, Nov 2006.

[47] Andreas P. Schnyder, Shinsei Ryu, Akira Furusaki, and Andreas W. W. Ludwig. Classification of topological insulators and superconductors in three spatial dimensions. *Phys. Rev. B*, 78:195125, Nov 2008.

[48] Alexei Kitaev, Vladimir Lebedev, and Mikhail Feigel'man. Periodic table for topological insulators and superconductors. In *AIP Conference Proceedings*. AIP, 2009.

[49] Shinsei Ryu, Andreas P Schnyder, Akira Furusaki, and Andreas W W Ludwig. Topological insulators and superconductors: tenfold way and dimensional hierarchy. *New Journal of Physics*, 12(6):065010, 2010.

[50] Alexander Altland and Martin R. Zirnbauer. Nonstandard symmetry classes in mesoscopic normal-superconducting hybrid structures. *Phys. Rev. B*, 55:1142–1161, Jan 1997.

[51] Jeffrey C. Y. Teo and C. L. Kane. Topological defects and gapless modes in insulators and superconductors. *Phys. Rev. B*, 82:115120, Sep 2010.

[52] C. L. Kane and E. J. Mele. Quantum spin hall effect in graphene. *Phys. Rev. Lett.*, 95:226801, Nov 2005.

[53] C. L. Kane and E. J. Mele. Z_2 topological order and the quantum spin hall effect. *Phys. Rev. Lett.*, 95:146802, Sep 2005.

[54] Markus König, Steffen Wiedmann, Christoph Brüne, Andreas Roth, Hartmut Buhmann, Laurens W. Molenkamp, Xiao-Liang Qi, and Shou-Cheng Zhang. Quantum spin hall insulator state in hgte quantum wells. *Science*, 318(5851):766–770, 2007.

[55] Xiao-Liang Qi and Shou-Cheng Zhang. Topological insulators and superconductors. *Rev. Mod. Phys.*, 83:1057, 2011.

[56] Solofo Groenendijk, Giacomo Dolcetto, and Thomas L. Schmidt. Fundamental limits to helical edge conductivity due to spin-phonon scattering. *Phys. Rev. B*, 97:241406, Jun 2018.

[57] Katja C. Nowack, Eric M. Spanton, Matthias Baenninger, Markus König, John R. Kirtley, Beena Kalisky, C. Ames, Philipp Leubner, Christoph Brüne, Hartmut Buhmann, Laurens W. Molenkamp, David Goldhaber-Gordon, and Kathryn A. Moler. Imaging currents in HgTe quantum wells in the quantum spin hall regime. *Nature Materials*, 12(9):787–791, Jun 2013.

[58] Chaoxing Liu, Taylor L. Hughes, Xiao-Liang Qi, Kang Wang, and Shou-Cheng Zhang. Quantum spin hall effect in inverted type-ii semiconductors. *Phys. Rev. Lett.*, 100:236601, Jun 2008.

[59] Ivan Knez, Rui-Rui Du, and Gerard Sullivan. Evidence for helical edge modes in inverted InAs/GaSb quantum wells. *Phys. Rev. Lett.*, 107:136603, Sep 2011.

[60] Conan Weeks, Jun Hu, Jason Alicea, Marcel Franz, and Ruqian Wu. Engineering a robust quantum spin hall state in graphene via adatom deposition. *Phys. Rev. X*, 1:021001, Oct 2011.

[61] Cheng-Cheng Liu, Wanxiang Feng, and Yugui Yao. Quantum spin hall effect in silicene and two-dimensional germanium. *Phys. Rev. Lett.*, 107:076802, Aug 2011.

[62] Yong Xu, Binghai Yan, Hai-Jun Zhang, Jing Wang, Gang Xu, Peizhe Tang, Wenhui Duan, and Shou-Cheng Zhang. Large-gap quantum spin hall insulators in tin films. *Phys. Rev. Lett.*, 111:136804, Sep 2013.

[63] F. Reis, G. Li, L. Dudy, M. Bauernfeind, S. Glass, W. Hanke, R. Thomale, J. Schäfer, and R. Claessen. Bismuthene on a sic substrate: A candidate for a high-temperature quantum spin hall material. *Science*, 2017.

[64] Liangzhi Kou, Yandong Ma, Ziqi Sun, Thomas Heine, and Changfeng Chen. Two-dimensional topological insulators: Progress and prospects. *The Journal of Physical Chemistry Letters*, 8(8):1905–1919, 2017.

[65] Tudor D. Stanescu. *Introduction to Topological Quantum Matter & Quantum Computation*. Apple Academic Press Inc., 2016.

[66] Jason Alicea. New directions in the pursuit of Majorana fermions in solid state systems. *Rep. Prog. Phys.*, 75:076501, 2012.

[67] Roman M. Lutchyn, Jay D. Sau, and S. Das Sarma. Majorana fermions and a topological phase transition in semiconductor-superconductor heterostructures. *Phys. Rev. Lett.*, 105:077001, Aug 2010.

[68] Yuval Oreg, Gil Refael, and Felix von Oppen. Helical liquids and majorana bound states in quantum wires. *Phys. Rev. Lett.*, 105:177002, Oct 2010.

[69] M. T. Deng, S. Vaitiekenas, E. B. Hansen, J. Danon, M. Leijnse, K. Flensberg, J. Nygård, P. Krogstrup, and C. M. Marcus. Majorana bound state in a coupled quantum-dot hybrid-nanowire system. *Science*, 354(6319):1557–1562, 2016.

[70] S. M. Albrecht, A. P. Higginbotham, M. Madsen, F. Kuemmeth, T. S. Jespersen, J. Nygård, P. Krogstrup, and C. M. Marcus. Exponential protection of zero modes in majorana islands. *Nature*, 531(7593):206–209, Mar 2016.

[71] Jason Alicea, Yuval Oreg, Gil Refael, Felix von Oppen, and Matthew P. A. Fisher. Non-abelian statistics and topological quantum information processing in 1d wire networks. *Nature Physics*, 7(5):412–417, Feb 2011.

[72] R. M. Lutchyn, E. P. A. M. Bakkers, L. P. Kouwenhoven, P. Krogstrup, C. M. Marcus, and Y. Oreg. Majorana zero modes in superconductor–semiconductor heterostructures. *Nature Reviews Materials*, 3(5):52–68, May 2018.

[73] D. Laroche, D. Bouman, D. J. van Woerkom, A. Proutski, C. Murthy, D. I. Pikulin, C. Nayak, R. J. J. van Gulik, J. Nygård, P. Krogstrup, L. P. Kouwenhoven, and A. Geresdi. Observation of the 4π-periodic Josephson effect in InAs nanowires. *ArXiv e-prints*, December 2017.

[74] Piers Coleman. *Introduction to Many-Body Physics*. Cambridge University Press, 2015.

[75] D. D. Osheroff, R. C. Richardson, and D. M. Lee. Evidence for a new phase of solid he^3. *Phys. Rev. Lett.*, 28:885–888, Apr 1972.

[76] A. J. Leggett. Interpretation of recent results on he^3 below 3 mk: A new liquid phase? *Phys. Rev. Lett.*, 29:1227–1230, Oct 1972.

[77] N. F. Mott and R. Peierls. Discussion of the paper by de Boer and Verwey. *Proceedings of the Physical Society*, 49:72–73, August 1937.

[78] Jun Kondo. Resistance minimum in dilute magnetic alloys. *Progress of Theoretical Physics*, 32(1):37–49, 1964.

[79] D. C. Tsui, H. L. Stormer, and A. C. Gossard. Two-dimensional magnetotransport in the extreme quantum limit. *Phys. Rev. Lett.*, 48:1559–1562, May 1982.

[80] R. B. Laughlin. Anomalous quantum hall effect: An incompressible quantum fluid with fractionally charged excitations. *Phys. Rev. Lett.*, 50:1395–1398, May 1983.

[81] L. D. Landau. The theory of a fermi liquid. *Journal of Experimental and Theoretical Physics*, 3:920, 1956.

[82] Thierry Giamarchi. *Quantum Physics in One Dimension*. Oxford University Press, Dec 2003.

[83] J Voit. Charge-spin separation and the spectral properties of luttinger liquids. *Journal of Physics: Condensed Matter*, 5(44):8305–8336, Nov 1993.

[84] F D M Haldane. Coupling between charge and spin degrees of freedom in the one-dimensional fermi gas with backscattering. *Journal of Physics C: Solid State Physics*, 12(22):4791–4799, Nov 1979.

[85] F D M Haldane. Luttinger liquid theory of one-dimensional quantum fluids. *Journal of Physics C: Solid State Physics*, 14(19):2585–2609, Jul 1981.

[86] Dmitrii L. Maslov and Michael Stone. Landauer conductance of luttinger liquids with leads. *Physical Review B*, 52(8):R5539–R5542, Aug 1995.

[87] I. Safi and H. J. Schulz. Transport in an inhomogeneous interacting one-dimensional system. *Physical Review B*, 52(24):R17040–R17043, Dec 1995.

[88] Hadar Steinberg, Gilad Barak, Amir Yacoby, Loren N. Pfeiffer, Ken W. West, Bertrand I. Halperin, and Karyn Le Hur. Charge fractionalization in quantum wires. *Nature Physics*, 4(2):116–119, Dec 2007.

[89] Y. Jompol, C. J. B. Ford, J. P. Griffiths, I. Farrer, G. A. C. Jones, D. Anderson, D. A. Ritchie, T. W. Silk, and A. J. Schofield. Probing spin-charge separation in a tomonaga-luttinger liquid. *Science*, 325(5940):597–601, Jul 2009.

[90] R. Shankar. Renormalization-group approach to interacting fermions. *Reviews of Modern Physics*, 66(1):129–192, Jan 1994.

[91] S. i. Tomonaga. Remarks on bloch's method of sound waves applied to many-fermion problems. *Progress of Theoretical Physics*, 5(4):544–569, Jul 1950.

[92] J. M. Luttinger. An exactly soluble model of a many-fermion system. *Journal of Mathematical Physics*, 4(9):1154–1162, Sep 1963.

[93] Jan von Delft and Herbert Schoeller. Bosonization for beginners - refermionization for experts. *Annalen der Physik*, 7(4):225–305, Nov 1998.

[94] E. Miranda. Introduction to bosonization. *Brazilian Journal of Physics*, 33(1), Mar 2003.

[95] Marc Bockrath, David H. Cobden, Jia Lu, Andrew G. Rinzler, Richard E. Smalley, Leon Balents, and Paul L. McEuen. Luttinger-liquid behaviour in carbon nanotubes. *Nature*, 397(6720):598–601, Feb 1999.

[96] C. Blumenstein, J. Schäfer, S. Mietke, S. Meyer, A. Dollinger, M. Lochner, X. Y. Cui, L. Patthey, R. Matzdorf, and R. Claessen. Atomically controlled quantum chains hosting a tomonaga–luttinger liquid. *Nature Physics*, 7(10):776–780, Aug 2011.

[97] Rosario Fazio, F. W. J. Hekking, and D. E. Khmelnitskii. Anomalous thermal transport in quantum wires. *Physical Review Letters*, 80(25):5611–5614, Jun 1998.

[98] Torsten Karzig, Gil Refael, Leonid I. Glazman, and Felix von Oppen. Energy partitioning of tunneling currents into luttinger liquids. *Physical Review Letters*, 107(17), Oct 2011.

[99] D. B. Gutman, Yuval Gefen, and A. D. Mirlin. Bosonization of one-dimensional fermions out of equilibrium. *Physical Review B*, 81(8), Feb 2010.

[100] E. Perfetto, G. Stefanucci, H. Kamata, and T. Fujisawa. Time-resolved charge fractionalization in inhomogeneous luttinger liquids. *Physical Review B*, 89(20), May 2014.

[101] Tobias Müller, Ronny Thomale, Björn Trauzettel, Erwann Bocquillon, and Oleksiy Kashuba. Dynamical transport measurement of the luttinger parameter in helical edges states of two-dimensional topological insulators. *Physical Review B*, 95(24), Jun 2017.

[102] Seigo Tarucha, Takashi Honda, and Tadashi Saku. Reduction of quantized conductance at low temperatures observed in 2 to 10 μm-long quantum wires. *Solid State Communications*, 94(6):413–418, May 1995.

[103] C. L. Kane and Matthew P. A. Fisher. Transmission through barriers and resonant tunneling in an interacting one-dimensional electron gas. *Physical Review B*, 46(23):15233–15262, Dec 1992.

[104] Karyn Le Hur, Bertrand I. Halperin, and Amir Yacoby. Charge fractionalization in nonchiral luttinger systems. *Annals of Physics*, 323(12):3037–3058, Dec 2008.

[105] V. Freulon, A. Marguerite, J.-M. Berroir, B. Plaçais, A. Cavanna, Y. Jin, and G. Fève. Hong-ou-mandel experiment for temporal investigation of single-electron fractionalization. *Nature Communications*, 6(1), Apr 2015.

[106] K.-V. Pham, M. Gabay, and P. Lederer. Fractional excitations in the luttinger liquid. *Physical Review B*, 61(24):16397–16422, Jun 2000.

[107] Sourin Das and Sumathi Rao. Spin-polarized scanning-tunneling probe for helical luttinger liquids. *Physical Review Letters*, 106(23), Jun 2011.

[108] Kalle Bendias, Saquib Shamim, Oliver Herrmann, Andreas Budewitz, Pragya Shekhar, Philipp Leubner, Johannes Kleinlein, Erwann Bocquillon, Hartmut Buhmann, and Laurens W. Molenkamp. High mobility HgTe microstructures for quantum spin hall studies. *Nano Letters*, 18(8):4831–4836, Jul 2018.

[109] C. L. Kane and Matthew P. A. Fisher. Thermal transport in a luttinger liquid. *Physical Review Letters*, 76(17):3192–3195, Apr 1996.

[110] Dik Bouwmeester, Jian-Wei Pan, Klaus Mattle, Manfred Eibl, Harald Weinfurter, and Anton Zeilinger. Experimental quantum teleportation. *Nature*, 390(6660):575–579, Dec 1997.

[111] Jian-Wei Pan, Dik Bouwmeester, Harald Weinfurter, and Anton Zeilinger. Experimental entanglement swapping: Entangling photons that never interacted. *Physical Review Letters*, 80(18):3891–3894, May 1998.

[112] Jian-Wei Pan, Dik Bouwmeester, Matthew Daniell, Harald Weinfurter, and Anton Zeilinger. Experimental test of quantum nonlocality in three-photon greenberger–horne–zeilinger entanglement. *Nature*, 403(6769):515–519, Feb 2000.

[113] CharlesH. Bennett, Francois Bessette, Gilles Brassard, Louis Salvail, and John Smolin. Experimental quantum cryptography. *Journal of Cryptology*, 5(1), 1992.

[114] Christopher Bäuerle, D Christian Glattli, Tristan Meunier, Fabien Portier, Patrice Roche, Preden Roulleau, Shintaro Takada, and Xavier Waintal. Coherent control of single electrons: a review of current progress. *Reports on Progress in Physics*, 81(5):056503, Apr 2018.

[115] A. Bertoni, P. Bordone, R. Brunetti, C. Jacoboni, and S. Reggiani. Quantum logic gates based on coherent electron transport in quantum wires. *Physical Review Letters*, 84(25):5912–5915, Jun 2000.

[116] Jukka P. Pekola, Olli-Pentti Saira, Ville F. Maisi, Antti Kemppinen, Mikko Möttönen, Yuri A. Pashkin, and Dmitri V. Averin. Single-electron current sources: Toward a refined definition of the ampere. *Reviews of Modern Physics*, 85(4):1421–1472, Oct 2013.

[117] G. Feve, A. Mahe, J.-M. Berroir, T. Kontos, B. Placais, D. C. Glattli, A. Cavanna, B. Etienne, and Y. Jin. An on-demand coherent single-electron source. *Science*, 316(5828):1169–1172, May 2007.

[118] M. Büttiker, H. Thomas, and A. Prêtre. Mesoscopic capacitors. *Physics Letters A*, 180(4-5):364–369, Sep 1993.

[119] J. Keeling, I. Klich, and L. S. Levitov. Minimal excitation states of electrons in one-dimensional wires. *Physical Review Letters*, 97(11), Sep 2006.

[120] J. Dubois, T. Jullien, F. Portier, P. Roche, A. Cavanna, Y. Jin, W. Wegscheider, P. Roulleau, and D. C. Glattli. Minimal-excitation states for electron quantum optics using levitons. *Nature*, 502(7473):659–663, Oct 2013.

[121] M. D. Blumenthal, B. Kaestner, L. Li, S. Giblin, T. J. B. M. Janssen, M. Pepper, D. Anderson, G. Jones, and D. A. Ritchie. Gigahertz quantized charge pumping. *Nature Physics*, 3(5):343–347, Apr 2007.

[122] Sylvain Hermelin, Shintaro Takada, Michihisa Yamamoto, Seigo Tarucha, Andreas D. Wieck, Laurent Saminadayar, Christopher Bäuerle, and Tristan Meunier. Electrons surfing on a sound wave as a platform for quantum optics with flying electrons. *Nature*, 477(7365):435–438, Sep 2011.

[123] Claire Wahl, Jérôme Rech, Thibaut Jonckheere, and Thierry Martin. Interactions and charge fractionalization in an electronic hong-ou-mandel interferometer. *Physical Review Letters*, 112(4), Jan 2014.

[124] A. Marguerite, C. Cabart, C. Wahl, B. Roussel, V. Freulon, D. Ferraro, Ch. Grenier, J.-M. Berroir, B. Plaçais, T. Jonckheere, J. Rech, T. Martin, P. Degiovanni, A. Cavanna, Y. Jin, and G. Fève. Decoherence and relaxation of a single electron in a one-dimensional conductor. *Physical Review B*, 94(11), Sep 2016.

[125] D. Ferraro, B. Roussel, C. Cabart, E. Thibierge, G. Fève, Ch. Grenier, and P. Degiovanni. Real-time decoherence of landau and levitov quasiparticles in quantum hall edge channels. *Physical Review Letters*, 113(16), Oct 2014.

[126] Artur O. Slobodeniuk, Edvin G. Idrisov, and Eugene V. Sukhorukov. Relaxation of an electron wave packet at the quantum hall edge at filling factor ν=2. *Physical Review B*, 93(3), Jan 2016.

[127] Patrick P. Hofer and Markus Büttiker. Emission of time-bin entangled particles into helical edge states. *Physical Review B*, 88(24), Dec 2013.

[128] Andreas Inhofer and Dario Bercioux. Proposal for an on-demand source of polarized electrons into the edges of a topological insulator. *Physical Review B*, 88(23), Dec 2013.

[129] D. Ferraro, C. Wahl, J. Rech, T. Jonckheere, and T. Martin. Electronic hong-ou-mandel interferometry in two-dimensional topological insulators. *Physical Review B*, 89(7), Feb 2014.

[130] Anders Ström, Henrik Johannesson, and Patrik Recher. Controllable spin entanglement production in a quantum spin hall ring. *Physical Review B*, 91(24), Jun 2015.

[131] G. Fève, J.-M. Berroir, and B. Plaçais. Time dependent electronic transport in chiral edge channels. *Physica E: Low-dimensional Systems and Nanostructures*, 76:12–27, Feb 2016.

[132] E. Weisz, H. K. Choi, M. Heiblum, Yuval Gefen, V. Umansky, and D. Mahalu. Controlled dephasing of an electron interferometer with a path detector at equilibrium. *Physical Review Letters*, 109(25), Dec 2012.

[133] Ivan P. Levkivskyi. Universal nonequilibrium states at the fractional quantum hall edge. *Physical Review B*, 93(16), Apr 2016.

[134] Iurii Chernii, Ivan P. Levkivskyi, and Eugene V. Sukhorukov. Fermi-edge singularity in chiral one-dimensional systems far from equilibrium. *Physical Review B*, 90(24), Dec 2014.

[135] Alexia Rod, Giacomo Dolcetto, Stephan Rachel, and Thomas L. Schmidt. Transport through a quantum spin hall antidot as a spectroscopic probe of spin textures. *Physical Review B*, 94(3), Jul 2016.

[136] D. Ferraro, J. Rech, T. Jonckheere, and T. Martin. Single quasiparticle and electron emitter in the fractional quantum hall regime. *Physical Review B*, 91(20), May 2015.

[137] Fabrizio Dolcini. Full electrical control of charge and spin conductance through interferometry of edge states in topological insulators. *Physical Review B*, 83(16), Apr 2011.

[138] F. Romeo, R. Citro, D. Ferraro, and M. Sassetti. Electrical switching and interferometry of massive dirac particles in topological insulator constrictions. *Physical Review B*, 86(16), Oct 2012.

[139] R. Citro, F. Romeo, and N. Andrei. Electrically controlled pumping of spin currents in topological insulators. *Physical Review B*, 84(16), Oct 2011.

[140] Eiki Iyoda, Takeo Kato, Kazuki Koshino, and Thierry Martin. Dephasing in single-electron generation due to environmental noise probed by hong-ou-mandel interferometry. *Physical Review B*, 89(20), May 2014.

[141] C. Grenier, R. Hervé, G. Fève, and P. Degiovanni. Electron quantum optics in quantum Hall edge channels. *Modern Physics Letters B*, 25(12n13):1053–1073, May 2011.

[142] Romain Vasseur, Kien Trinh, Stephan Haas, and Hubert Saleur. Crossover physics in the nonequilibrium dynamics of quenched quantum impurity systems. *Physical Review Letters*, 110(24), Jun 2013.

[143] Florian Elste, David R. Reichman, and Andrew J. Millis. Effect of a coulombic dot-lead coupling on the dynamics of a quantum dot. *Physical Review B*, 81(20), May 2010.

[144] P. Wächter, V. Meden, and K. Schönhammer. Charging of a quantum dot coupled to luttinger-liquid leads. *Physical Review B*, 76(12), Sep 2007.

[145] Igor V. Lerner, Vladimir I. Yudson, and Igor V. Yurkevich. Quantum wire hybridized with a single-level impurity. *Physical Review Letters*, 100(25), Jun 2008.

[146] Francesco Giazotto and María José Martínez-Pérez. The josephson heat interferometer. *Nature*, 492(7429):401–405, Dec 2012.

[147] S. Gasparinetti, K. L. Viisanen, O.-P. Saira, T. Faivre, M. Arzeo, M. Meschke, and J. P. Pekola. Fast electron thermometry for ultrasensitive calorimetric detection. *Physical Review Applied*, 3(1), Jan 2015.

[148] J. D. Fletcher, P. See, H. Howe, M. Pepper, S. P. Giblin, J. P. Griffiths, G. A. C. Jones, I. Farrer, D. A. Ritchie, T. J. B. M. Janssen, and M. Kataoka. Clock-controlled emission of single-electron wave packets in a solid-state circuit. *Physical Review Letters*, 111(21), Nov 2013.

[149] M. Kataoka, N. Johnson, C. Emary, P. See, J. P. Griffiths, G. A. C. Jones, I. Farrer, D. A. Ritchie, M. Pepper, and T. J. B. M. Janssen. Time-of-flight measurements of single-electron wave packets in quantum hall edge states. *Physical Review Letters*, 116(12), Mar 2016.

[150] Ch Grenier, R Hervé, E Bocquillon, F D Parmentier, B Plaçais, J M Berroir, G Fève, and P Degiovanni. Single-electron quantum tomography in quantum hall edge channels. *New Journal of Physics*, 13(9):093007, Sep 2011.

[151] Roy J. Glauber. Coherent and incoherent states of the radiation field. *Physical Review*, 131(6):2766–2788, Sep 1963.

[152] Roy J. Glauber. The quantum theory of optical coherence. *Physical Review*, 130(6):2529–2539, Jun 1963.

[153] Roy J. Glauber. Photon correlations. *Physical Review Letters*, 10(3):84–86, Feb 1963.

[154] Ivan P. Levkivskyi and Eugene V. Sukhorukov. Energy relaxation at quantum hall edge. *Physical Review B*, 85(7), Feb 2012.

[155] D. Ferraro, A. Feller, A. Ghibaudo, E. Thibierge, E. Bocquillon, G. Fève, Ch. Grenier, and P. Degiovanni. Wigner function approach to single electron coherence in quantum hall edge channels. *Physical Review B*, 88(20), Nov 2013.

[156] P. W. Anderson. Infrared catastrophe in fermi gases with local scattering potentials. *Physical Review Letters*, 18(24):1049–1051, Jun 1967.

[157] Gerald D. Mahan. *Many-Particle Physics*. Springer US, 2000.

[158] S. Takei, M. Milletarì, and B. Rosenow. Nonequilibrium electron spectroscopy of luttinger liquids. *Physical Review B*, 82(4), Jul 2010.

[159] V. Meden and K. Schönhammer. Spectral functions for the tomonaga-luttinger model. *Physical Review B*, 46(24):15753–15760, Dec 1992.

[160] C. Altimiras, H. le Sueur, U. Gennser, A. Cavanna, D. Mailly, and F. Pierre. Non-equilibrium edge-channel spectroscopy in the integer quantum hall regime. *Nature Physics*, 6(1):34–39, Oct 2009.

[161] H. le Sueur, C. Altimiras, U. Gennser, A. Cavanna, D. Mailly, and F. Pierre. Energy relaxation in the integer quantum hall regime. *Physical Review Letters*, 105(5), Jul 2010.

[162] Alessandro Silva. Statistics of the work done on a quantum critical system by quenching a control parameter. *Physical Review Letters*, 101(12), Sep 2008.

[163] Spyros Sotiriadis, Gabor Takacs, and Giuseppe Mussardo. Boundary state in an integrable quantum field theory out of equilibrium. *Physics Letters B*, 734:52–57, Jun 2014.

[164] K. Washio, R. Nakazawa, M. Hashisaka, K. Muraki, Y. Tokura, and T. Fujisawa. Long-lived binary tunneling spectrum in the quantum hall tomonaga-luttinger liquid. *Physical Review B*, 93(7), Feb 2016.

[165] Kosuke Itoh, Ryo Nakazawa, Tomoaki Ota, Masayuki Hashisaka, Koji Muraki, and Toshimasa Fujisawa. Signatures of a non-thermal metastable state in copropagating quantum hall edge channels. *ArXiv e-prints*, 2018.

[166] J. Eisert, M. Friesdorf, and C. Gogolin. Quantum many-body systems out of equilibrium. *Nature Physics*, 11(2):124–130, Feb 2015.

[167] Luca D'Alessio, Yariv Kafri, Anatoli Polkovnikov, and Marcos Rigol. From quantum chaos and eigenstate thermalization to statistical mechanics and thermodynamics. *Advances in Physics*, 65(3):239–362, May 2016.

[168] Fabian H L Essler and Maurizio Fagotti. Quench dynamics and relaxation in isolated integrable quantum spin chains. *Journal of Statistical Mechanics: Theory and Experiment*, 2016(6):064002, Jun 2016.

[169] Toshiya Kinoshita, Trevor Wenger, and David S. Weiss. A quantum newton's cradle. *Nature*, 440(7086):900–903, Apr 2006.

[170] M. Gring, M. Kuhnert, T. Langen, T. Kitagawa, B. Rauer, M. Schreitl, I. Mazets, D. A. Smith, E. Demler, and J. Schmiedmayer. Relaxation and prethermalization in an isolated quantum system. *Science*, 337(6100):1318–1322, Sep 2012.

[171] S. Trotzky, Y-A. Chen, A. Flesch, I. P. McCulloch, U. Schollwöck, J. Eisert, and I. Bloch. Probing the relaxation towards equilibrium in an isolated strongly correlated one-dimensional bose gas. *Nature Physics*, 8(4):325–330, Feb 2012.

[172] Marcos Rigol, Vanja Dunjko, Vladimir Yurovsky, and Maxim Olshanii. Relaxation in a completely integrable many-body quantum system: AnAb InitioStudy of the dynamics of the highly excited states of 1d lattice hard-core bosons. *Physical Review Letters*, 98(5), Feb 2007.

[173] Lev Vidmar and Marcos Rigol. Generalized gibbs ensemble in integrable lattice models. *Journal of Statistical Mechanics: Theory and Experiment*, 2016(6):064007, Jun 2016.

[174] M. A. Cazalilla. Effect of suddenly turning on interactions in the luttinger model. *Physical Review Letters*, 97(15), Oct 2006.

[175] D. M. Kennes, C. Klöckner, and V. Meden. Spectral properties of one-dimensional fermi systems after an interaction quench. *Physical Review Letters*, 113(11), Sep 2014.

[176] J. M. Leinaas and J. Myrheim. On the theory of identical particles. *Il Nuovo Cimento B (1971-1996)*, 37(1):1–23, Jan 1977.

[177] Frank Wilczek. Quantum mechanics of fractional-spin particles. *Phys. Rev. Lett.*, 49:957–959, Oct 1982.

[178] Sumathi Rao. *Introduction to abelian and non-abelian anyons*, pages 399–437. Springer Singapore, Singapore, 2017.

[179] Jürg Fröhlich. *Statistics of Fields, the Yang-Baxter Equation, and the Theory of Knots and Links*, pages 71–100. Springer US, Boston, MA, 1988.

[180] Sankar Das Sarma, Michael Freedman, and Chetan Nayak. Majorana zero modes and topological quantum computation. *npj Quantum Information*, 1(1), Oct 2015.

[181] Netanel H. Lindner, Erez Berg, Gil Refael, and Ady Stern. Fractionalizing Majorana fermions: Non-Abelian statistics on the edges of Abelian quantum Hall states. *Phys. Rev. X*, 2:041002, 2012.

[182] Yu I. Manin. *Vychislimoe i Nevychislimoe (Computable and Noncomputable)*. Sov. Radio (Moscow), 1980.

[183] Richard P. Feynman. Simulating physics with computers. *International Journal of Theoretical Physics*, 21(6):467–488, Jun 1982.

[184] Richard P. Feynman. Quantum mechanical computers. *Foundations of Physics*, 16(6):507–531, Jun 1986.

[185] Deutsch D. Quantum theory, the church–turing principle and the universal quantum computer. *Proceedings of the Royal Society of London A: Mathematical, Physical and Engineering Sciences*, 400(1818):97–117, 1985.

[186] P. W. Shor. Algorithms for quantum computation: Discrete logarithms and factoring. *Proceedings of the 35th Annual Symposium on Foundations of Computer Science*, pages 124–134, 1994.

[187] Adrian Hutter and Daniel Loss. Quantum computing with parafermions. *Phys. Rev. B*, 93:125105, Mar 2016.

[188] Michael A. Nielsen and Isaac L. Chuang. *Quantum Computation and Quantum Information*. Cambridge University Press, 2009.

[189] Daniel Litinski and Felix von Oppen. Quantum computing with majorana fermion codes. *Phys. Rev. B*, 97:205404, May 2018.

[190] Daniel Litinski, Markus S. Kesselring, Jens Eisert, and Felix von Oppen. Combining topological hardware and topological software: Color-code quantum computing with topological superconductor networks. *Phys. Rev. X*, 7:031048, Sep 2017.

[191] Pierre Pfeuty. The one-dimensional ising model with a transverse field. *Annals of Physics*, 57(1):79 – 90, 1970.

[192] Stefan Backens, Alexander Shnirman, Yuriy Makhlin, Yuval Gefen, Johan E. Mooij, and Gerd Schön. Emulating majorana fermions and their braiding by ising spin chains. *Phys. Rev. B*, 96:195402, Nov 2017.

[193] Eduardo Fradkin and Leo P. Kadanoff. Disorder variables and para-fermions in two-dimensional statistical mechanics. *Nuclear Physics B*, 170(1):1 – 15, 1980.

[194] Jason Alicea and Paul Fendley. Topological phases with parafermions: theory and blueprints. *Ann. Rev. Cond. Mat. Phys.*, 7:119, March 2016.

[195] Ye Zhuang, Hitesh J. Changlani, Norm M. Tubman, and Taylor L. Hughes. Phase diagram of the Z_3 parafermionic chain with chiral interactions. *Phys. Rev. B*, 92:035154, Jul 2015.

[196] Rodney J. Baxter. *Exactly Solved Models in Statistical Mechanics (Dover Books on Physics)*. Dover Publications, 2008.

[197] Michael H. Freedman, Michael Larsen, and Zhenghan Wang. A modular functor which is universal for quantum computation. *Communications in Mathematical Physics*, 227(3):605–622, Jun 2002.

[198] Lukasz Fidkowski and Alexei Kitaev. Topological phases of fermions in one dimension. *Phys. Rev. B*, 83:075103, 2011.

[199] Ari M. Turner, Frank Pollmann, and Erez Berg. Topological phases of one-dimensional fermions: An entanglement point of view. *Phys. Rev. B*, 83:075102, Feb 2011.

[200] Christoph P. Orth, Rakesh P. Tiwari, Tobias Meng, and Thomas L. Schmidt. Non-abelian parafermions in time-reversal invariant interacting helical systems. *Phys. Rev. B*, 91:081406(R), 2015.

[201] Yuval Vinkler-Aviv, Piet W. Brouwer, and Felix von Oppen. Z4 parafermions in an interacting quantum spin hall josephson junction coupled to an impurity spin. *Phys. Rev. B*, 96(19):195421, Nov 2017.

[202] C. Fleckenstein, N. Traverso Ziani, and B. Trauzettel. $\mathbb{Z}_4$ parafermions in weakly interacting superconducting constrictions at the helical edge of quantum spin hall insulators. *ArXiv e-prints*, 2018.

[203] Jelena Klinovaja and Daniel Loss. Parafermions in interacting nanowire bundle. *Phys. Rev. Lett.*, 112:246403, 2013.

[204] Jelena Klinovaja and Daniel Loss. Time-reversal invariant parafermions in interacting Rashba nanowires. *Phys. Rev. B*, 90:045118, Jul 2014.

[205] Christopher J. Pedder, Tobias Meng, Rakesh P. Tiwari, and Thomas L. Schmidt. Missing shapiro steps and the 8π-periodic josephson effect in interacting helical electron systems. *Phys. Rev. B*, 96:165429, October 2017.

[206] David J. Clarke, Jason Alicea, and Kirill Shtengel. Exotic non-Abelian anyons from conventional fractional quantum Hall states. *Nat. Comm.*, 4:1348, 2013.

[207] Abolhassan Vaezi. Superconducting analogue of the parafermion fractional quantum hall states. *Physical Review X*, 4(3), Jul 2014.

[208] Aaron Chew, David F. Mross, and Jason Alicea. Fermionized parafermions and symmetry-enriched majorana modes. *Phys. Rev. B*, 98:085143, Aug 2018.

[209] Leonardo Mazza, Fernando Iemini, Marcello Dalmonte, and Christophe Mora. Poor man's parafermions in a lattice model with even multiplet pairing. arXiv:1801.08548 [cond-mat], January 2018.

[210] Emilio Cobanera and Gerardo Ortiz. Fock parafermions and self-dual representations of the braid group. *Phys. Rev. A*, 89(1):012328, January 2014.

[211] Paul Fendley. Free parafermions. *J. Phys. A: Math. Theor.*, 47(7):075001, 2014.

[212] Nick Bultinck, Dominic J. Williamson, Jutho Haegeman, and Frank Verstraete. Fermionic matrix product states and one-dimensional topological phases. *Phys. Rev. B*, 95:075108, Feb 2017.

[213] Ole Jürgensen, Florian Meinert, Manfred J. Mark, Hanns-Christoph Nägerl, and Dirk-Sören Lühmann. Observation of density-induced tunneling. *Phys. Rev. Lett.*, 113:193003, Nov 2014.

[214] F. Meinert, M. J. Mark, K. Lauber, A. J. Daley, and H.-C. Nägerl. Floquet engineering of correlated tunneling in the bose-hubbard model with ultracold atoms. *Phys. Rev. Lett.*, 116:205301, May 2016.

[215] S. Baier, M. J. Mark, D. Petter, K. Aikawa, L. Chomaz, Z. Cai, M. Baranov, P. Zoller, and F. Ferlaino. Extended bose-hubbard models with ultracold magnetic atoms. *Science*, 352(6282):201–205, 2016.

[216] S. Kivelson, W.-P. Su, J. R. Schrieffer, and A. J. Heeger. Missing bond-charge repulsion in the extended hubbard model: Effects in polyacetylene. *Phys. Rev. Lett.*, 58:1899–1902, May 1987.

[217] J.E. Hirsch. Bond-charge repulsion and hole superconductivity. *Physica C: Superconductivity*, 158(3):326 – 336, 1989.

[218] J.E. Hirsch. Inapplicability of the hubbard model for the description of real strongly correlated electrons. *Physica B: Condensed Matter*, 199-200:366 – 372, 1994.

[219] Matteo Acciai, Matteo Carrega, Jérôme Rech, Thibaut Jonckheere, Thierry Martin, and Maura Sassetti. Probing interactions via nonequilibrium momentum distribution and noise in integer quantum hall systems at ν=2. *Physical Review B*, 98(3), Jul 2018.

[220] Eduardo Fradkin. *Field Theories of Condensed Matter Physics*. Cambridge University Press, 2013.

[221] Ryogo Kubo. Statistical-mechanical theory of irreversible processes. i. general theory and simple applications to magnetic and conduction problems. *Journal of the Physical Society of Japan*, 12(6):570–586, 1957.

[222] Luca Vannucci, Flavio Ronetti, Giacomo Dolcetto, Matteo Carrega, and Maura Sassetti. Interference-induced thermoelectric switching and heat rectification in quantum hall junctions. *Physical Review B*, 92(7), Aug 2015.

[223] G. Dolcetto, F. Cavaliere, and M. Sassetti. Magnetic ac control of the spin textures in a helical luttinger liquid. *Physical Review B*, 89(12), Mar 2014.

[224] M A Cazalilla and Ming-Chiang Chung. Quantum quenches in the luttinger model and its close relatives. *Journal of Statistical Mechanics: Theory and Experiment*, 2016(6):064004, Jun 2016.

[225] F. M. Gambetta, F. Cavaliere, R. Citro, and M. Sassetti. Universal transport dynamics in a quenched tunnel-coupled luttinger liquid. *Physical Review B*, 94(4), Jul 2016.

[226] Fernando Iemini, Christophe Mora, and Leonardo Mazza. Topological phases of parafermions: A model with exactly solvable ground states. *Phys. Rev. Lett.*, 118:170402, Apr 2017.